

SLAC-479
UC-414

GENERATION AND CHARACTERIZATION OF SUB-PICOSECOND ELECTRON BUNCHES*

Pamela Hsienping Kung

Stanford Linear Accelerator Center
Stanford University, Stanford, CA 94309

SLAC-REPORT-479
March 1996

Prepared for the Department of Energy
under contract number DE-AC03-76SF00515

Printed in the United States of America. Available from the National Technical Information Service, U.S. Department of Commerce, 5285 Port Royal, Springfield, Virginia 22161

*Ph.D. thesis, Stanford University, Stanford, CA.

Abstract

SUNSHINE (Stanford University Short Intense Electron Source), a facility to generate high-intensity, sub-picosecond electron bunches hence coherent radiation in the far-infrared (FIR), is realized. The system is composed mainly of an rf gun with a thermionic cathode and an alpha magnet serving as the bunch compressor. The electron beam is then accelerated to 30 MeV by a linac. The coherent radiation generated by the electron bunches cover the wavelength ranging from $40\ \mu\text{m}$ to more than 1 millimeter.

Simulations of the beam dynamics in the rf gun are discussed in Chapter 2. The shock wave instability for low energy beams due to space charge force is studied in Chapter 3.

The principle of magnetic compression is presented in Chapter 4. The bunch length calculation, both the simplified first order matrix formulation and actual computation including the divergence effects are also discussed in Chapter 4

Both synchrotron and transition radiation from the electron beam are proved to be coherent. Indirect and direct measurements for the bunch length in comparison with simulations are shown in Chapter 5. Various effects that affect the bunch length and the reasons for discrepancy are described.

My main contributions to this project are the formulation of shock wave instability, the first order matrix formulation of bunch compression, computations by six dimensional phase space coordinate trackings and collaboration in radiation and bunch length measurements.

Throughout this thesis, cgs units are used. When conversion to MKS is necessary, the factors are enclosed in brackets.

Acknowledgements

I am very fortunate to have Professor Helmut Wiedemann as my thesis advisor. He introduced and encouraged me into the field of accelerator physics and gave me this exciting topic on sub-picosecond electron bunches. This work would not have been done without his vision and guidance.

I am also grateful to my readers — Professor Pantell and Pianetta for taking their time to give me suggestions.

Thanks go to Michael Borland who showed me how to use MASK. He also graciously let me use his codes: RFGUN, ELEGANT and other utility programs on SSRL VAX SSRL01.

My colleagues: David Bocek, Michael Hernandez and Hung-chi Lihn, have helped me in numerous occasions in this project. I cannot list each contribution from each person so I apologize if I have missed anything. David Bocek is the one who worked out the optical collection efficiency for synchrotron radiation. Hung-chi Lihn wrote many routines for SUNSHINE: the routines for calculating the total radiation energy for transition radiation and synchrotron radiation, the control program for Michelson interferometer and data acquisition program for LeCroy oscilloscope and the program to infer the bunch length from a Michelson interferogram.

I am also in great debt to Jim Sebek for being patient in many exhausting discussions and giving so many valuable suggestions. He also helped me a lot on hardware.

Finally and most of all, I thank my husband, Terry, who has been a constant source of support and serenity. This work is dedicated to him.

Contents

Abstract	ii
Acknowledgements	iii
1 Introduction	1
1.1 Overview	3
1.1.1 RF Gun Overview	3
1.1.2 Beamline Overview	7
1.2 Coherent Radiation	7
1.2.1 Temporal Coherence	10
1.2.2 Spatial Coherence	14
1.3 Characterization of Sub-picosecond Bunches	14
1.3.1 Synchrotron Radiation	15
1.3.2 Transition Radiation	16
2 Beam Dynamics in the RF Gun and Simulations	20
2.1 Nominal Running Conditions	26
2.1.1 Bunching by RF Acceleration	26
2.1.2 Electron Beam Parameters at the Gun Exit	38
2.2 Effect of Acceleration	40
2.3 Effect of Cathode Current Density	42
2.3.1 Oscillations in Longitudinal Phase Space	48
2.4 Photo-Cathode	56

3	Shock Wave Instability	60
3.1	Derivation of the Equation of Motion	60
3.1.1	Continuum Approximation	61
3.1.2	Radial Force	64
3.1.3	Equation of Motion in the Beam Frame	65
3.2	Discussion	68
3.2.1	Classification of the System	68
3.2.2	Space Charge Wave in a Uniform, Monochromatic Beam . . .	69
3.2.3	Symmetry Properties	70
3.2.4	Shock Wave Instability	70
3.3	Difference Scheme and Numerical Results	75
3.3.1	Validity of the FTCS Scheme	77
3.3.2	Gaussian Distribution without Acceleration	78
3.3.3	Trapezoidal Distribution without Acceleration	78
3.3.4	Effect of Current Density	81
3.3.5	Effect of Acceleration	81
3.3.6	Conclusion	86
4	Bunch Compression and Computation	88
4.1	Overview of the Alpha Magnet	89
4.2	First Order Matrix Formulation	92
4.2.1	Drift Space	94
4.2.2	Dipole	94
4.2.3	Alpha Magnet	95
4.2.4	GTL	96
4.2.5	Travelling Wave Linac	97
4.3	Bunch Length Computation	98
4.3.1	First Order Prediction	98
4.3.2	Estimation of Bunch Lengthening after the Linac	103
4.3.3	Estimation of the Divergence Effect	104
4.3.4	Actual Calculation	108

5	Experimental Results and Discussion	123
5.1	Introduction	123
5.2	Setup	124
5.2.1	Beamline	124
5.2.2	Radiation Stations	125
5.2.3	Michelson Interferometer	128
5.3	Momentum Spectra of the Beam from the Gun	131
5.3.1	“Cold” Cathode Operation	132
5.3.2	“Hot” Cathode Operation	136
5.3.3	ABBs On	138
5.4	Momentum Spectrum of the Beam from the Linac	142
5.5	Observation of Coherent Radiation	144
5.5.1	Elimination of Other Sources of Radiation	144
5.5.2	Proof of Coherent Radiation	144
5.6	Radiation Power Compared with the Prediction	146
5.6.1	Comparison	146
5.6.2	Variation of Bunch Length in a Macro-Pulse	148
5.6.3	Correction due to Collection Efficiency	151
5.6.4	Comparison of Expected to Measured Radiation	152
5.7	Bunch Length Measurement	153
5.7.1	Comparison with the Simulation	155
5.7.2	Bunch Length versus Alpha Compression	158
5.8	Discussion	162
5.8.1	Main Reasons that Limit Bunch Compression	162
5.8.2	Reasons for Discrepancy	168
5.9	Conclusion	175
5.9.1	Summary of Results	175
5.9.2	How to Improve	176
A	List of Notations	179
A.1	Miscellaneous	179

A.2 Bunch Length	180
B Running Mean with a Gaussian Filter	181
Bibliography	186

List of Tables

1.1	rf gun parameters.	5
1.2	Electron beam parameters.	7
2.1	Beam parameters at the gun exit for the nominal bunch.	38
2.2	Beam parameters at the gun exit for the core of the beam.	39
2.3	Beam parameters at the gun exit of a photo-cathode beam.	58
4.1	Bunch lengthening due to finite divergence compared with the velocity effect.	105
5.1	Expected total radiation energy compared with measured values.	147
5.2	Expected total radiation energy compared with measured values after including various factors.	153

List of Figures

1.1	Peak power of existing light sources.	2
1.2	rf gun assembly.	4
1.3	Profile of the normalized accelerating field.	5
1.4	B_ϕ and E_ϕ vs z	6
1.5	Top and side view of the beam line.	8
1.6	Top view of GTL.	9
1.7	Coherent enhancement for synchrotron radiation.	13
1.8	An electron crosses the boundary of vacuum and a wall.	16
2.1	Boundary of the first cell in MASK.	21
2.2	FFT of the normalized peak accelerating field.	22
2.3	Phases of four electrons relative to the rf fields at the cathode a) and exit of the first cell b).	23
2.4	Same as Figure 2.3 for higher rf fields.	24
2.5	Longitudinal phase distributions at the gun exit for different accelerating fields.	25
2.6	Longitudinal phase space at $z = \lambda_{rf}/12$	27
2.7	Longitudinal phase space at $z = \lambda_{rf}/6$	28
2.8	Longitudinal phase space at the exit of the first cell.	29
2.9	Longitudinal phase space at $z = 5\lambda_{rf}/12$	30
2.10	Longitudinal phase space at $z = 7\lambda_{rf}/12$	31
2.11	Longitudinal phase space at the gun exit.	32
2.12	Momentum distribution and useful particles.	34
2.13	Central momentum and momentum spread vs distance in the gun.	35

2.14	<i>FWHM</i> and equivalent width vs distance in the gun.	36
2.15	Current vs distance in the gun.	37
2.16	Transverse phase space and beam ellipses at the gun exit for all electrons a) and useful electrons b).	40
2.17	Central momentum and momentum spread a), and normalized current b) vs the accelerating field.	41
2.18	Bunch length a) and geometric emittance b) vs the acceleration.	43
2.19	Central momentum a), and normalized output current b) vs cathode current density.	43
2.20	Bunch length a) and geometric emittance vs cathode current density.	44
2.21	Transverse phase space at the gun exit for $E_{p2} = 75 \text{ MV/m}$, $J = 0.1 \text{ A/cm}^2$	45
2.22	Transverse phase space at the gun exit for $E_{p2} = 75 \text{ MV/m}$, $J = 80 \text{ A/cm}^2$	46
2.23	Longitudinal phase space at the gun exit for $J = 0.1$ a), and 80 A/cm^2 b).	47
2.24	Longitudinal phase space after compression for $J = 0.1$ a), and 40 A/cm^2 b).	47
2.25	Plasma frequency vs cathode current density.	49
2.26	FFT of the peak accelerating field in a high current MASK run.	51
2.27	Longitudinal phase spaces at the gun exit for different longitudinal mesh sizes in MASK.	52
2.28	Longitudinal phase spaces after compression for different longitudinal mesh sizes in MASK.	53
2.29	Analytic and discrete dispersion relation for a circular wave guide.	54
2.30	Longitudinal phase space at the gun exit for a photo-cathode beam.	57
2.31	Transverse phase space at the gun exit for a photo-cathode beam.	58
3.1	Plasma parameters as a function of cathode current density.	63
3.2	Estimated breaking time vs bunch length in the beam frame for an initially mono-chromatic bunch.	73

3.3	Evolution of the density a) and momentum deviation b) of a gaussian bunch in the beam frame without acceleration.	79
3.4	Evolution of the density a) and momentum deviation b) of a trapezoidal bunch in the beam frame without acceleration.	80
3.5	Evolution of the a) density and b) momentum deviation of a trapezoidal bunch of half of total charges in the beam frame.	82
3.6	Evolution of the density of a trapezoidal bunch in the beam frame after the center is accelerated.	83
3.7	Evolution of the momentum deviation of a trapezoidal bunch in the bunch frame after the center is accelerated.	84
3.8	Evolution of the density a) and momentum deviation b) of a trapezoidal bunch in the bunch frame after the center is accelerated.	85
4.1	Particle trajectories in an alpha magnet for different momenta.	90
4.2	Bunch length at the linac exit as a function of the bunch length at the entrance a), and x_{\max} in the alpha magnet b).	99
4.3	Bunch length at the linac exit vs central momentum for a fixed alpha gradient.	102
4.4	First order effect on longitudinal phase space after a drift space a), and after compression b).	106
4.5	Divergence effect on longitudinal phase space after the same drift length as in Figure 4.4a).	107
4.6	Measured longitudinal gradient profile of a short quadrupole and the trapezoidal model.	109
4.7	Longitudinal phase space at the linac entrance a), transition radiator b).	111
4.8	Same as Figure 4.6b) with lower energy scraper in.	112
4.9	Histogram in time a) and form factor b) at the transition radiator.	114
4.10	Calculated equivalent width of the shortest bunch vs the cathode current density.	115
4.11	Calculated peak current of the shortest bunch vs the cathode current density.	116

4.12	Longitudinal phase spaces at the transition radiator with same alpha magnet but different quadrupoles.	117
4.13	Histogram in time a) and form factor b) for Figure 4.12.	118
4.14	Longitudinal phase space at the transition radiator with a higher linac acceleration.	120
4.15	Equivalent bunch length at the linac exit vs linac acceleration.	120
4.16	Bunch length vs linac entrance phase.	121
5.1	Top view of GTL.	124
5.2	Top view of LTD.	126
5.3	Side view of the beam line and radiation stations for a) transition radiation, b) synchrotron radiation.	127
5.4	Schematic drawing of the Michelson interferometer.	129
5.5	Gun power in a macro-pulse.	131
5.6	GTL electron spectrum.	133
5.7	Spectral plot for a normal run (cold cathode) in a macro-pulse.	134
5.8	Central momentum a) and electron current b) versus time in a macro-pulse for a cold cathode.	135
5.9	GTL electron momentum spectrum in a macro-pulse for a hot cathode.	136
5.10	Spectral plot of a macro-pulse for a hot cathode.	137
5.11	Central momentum a) and T1 signal b) versus time in a macro-pulse for a hot cathode.	139
5.12	Spectral plot of a macro-pulse with the ABB's on.	140
5.13	Central momentum a) and T1 signal b) versus time in a macro-pulse with the ABB's on.	141
5.14	Spectral plot for a linac beam.	143
5.15	Bolometer signal versus $\sum_i N_{e,i}^2$ for synchrotron a) and transition radiation b).	145
5.16	Effective peak field in the 2nd cell versus time in a macro-pulse.	150
5.17	Michelson scan a) with its uncorrected and corrected spectrum b).	154
5.18	Central peak of the interferogram	155

5.19	Corrected spectrum compared with the overall form factors.	156
5.20	Measured and calculated average bunch length in a macro-pulse versus alpha gradient.	159
5.21	Measured and most “prominent” bunch in calculations in a macro-pulse vs the alpha gradient.	160
5.22	Peak electron current as a function of the alpha magnet.	161
5.23	Peak electron current as a function of bunch length.	162
5.24	Scan for the shortest bunch, $FWHM = 110 \mu m$ for the path length. .	164
5.25	Longitudinal phase space a) and b) and histograms at the transition radiator b) for normal and reduced aperture including the divergence effect.	171
B.1	FFT of rectangular windows for running means of 3, 5, 7 and 9-point.	182
B.2	Weights of binomial filters of 3, 5, 7 and 9-points in the time domain.	182
B.3	FFTs of binomial windows for running means of 3, 5, 7 and 9-point. .	183
B.4	Weights of Gauss filters of 3, 5, 7 and 9 points in the time domain. .	185
B.5	FFT of Gaussian filters of 3, 5, 7 and 9-point running mean.	185

Chapter 1

Introduction

The goal of the SUNSHINE project is to produce sub-picosecond electron bunches and the coherent far-infrared (FIR) radiation from such bunch distributions. There is a lack of alternative high intensity FIR sources in this wavelength regime which could be covered by the source described here. Figure 1.1 [1] shows the availability of existing light sources. At the low end of the spectrum, there are microwave sources; at the high end in the ultra-violet (UV) and x-ray regime, there are synchrotron radiation storage rings. In the middle, visible light, optical lasers are abundant. But between infrared and microwave in the FIR region, the longest wavelength laser at $10\ \mu\text{m}$ is the CO_2 laser which is not tunable.

Coherent radiation from electrons was first predicted by H. Motz in 1951 [2] and later analyzed theoretically by F. Michel [3] but it was not observed until recently because bunches in older accelerators are not short enough compared with the vacuum chamber for the radiation to propagate [4]. Coherent synchrotron radiation was first observed by a group led by Nakazato in 1989 [5] and Blum in 1991 [6]. Coherent transition radiation was first observed by U. Happek et. al. in 1985 [7] and Y. Shibata et. al. [8] in 1992. But since the bunch lengths in these accelerators are several picosecond long, the radiation is in the mm range. If we compress electron bunches further into the sub-picosecond range, the coherent radiation they produce would be in the FIR range thus filling the gap in Figure 1.1. In addition, since the radiation is coherent, we get an extra boost of power, which is proportional to the number

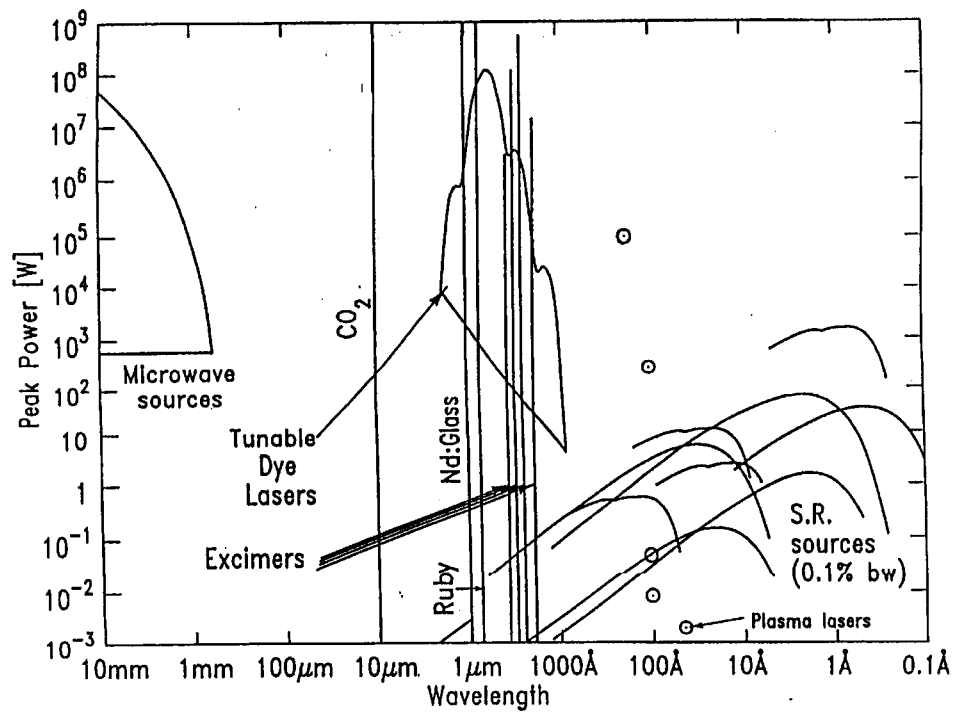


Figure 1.1: Peak power of existing light sources.

of electrons in a bunch, on top of ordinary incoherent radiation. The condition for temporal coherence will be derived in Section 1.2.1.

Short bunches hence coherent radiation can be achieved by different methods. For a circular machine, an isochronous ring can be used [9]. For our beam, this is done by the combination of an rf gun and alpha magnet which is our bunch compressor. The principle of bunch compression by an alpha magnet will be discussed in Chapter 4.

My main contributions to this project are the formulation of shock wave instability which is discussed in Chapter 3, the first order matrix formulation of bunch compression, actual computations by six dimensional phase space coordinate trackings and collaboration in radiation and bunch length measurements.

In this chapter, the overview of SUNSHINE including the rf gun and beam line will be presented and theoretical background for coherent radiation, synchrotron radiation and transition radiation will be discussed briefly.

1.1 Overview

1.1.1 RF Gun Overview

The rf gun in SUNSHINE was designed and built in a collaboration between Varian Assoc. and the Stanford Synchrotron Radiation Laboratory (SSRL) [10, 11]. It consists of 1-1/2-cell resonant cavity operating at 2856 MHz (f_{rf}), $\pi/2$ standing wave mode and a thermionic cathode. It accelerates the electron beam to about 2.5 MeV. Figure 1.2 shows the cross section of the gun. A side coupled cavity between the two cells acts as the rf connection between both. Figure 1.3 shows the normalized accelerating field profile along with the longitudinal cross section of the cavity. The field in the first cell is chosen to be lower than in the second cell to reduce back-bombardment which can cause uncontrollable heat up of the cathode. A detailed discussion of the design criteria for this rf gun can be found in Michael Borland's thesis [12] and [10, 11]. Some rf gun parameters are summarized in Table 1.1 where λ_{rf} is the rf wavelength. Indices 1 or 2 stands for the quantity in the first or second

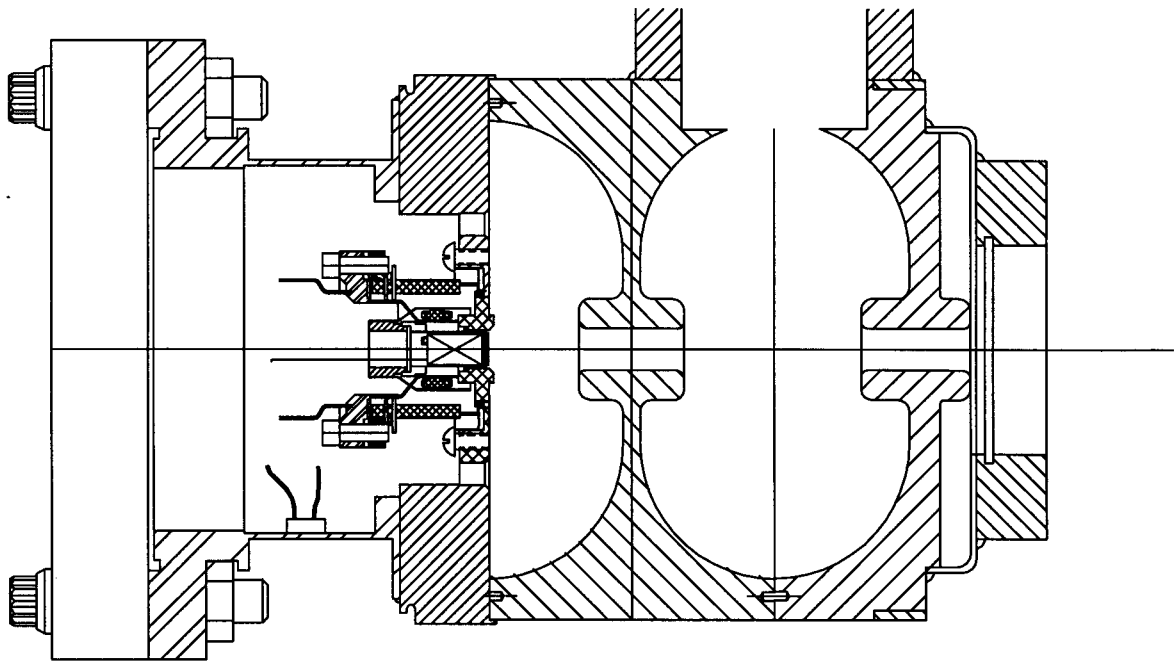


Figure 1.2: rf gun assembly.

f_{rf}	2855.835	MHz	λ_{rf}	10.50	cm
E_{p2}/E_{p1}	2.9		Q_0	14000	
cathode radius	3	mm	T_{cath}	~ 950	$^{\circ}\text{C}$
R_1	2.44	$\text{M}\Omega$	R_2	8.45	$\text{M}\Omega$
l_1	2.624	cm	l_2	5.248	cm
$l_{\text{eff},1}$	1.82	cm	$l_{\text{eff},2}$	3.45	cm
filling time	800	ns			

Table 1.1: rf gun parameters.

cell. The effective length in the i^{th} cell $l_{\text{eff},i}$ is defined as the voltage divided by the peak accelerating field $E_{pi} = \max E(z)$ in that cell:

$$l_{\text{eff},i} = \frac{\int_i dz E_z}{E_{pi}}$$

l_i and R_i are the length and shunt impedance of the i^{th} cell. T_{cath} is the operational temperature for the cathode and Q_0 the quality factor for the $\pi/2$ mode.

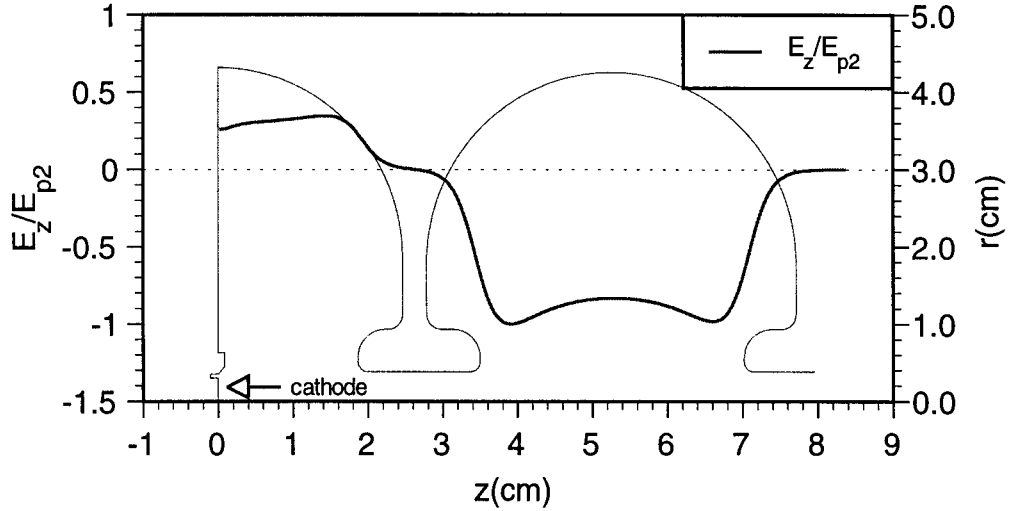


Figure 1.3: Profile of the normalized accelerating field and gun geometry.

Figure 1.4 shows the azimuthal magnetic field and radial electric field profile at a radius of 1 mm for a peak accelerating field in the second cell of 75 MV/m which is the designed value. The radial force was designed to focus the electron beam toward the exit in order to compensate for space charge force.

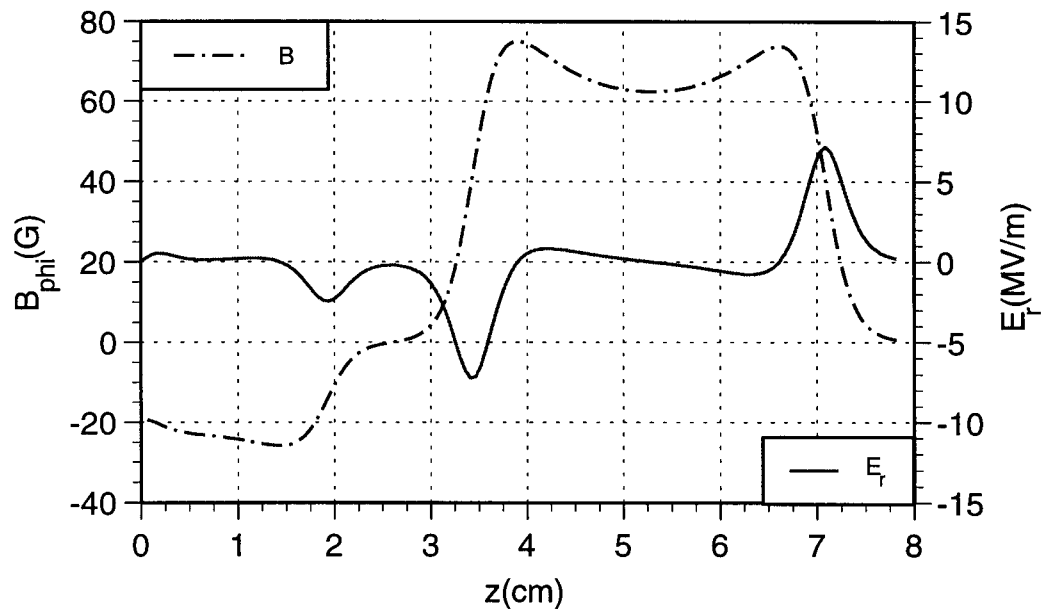


Figure 1.4: B_{ϕ} and E_{ϕ} versus z for $E_{p2} = 75$ MV/m.

number of bunches	\sim	3000	per macro-pulse
N_e	\lesssim	6×10^8	per bunch
macro-pulse length		1	μs
repetition rate		10	Hz
E	\lesssim	30	MeV

Table 1.2: Electron beam parameters.

1.1.2 Beamline Overview

The side and top views of the beam line are shown in Figure 1.5. There are two parts: from the gun to the alpha magnet then to the linac (GTL) and linac to the beam dump at the end (LTD). The first part — GTL, serves several purposes: first to focus the beam into the alpha magnet, which is the bunch compressor; for an efficient energy selection and also to maximize the transmission into the linac. After the bunch is compressed by the alpha magnet, which will be discussed in Chapter 4, the beam is further accelerated to 30 MeV by a linear accelerator (linac). The source points of the radiation are located after the linac shown in Figure 1.5. Figure 1.6 shows the top view of GTL and beginning of the linac. Table 1.2 lists some parameters of the electron beam.

1.2 Coherent Radiation

There are two types of coherence: temporal and spatial coherence. A finite source size in transverse phase space contributes to spatial incoherence and a finite longitudinal bunch length to temporal incoherence. If the length and transverse emittance of the source are much smaller than the wavelength of interest, the radiation becomes both temporally and spatially coherent; i.e., radiation emitted from different parts of a bunch would be in phase. This is highly desirable since the *brightness* of a photon beam, which is the photon density in six-dimensional phase space, is greatly enhanced if the radiation is coherent. For the electron beam considered here, these two conditions are both true in the FIR regime and will be discussed below.

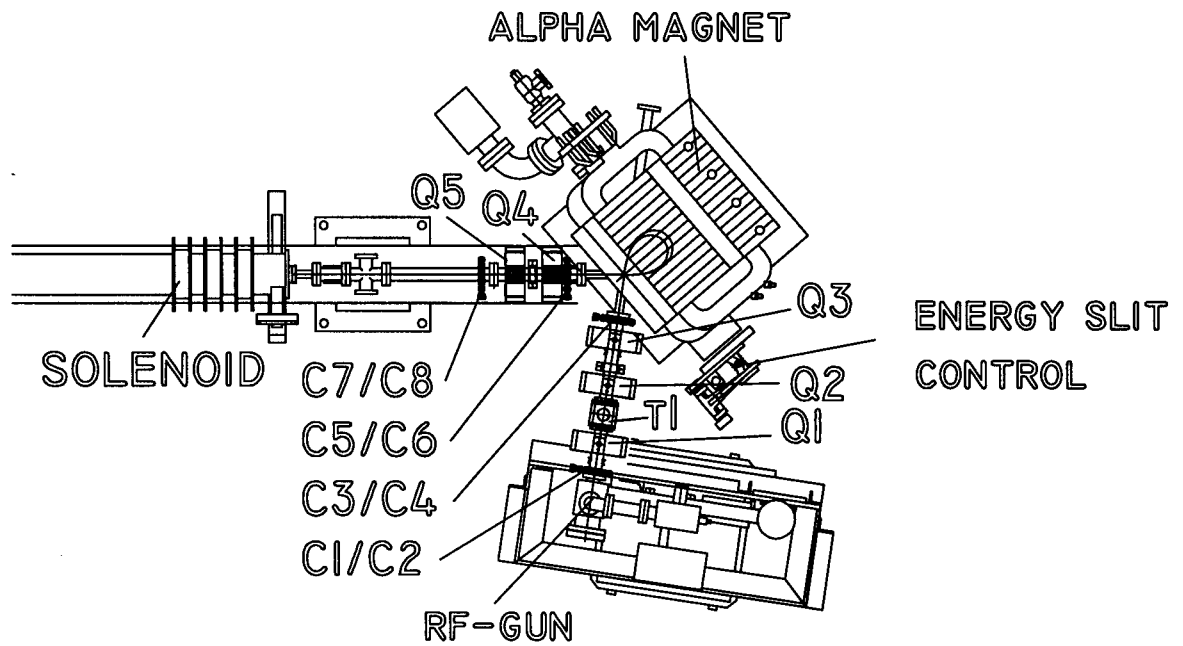


Figure 1.6: Top view of GTL and the linac entrance.

1.2.1 Temporal Coherence

The criteria for temporal coherence can be derived by superposition of the field emitted by each electron in a bunch. Suppose the position between the bunch center and the observation point is \mathbf{R} and $\mathbf{x}_j = x_j \hat{\mathbf{n}}_j = \mathbf{R} + \mathbf{r}_j$ is the position of the j^{th} particle. The field radiated by a bunch of N charged particles is [13]

$$\begin{aligned} \mathbf{E}(k) &= \sum_{j=1}^N \mathbf{E}_j(k) e^{i\mathbf{k}_j \cdot \mathbf{x}_j} \\ &= \sum_{j=1}^N \mathbf{E}_j(k) e^{ik\hat{\mathbf{n}}_j \cdot \mathbf{r}_j} e^{ik\hat{\mathbf{n}}_j \cdot \mathbf{R}}, \end{aligned} \quad (1.1)$$

where $\mathbf{k}_j = k\hat{\mathbf{n}}_j = (\omega/c)\hat{\mathbf{n}}_j$ is the wave vector of the j^{th} particle. If $R \gg r_j$, i.e. if we consider the *far-field* limit, then $\hat{\mathbf{n}}_j \approx \hat{\mathbf{n}}$ or $\mathbf{E}_j(k) \approx E_j(k)\hat{\mathbf{n}}$ and the square of the absolute value of the total electric field in (1.1) becomes

$$\begin{aligned} |\mathbf{E}(k)|^2 &\approx \left| \sum_{j=1}^N E_j(k) e^{ik\hat{\mathbf{n}}_j \cdot \mathbf{r}_j} \right|^2 \\ &= \sum_{j=1}^N P_j(k) + \sum_{j \neq l} E_j(k) E_l^*(k) e^{ik(\mathbf{r}_j - \mathbf{r}_l) \cdot \hat{\mathbf{n}}}, \end{aligned} \quad (1.2)$$

where $P_j(k) = |E_j(k)|^2$. There are two contributions in the above: the first term is the incoherent radiation from the radiation by each particle and the second term from interference of fields by different particles. The latter is the coherent contribution which will be shown to become significant under certain limit.

For a monochromatic bunch, $P_j(k) = P(k)$, the two terms in (1.2) are simply

$$P_1^{\text{mono}}(k) = NP(k) \quad (1.3)$$

$$P_2^{\text{mono}}(k) = P(k) \sum_{j \neq l}^N e^{ik(\mathbf{r}_j - \mathbf{r}_l) \cdot \hat{\mathbf{n}}}. \quad (1.4)$$

If the external field that causes the bunch to radiate is identical for all particles in the bunch, for example, a dipole field for synchrotron radiation, the global phase is the same for all particles and the relevant phase between particles is determined solely by the particle positions, $k\mathbf{r}_j \cdot \hat{\mathbf{n}}$, if we use a classical approach. So we can pull the complex fields in the second term in (1.2) together to get (1.4).

Since $N \gg 1$, the summation in the above can be approximated by an integral. For a given bunch distribution function $f(\mathbf{r})$ such that $N = N \int d\mathbf{r} f(\mathbf{r})$, (1.4) becomes

$$\begin{aligned} P_2^{\text{mono}}(k) &\approx N(N-1)P(k) \int d^3r \int d^3r' e^{ik(\mathbf{r}-\mathbf{r}')\cdot\hat{\mathbf{n}}} f(\mathbf{r}) f(\mathbf{r}') \\ &\approx N^2 P(k) |F(k)|^2, \end{aligned} \quad (1.5)$$

where $|F(k)|^2$ is the *form factor* defined by the square of the Fourier transform of the normalized distribution function,

$$|F(k)|^2 = \left| \int d^3r e^{ik\mathbf{r}\cdot\hat{\mathbf{n}}} f(\mathbf{r}) \right|^2. \quad (1.6)$$

If the bunch distribution is azimuthally symmetric about the propagation direction $\hat{\mathbf{z}}$ and $\hat{\mathbf{n}} \parallel \hat{\mathbf{z}}$, (1.6) can be simplified to

$$|F(k)|^2 = \left| \int_{-\infty}^{\infty} d\zeta e^{ik\zeta} f(\zeta) \right|^2. \quad (1.7)$$

Note that $|F(k)|^2$ approaches unity in the long wavelength (low frequency) limit, i.e.

$$|F(k)|^2 \approx 1 \quad \text{for } k \rightarrow 0;$$

so (1.4) becomes

$$P_{\text{coh}}^{\text{mono}}(k) \approx N^2 P(k) \quad \text{for } k \rightarrow 0, \quad (1.8)$$

which comes naturally since $e^{ik\hat{\mathbf{n}}\cdot(\mathbf{r}_i-\mathbf{r}_j)} \sim 1$ at long wavelengths in (1.4). That is, the phases between individual particles are temporally coherent and the radiation scales as the square of the number of particles in a bunch. In the high frequency (short wavelength) limit, the coherent contribution vanishes since the form factor becomes zero asymptotically,

$$|F(k)|^2 \approx 0 \quad \text{for } k \rightarrow \infty,$$

because the phases of different particles add up randomly to be zero. This causes the radiation to be proportional to the number of particle only,

$$P_{\text{tot}}(k) = P_{\text{inc}}^{\text{mono}}(k) = NP(k).$$

Let us look at the form factors for two typical bunch distributions: uniform and Gaussian distribution. For a uniform bunch distribution of width $2\sigma_z$, we have

$$f(z) = \begin{cases} \frac{1}{2\sigma_z} & \forall |z| < 2\sigma_z \\ 0 & \text{otherwise} \end{cases}.$$

The form factor is

$$|F(k)|^2 = \left(\frac{\sin k\sigma_z}{k\sigma_z} \right)^2. \quad (1.9)$$

from (1.7). For a Gaussian bunch,

$$f(z) = \frac{1}{\sqrt{2\pi}\sigma_z} e^{-\frac{z^2}{2\sigma_z^2}},$$

the form factor is also Gaussian,

$$|F(k)|^2 = e^{-(k\sigma_z)^2}. \quad (1.10)$$

Naturally, a uniform bunch has more high frequency components than a Gaussian bunch because of the sharp edges.

For wavelengths longer than the vacuum chamber dimensions, the radiation is suppressed and cannot propagate [4]. If the bunch length can be compressed to be smaller than the vacuum chamber dimensions which is in cm range, the radiated power is coherent at wavelengths equal and longer than the bunch length. For producing FIR radiation, with wavelengths between a few μm to mm, the electron bunches in SUNSHINE must be no longer than few hundred μm , or equivalently, in the sub-picosecond range.

The radiation is in general not monochromatic but has a frequency dependence which depends on the process creating it and the bunch distribution as in (1.5). A special case occurs if the spectrum is flat; that is, $P(k)$ is independent of frequency, then the coherent radiation spectrum is determined solely by the bunch distribution from (1.5). This is the case for transition radiation which greatly simplifies the task to infer the bunch distribution since the spectrum resembles the form factor which is determined by the bunch distribution. We will use this property as a method to characterize the electron bunches. Transition radiation will be described in the next section.

Example of Coherent Synchrotron Radiation

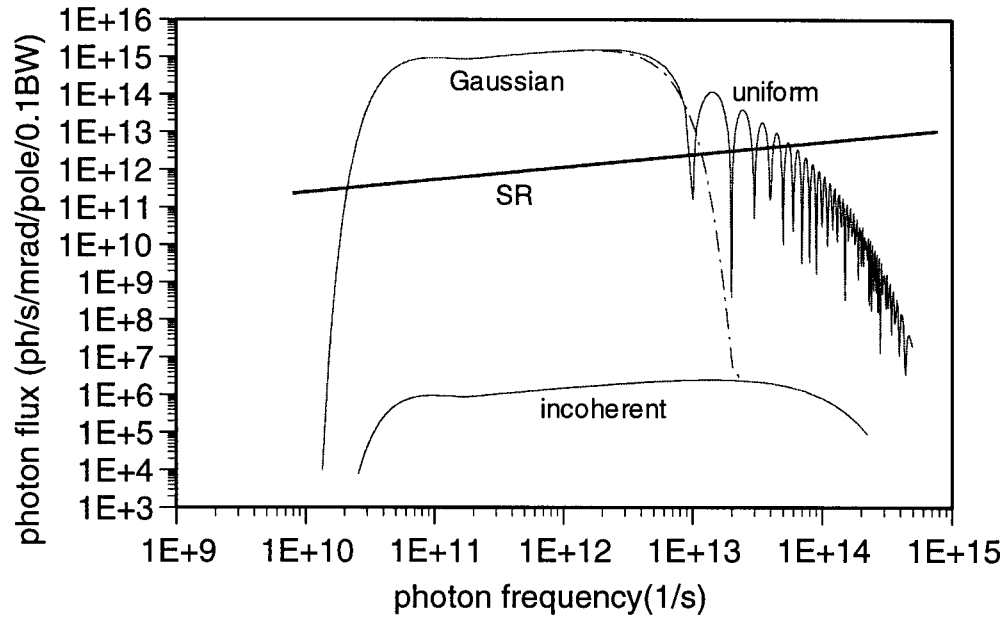


Figure 1.7: Coherent enhancement compared with incoherent synchrotron radiation (SR) for a typical storage ring for different bunch distributions.

Figure 1.7 shows the coherent enhancement of synchrotron radiation on top of the incoherent part for 3000 bunches/pulse, 10 pulses per second (pps), each of length $2\sigma_z = 0.2 \text{ ps} \doteq 60 \mu\text{m}$ and 5×10^8 electrons in a dipole field of 1.9 kG. The coherent part of the radiation spectrum which is in FIR is boosted by a factor of 5×10^8 larger than ordinary incoherent synchrotron radiation, outperforming a typical synchrotron storage ring. Furthermore, since the bunch distribution determines the form factor, a uniform distribution creates more high frequency components compared to a Gaussian distribution as in (1.9) and (1.10). Bunches in a linear accelerator with magnetic compression are usually sharper than a Gaussian, which give us another advantage at high frequencies.

1.2.2 Spatial Coherence

When the transverse source size is finite, the radiation at different parts of the wave front interferes due to path length differences and displays a diffraction pattern. The actual pattern depends on the wavelength λ and transverse bunch distribution. For a Gaussian particle beam, when the emittance of the particle beam is smaller than that of the photon beam [14]

$$\epsilon_{x,y} \leq \epsilon_{\text{ph},x,y} = \frac{\lambda}{4\pi}, \quad (1.11)$$

the radiation distribution is *diffraction limited* and spatially coherent. Apparently this condition is more stringent at short wavelengths. Note that (1.11) is derived assuming a Gaussian transverse particle distribution. For other distributions, some similar limitation should be used.

Let us see what the limit in FIR is. At $\lambda = 100 \mu\text{m}$, (1.11) becomes,

$$\epsilon_{x,y} \leq 8 \times 10^{-6} \text{ m}. \quad (1.12)$$

The emittance of the core of our beam at the gun exit is designed to be about 1 mm·mrad, which increases to about 10 mm·mrad in GTL due to higher order terms in the quadrupoles and alpha magnet. The measured emittance in GTL of the SSRL injector, which is a similar beam line, was about 10 mm·mrad [12]. During the linac acceleration, the emittance reduces by factor of 12 to become less than 1 mm·mrad. So (1.12) is true for our beam in FIR.

Therefore, the radiation from our electron beam is both spatially and temporally coherent, which means that the radiation from different parts of the electron bunch are in phase in FIR. At shorter wavelengths than $10 \mu\text{m}$, (1.12) is less true.

1.3 Characterization of Sub-picosecond Bunches

The fastest streak cameras currently available are of picosecond resolution and it is not possible to measure the bunch lengths of sub-picosecond electron bunches directly in the time domain. We can only characterize the nature of them indirectly

by the radiation they generate. Two types of radiation were observed: synchrotron and transition radiation which will be discussed briefly in the next section.

The radiation was characterized by three methods: radiation energy in a macro-pulse as a function of the electron beam current, total radiation measurement and Michelson interferometer. First, the coherence of the radiation was established by measuring the radiation energy versus electron beam current. Then from the total radiation in a macro-pulse, the average bunch length can be deduced for the measured electron current. Finally, with a Michelson interferometer, the bunch length can be derived following the discussion in Section 1.2.1 that the particle distribution determines the spectrum of coherent transition radiation. The experimental results and principle of Michelson interferometer will be discussed in Chapter 5. Synchrotron and transition radiation will be briefed below.

1.3.1 Synchrotron Radiation

Synchrotron radiation is emitted by a charged particle when being deflected by a magnetic dipole field. In our beam line, this bending magnet is at the end (see Figure 1.5). Since the spectrum of synchrotron radiation has been derived in the literature [15–18], the result is simply given below without derivation. The photon flux per deflection angle ψ for a beam of current I and energy $E = \gamma m_e c^2$ is

$$\frac{d^2 N_{\text{ph}}}{d\psi dt} = \frac{4\alpha}{9} \gamma \frac{\Delta\omega}{\omega} \frac{I}{e} S(\omega/\omega_c), \quad (1.13)$$

where S is an integral function of the modified Bessel function $K_{5/3}$,

$$S(x) = \frac{9\sqrt{3}}{8\pi} \frac{\omega}{\omega_c} \int_{\omega/\omega_c}^{\infty} K_{5/3}(\xi) d\xi, \quad (1.14)$$

and ω_c is the critical photon frequency determined by the beam energy and bending radius ρ ,

$$\omega_c = \frac{3}{2} c \frac{\gamma^3}{\rho}. \quad (1.15)$$

For two extreme cases, $\omega \ll \omega_c$ and $\omega \gg \omega_c$, the Bessel function can be approximated and S is simplified greatly. We get

$$\frac{d^2 N_{\text{ph}}}{d\psi dt} \approx C_\psi EI \frac{\Delta\omega}{\omega} 1.3333x^{1/3} \quad (\omega \ll \omega_c) \quad (1.16)$$

$$\frac{d^2 N_{\text{ph}}}{d\psi dt} \approx C_\psi EI \frac{\Delta\omega}{\omega} 0.77736 \frac{\sqrt{x}}{e^x} \quad (\omega \gg \omega_c), \quad (1.17)$$

where $x = \omega/\omega_c$ and $C_\psi = 3.967 \times 10^{19}$ photons/(s·rad·A·GeV).

1.3.2 Transition Radiation

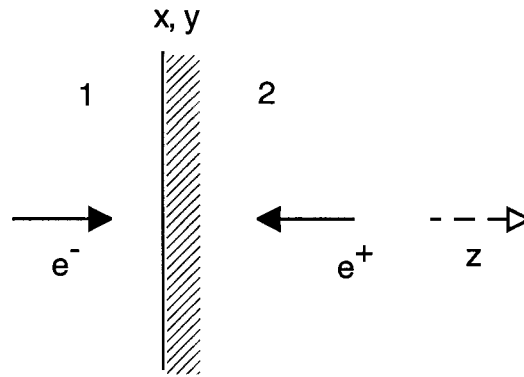


Figure 1.8: An electron with a constant velocity crosses the boundary of vacuum and a perfectly conducting, infinite wall.

Transition radiation occurs when a charged particle passes through an interface of media with different dielectric constants [16, 19–21]. The simplest case is a charge particle hitting a perfectly conducting, infinite wall with normal incidence sketched in Figure 1.8. At a large distance and in the low frequency limit [19], the problem reduces to solving the source free radiation fields from the particle and its image charge of the opposite sign. The radiation is created at the moment when the two charges collide head-on. Let the velocity of the charged particle be $\mathbf{v} = \beta c \hat{\mathbf{z}}$. The source-free fields are plane waves,

$$\begin{aligned} \mathbf{H} &= \frac{1}{c} \dot{\mathbf{A}} \times \mathbf{n} \\ \mathbf{E} &= \frac{1}{c} (\dot{\mathbf{A}} \times \mathbf{n}) \times \mathbf{n}, \end{aligned}$$

where the Lienard-Weichart potential for a moving charge is

$$\mathbf{A} = \left[\frac{e\boldsymbol{\beta}}{R_0(1 - \boldsymbol{\beta} \cdot \mathbf{n})} \right]_{\text{ret}}$$

R_0 is the distance from the observation point to the origin which is near the charge and $\mathbf{n} = \mathbf{R}_0/R_0$ the unit vector; the subscript _{ret} emphasizes that the expression must be evaluated at the retarded time when the radiation is emitted. From the fields we can derive the Poynting vector $\mathbf{S} = c/(4\pi) \mathbf{E} \times \mathbf{H}$ and after a Fourier transform into the frequency domain, we get the angular and spectral distribution of the energy density of the radiation at an angle $\theta = \cos^{-1}(\mathbf{n} \cdot \hat{\mathbf{z}})$ with respect to the z axis,

$$\begin{aligned} \frac{d^2\varepsilon}{d\omega d\Omega} &\approx \frac{c}{4\pi^2} R_0^2 |\mathbf{H}(\omega)|^2 \\ &= \frac{e^2}{\pi^2 c} \frac{\beta^2 \sin^2 \theta}{(1 - \beta^2 \sin^2 \theta)^2}. \end{aligned} \quad (1.18)$$

The radiated energy is azimuthally uniform as expected. Note that the above is valid for the low frequency limit, $\omega \ll 1/\tau$ where τ is the duration of the collision. This is true for all frequencies for a perfect conductor since the collision takes place almost instantaneously.

For an ultra-relativistic particle ($\beta \approx 1$), the radiation distribution has a maximum at an angle $\theta \sim 1/\gamma$ with respect to the beam axis and no radiation in the forward direction ($\theta = 0$) from (1.18). By integrating (1.18) with respect to Ω , the integrated spectral energy density scales like $\ln \gamma$ if $\gamma \gg 1$,

$$\frac{d\varepsilon}{d\omega} = \left[\frac{c}{4\pi} Z_0 \right] \frac{e^2 \ln \gamma}{\pi c 2}, \quad (1.19)$$

where it is divided by 2 because only half of the radiation is collected on one side of the wall and $Z_0 = \sqrt{(\mu_0/\epsilon_0)} = 377 \text{ Ohm}$ is the impedance of free space. Eq. (1.19) is independent of frequency which provides a convenient way of measuring the electron bunch distribution by measuring the spectrum of coherent transition radiation as discussed earlier. For a good conductor ($\epsilon \gg 1$), the spectrum is approximately constant over a large range of frequency well beyond microwave region. In the infrared and above, the conductivity becomes complex and depends on frequency; until near ultra-violet a good conductor becomes transparent [16].

The total radiation energy scales inversely with the bunch length for a monochromatic particle beam,

$$P_{\text{coh}}^{\text{mono}} \sim N^2 \int |F(k)|^2 \frac{dk}{2\pi} = N^2 \int |f(z)|^2 dz \sim \frac{N^2}{l} \quad (1.20)$$

since $f(z) \sim 1/l$ where l is the bunch length.

For a non-perfect conductor with normal incidence, we have to solve the electromagnetic wave equations for a point source by matching the appropriate boundary conditions,

$$\begin{aligned}\nabla^2 \mathbf{A} - \frac{\epsilon_i}{c^2} \frac{\partial^2 \mathbf{A}}{\partial t^2} &= -\frac{4\pi}{c} e\mathbf{v}\delta(\mathbf{r} - \mathbf{v}t), \\ \nabla^2 \phi - \frac{\epsilon_i}{c^2} \frac{\partial^2 \phi}{\partial t^2} &= -\frac{4\pi}{c} e\delta(\mathbf{r} - \mathbf{v}t),\end{aligned}$$

where ϵ_i is the dielectric constant in the i^{th} medium. In our case, the interface is between vacuum ($\epsilon_1 = 1$) and an aluminum foil ($\epsilon_2 = \epsilon \gg 1$). The solutions can be decomposed into two components: the homogeneous solution ($\phi_{\text{photon}}, \mathbf{A}_{\text{photon}}$) which are the radiation fields and the inhomogeneous solution. The boundary conditions at the interface require that E_{\parallel} and D_{\perp} are continuous and $\nabla \cdot \mathbf{E}_{\text{photon}} = 0$ everywhere.

The fields can be solved more easily by a Fourier transform,

$$\Phi(\mathbf{r}, t) = \int \Phi(\mathbf{k}, \omega) e^{i(\mathbf{k} \cdot \mathbf{r} - \omega t)} d^3k d\omega,$$

where Φ stands for \mathbf{A} or ϕ . The derivation is detailed in [21] and [20], so only the result is presented here. For a head-on incidence from vacuum into a wall, the intensity of the backward radiation is

$$\frac{d^2\epsilon}{d\omega d\Omega} = \frac{e^2 \beta^2 \sin^2 \theta \cos^2 \theta}{\pi^2 c (1 - \beta^2 \cos^2 \theta)^2} \left| \frac{(\epsilon - 1) (1 - \beta^2 + \beta \sqrt{\epsilon - \sin^2 \theta})}{(1 + \beta \sqrt{\epsilon - \sin^2 \theta}) (\epsilon \cos \theta + \sqrt{\epsilon - \sin^2 \theta})} \right|^2. \quad (1.21)$$

Note that if ϵ depends on frequency, the radiation is no longer frequency independent in the above. The special case for normal incidence on a perfect conducting wall in (1.18) can be recovered by setting $\epsilon = \infty$ in (1.21).

For a most general case, oblique incidence with an incident angle ψ with respect to z axis on a non-perfect conducting wall, the velocity of the incident particle becomes $\mathbf{v} = \beta c (\sin \psi, 0, \cos \psi) = c(\beta_x, 0, \beta_z)$. The derivation is not different except that the electric field of parallel and perpendicular polarization must be treated separately when matching the boundary conditions at the interface. The intensity for the backward radiation is

$$\frac{d^2\epsilon_{\parallel}}{d\omega d\Omega} = \frac{e^2 \beta_z^2 \cos^2 \theta |\epsilon - 1|^2}{\pi^2 c [(1 - \beta_x^2 \cos^2 \theta_x)^2 - \beta_z^2 \cos^2 \theta]^2 \sin \theta} \times \quad (1.22)$$

$$\frac{d^2 \varepsilon^\perp}{d\omega d\Omega} = \frac{e^2 \beta_x^2 \beta_z^4 \cos^2 \theta_y \cos^2 \theta |\epsilon - 1|^2}{\pi^2 c \left[(1 - \beta_x \cos \theta_x)^2 - \beta_z^2 \cos^2 \theta \right] \sin^2 \theta} \times \frac{1}{\left| (1 + \beta_z \sqrt{\epsilon - \sin^2 \theta} - \beta_x \cos \theta_x) (\sqrt{\epsilon - \sin^2 \theta} + \cos \theta) \right|^2}, \quad (1.23)$$

where $\theta_{x,y}$ is the angle between the observer and the x or y axis which is defined by $\cos \theta_x = \sin \theta \cos \varphi$ and $\cos \theta_y = \sin \theta \sin \varphi$. φ is the azimuthal angle in the $x-y$ plane. Unlike the case for normal incidence, the energy distribution now has an azimuthal dependence. The case for normal incidence in (1.21) can be restored by setting $\psi = 0$ and $\beta_x = \beta_y = 0$ in (1.22) and (1.23).

Chapter 2

Beam Dynamics in the RF Gun and Simulations

The dynamics of charged particles in an rf gun is complicated by the variation of rf fields in space and time, beam loading and in particular, by space charge effect for a dense and low energy beam. To evaluate the evolution of a beam emitted from a cathode with thermal energies and accelerated to relativistic energies upon exit, computer simulation is required.

The simulation was done primarily by the program MASK [22] and additionally by RFGUN [12]. RFGUN integrates the Lorentz equation using a fourth order Runge-Kutta method by expansions of the fields around the beam axis to the third order and does not consider space charge effect. Results from RFGUN agree well with MASK for a very small current density.

MASK uses a particle-in-cell (PIC) (sometimes referred to as particle-mesh) algorithm to integrate Maxwell's equations for macro-particles including self-fields in a user-defined cavity mapped by rectangular meshes. The electron beam is represented by macro-particles, emitted uniformly and randomly by a cold cathode at a given cathode current density and cavity fields. Since the code uses rectangular grids, the mesh sizes must be much smaller than the rf wave length and also sufficiently small to represent the actual structure in the cavity in order to avoid transient fields. There is a compromise between accuracy and computational time. The longitudinal mesh

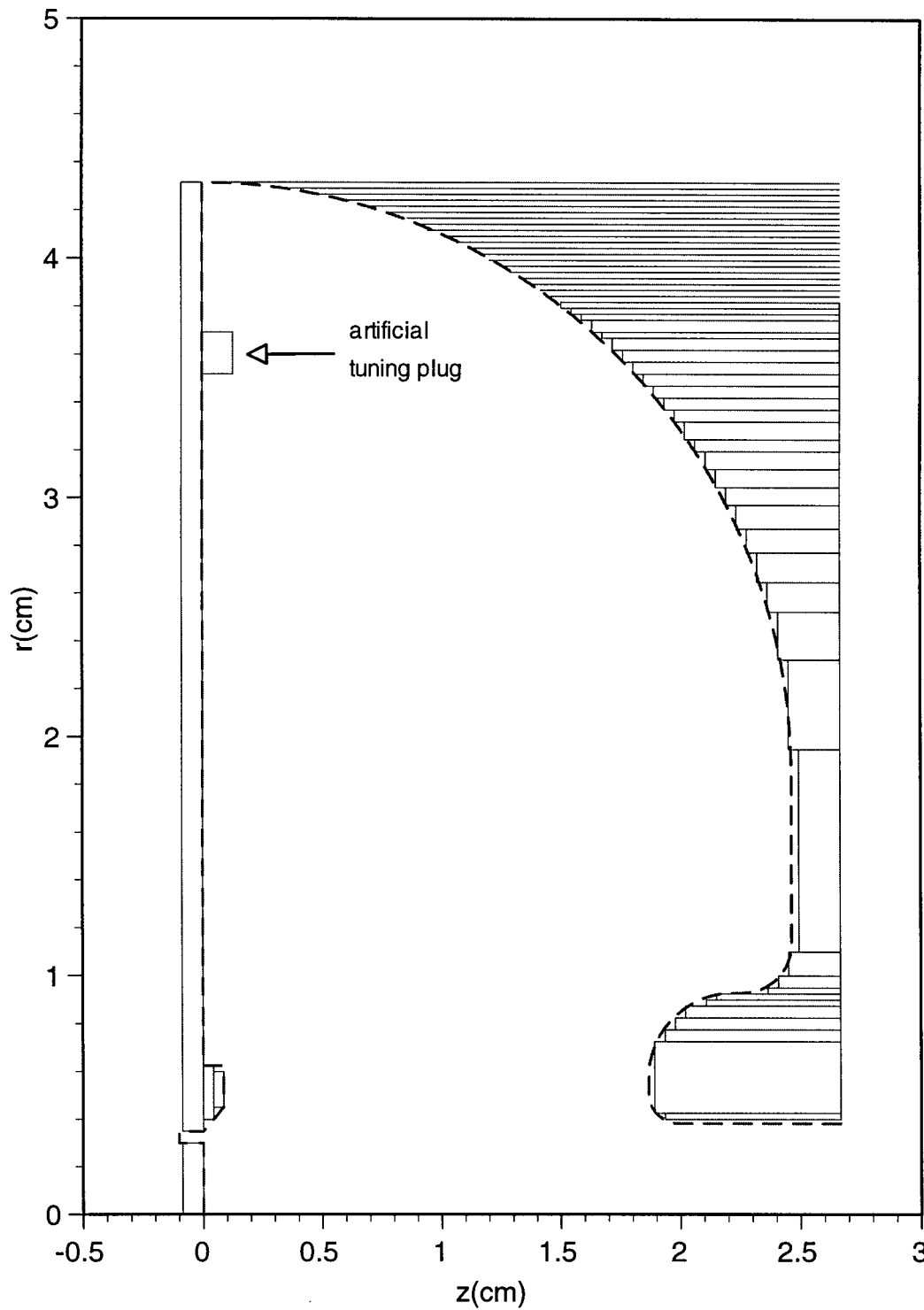


Figure 2.1: Boundary of the first cell in MASK compared with the actual gun.

size was chosen to be 0.4 mm for both cells and radial mesh size to be 0.25 mm for the first cell and 1.1 mm for the second cell. A smaller radial mesh size in the first cell is necessary to model the fields in the vicinity of the cathode. Figure 2.1 shows the comparison of the cavity boundary used in MASK with the actual surface geometry in the first cell. The rectangles are filled with metal by MASK. An artificial tuning plug was added in the first MASK cell to allow the adjustment of the resonant frequency [12].

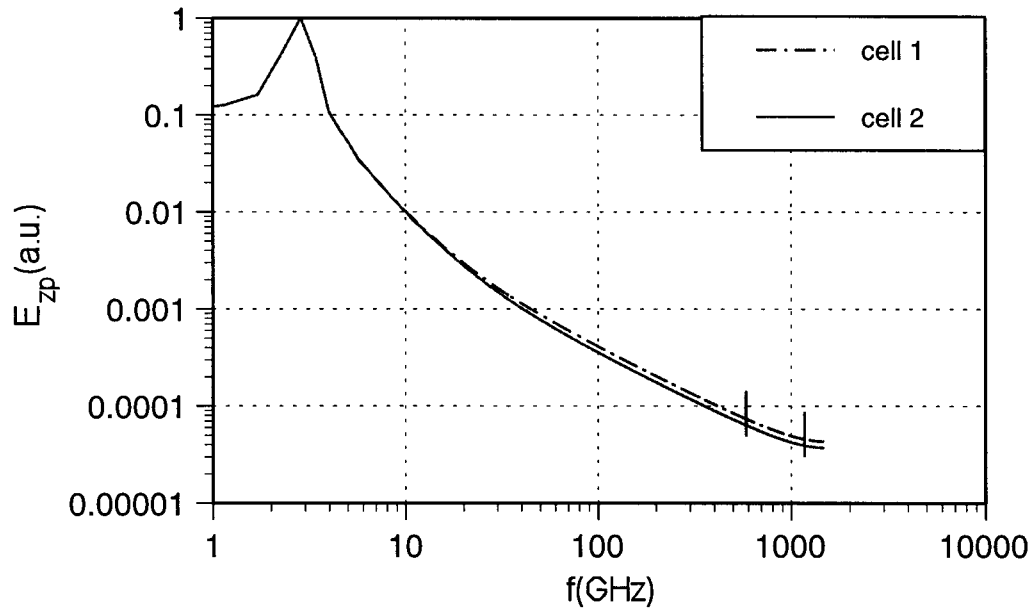


Figure 2.2: FFT of the normalized peak accelerating field. The resolution is 0.57 GHz.

The actual gun requires about 800 ns to reach equilibrium which is more than 2000 rf cycles. Since it takes 4 to 6 CPU hours to finish a MASK run on a VAX DEC5000, to simulate the gun efficiently, the cells in MASK are not driven to equilibrium and the wall loss is not taken into account. The locations and currents of the antennas in both cells, which are 180° out of phase, are chosen such that only the fundamental mode is excited which can be seen from the fast Fourier transform (FFT) of the peak accelerating field in the first cell (E_{p1}) and second cell (E_{p2}) in Figure 2.2 when the rf fields were being ramped up. This approach allows the accelerating field to reach

a steady value after only five cycles before the beam is turned on.

The field distribution at the end of a five cycles MASK run with an empty gun is saved for later runs with particles. Since the fields deposited by a previous bunch are small and the effect of steady state beam loading is equivalent to lower fields in the gun seen by next bunches [12], this allows a simulation to be done for only one rf period. The jagged geometry of the MASK cells due to the finite mesh sizes gives resonant frequencies different from 2856 MHz, hence it introduces a phase difference about $178.6^\circ - 178.9^\circ$ instead of 180° between two cells at the end of five cycles. This error is deemed acceptable.

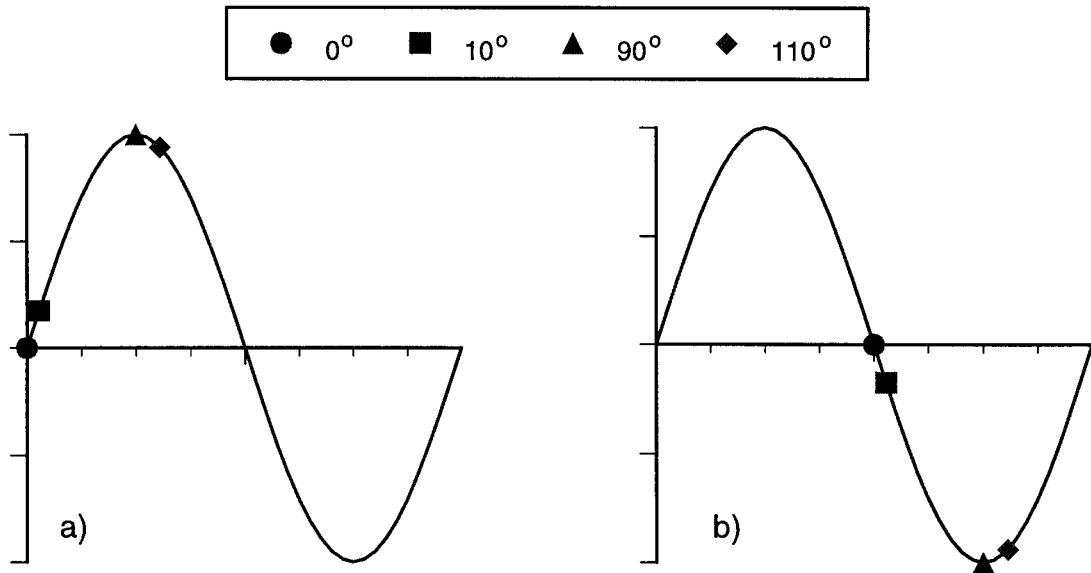


Figure 2.3: Phases of four electrons emitted at $\phi_0 = 0^\circ, 10^\circ, 90^\circ, 110^\circ$ relative to the rf fields at the cathode a) and exit of the first cell b).

The gun was designed for electrons emitted at 0° of the rf phase to ride in accelerating phase throughout acceleration. At the end of half an rf cycle (180°), the first particles exit the first cell and enter the second cell when the accelerating field changes sign. After one full rf cycle the first particles exit the gun. Figure 2.3 shows the phases of particles relative to the rf fields at four different initial phases $\phi_0 = 0^\circ,$

10° , 90° and 110° at the beginning and at the exit of the first cell for a normal run. Naturally, particles that are emitted at a phase of 180° or later experience only deceleration and cannot leave the cathode. The ones emitted later than 90° experience more deceleration than acceleration and are lost within the gun. Only particles emitted between 0° to 90° can possibly be accelerated out of the gun.

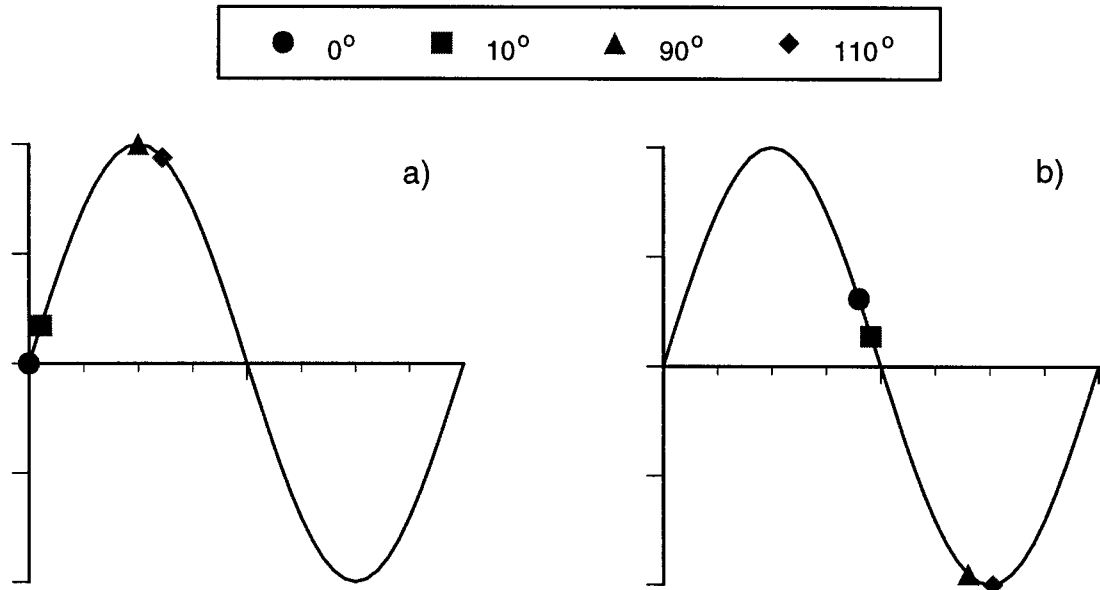


Figure 2.4: Same as Figure 2.3 for higher rf fields.

If the acceleration is larger than the nominal value, particles emitted at 0° by the cathode exit the first cell earlier than 180° before the field changes sign and slightly later particles can exit without experiencing deceleration illustrated in Figure 2.4. If the field is sufficiently high, particles emitted over some range of initial phase undergo the same overall acceleration. The result is a small energy spread at the head of the bunch at the gun exit.

Figure 2.5 shows the longitudinal phase space distributions — momentum versus exit time at the gun exit by RFGUN with three different accelerating fields of $E_{p2} = 120, 75$ and 50 MV/m. The distributions always have sharp rise times about 10

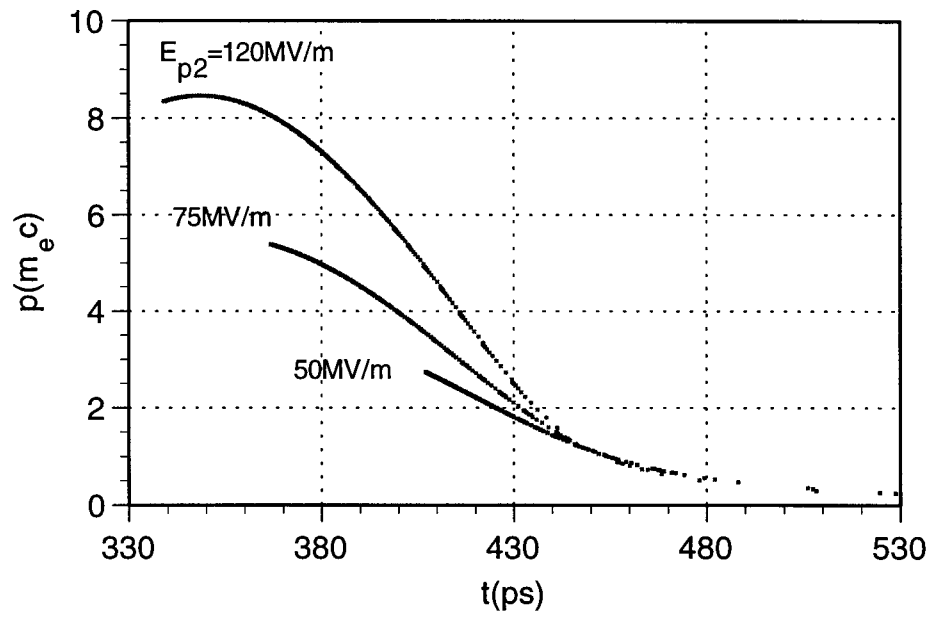


Figure 2.5: Longitudinal phase distributions at the gun exit for different accelerating fields.

to 20 ps and long low energy tails about 200 ps in time, accompanied by a large momentum spread from quasi-relativistic energies down to almost zero due the sinusoidal variation of rf fields in time. At higher rf fields, besides earlier exit times and higher momenta, the sinusoidal shape in the distribution is more pronounced leading to a smaller relative energy spread as demonstrated earlier. This provides a good source for a free electron laser [12, 23] which requires a mono-chromatic particle beam. But such a distribution does not serve as a good candidate for bunch compression into shorter bunches because it requires a monotonic and negative slope in longitudinal phase as will be discussed in Chapter 4.

For optimum bunch compression, normal running conditions for the gun use a peak accelerating field in the second cell of 75 MV/m and a cathode current density between 10 and 20 A/cm². Only about half of the particles, concentrated in the first 10–20 ps, have high enough energies to be really useful. The micro-bunch distribution repeats every 350 ps for a macro-pulse of about 1 μ s corresponding to the duration of the rf pulse.

2.1 Nominal Running Conditions

The bunch distribution for nominal running conditions is optimized for bunch compression for the gun. In the following, all simulations were done using a peak accelerating field in the second cell of 75 MV/m and a cathode current density of 12 A/cm² which gives a current of 3.4 A at the cathode. It reduces to about only one fifth upon exit due to particle loss. However, the peak current at the gun exit doubles because of rf bunching. Rf bunching and beam parameters at the gun exit which will be discussed in this section.

2.1.1 Bunching by RF Acceleration

The longitudinal phase space distribution together with the projections of the particle density both in time and momentum are shown in Figure 2.6 through 2.11 at various locations along the gun axis. In these histograms, a bin in time and

momentum of 1 ps and $0.05 m_e c$ has been used.

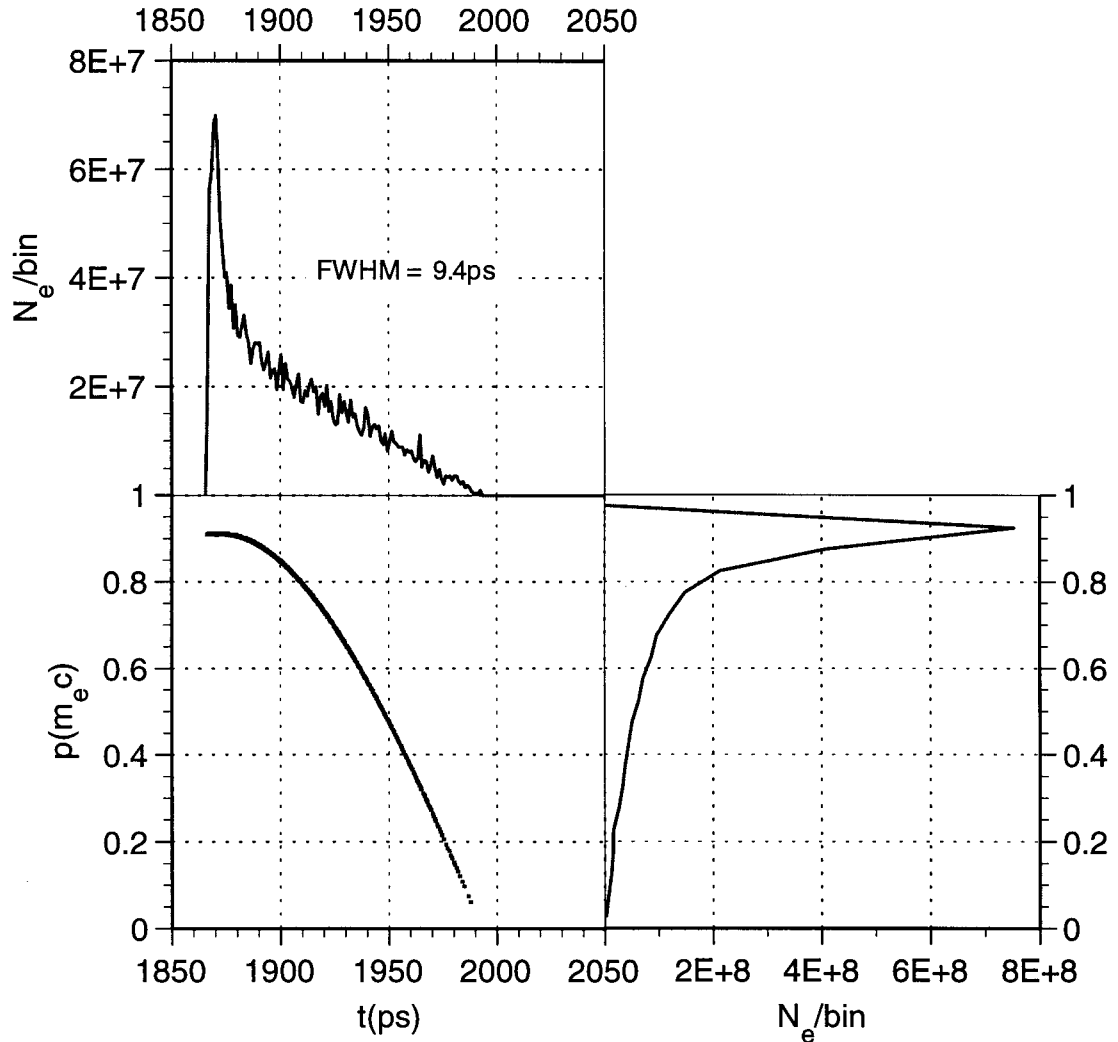


Figure 2.6: Longitudinal phase space at $z = 0.87 \text{ cm} = \lambda_{\text{rf}}/12$.

From Figure 2.6, most electrons are already bunched by the rf accelerating field both in time and momentum less than 1 cm away from the cathode. The bunch length has a full width at half maximum (*FWHM*) of 9.4 ps which does not change significantly during the acceleration. The peak current has increased to 5.2 A, 50% more than the current (3.4 A) at the cathode.

Of all electrons that are emitted at an accelerating phase ($0^\circ - 180^\circ$), the ones

emitted later than 90° are not useful because they experience mainly deceleration (see Figure 2.3). Of all electrons emitted at proper phases, the ones that are slightly later than the first particles experience higher acceleration initially hence they get pushed both forward in time and upward in momentum in phase space resulting the sinusoidal shape at the beginning of the bunch in Figure 2.6 and a momentum spread of about $\pm 4\%$.

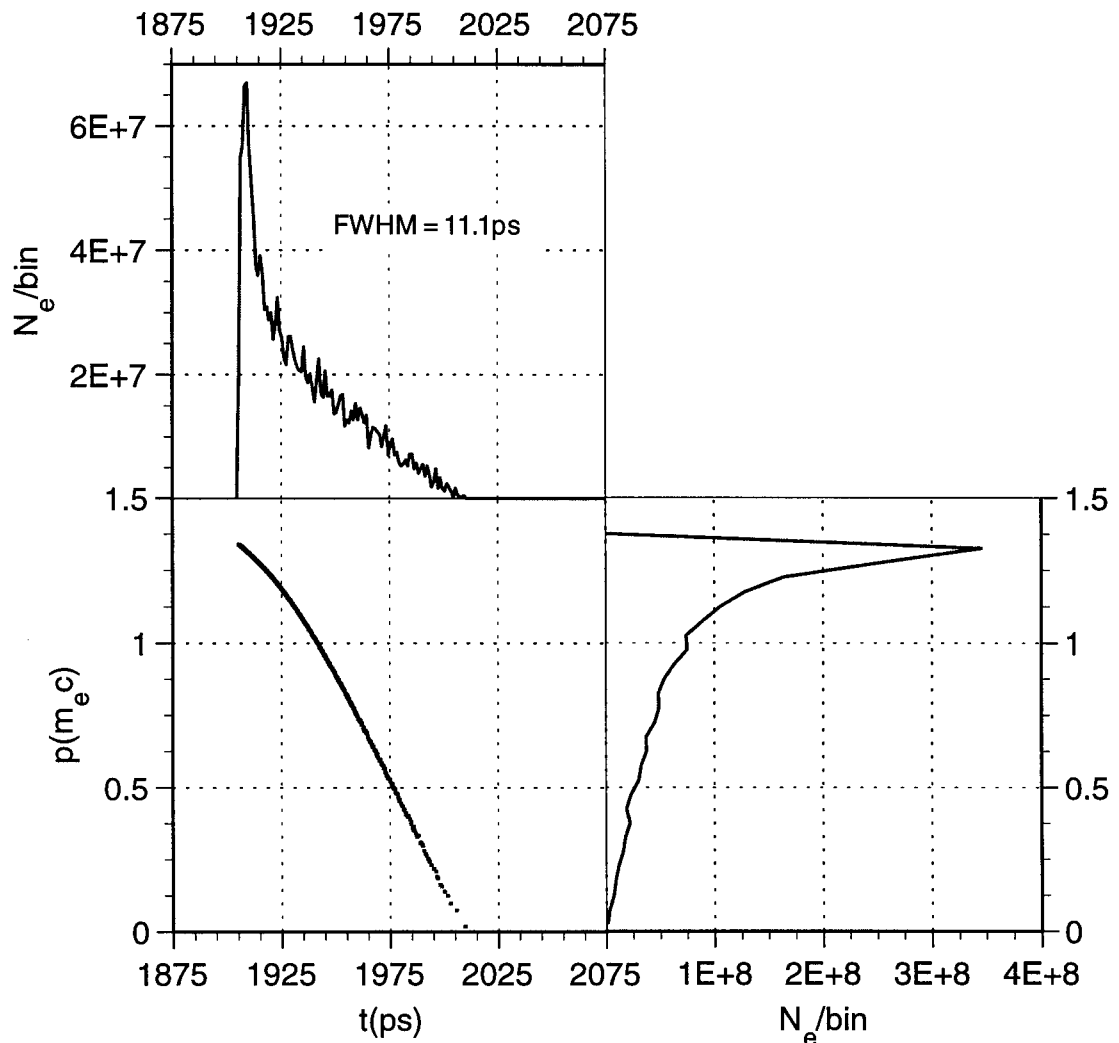


Figure 2.7: Longitudinal phase space at $z = 1.749 \text{ cm} = \lambda_{\text{rf}}/6$.

As time goes on, later particles inevitably experience some deceleration shown in

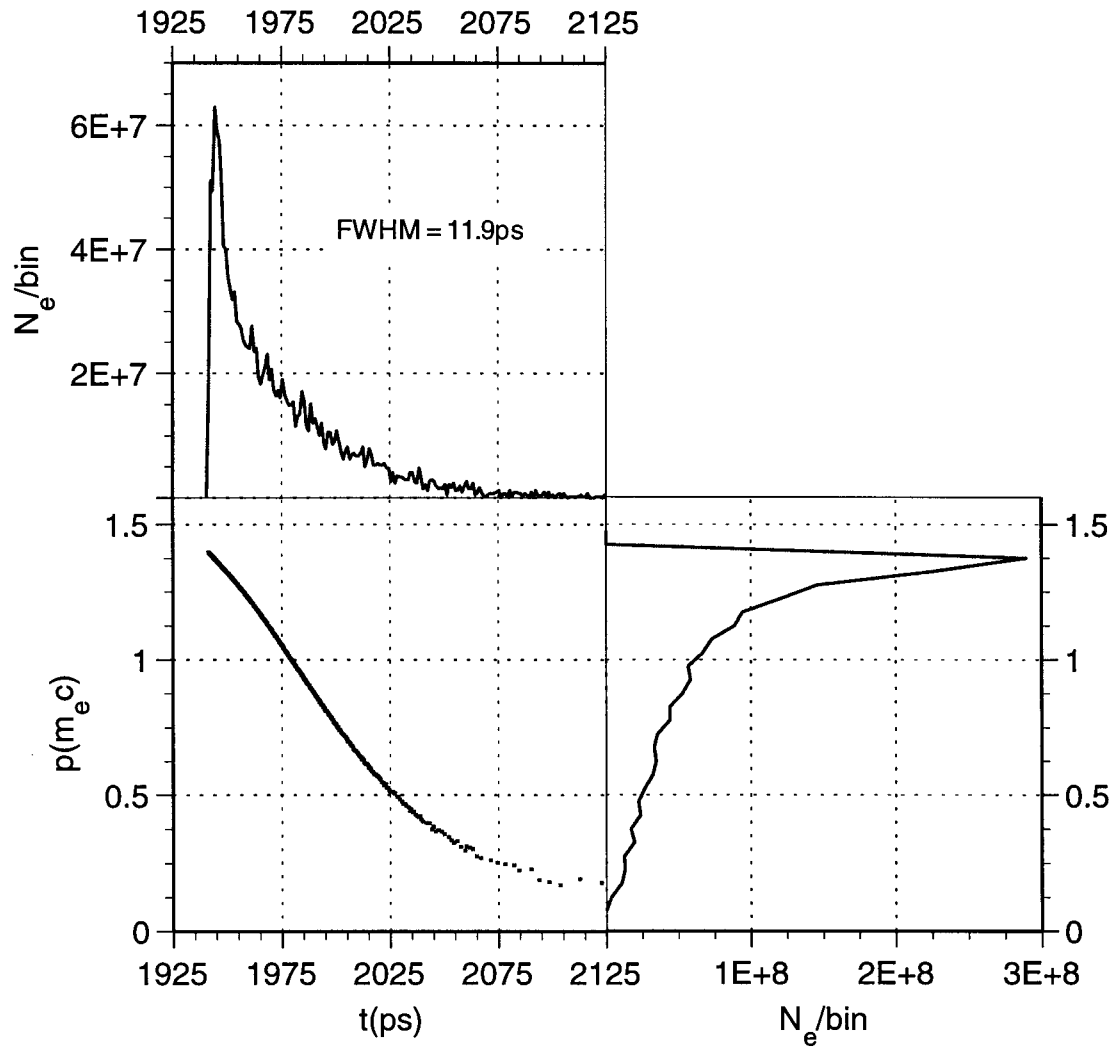


Figure 2.8: Longitudinal phase space at $z = 2.624 \text{ cm} = \lambda_{\text{rf}}/4$ (exit of the first cell).

Figure 2.3 so they get pushed downward in momentum as indicated in Figure 2.7. Eventually in the middle of the drift tube between both cells, at the exit of the first cell (see Figure 1.3), the distribution becomes almost monotonic again in Figure 2.8. Also the bunch length becomes slightly longer at the exit of the first cell due to the drift.

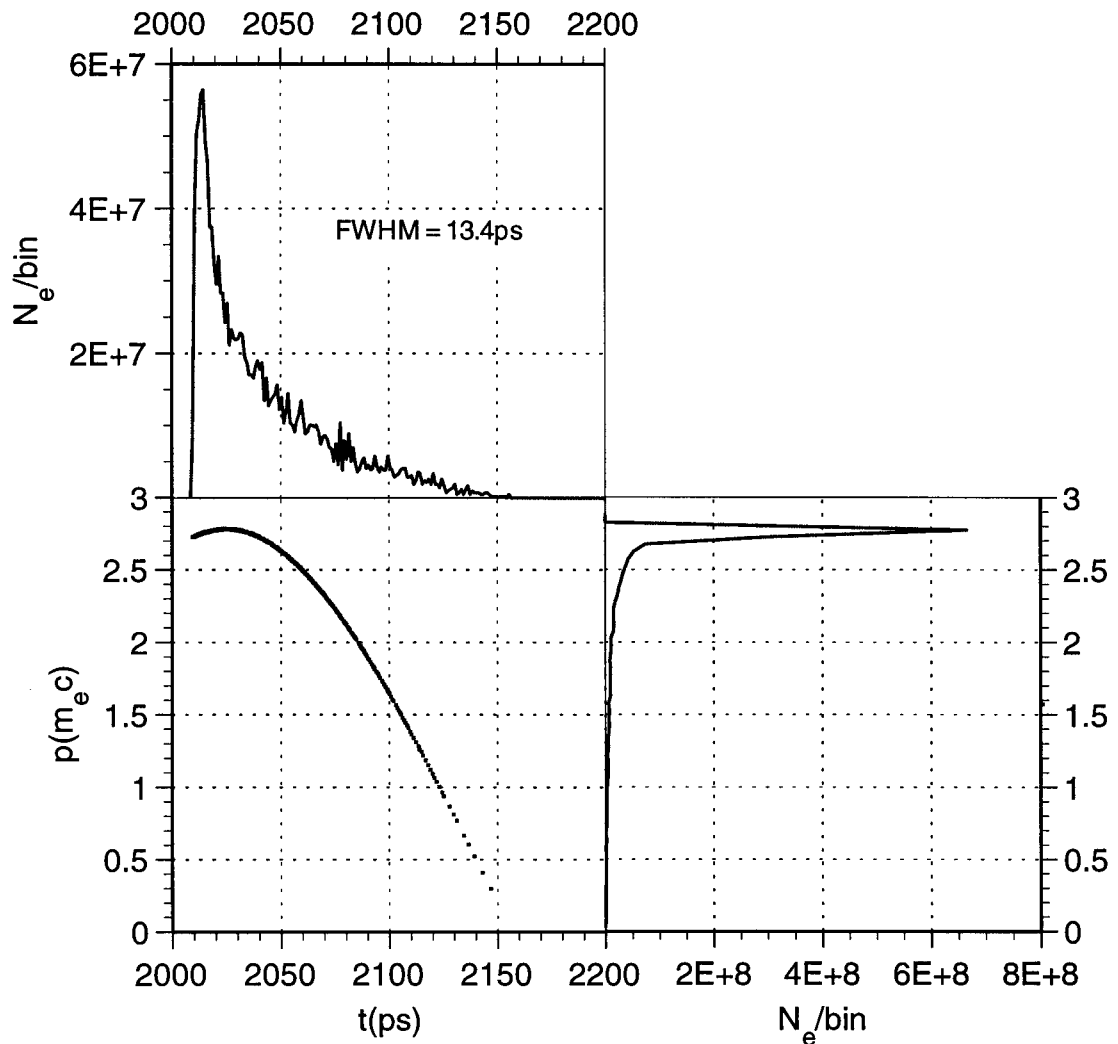


Figure 2.9: Longitudinal phase space at $z = 4.374 \text{ cm} = 5\lambda_{\text{rf}}/12$.

In the second cell, this longitudinal bunching repeats again as shown by Figure 2.9 – 2.11. Notice how little the bunch length has changed throughout the acceleration

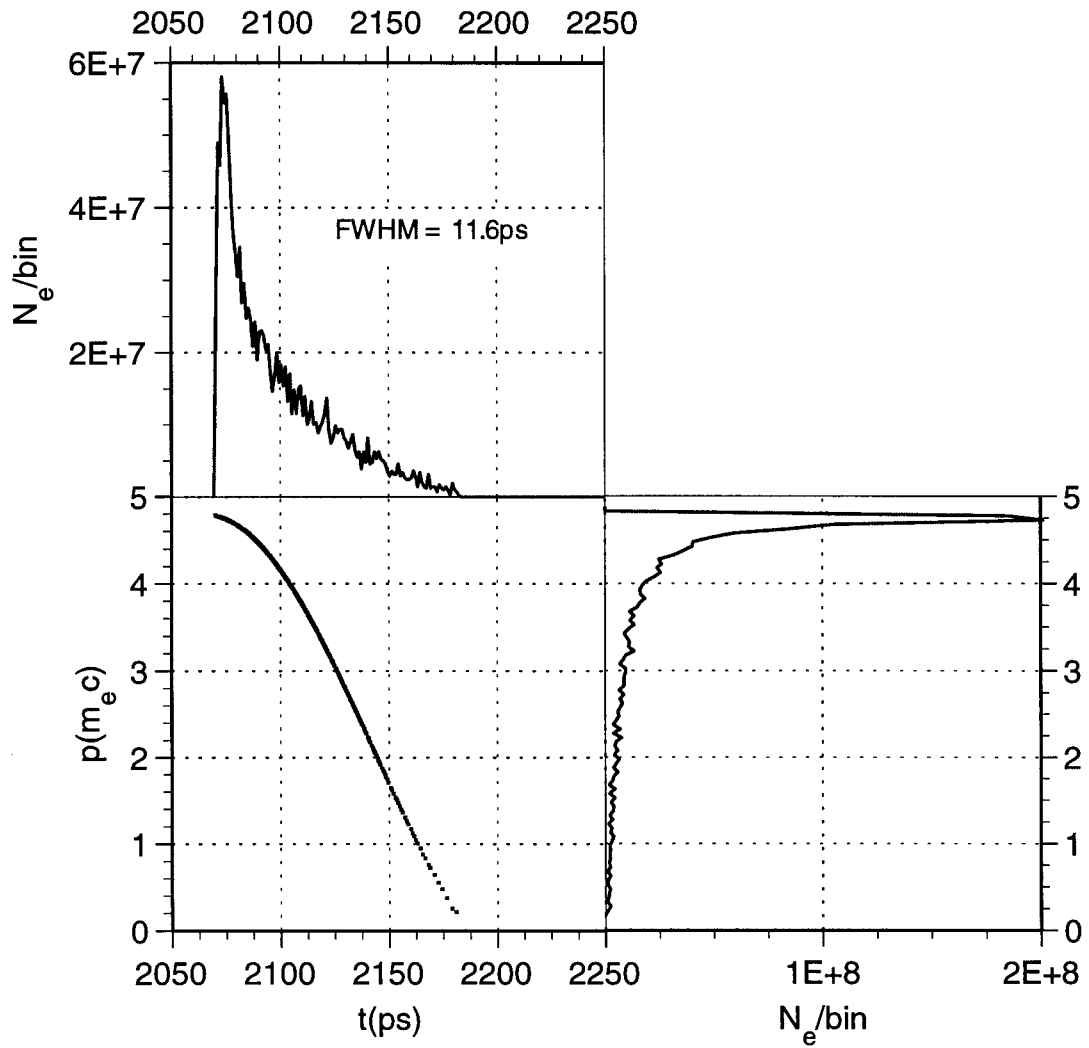


Figure 2.10: Longitudinal phase space at $z = 6.123 \text{ mm} = 7\lambda_{\text{rf}}/12$.

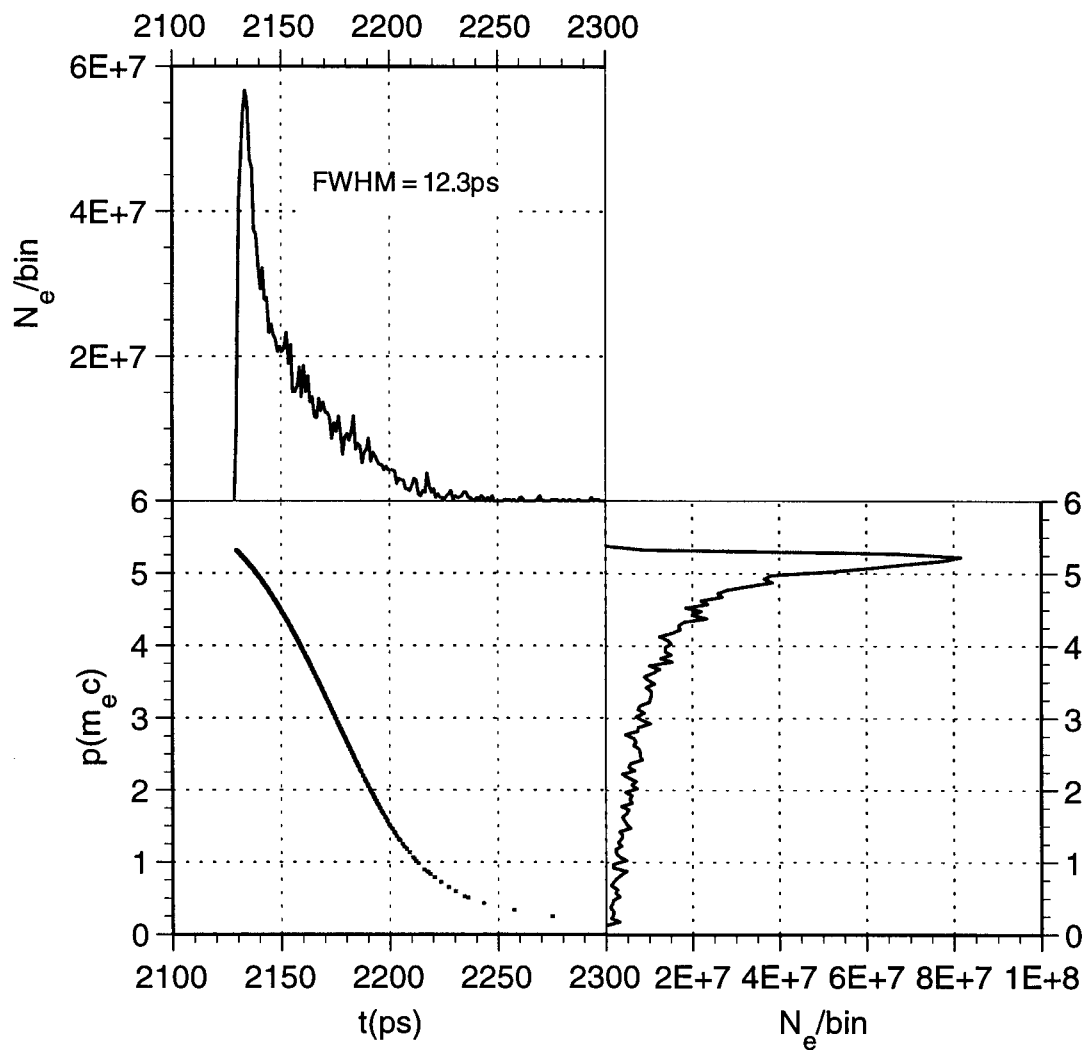


Figure 2.11: Longitudinal phase space at the gun exit.

because the bunching happens rather early while particles are still sub-relativistic shown in Figure 2.6. It only becomes slightly larger at the exit of both cells due to the drift tubes.

Since electrons emitted near 90° just do not stay in the acceleration phase long enough, by the time they reach the second cell, the fields already have changed sign; so they experience very little overall acceleration. The consequence is only less than a quarter of particles that are emitted by the cathode actually exit the gun. At the gun exit, the temporal tail of the particle distribution is about 100 ps. The momentum distribution resembles an asymmetric triangle and about 45% of the micro-bunch is under the peaks in both momentum and time distribution. The distribution has a *FWHM* in time of about 12 ps and a *FWHM* of about $\pm 6\%$ in momentum around the *central momentum* p_0 which is defined as the most populated momentum bin.¹ We are only interested in the *useful* part which is the electrons under the shaded peak in the momentum distribution (see in Figure 2.12) comprising the core. Incidentally, they are also the ones that are bunched in time. Note in Figure 2.11 the monotonically negative slope between momenta and exit times and the small area the electron bunch occupies in phase space. This area represents the longitudinal emittance of the beam and provides a good basis for further bunch compression to even shorter values as will be demonstrated in Chapter 4.

To visualize rf bunching in the gun, some beam parameters are plotted as functions of the distance along the axis in the gun in Figure 2.13 through 2.15. From the central momentum versus distance in Figure 2.13, we can see that the acceleration is almost linear except near the exit of both cells in the drift tubes. The relative momentum spread $\Delta p/p_0$, which is defined as the *FWHM* in momentum divided by the central momentum, displays less regularity as a function of the distance. It increases slightly in the first cell toward the exit because the bunch distribution becomes less sinusoidal in the drift tube shown in Figure 2.6 – 2.8. At the beginning of the second cell, the reduced momentum spread is partially due to more sinusoidal shape of the bunch

¹The *average* and *rms* value are not good descriptions for a highly asymmetric distribution such as the beam from an rf gun. The beam distribution is neither gaussian nor rectangular so *FWHM* and *equivalent width* are used for both momentum deviation and bunch length. (see Appendix B for the definition of the equivalent width).

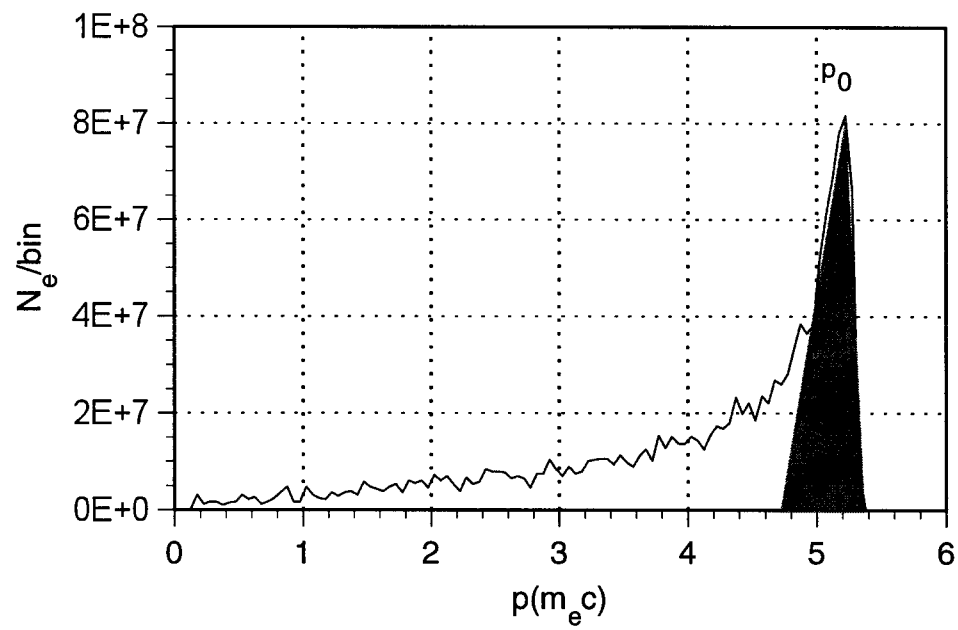


Figure 2.12: Momentum distribution and useful particles at the gun exit.

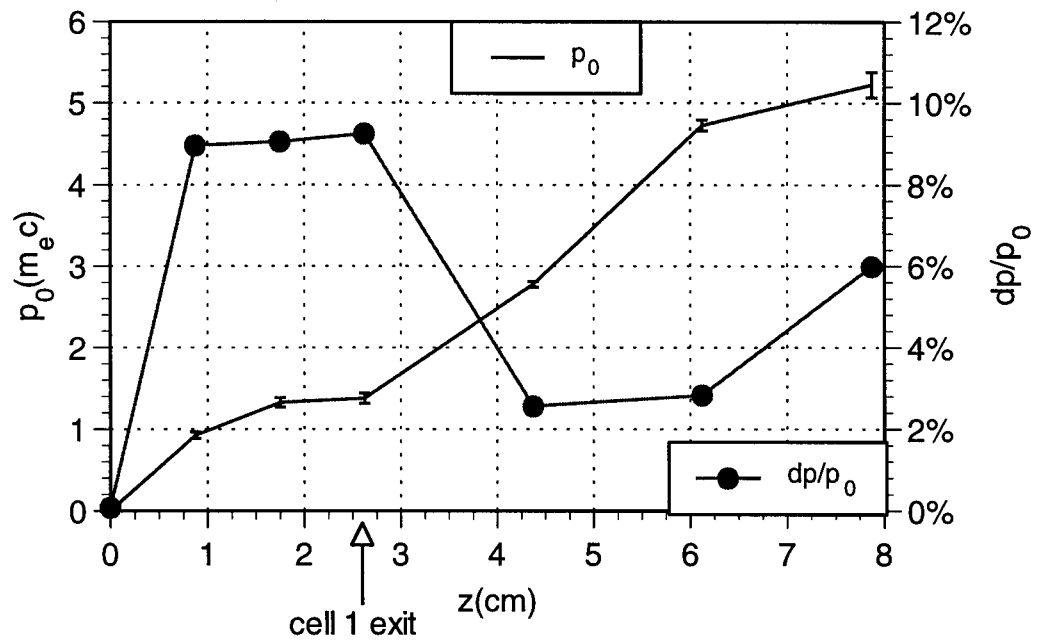


Figure 2.13: Central momentum and relative momentum spread versus distance in the gun.

distribution from rf bunching in Figure 2.9, partially because of a higher central momentum. Again toward the gun exit, the relative momentum spread increases slightly due to the drift tube.

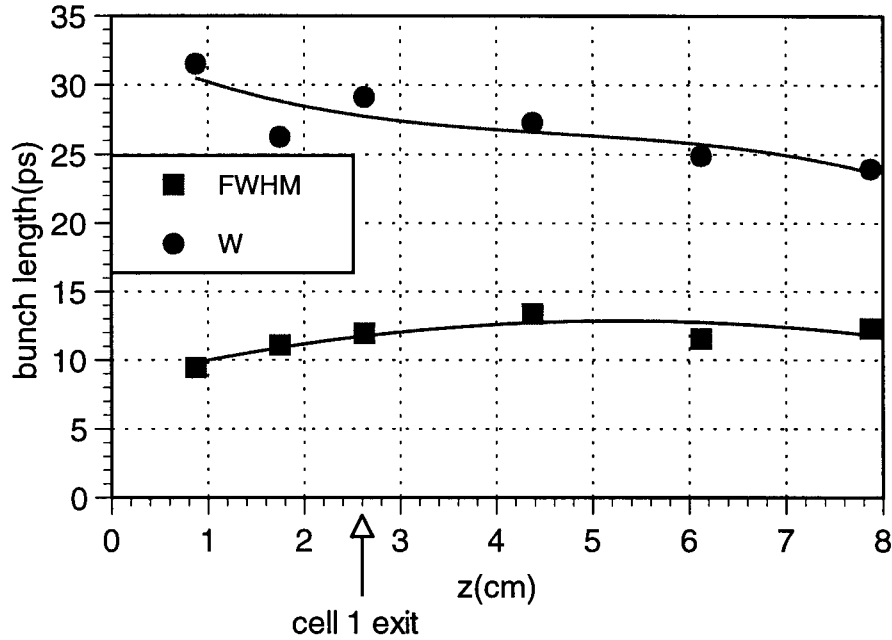


Figure 2.14: *FWHM* and equivalent width (W) versus distance in the gun.

The bunch length — *FWHM* and *equivalent width* (W) in Figure 2.14, does not change much throughout the gun because most of bunching happens early. The *FWHM* and equivalent width exhibit slightly different trends because of the difference in bunch distribution along the gun.

The gun current in Figure 2.15 shows that rf bunching increases the peak current, which is defined as charges within the full momentum spread around the central momentum (the shaded area in Figure 2.12) divided by the length of time they occupy, by a factor of two of the cathode current. The fluctuation along the distance in the gun is due both to particle loss and change in the bunch length. On the other hand, the average current, which is the total charge divided by the rf period, decreases drastically initially to only one third but otherwise gently for most of the gun because

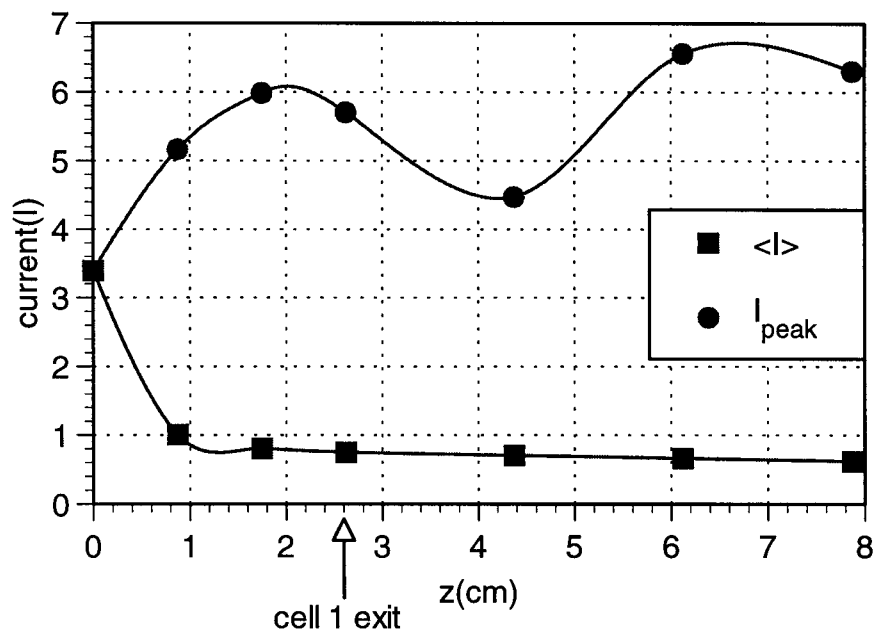


Figure 2.15: Average and peak current versus distance in the gun.

p_0c	2.66	MeV	γ_0	5.3
β_0	0.98			
$\langle I_{\text{exit}} \rangle$	0.62	A	\hat{I}_{exit}	6.3 A
$FWHM_t$	12.3	ps	W	24.0 ps
$\Delta p/p_0$	± 6.0	%		

Table 2.1: Beam parameters at the gun exit for $E_{p2} = 75 \text{ MV/m}$ and $J = 12 \text{ A/cm}^2$.

the particle loss happens mainly in the beginning of acceleration when the energy is lowest.

2.1.2 Electron Beam Parameters at the Gun Exit

The transverse phase space distribution at the gun exit is plotted in Figure 2.16 along with the beam ellipse of 2σ 's where σ_x and $\sigma_{x'}$ are the root mean squares (rms) of the horizontal beam size and divergence. Only the horizontal plane is presented here since the beam is cylindrically symmetric. What distinguishes the useful particles from those in the tail is not so much the beam size but the divergence. The gun is designed to focus the beam toward the exit so the core of the beam has a negative rms angular divergence. But the tail electrons are lower in energy and are therefore over focused.

The parameters at the gun exit for all electrons in a micro-bunch are summarized in Table 2.1. γ_0 and β_0 are the energy and speed of the central particles. The average output current $\langle I_{\text{exit}} \rangle$ is the total charge that exits the gun, Q_{exit} divided by the rf period and the peak current \hat{I}_{exit} is the charge of the useful electrons divided by the time they occupy. W is the equivalent width.

The parameters of the useful electrons compared with the ones of the whole bunch at the gun exit are listed in Table 2.2 where the geometric emittance is defined as²

$$\epsilon_x = \sqrt{\langle x^2 \rangle \langle x'^2 \rangle - \langle xx' \rangle^2}. \quad (2.1)$$

Q_{cath} is the total charge that is emitted by the cathode in an rf period.

From Table 2.2, only about one fifth of charges emitted by the cathode actually exit the gun; that is, out of an rf period (360°), the ones emitted before about 70°

²Some people include π in the emittance.

	all electrons		useful electrons	
ϵ_x	8.3	mm·mrad	ϵ_x	0.94 mm·mrad
$2\sigma_x$	0.67	mm	$2\sigma_x$	0.47 mm
$2\sigma_{x'}$	52.7	mrad	$2\sigma_{x'}$	17.8 mrad
$Q_{\text{exit}}/Q_{\text{cath}}$	18	%	$Q_{\text{exit}}/Q_{\text{cath}}$	8.2 %

Table 2.2: Beam parameters of the nominal bunch at the gun exit for all and useful electrons.

get out of the gun. Of these electrons, only 45% is actually useful; that is, only the ones that are emitted by about 30° make up the core of the beam. The emittance of the useful electrons is much smaller than the overall emittance which is clear from the transverse phase space in Figure 2.16 since particles at large angles or distances from the center contribute much to the rms values of x and x' . The main difference between the useful and tail part of a bunch is the divergence: at the gun exit, the core of the beam is converging while the tail of the beam is diverging.

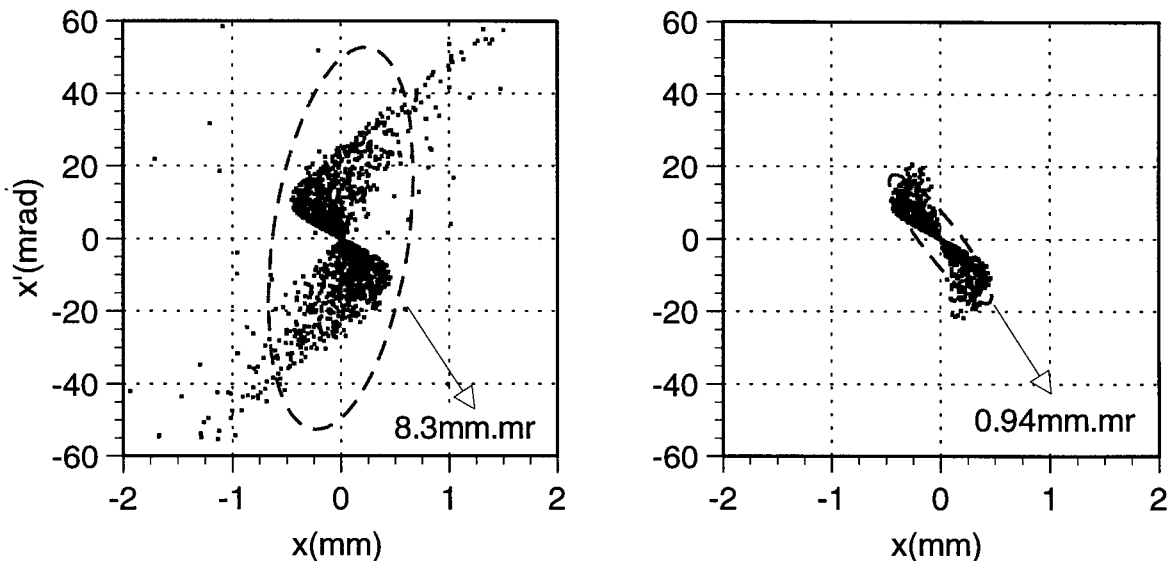


Figure 2.16: Transverse phase space and beam ellipses at the gun exit for all electrons a) and useful electrons b) for normal running conditions.

2.2 Effect of Acceleration

The central momentum and average and peak output currents at the gun exit are plotted in Figure 2.17 as functions of the accelerating field for a fixed cathode current density (12 A/cm^2). The vertical bars represent the *FWHM*s in the momentum distributions shown along with the relative momentum spread. The currents are normalized to the cathode current.

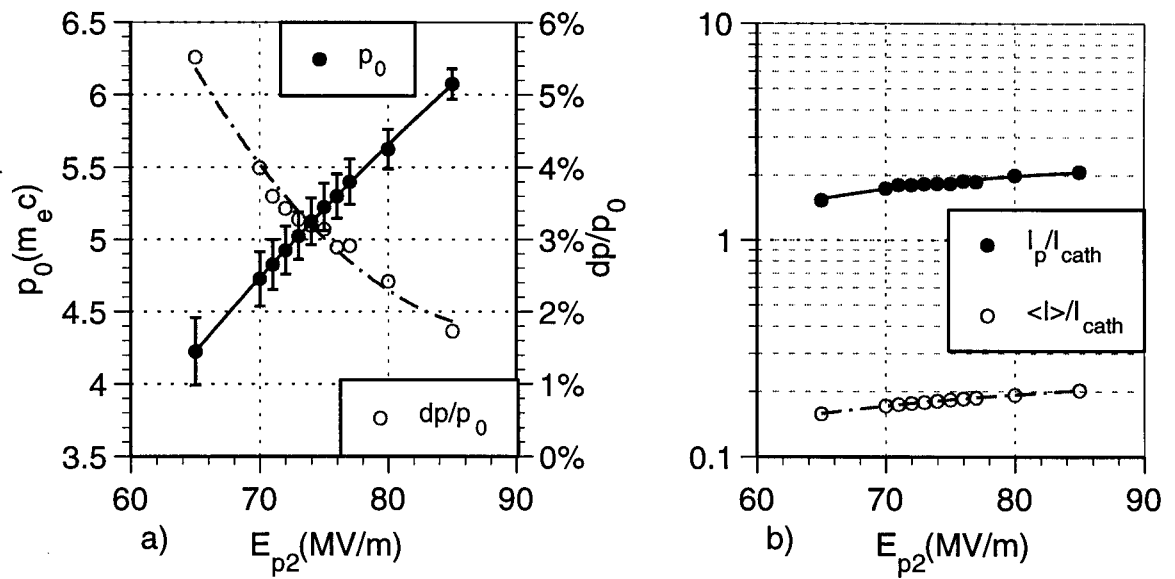


Figure 2.17: Central momentum along with relative momentum spread a), and normalized average and peak current b) at the gun exit versus E_{p2} for $J = 12 \text{ A/cm}^2$.

Both the average and peak output current increase slowly with the field strength because more electrons are accelerated out of the gun. The average output current is slightly less than one fifth of the cathode current, indicating that only electrons emitted at less than about 70° exit the gun. This can be expected because those emitted later than that experience little overall acceleration. Of all electrons that exit the gun, about half are really useful (see Table 2.2). So actually, the useful part of the beam is only about one tenth of all electrons emitted by the cathode in one rf cycle.

The peak current is taken from the useful electrons which are concentrated in the head of a bunch in time. Like the average output current, it also increases with the acceleration and rf bunching increases the peak current by a factor of two above the cathode current.

The absolute momentum spread does not change much with the field from Figure 2.17, but since the central momentum increases almost linearly with the accelerating field, the relative momentum spread decreases significantly. This is a result of the sinusoidal shape in longitudinal phase space at the gun exit for a high accelerating field (see Figure 2.5).

Figure 2.18 shows the bunch length ($FWHM_t$) and horizontal emittance for both all and the useful electrons at the gun exit versus the accelerating field. The bunch length decreases gently with the field due to stronger rf bunching. The emittance behaves the same except for some statistical fluctuation. The decrease of the emittance with the acceleration is a result of increased momentum, for the normalized emittance is a constant determined by the emittance at the cathode,

$$\epsilon_{x,n} = \sqrt{\langle x^2 \rangle \langle p_x^2 \rangle - \langle xp_x \rangle^2} = p_{z,\text{rms}} m_e c \epsilon_x. \quad (2.2)$$

where $p_{z,\text{rms}}$ is determined by the cathode temperature. Note that the rms emittance is only an approximate description for the phase space area of a non-Gaussian distribution.

2.3 Effect of Cathode Current Density

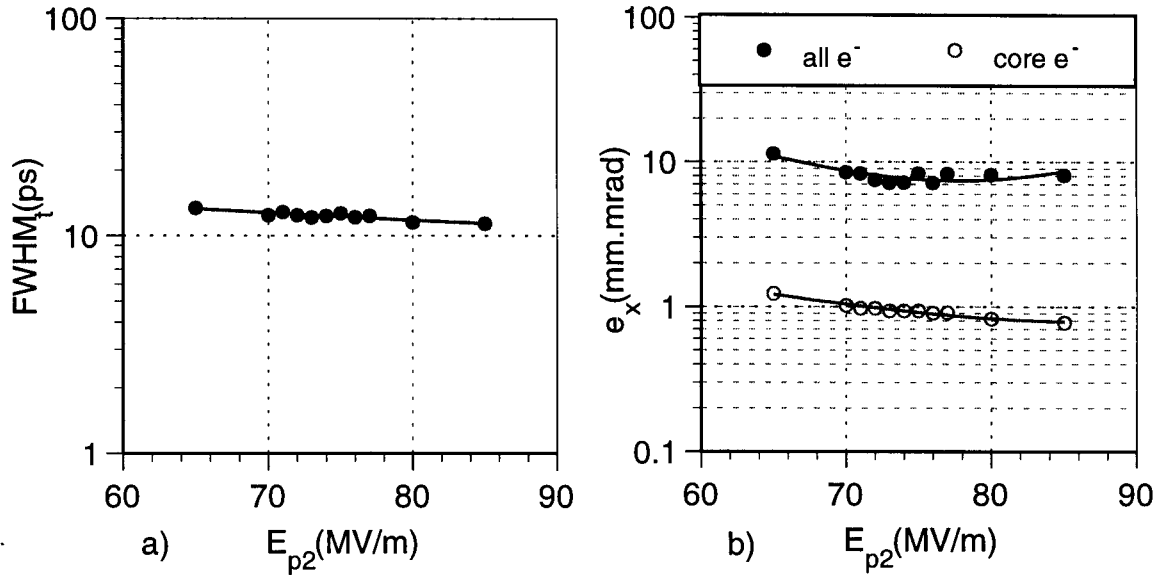


Figure 2.18: Bunch length a) and horizontal geometric emittance b) at the gun exit versus E_{p2} for $J = 12 \text{ A/cm}^2$.

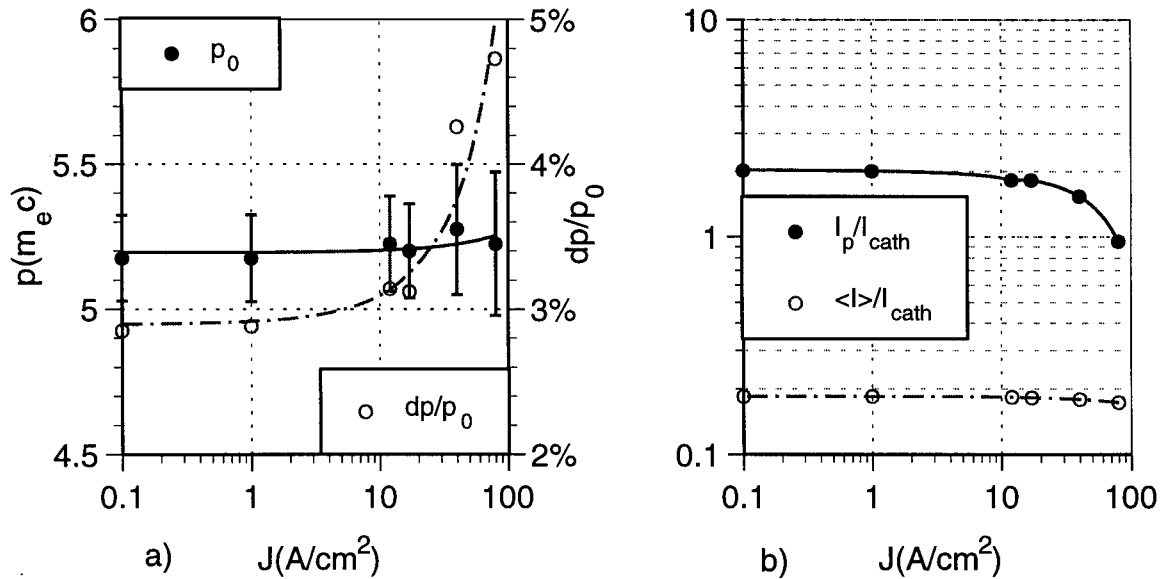


Figure 2.19: Central momentum a) and normalized average output and peak current b) versus cathode current density for $E_{p2} = 75 \text{ MV/m}$.

The central momentum, and normalized average and peak output currents at the gun exit as functions of the cathode current density for a fixed accelerating field ($E_{p2} = 75 \text{ MV/m}$) are sketched in Figure 2.19. There is a slight increase in central momentum with the cathode current density due to longitudinal space charge since electrons in the front are pushed forward by trailing electrons. The larger longitudinal space charge force from a higher current density also introduces a larger energy spread, especially above 10 A/cm^2 . The average output beam current at the gun exit is mostly a fixed fraction, slightly less than one fifth, of the cathode current and decreases very slightly at high current densities. But the peak current reaches twice the cathode current below 10 A/cm^2 due to rf bunching and decreases drastically above 10 A/cm^2 because charges at the head of a bunch are much denser so they are more affected by space charge.

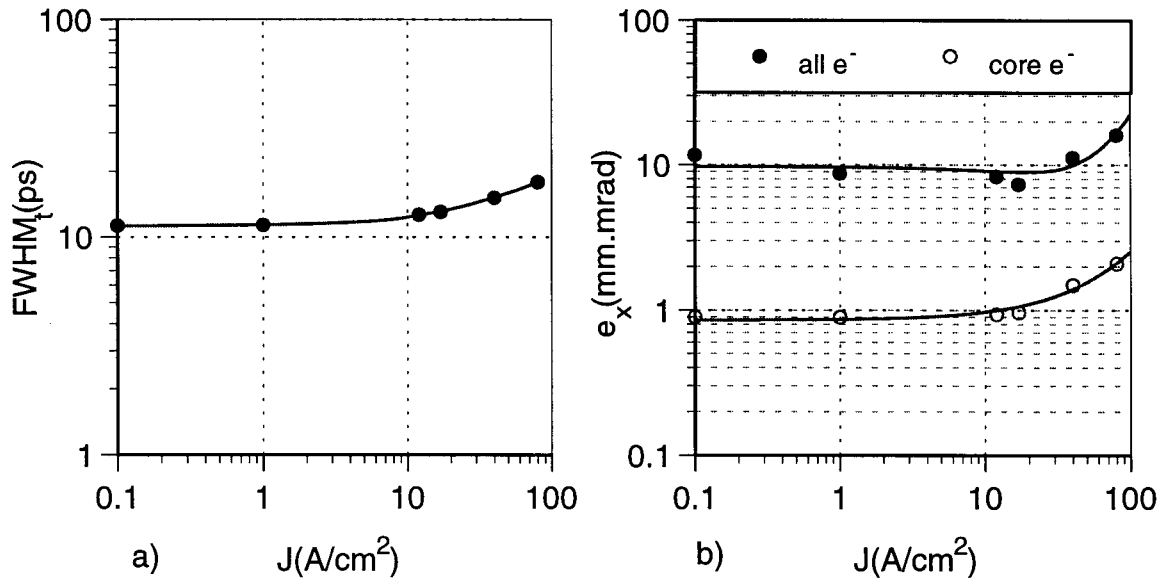


Figure 2.20: Bunch length a) and geometric emittance from all and core electrons b) at the gun exit versus cathode current density for $E_{p2} = 75 \text{ MV/m}$.

Figure 2.20 shows the bunch length and emittance at the gun exit versus the cathode current density. For high current densities, transverse space charge force degrades the transverse emittance significantly, again especially above 10 A/cm^2 .

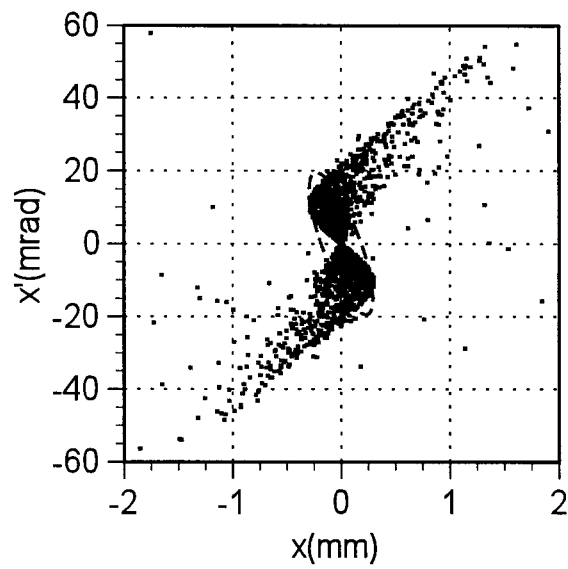


Figure 2.21: Transverse phase space and phase ellipse for the core of the beam at the gun exit for $E_{p2} = 75 \text{ MV/m}$, $J = 0.1 \text{ A/cm}^2$.

To illustrate the effect, let us compare the transverse phase space and phase ellipses for the cores of the beam at the gun exit for a very low and very high current density, pictured in Figure 2.21 and 2.22. The particle distribution becomes much diffused and beam size larger for a large current density.

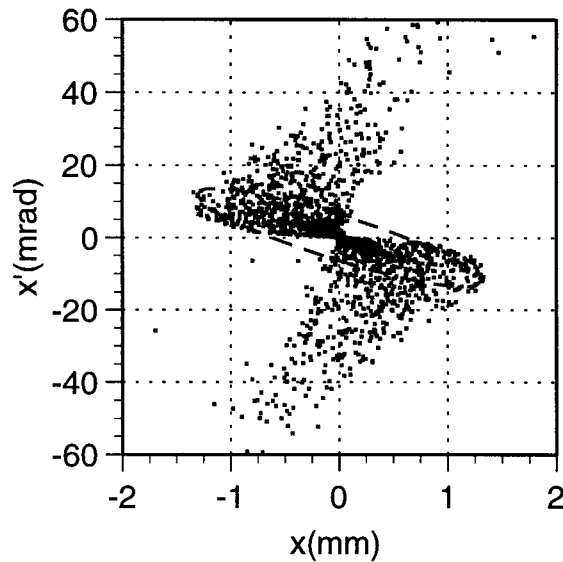


Figure 2.22: Transverse phase space and phase ellipse for the core of the beam at the gun exit for $E_{p2} = 75 \text{ MV/m}$, $J = 80 \text{ A/cm}^2$.

The effect of space charge on longitudinal phase space is different from transverse phase space. Compare the longitudinal phase space at the gun exit for a very small or large cathode current density at a fixed field in Figure 2.23; not only does longitudinal space charge lengthen a bunch, it also introduces some high frequency oscillations and structures in the head of a bunch at about $100 - 167 \text{ GHz}$. The magnitude of the oscillation also increases with the current density. The structures become more evident after compression comparing the results for $J = 0.1$ and 40 A/cm^2 in Figure 2.24. The oscillatory instability compared to the low current case is obvious. At even higher current density, the “pockets” start migrating and smearing out into each other and become less distinct. Bunch compression will be discussed in the next Chapter. Some observations of this oscillation are discussed below in the next section.

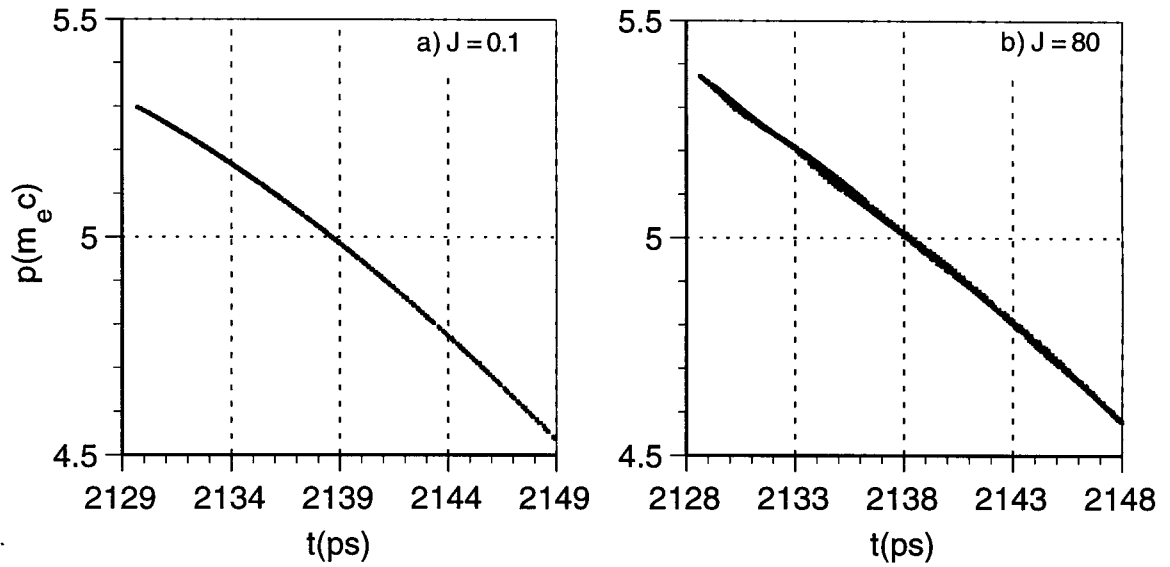


Figure 2.23: Longitudinal phase space at the gun exit for $J = 0.1$ a), and 80 A/cm^2 b).

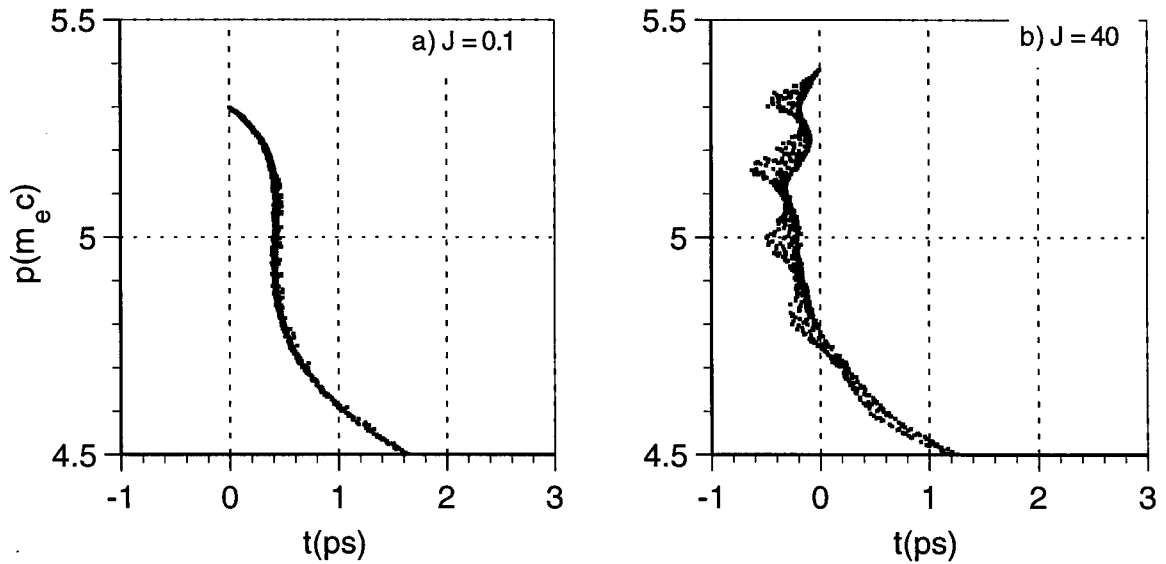


Figure 2.24: Longitudinal phase space after compression for $J = 0.1$ a), and 40 A/cm^2 b).

2.3.1 Oscillations in Longitudinal Phase Space

For a higher and higher current density, longitudinal phase space exhibits some high frequency oscillation and structures about 100 – 167 GHz shown in Figure 2.23. This was attributed to plasma oscillation in [12]. However, the angular plasma frequency should be a function of the particle density n which is a function of the cathode current density [24],

$$\omega_p^2 = \frac{4\pi n e^2}{\gamma^3 m_e}. \quad (2.3)$$

Yet, we do not see the frequency of the oscillation change with the current density which rules out the possibility of plasma oscillation. To show how it depends on the cathode current density, the particle density n at the cathode can be expressed in terms of the current density:

$$n = \frac{J(T_{\text{cath}})}{e\beta c}, \quad (2.4)$$

where the cathode current density J is a function of the temperature. For normal operations, $T_{\text{cath}} \sim 950^\circ\text{C} = 0.11\text{ eV}$ at the cathode (see Table 1.1), which gives an rms initial speed of about $8 \times 10^{-4}c$. The particle density at the gun exit is easier to calculate in terms of the output current. Since the oscillation is present only for the first 20 ps where the beam is much denser longitudinally, we shall take the peak output current. The peak output current at the exit is about twice as large as the cathode current (see Figure 2.17 and 2.19) due to rf bunching,

$$n_{\text{exit}} \approx \frac{2Jr_c^2}{(2\sigma_r)^2 e\beta c}, \quad (2.5)$$

where σ_r is the rms beam radius and r_c the cathode radius. At the gun exit, $2\sigma_r = 2\sqrt{2}\sigma_x \approx 0.7\text{ mm}$ and $\beta \approx 0.98$ for the core of the beam (see Table 2.2). Figure 2.25 shows the approximate plasma frequency $f_p = \omega_p/(2\pi)$ versus the cathode current at the cathode and gun exit.

Here are some observations about the density oscillation:

- Higher current density in MASK causes only larger oscillation and structures, but does not affect the periodicity. From Figure 2.25, the plasma frequency is much lower than the frequency of the observed oscillation; also it should increase

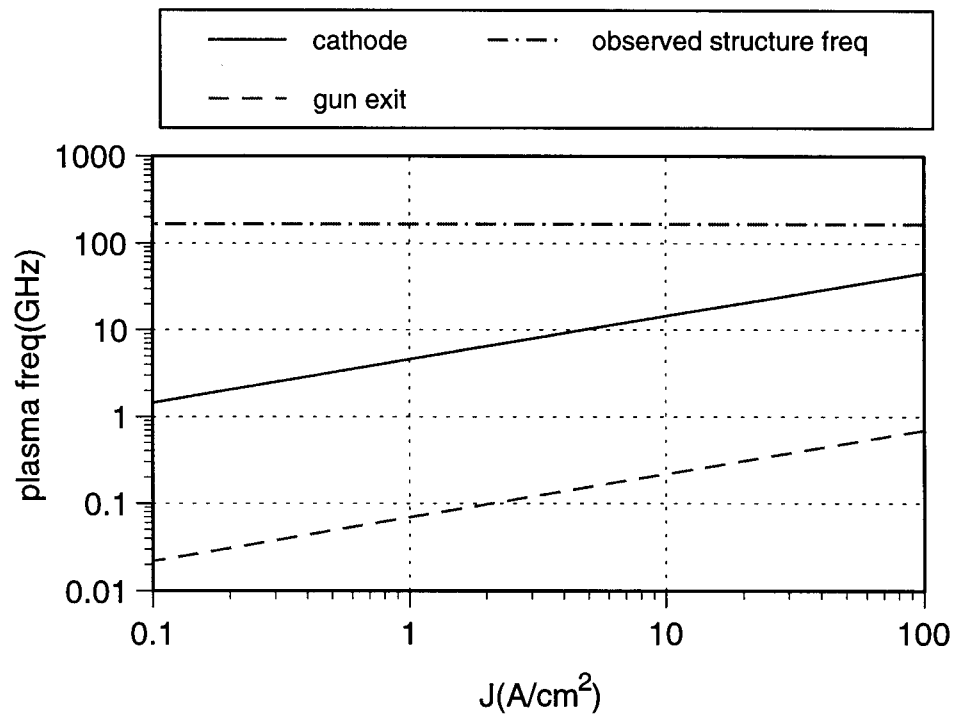


Figure 2.25: Plasma frequency (f_p) versus cathode current density.

with the cathode current which is not what simulations show. Therefore the oscillation is not likely to be plasma oscillation.

- The oscillation is independent of the field strength.
- The oscillation is independent of the time step size in simulations.³
- Changing the weight — the charge each macro-electron represents does not affect the oscillation frequency. Larger weight, i.e. fewer macro-particles used in a simulation, only yields a coarser result due to larger statistical fluctuation of the forces between particles.
- Since the gun is a high- Q system, the oscillation is unlikely due to higher modes excited by the beam. Though the cell geometry in MASK does not resemble the real gun perfectly due to finite mesh sizes, there are no structures of the dimension (1 – 2 mm) which would hint the 100 – 167 GHz oscillation observed. Also in all MASK simulations, only the fundamental mode is excited and the FFT of the normalized peak fields shown in Figure 2.26 for a high current MASK run also confirms that. The higher order modes are higher compared with the FFT for a no-beam MASK run in Figure 2.2, but still many orders of magnitude below the fundamental mode; nothing around a few hundred GHz seem strong enough to cause particle density oscillation.

The oscillation is present only in longitudinal phase space and absent transversely for a high-current beam shown in Figure 2.22, compared with Figure 2.16 and 2.21 for low currents. Since it increases in magnitude with the cathode current density, one may suspect that longitudinal space charge force might be the cause.

In fact, the only parameter that has any effect on this oscillation is the longitudinal mesh size. The longitudinal phase space at the gun exit for a regular ($\Delta z = 0.43$ mm),

³Provided that the time step size Δt satisfies the Courant condition [25] for numerical stability:

$$\Delta t \leq \frac{\min(\Delta z, \Delta r)}{\sqrt{2}u_{\max}} \leq \frac{\min(\Delta z, \Delta r)}{\sqrt{2}c},$$

where u_{\max} is the maximum propagation speed of the system.

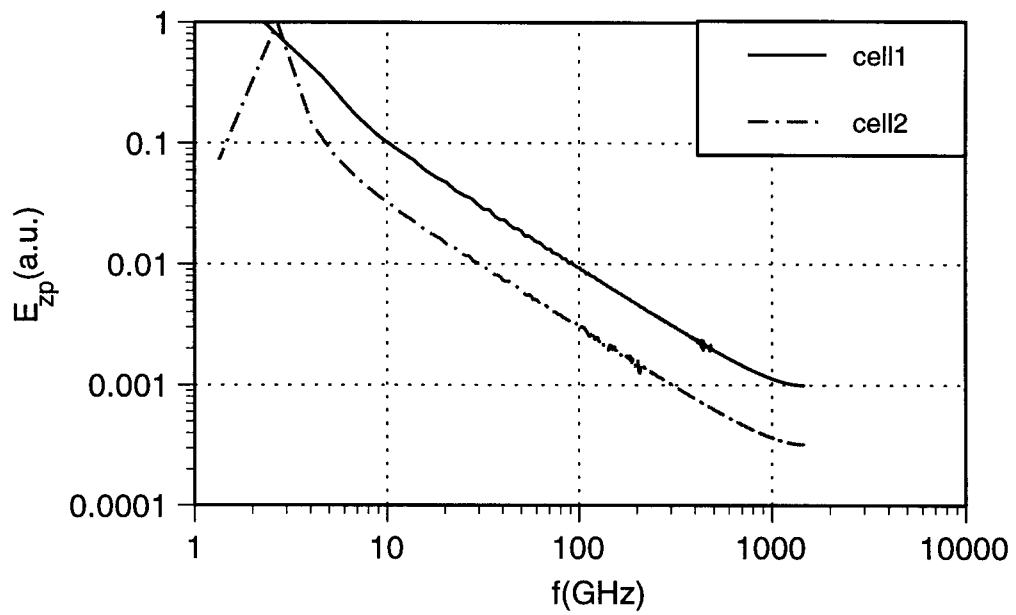


Figure 2.26: FFT of the normalized peak accelerating field in a MASK run with $J = 80 \text{ A/cm}^2$. The resolution is 2.9 GHz.

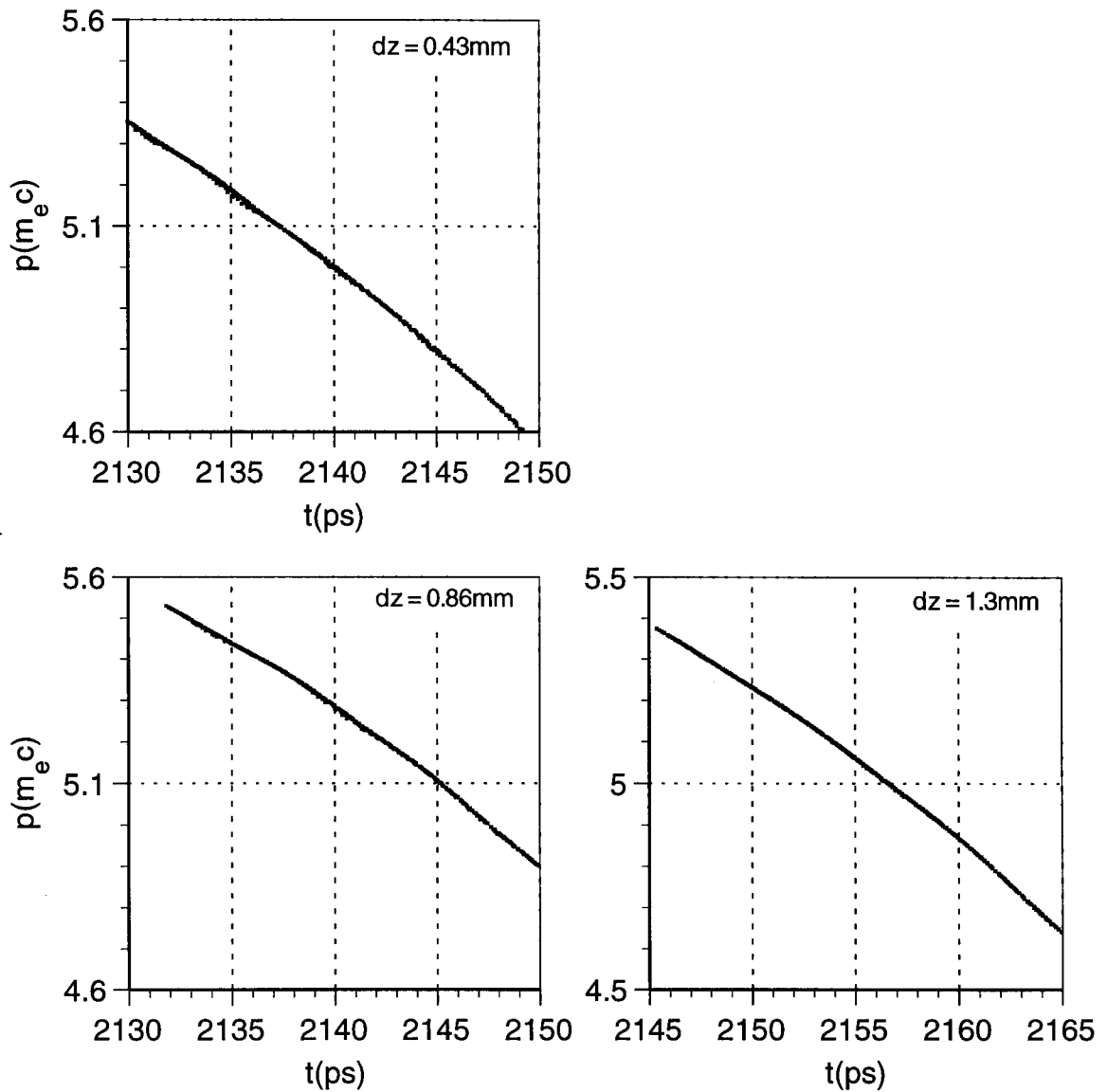


Figure 2.27: Longitudinal phase spaces at the gun exit for different longitudinal mesh sizes in MASK.

double and triple longitudinal mesh size are shown in Figure 2.27. For the run with a double mesh size, the oscillation period becomes longer and almost disappears when it is tripled. Because fields are averaged over larger areas for a larger mesh size, the results are not necessarily an indication of a numerical artifact. The output energies

and slopes are slightly different because larger mesh sizes make the geometry less smooth hence introduces different phase differences up to $180^\circ \pm 5^\circ$ between two cells. This reduced oscillations for a larger mesh is easier to see after compression shown in Figure 2.28.

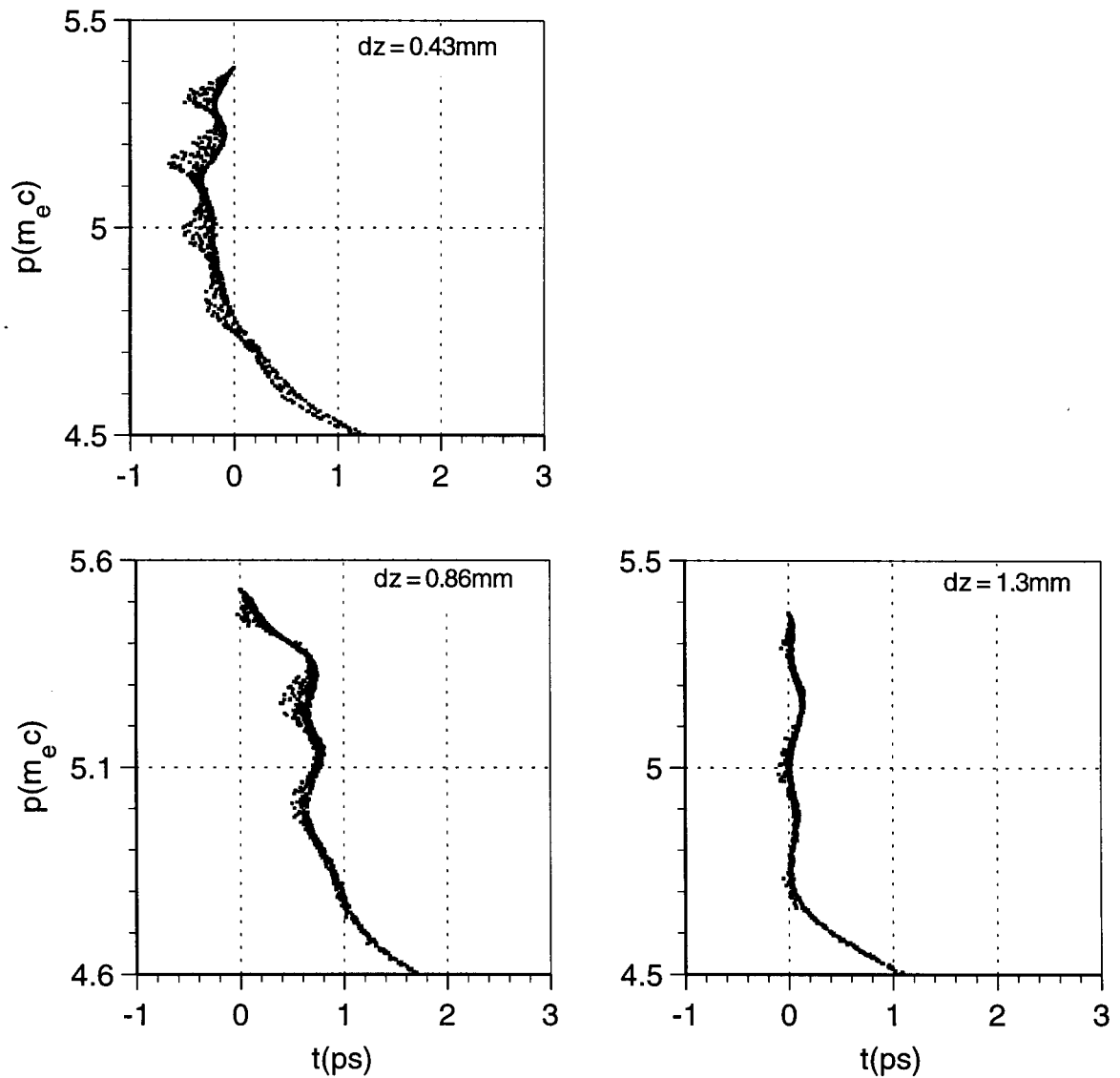


Figure 2.28: Longitudinal phase spaces after compression for different longitudinal mesh sizes in MASK.

A more careful analysis of the longitudinal dynamics due to space charge force shows that this peculiar phenomenon, which we call *shock wave instability*, is due to the rapidly changing longitudinal charge density and will be discussed in the next chapter.

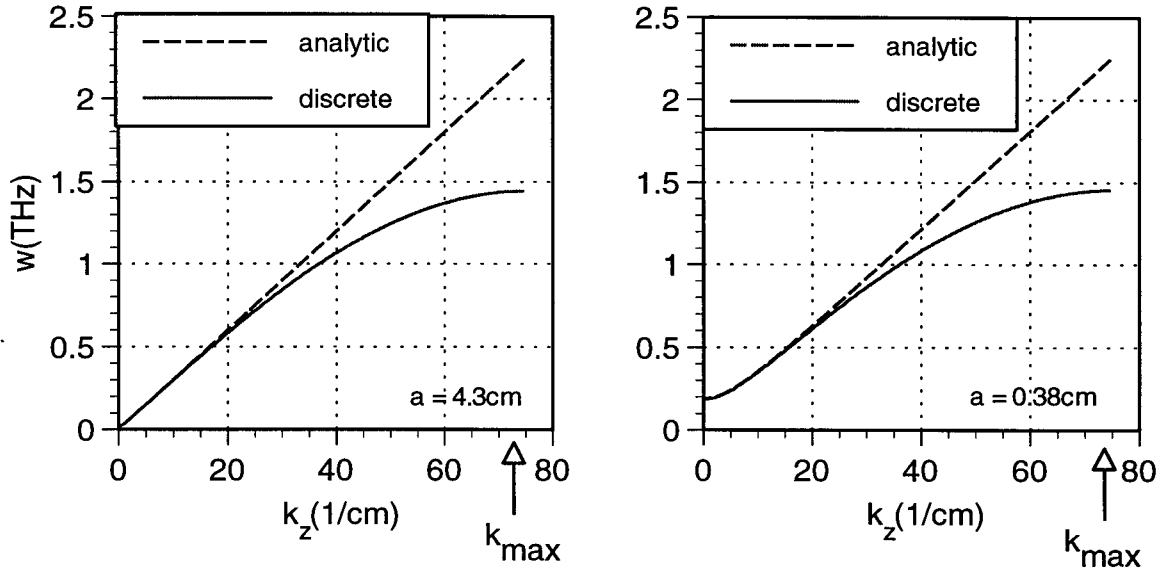


Figure 2.29: Analytic and discrete dispersion relation for a circular wave guide.

A word of caution in interpreting the numerical results: like all numerical methods, the dynamics of electrons in the gun by MASK is discretized and there is a difference between the analytic dispersion relation and discrete one [26] due to aliasing. Since the actual dispersion relation for the gun cannot be derived explicitly, we shall resolve to a circular wave guide, assuming that new modes introduced by the electron beam are much smaller in magnitude compared with existing TM or TE modes of an empty wave guide, which are homogeneous solutions to the Maxwell's equations. The analytic dispersion relation for a circular wave guide is [16]

$$\left(\frac{\omega}{c}\right)^2 = k_z^2 + \left(\frac{p_{nm}}{a}\right)^2, \quad (2.6)$$

where p_{nm} is the m^{th} root of the Bessel function J_n . For the fundamental TM mode, TM_{01} , $p_{01} = 2.405$.

The dispersion relation for a discretized circular wave guide is [26]

$$\left(\frac{\sin \frac{\omega \Delta t}{2}}{\frac{c \Delta t}{2}}\right)^2 = \left(\frac{\sin \frac{k_z \Delta z}{2}}{\frac{\Delta z}{2}}\right)^2 + \left(\frac{\sin \frac{p_{nm} \Delta r}{2a}}{\frac{\Delta r}{2}}\right)^2 \quad (2.7)$$

where Δt is the time step and Δz , Δr are the longitudinal and radial mesh size; a is the radius of the wave guide. A factor of 2 is included in all denominators and numerators in (2.7) because MASK uses an interleaved leap-frog scheme in both time and space.

Let us consider the TM_{01} mode and the parameters used in regular MASK simulations ($\Delta z = 0.4$ mm, $\Delta t = 0.17$ ps) for now. The difference between (2.6) and (2.7) is shown in Figure 2.29 up to the maximum wave number ($k_{z,\max} = \pi/\Delta z$) limited by the mesh size. The radius of the gun body, 4.3 cm and the drift tube, 0.38 cm, are used (see Figure 1.2 and 1.3). The discretized system represents the actual one better at lower frequencies. The errors for the phase velocity at the angular frequency of the structures in longitudinal phase space in simulations ($f \sim 167$ GHz, $\omega \sim 1$ THz) are -8.8% and -8.6% at the gun body and drift tube. But the errors for the group velocity at which the wave energy propagates is much larger. From (2.6) we get

$$\begin{aligned} v_g^A &= 0.9999c \text{ for } r = 4.3 \text{ cm,} \\ v_g^A &= 0.98c \text{ for } r = 0.38 \text{ cm,} \end{aligned}$$

at 1 THz. The superscript ^A emphasizes that these are the group velocities for the analytic system. But the group velocity for the discretized system derived from (2.7) is only $0.7c$ in both the gun body and drift tube at the same frequency, rendering an error as large as -30% . That is, the energy at this particular frequency of the observed oscillation propagates at 30% lower speed than in the actual circular wave guide.

At higher frequencies, the two curves deviate more until at $k_{z,\max}$, the group velocity for the discretized system is zero. That is, it becomes a standing wave while the analytic system is always a travelling wave guide. The standing wave mode in a numerical system can linger for a long time so the numerical result at $k_{z,\max}$ cannot be relied on at all.

Therefore we must interpret simulated results with some caution and the oscillations in longitudinal phase space in MASK simulations may be only qualitatively but not quantitatively true. For an even larger Δz , such as double or triple mesh size used in Figure 2.27 and 2.28, the discrete dispersion relation deviates even more than the ones in Figure 2.29 so the results are less reliable.

Since the discrete system only approaches the analytic one at zero frequency, to simulate the dynamics of electrons in the gun faithfully, one needs to use as small a mesh size as practically possible to get a large $k_{z,\max}$ to cover the highest frequency of interest. In our case, this upper limit is set by the smaller of the bunch length and the dimension of the smallest structure in the gun (d):

$$\Delta z \ll \min (FWHM_t \beta c, d), \quad (2.8)$$

in addition to the familiar Courant condition. $d \sim 1$ mm for the first cell and $d \sim 3$ mm for the second cell. Actually the above is stricter for the first cell when the velocity of the beam is lower.

2.4 Photo-Cathode

Although our gun is not equipped with a laser, simulating a photo-cathode beam is possible for MASK allows shaping of the pulse at the cathode. The simulation was done with the same field strength, $E_{p2} = 75$ MV/m, as in normal running conditions. The beam pulse at the cathode is assumed to be a 5 ps-long square pulse with a total charge of 5 nC. The initial phase ϕ_0 should be chosen to minimize the emittance upon exit and is given by [27]

$$\left(\frac{\pi}{2} - \phi_0 \right) \sin \phi_0 = \frac{1}{2\alpha}, \quad (2.9)$$

where

$$\alpha \equiv \frac{eE_0}{2mc^2k}.$$

E_0 is the peak accelerating field and $k = 2\pi/\lambda$. Unfortunately, for the field ratio of 2.9 between the two cells for our gun (see Table 1.2), which was not designed with a photo-cathode in mind, the above condition has no solution. Obviously, for a

photo-cathode, one would opt for equal fields in both cells to accelerate electrons as fast as possible to reduce the initial space charge effect when the beam is very low in energy but high in intensity. Since (2.9) has no solution, the emitting phase was chosen arbitrarily to be 20° . The longitudinal and transverse phase space at the gun exit are plotted in Figure 2.30 and 2.31. The beam parameters at the gun exit are listed in Table 2.3.

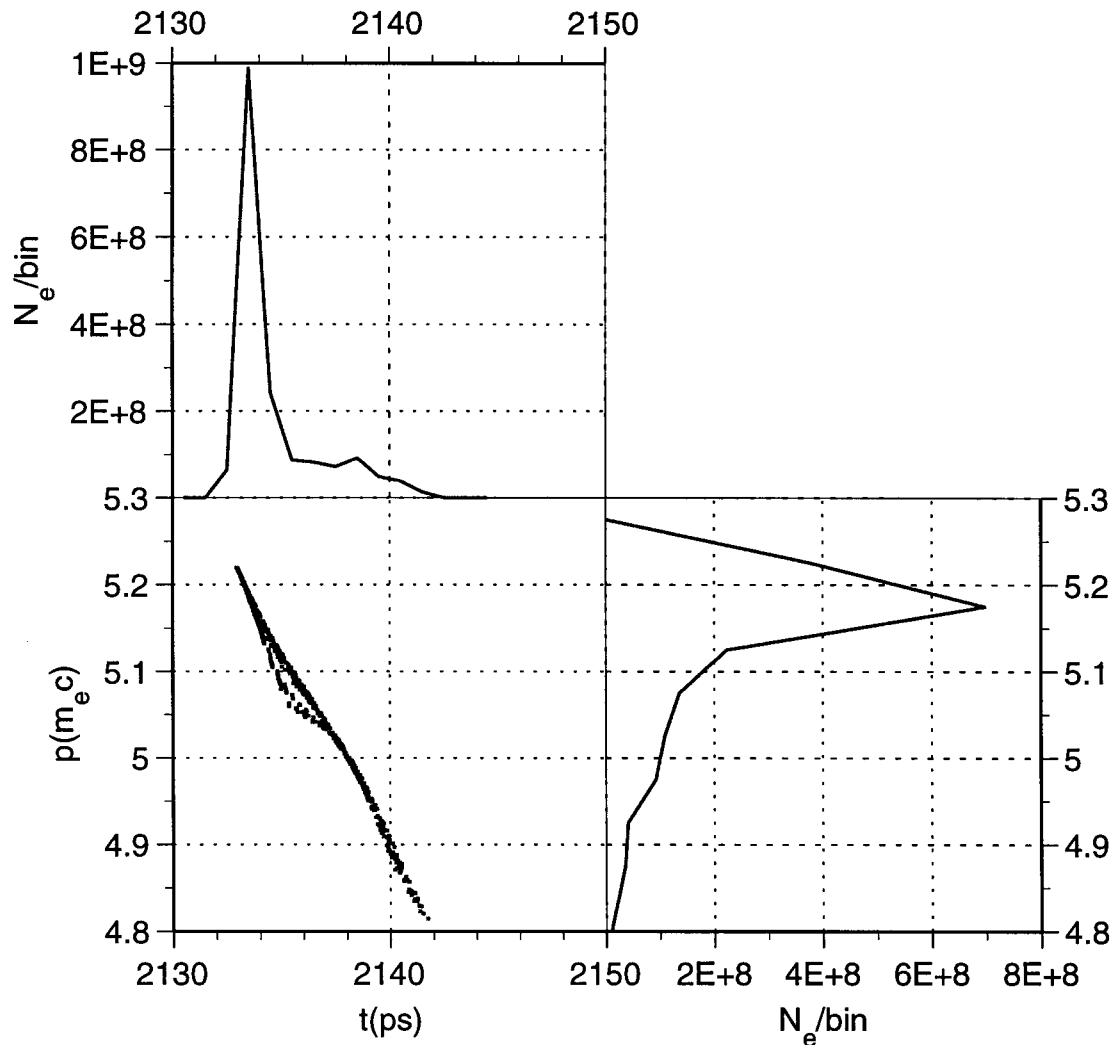


Figure 2.30: Longitudinal phase space at the gun exit for a photo-cathode beam.

Again in longitudinal phase space, we observe the high frequency oscillation as

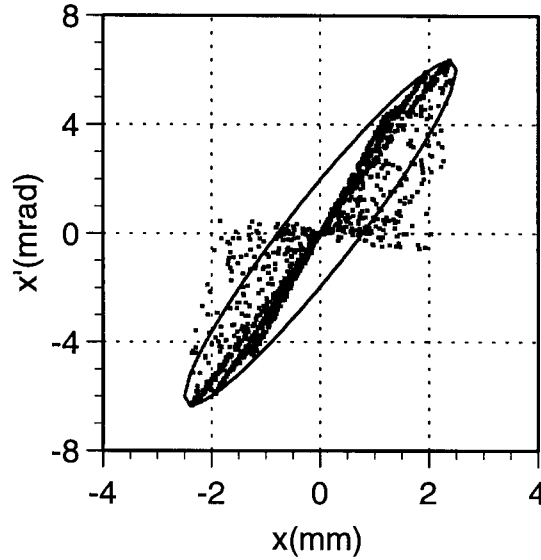


Figure 2.31: Transverse phase space at the gun exit for a photo-cathode beam.

p_0c	2.64	MeV		
$\langle I_{\text{exit}} \rangle$	0.79	A	\hat{I}_{exit}	13 A
Q_{exit}	277	pC	$Q_{\text{exit}}/Q_{\text{cath}}$	5.5 %
$FWHM_t$	1.2	ps	W	± 1.8 %
$\Delta p/p_0$	± 1.8	%	ϵ_x	1.2 mm-mrad
$2\sigma_x$	2.4	mm	$2\sigma_{x'}$	6.5 mrad

Table 2.3: Beam parameters at the gun exit for a photo-cathode beam for $E_{p2} = 75$ MV/m, total charge of 5 nC, 5 ps-long pulse.

in the previous case of a thermionic cathode in Figure 2.23. The beam concentrates mostly in the first 2 ps followed by a rather thin tail. The emittance is slightly larger than that from the core of the beam in normal running conditions (see Table 2.2) due to much larger transverse space charge effect. There is a great loss of charge, mostly happening early in acceleration when the beam is most vulnerable to space charge force. So only 5.5% of the charge emitted by the cathode remains at the gun exit, compared with almost 18% "survival" rate for a thermionic gun in Table 2.2. This results in an average output current in a bunch only slightly larger than from a thermionic cathode.

From Figure 2.30, a photo-cathode beam can be compressed to a length comparable to or shorter than the one from a thermionic cathode and the peak current can be in excess of hundreds of amperes. A photo-cathode gun has the obvious advantages of no back-bombardment, naturally short bunches and small momentum deviation at the expense of much greater complexity and cost. Also, a photo-cathode gives lower average electron current in a macro-pulse because not every bucket in a macro-pulse is filled. This is important if the process being studied involves time-averaged power, such as spectroscopy.

Chapter 3

Shock Wave Instability

In this chapter a theoretical model is developed to describe qualitatively the charge density oscillations in longitudinal phase space in simulations discussed in Section 2.3.1. The variation of the longitudinal particle density can cause the space charge wave to form a shock wave. The mechanics of this shock wave instability will be derived and discussed.

3.1 Derivation of the Equation of Motion

The longitudinal equation of motion of a charged beam under its own force is investigated using a 1D fluid model. Electrons in a bunch are considered as a continuous fluid because it is easier to see the dynamics. First let us show that this is a valid approximation.

3.1.1 Continuum Approximation

A particle beam behaves as a continuous fluid only when its plasma parameter Λ is much larger than one [24, 28]:¹

$$\Lambda \equiv n\lambda_D^3 \gg 1, \quad (3.1)$$

where n is the number density and λ_D is the Debye length beyond which the screening of the Coulomb potential from surrounding electrons becomes significant. It is determined by the density and temperature, T , of a fluid,

$$\lambda_D \equiv \sqrt{\frac{T}{4\pi n e^2}}. \quad (3.2)$$

Eq. (3.1) means that the number of particles in a Debye cube has to be sufficiently large. The plasma parameter is important such that when (3.1) is true, the system has the following properties [24, 29]:

- plasma frequency \gg collision frequency;
- mean inter-particle distance ($n^{-1/3}$) \gg closest approach between two particles;
- probability of large-angle collisions is small;
- probability of 3-body collisions is small;
- average kinetic energy \gg average potential energy.

In other words, the collective behaviour dominates the statistic fluctuation from individual particles.

If we assume that the radius of the beam is small so that non-linear rf field components are small, then an electron slice emitted from the cathode at the same phase would have the same rms momentum spread ($p_{\text{cath}} \sim 10^{-3} m_e c$) throughout the

¹Sometimes the plasm parameter is defined as

$$\Lambda = \frac{1}{n\lambda_D^3}.$$

gun at $T \sim 950^\circ\text{C} = 0.11\text{ eV}$ (see Table 1.2); i.e., we assume that the acceleration does not change the entropy of the system significantly for particles at small radii, therefore the temperature stays the same. This is more true for the transverse temperature since the radial momentum changes little from the focusing by the radial electric field, but not entirely so for the longitudinal temperature. For a system with a mean velocity \bar{v} in the longitudinal direction, the longitudinal temperature is defined as [30,31]

$$kT_{\parallel} \equiv \frac{m}{n} \int dv (v - \bar{v})^2 f(v), \quad (3.3)$$

where $f(v)$ is the velocity distribution function. Non-linear fields in the rf gun introduce additional velocity spread thus increase the longitudinal temperature. But since our beam occupies a very thin area in longitudinal phase space at a given time (see Figure 2.6 – 2.11), the temperature increase is small. Also, since $\Lambda \propto n^{-1/2}T^{3/2}$ from (3.1) and (3.2), a constant temperature approximation gives an underestimate of the plasma parameter, so the longitudinal temperature increase is not a problem.

In the following, quantities with superscript * indicate those in the beam frame unless otherwise stated and the Greek counterpart of (t, z) , (τ, ζ) , stands for time and space coordinate in the beam frame.

The number density at the cathode and gun exit in the laboratory system are expressed in (2.4) and (2.5). In the beam system, the density is smaller by γ :

$$n^* = \frac{n}{\gamma},$$

So the plasma parameter is larger in the beam frame by a factor of $\sqrt{\gamma}$;

$$\Lambda^* = \sqrt{\gamma}\Lambda.$$

Figure 3.1 shows the plasma parameter at the cathode and exit of the first cell and gun exit in the beam frame as a function of the cathode current density. Λ^* throughout the gun would fall between these curves. We can see that the fluid approximation is not as good for a cathode current above 20 A/cm^2 . But this estimate is pessimistic since we use a constant cathode temperature approximation. Because a larger cathode current is produced by a higher cathode temperature, all curves would be a little more convex at higher current densities. Also since the beam is accelerated quickly once it

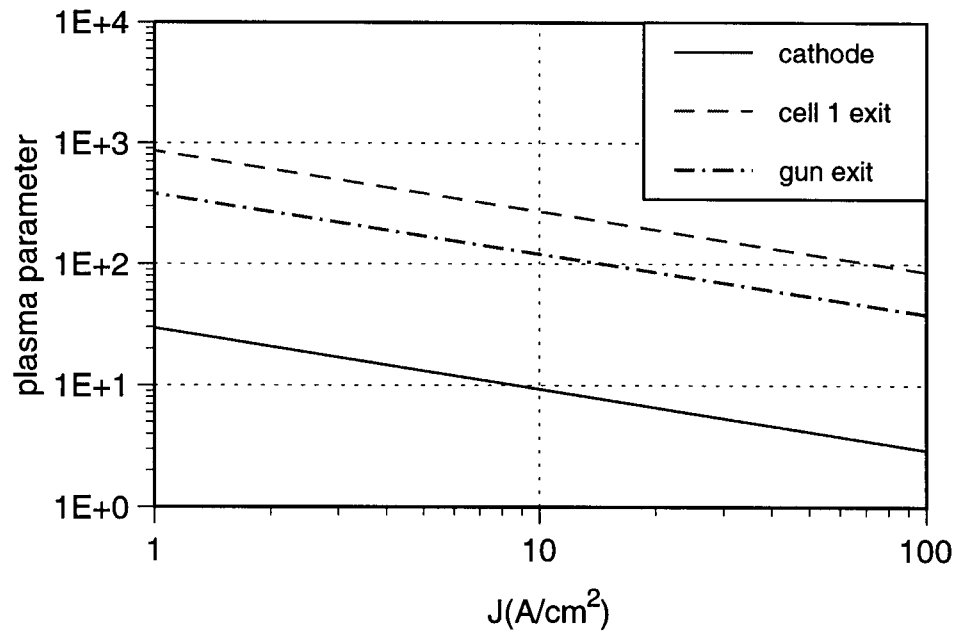


Figure 3.1: Plasma parameter in the beam frame as a function of cathode current density.

is emitted by the cathode, Λ^* should increase rapidly from the value at the cathode. We expect that the fluid approximation would extend to even higher cathode current density for most part of the acceleration. So the condition in (3.1) is still quite true in both frames for our beam which uses a cathode current density slightly above 10 A/cm^2 during normal runnings.

3.1.2 Radial Force

Let us show first that the transverse force either from external rf fields or space charge field is negligible in comparison with the longitudinal force at small radii. If the radius is small, we can ignore the radial dependence of the magnetic field due to space charge which scales like

$$\mathbf{B}_{\text{sc}}^* \propto v \hat{\phi}, \quad (3.4)$$

where v is the relative speed to the bunch center and $\hat{\phi}$ is the azimuthal unit vector. The $\frac{v}{c} \times \mathbf{B}_{\text{sc}}^*$ term is of second order for $v \ll c$.

The fields transform like [16],

$$\mathbf{E}^* = \gamma_0 (\mathbf{E} + \boldsymbol{\beta}_0 \times \mathbf{B}) - \frac{\gamma_0^2}{\gamma_0 + 1} \boldsymbol{\beta}_0 (\boldsymbol{\beta}_0 \cdot \mathbf{E}) \quad (3.5)$$

$$\mathbf{B}^* = \gamma_0 (\mathbf{B} - \boldsymbol{\beta}_0 \times \mathbf{E}) - \frac{\gamma_0^2}{\gamma_0 + 1} \boldsymbol{\beta}_0 (\boldsymbol{\beta}_0 \cdot \mathbf{E}), \quad (3.6)$$

where $\boldsymbol{\beta}_0 = \beta_0 \hat{\mathbf{z}}$ is the speed and γ_0 the energy of the beam center in the laboratory frame. For our gun in the TM_{010} mode, only E_z , E_r and B_ϕ are non-zero, hence we have

$$\mathbf{E}_{\text{ext}}^* = E_z \hat{\mathbf{z}} - \gamma_0 (E_r - \beta_0 B_\phi) \hat{\mathbf{r}} \quad (3.7)$$

$$\mathbf{B}_{\text{ext}}^* = \gamma_0 (B_\phi - \beta_0 E_r) \hat{\phi}. \quad (3.8)$$

Since $\beta_0 \sim 1$ and E_r and B_ϕ are of the same order (in Gaussian unit) (see Figure 1.4), so the radial components in (3.7) and (3.8) are small compared with E_z . Furthermore, for a small r , we know that [16]

$$E_r \sim B_\phi \sim \frac{r}{b},$$

where b is the pipe radius. So we only need to consider the longitudinal electric field

$$\mathbf{E}_{\text{ext}}^* \approx E_z \hat{\mathbf{z}}$$

and may ignore the $\frac{\mathbf{v}}{c} \times \mathbf{B}_{\text{ext}}^*$ term in the force.

3.1.3 Equation of Motion in the Beam Frame

Let $p_0 mc$ be the momentum of the beam center in the laboratory frame. An off-momentum particle with a momentum $(p_0 + \Delta p) mc$ in the laboratory frame has a 4-momentum in the beam frame which moves with $\beta_0 c$:

$$\begin{pmatrix} p^* \\ \gamma^* \end{pmatrix} = \begin{pmatrix} \gamma_0 & -p_0 \\ -p_0 & \gamma_0 \end{pmatrix} \begin{pmatrix} p_0 + \Delta p \\ \gamma_0 + \Delta\gamma \end{pmatrix}.$$

Since $\Delta\gamma \approx \beta_0 \Delta p + \Delta p^2 / (2\gamma_0^3)$, we get

$$\begin{pmatrix} p^* \\ \gamma^* \end{pmatrix} \approx \begin{pmatrix} \frac{\Delta p}{\gamma_0} - \frac{p_0}{2\gamma_0^3} \Delta p^2 \\ 1 + \frac{\Delta p^2}{2\gamma_0^2} \end{pmatrix} = \begin{pmatrix} \beta_0 \mu \left(1 - \frac{\beta_0^2}{2} \mu\right) \\ 1 + \frac{\beta_0^2}{2} \mu^2 \end{pmatrix}, \quad (3.9)$$

where

$$\mu \equiv \frac{\Delta p}{p_0}$$

is the relative momentum deviation.² If we only keep the first order terms, (3.9) becomes

$$\begin{pmatrix} p^* \\ \gamma^* \end{pmatrix} \approx \begin{pmatrix} \beta_0 \mu \\ 1 \end{pmatrix}.$$

If the time is short enough, the momentum change in the beam frame $dp^* \approx \beta_0 d\mu$ because $\mu d\beta_0$ is of the next order. Then we can treat β_0 as a constant and the Lorentz force is

$$mc \frac{dp^*}{d\tau} \approx mc \beta_0 \frac{d\mu}{d\tau} \approx q [E_z(\zeta, \tau) + E_{\text{sc}}^*(\zeta, \tau)]. \quad (3.10)$$

The space charge field in the beam frame is

$$E_{\text{sc}}^* = -\frac{\partial \Phi_{\text{sc}}^*}{\partial \zeta} - \frac{1}{c} \frac{\partial A_{\text{sc}}^*}{\partial \tau}, \quad (3.11)$$

²This rather unusual choice of notation will become clear later.

where the scalar and vector potential are related to the volume charge density $\tilde{\rho}^*$ like

$$\Phi_{\text{sc}}^* = \int d^3r \frac{\tilde{\rho}^*}{r} \quad (3.12)$$

$$A_{\text{sc}}^* = \frac{1}{c} \int d^3r \frac{\tilde{\rho}^* v}{r}. \quad (3.13)$$

Since $v \ll c$, we only need to keep Φ_{sc}^* which is equivalent to the long wavelength limit [32] when the space charge impedance is purely capacitive and the space charge potential is linearly proportional to the line density of a bunch,

$$\Phi_{\text{sc}}^* = Ngq\rho^*(\zeta, \tau), \quad (3.14)$$

where ρ^* is the normalized line density,

$$1 = \int_{-\infty}^{\infty} \rho^* d\zeta.$$

The line density is related the laboratory system ρ by

$$\rho^* = \frac{\rho}{\gamma_0}.$$

The dimensionless coefficient g , determined by the geometry of the environment and beam, is of order 1 [32,33] and N is the number of charges in the bunch. For a round pipe of radius b and beam radius a , the asymptotic value in the long wave limit gives $g = 1/2 + 2 \ln(b/a)$ [32]³ if a is much smaller than the bunch length. Inserting (3.14) in (3.10), we get

$$\frac{d\mu}{d\tau} = -\frac{Ngq^2}{\beta_0 mc} \frac{\partial \rho^*}{\partial \zeta} + \frac{q}{\beta_0 mc} E_{\text{tot}}^*(\zeta, \tau). \quad (3.15)$$

To solve the motion, we need another equation for ρ^* . Let $\Psi^*(\zeta, \tau, \mu)$ be the normalized density function in phase space so ρ^* is just the integral of Ψ^* with respect to μ ,

$$\rho^*(\tau, \zeta) = \int_{-\infty}^{\infty} d\mu \Psi^*(\zeta, \tau, \mu).$$

Since we know that the collision frequency is very small compared to the plasma frequency, which ranges from a few hundred MHz to 10 GHz in the laboratory frame

³There is some controversy about what the first constant in g should be. Different values (0, 0.5, 1) can be found in the literature, depending on what beam model is used [32–34].

(see Figure 2.25), we can use the Vlasov equation [24, 33] which is also called the collisionless Boltzman equation,

$$0 = \frac{d\Psi^*}{d\tau} = \frac{\partial\Psi^*}{\partial\tau} + \frac{\partial\Psi^*}{\partial\zeta} \frac{d\zeta}{d\tau} + \frac{\partial\Psi^*}{\partial\mu} \frac{d\mu}{d\tau}. \quad (3.16)$$

Integrating (3.16) over μ , the second term becomes

$$\int d\mu v \frac{\partial\Psi^*}{\partial\zeta} = \frac{\partial}{\partial\zeta} \int d\mu v \Psi^*.$$

Using (3.15), the third term becomes

$$\int d\mu \frac{qE_{\text{tot}}^*}{\beta_0 mc} \frac{\partial\Psi^*}{\partial\mu} = \frac{qE_{\text{tot}}^*}{\beta_0 mc} \int d\mu \frac{\partial\Psi^*}{\partial\mu} = 0,$$

because the total electric field $E_{\text{tot}}^* = E_z^* + E_{\text{sc}}^*$ has no explicit dependence on the momentum. We have also assumed that $\Psi^*(\mu = -\infty) = \Psi^*(\mu = \infty) = 0$. Therefore (3.16) becomes

$$\frac{\partial\rho^*}{\partial t} + \frac{\partial}{\partial\zeta} \int d\mu v \Psi^* = 0. \quad (3.17)$$

We make a further assumption that the distribution function in momentum is a delta function,

$$\Psi(\zeta, \tau, \mu) = \rho(\zeta, \tau) \delta(\mu - \tilde{\mu}(\zeta, \tau)).$$

That is, we completely ignore the momentum spread. This is equivalent to saying that the beam is cold, so there is no momentum spread in phase space. Since the cathode temperature is pretty low, and the acceleration does not change the momentum spread of electrons at small radii too much, the temperature is approximately constant. For a cold fluid, (3.17) becomes the continuity equation:

$$\frac{\partial\rho^*}{\partial\tau} + \frac{\partial}{\partial\zeta} (v\rho^*) = 0. \quad (3.18)$$

We further write v in terms of the momentum spread and to first order, it scales linearly with the momentum spread,

$$v \approx \beta_0 c \mu. \quad (3.19)$$

Actually, for a circular machine, the relative speed is [14]

$$v \approx \beta_0 c \gamma_0^2 \eta_0 \mu, \quad (3.20)$$

where η_0 is the zeroth order *slippage factor*,

$$\eta_0 = \frac{1}{\gamma_0^2} - \frac{1}{\gamma_{tr}^2}. \quad (3.21)$$

γ_{tr} is the *transition energy* defined by the *momentum compaction factor* α_c ,

$$\gamma_{tr} = \frac{1}{\sqrt{\alpha_c}}.$$

Since $\gamma_{tr} = \infty$ for a linear machine, (3.20) just yields (3.19).

Using (3.20), we get the convective derivative of μ ,

$$\frac{d\mu}{d\tau} = \frac{\partial\mu}{\partial\tau} + \beta_0 c \gamma_0^2 \eta_0 \mu \frac{d\mu}{d\zeta}. \quad (3.22)$$

Since the longitudinal electric field is the same in the laboratory and beam frame, we can drop *. Eliminating v and keeping only the first order terms, we get a system of two coupled nonlinear partial differential equations governing the evolution of the particle density and momentum spread at an instance:

$$\frac{\partial}{\partial\tau} \begin{pmatrix} \rho^* \\ \mu \end{pmatrix} + \frac{\partial}{\partial\zeta} \begin{pmatrix} \beta_0 c \gamma_0^2 \eta_0 \rho^* \mu \\ \frac{N q q^2}{\beta_0 m c} \rho^* \end{pmatrix} = \begin{pmatrix} 0 \\ \frac{q E_z}{\beta_0 m c} \end{pmatrix}. \quad (3.23)$$

From now on, we shall restrict the discussion in the beam frame and I shall drop * on ρ^* . Properties of this system will be discussed below.

3.2 Discussion

Space charge force, being proportional to Nq^2 , is independent of the sign of charges which is expected since it is always repulsive. Also, the variation of the density modifies the momentum distribution which in turn modifies the density. Naturally, for an infinitely long bunch with a uniform charge distribution ($\partial\rho/\partial\zeta = 0$), there is no longitudinal space charge force.

3.2.1 Classification of the System

The system in (3.23) is hyperbolic [35] for a circular machine below transition ($\eta_0 > 0$) or a linear accelerator, which means that the initial conditions propagate

along two *characteristics* satisfying

$$\frac{d\zeta}{d\tau} = \frac{-A\mu \pm \sqrt{(A\mu)^2 + 4AB\rho}}{2B} \quad (3.24)$$

in the (ζ, τ) plane where $A = \beta_0 c \gamma_0^2 \eta_0$, $B = Ngq^2 / (\beta_0 cm)$. It does not grow exponentially over time. But for a machine above transition ($\eta_0 < 0$), (3.23) becomes elliptic which grows exponentially for small disturbances as an initial value problem [36]. This is called the *negative mass instability* for unbunched beams in machines above transition [33]. For bunched beams above transition, synchrotron oscillation has to be added in (3.23) which acts as a stabilizing mechanism. Here we limit the discussion to a hyperbolic system; that is, a machine below transition.

Although for a linear accelerator, or a circular accelerator below transition, the system does not grow exponentially, it exhibits a different type of instability which we call *shock wave instability* since the system has a tendency to form a shock wave for any finite density variation. Generally this is not a problem because most particle bunches in accelerators are rather long (in the centimeter range) with smooth density profiles. But since we are concerned with short bunches, it can be a limit for the peak current.

3.2.2 Space Charge Wave in a Uniform, Monochromatic Beam

Let us ignore acceleration for a while and start with an initially uniform, monochromatic beam with a small density perturbation,

$$\begin{aligned} \rho(\zeta, 0) &= \rho_0 + \rho_1(\zeta, 0) \\ \mu(\zeta, 0) &= 0. \end{aligned}$$

Eq. (3.23) can be linearized into a wave equation,

$$\frac{\partial^2}{\partial \tau^2} \begin{pmatrix} \rho_1 \\ \mu \end{pmatrix} - u_0^2 \begin{pmatrix} \rho_1 \\ \mu \end{pmatrix} = 0, \quad (3.25)$$

where the wave velocity depends on the charge density,

$$u_0 = \pm \sqrt{\frac{gq^2\gamma_0^2\eta_0}{m} N \rho_0}. \quad (3.26)$$

u_0 can be considered as the “sound” speed in the electron gas and any disturbance travels at u_0 . The space charge wave for a higher density beam has a higher speed. For our beam $N \sim 10^9$ at the gun exit and $\rho_0 \sim (\beta_0 c \cdot \delta t \cdot \gamma_0)^{-1} \simeq (19 \text{ mm})^{-1}$. Using $\delta t \sim 13 \text{ ps}$, $\beta_0 \approx 0.98$ and $\gamma_0 \approx 5.1$, the space charge field is 200 – 300 V/m and the space charge wave has a velocity

$$u_0 \sim 4 \times 10^6 \text{ m/s} = 0.01c. \quad (3.27)$$

3.2.3 Symmetry Properties

If there is no acceleration and ζ is replaced by $-\zeta$, the second equation in (3.23) is invariant for

$$\mu(\zeta, \tau) = -\mu(-\zeta, \tau). \quad (3.28)$$

Consequently, we get

$$\rho(\zeta, \tau) = \rho(-\zeta, \tau). \quad (3.29)$$

That is, if the density is symmetric then the momentum deviation is anti-symmetric.

3.2.4 Shock Wave Instability

Eq. (3.23) is strikingly similar to a one-dimensional isentropic, compressible fluid [37, 38] except for the convection term $v\partial v/\partial x$ which has been left out from (3.22) to (3.23),

$$\frac{\partial \rho}{\partial t} + \frac{\partial}{\partial z}(\rho v) = 0 \quad (3.30)$$

$$\frac{\partial v}{\partial t} + v \frac{\partial v}{\partial x} + \frac{c_s^2}{\rho} \frac{\partial \rho}{\partial x} = 0, \quad (3.31)$$

where $c_s = c_s(\rho)$ is the sound speed in the fluid. For an 1D adiabatic ideal gas, $c_s = dp/d\rho \sim \rho$ where p is the pressure.

What happens in a fluid like this is that the local propagation speed of the wave increases with density; i.e., the higher density part travels faster than the low density part. So the profile becomes steeper and steeper until eventually a shock wave front forms and the system becomes discontinuous [37].

In general the local propagation speed of the non-linear wave u is a function of ρ and μ and each point may have a different propagation speed. Let us find the d'Alembert's solution for (3.23),

$$\rho(\zeta, \tau) = f(\zeta - u\tau) \quad (3.32)$$

$$\mu = \mu(\rho), \quad (3.33)$$

where $u = u(\rho)$. The partial derivatives of ρ are straightforward to evaluate:

$$\frac{\partial \rho}{\partial \tau} = -\frac{uf'}{1 + \tau \frac{du}{d\rho} f'} \quad (3.34)$$

$$\frac{\partial \rho}{\partial \zeta} = \frac{f'}{1 + \tau \frac{du}{d\rho} f'}. \quad (3.35)$$

Using $\partial \mu / \partial \tau = (d\mu/d\rho)(\partial \rho / \partial \tau)$, $\partial \mu / \partial \zeta = (d\mu/d\rho)(\partial \rho / \partial \zeta)$, (3.23) becomes

$$-u + A\mu + A\rho \frac{d\mu}{d\rho} = 0 \quad (3.36)$$

$$-u \frac{d\mu}{d\rho} + B = 0. \quad (3.37)$$

We can then solve for u as a function of ρ and μ ,

$$\begin{aligned} u &= \frac{A\mu \pm \sqrt{(A\mu)^2 + 4AB\rho}}{2} \\ &= \frac{\beta_0 c \gamma_0^2 \eta_0 \mu}{2} \pm \frac{1}{2} \sqrt{(\beta_0 c \gamma_0^2 \eta_0 \mu)^2 + \frac{4gq^2 \gamma_0^2 \eta_0}{m} N\rho}. \end{aligned} \quad (3.38)$$

If $|\mu| \ll \sqrt{\frac{4gq^2}{(\beta_0 c)^2 m \gamma_0^2 \eta_0}} N\rho$, the local propagation speed becomes

$$u \approx \frac{\beta_0 c \gamma_0^2 \eta_0}{2} \mu \pm \sqrt{\frac{gq^2 \gamma_0^2 \eta_0}{m} N\rho}. \quad (3.39)$$

If the beam is almost uniform ($\rho \sim \rho_0$), then (3.39) becomes

$$u \approx u_0 + \frac{v}{2}. \quad (3.40)$$

where we have used (3.20) and (3.26). Note that the local propagation speed is not u_0 but u_0 plus half of the relative speed to the beam center.

(3.38) is a monotonically increasing function of μ ,

$$\frac{\partial u}{\partial \mu} = \frac{A}{2} \pm \frac{A^2 \mu}{2\sqrt{(A\mu)^2 + 4AB\rho}} \geq 0; \quad (3.41)$$

i.e., the propagation speed is higher for the high-momentum part than the low-momentum part. Eq.(3.41) suggests that not only does a bunch spread out but also the density and momentum deviation in the wave front will steepen due to a higher propagating speed similar to the phenomena in neutral plasmas [39–41] and water waves. Eventually a shock front may develop somewhere when $\partial\rho/\partial\zeta = \pm\infty$; this happens when the denominator of (3.35) becomes zero. Since different parts of the wave may travel at different speeds, the *breaking time* is the *smallest* non-negative value that satisfies

$$\tau_{\text{break}} = -\frac{1}{\frac{du}{d\rho} f'}. \quad (3.42)$$

In general, $du/d\rho = \partial u/\partial\rho + (\partial u/\partial\mu)(d\mu/d\rho) \neq 0$ and can be of either sign. Only an infinitely uniform beam ($f' = 0$) will never form a shock wave since $\tau_{\text{break}} = \infty$ everywhere. As long as there is a finite density variation ($f' \neq 0$) somewhere, sometime, (3.42) can have a non-negative solution. For $\tau \geq \tau_{\text{break}}$, the shock wave front in ρ and μ becomes discontinuous and (3.23) can no longer describe the system afterwards. It is like breakers in ocean leaving ripples behind. This means that certain higher derivatives which act as diffusion that have been neglected become significant.

The breaking time is not possible to calculate analytically for an arbitrary density function. We can approximate it for very simple cases. For an initially monochromatic bunch of length l , $\rho \sim 1/l$, $du/d\rho \sim \partial u/\partial\rho = \sqrt{gq^2\gamma_0^2\eta_0 N/(m\rho)}$ and $\rho' \sim 2/l^2$ at $\tau = 0$, the breaking time for the front of the whole bunch using (3.42) becomes

$$\tau_{\text{break}} \sim \sqrt{\frac{m}{gq^2\gamma_0^2\eta_0 N}} \frac{l^3}{2}. \quad (3.43)$$

This versus bunch length for different numbers of particles in a linear machine ($\gamma_0^2\eta_0 = 1$) is plotted in Figure 3.2. For our beam at the gun exit, $\tau_{\text{break}} \sim 1.9$ ns in

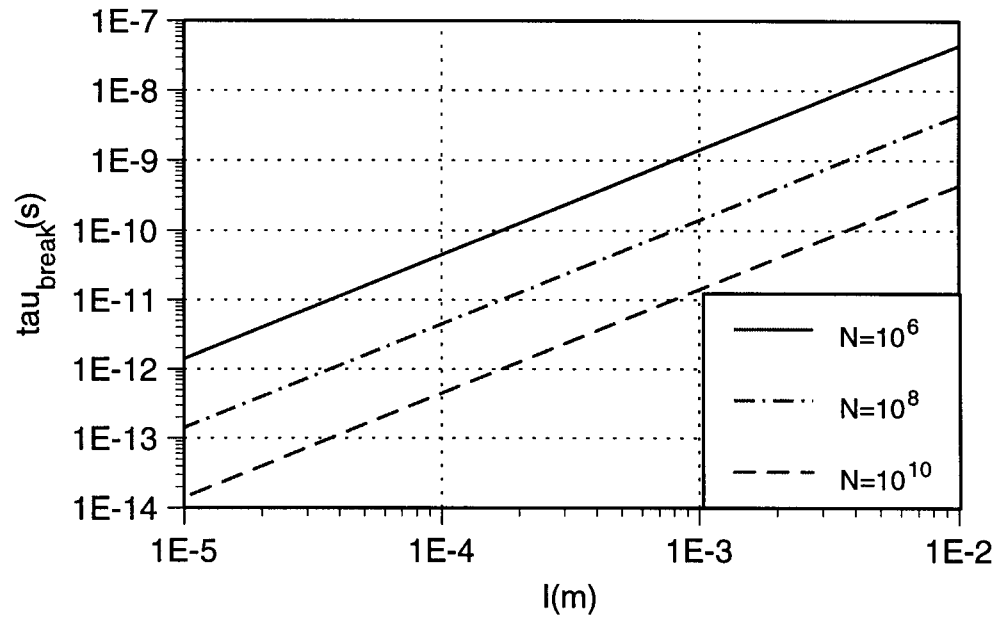


Figure 3.2: Estimated breaking time for the whole bunch versus bunch length for different N in the beam frame for an initially mono-chromatic bunch.

the beam frame which is too long for our system. But (3.43) is a very crude estimate for the breaking time of the front of the whole bunch. Some local fluctuation may break even earlier.

Since this tendency to form a shock is intrinsic for any beam with a finite density variation, the difference between a smoother and a sharper initial bunch distribution is how long it takes to break. For a smoother density profile, the onset of the shock wave takes a longer time from (3.42). In fact, Funk, et. al. showed that the shock singularity exists using different numerical methods, including Taylor expansion, method of characteristics and finite difference methods for different initial density distributions [38].

Normally the shock wave instability should not be a problem at all if the breaking time is much larger than the time of interest in an accelerator. Also since a bunch stretches longer and longer along the machine due to the velocity spread if the initial momentum distribution is not mono-chromatic, it is not a serious problem unless the goal is to achieve short and intense bunches. From (3.23), we see that the modulation to the relative momentum spread $\partial\mu/\partial\tau$ is most damaging for a short, intense, low-energy charged beam, since $\beta_0 \sim 0$ in the coefficient of ρ in (3.23), and the larger the density variation, the less time it takes to form a shock front from (3.42). Hence it is not preferable to have a very short and intense bunch when the energy is low. Although this instability is not destructive per se, since the beam is not destroyed or lost but rather develops wave structures and lengthened, it can cast a limit on how short the bunch can be for an intense beam current. The best way to combat it is acceleration as fast as possible. Even though the longitudinal electric field is the same in the beam or laboratory frame, for higher-energy beams, any effect takes γ times longer to develop.

If one wants to investigate this effect by numerical simulations in a particle-in-cell code, it is important to choose a mesh size much smaller than the rise time of the density distribution. That is,

$$\frac{\Delta z}{\beta_0 c} \ll \text{rise time}, \quad (3.44)$$

in addition to the condition that Δz must be much smaller than the dimension of the smallest structure in the gun in (2.8) to avoid aliasing in the discrete dispersion

relation discussed in Section 2.3.1. For our beam, this means $\Delta z \ll FWHM \cdot 0.98c \sim 3.5 \text{ mm}$ at the gun exit (see Table 2.1). This explains why the structures and oscillation in the longitudinal phase distributions in MASK simulations are less and less pronounced for a larger and larger mesh size because the density and space charge field are averaged over larger areas. Actually, the condition in (3.44) is stricter when electrons are closer to the cathode because the energy is low. Also, the instability takes some time to build up, which explains why we see the instability developed later in the gun as in Figure 2.6–2.11. Looking at (3.23) again, we will notice that the variation of the density plays an important role in driving the non-linear space charge wave and we expect that the frequencies are determined by the rise time of the density profile, which is what we have observed in MASK simulations and the simulations of 1D space charge waves for different initial density distributions in the following section.

3.3 Difference Scheme and Numerical Results

The most natural way, either numerically or analytically, to solve a hyperbolic system is the characteristics method [35] since the partial differential equation (PDE) decouples into two ordinary differential equations (ODE). But the difficulties in implementing such a method lie in both defining grids along the characteristics for a non-linear system and interpolating the boundary conditions and end result between grid points. So I have elected to use the more usual difference schemes.

Since (3.23) is valid only instantaneously, the time step $\Delta\tau$ has to be sufficiently small which imposes an upper limit on the mesh size $\Delta\zeta$ from the Courant condition. For the interior grid points, the simple Forward-Time-Centered-Space (FTCS) difference scheme is used [25]. This is an explicit method since an implicit scheme would be very hard for a non-linear system. For two boundary points one-sided difference scheme is used. The domain is chosen to be large enough such that at the boundary points, $\rho \approx 0$, $\mu = 0$, the contribution is too little to influence interior points. The accelerating field is modeled as

$$E(t, z) = E(z) \sin \omega t, \quad (3.45)$$

where $E(z)$ is piece-wise constant:

$$E(z) = \begin{cases} -E_1 & \forall z \in [0, l_{\text{eff},1}] \\ E_2 & \forall z \in [z_{21}, z_{21} + l_{\text{eff},2}] \\ 0 & \text{otherwise} \end{cases} .$$

E_i is defined as the voltage difference across cell i divided by the effective length $l_{\text{eff},i}$ which is given in Table 1.1 and z_{21} is chosen as the point where the electric field in the second cell falls to less than 10% of the peak field (see Figure 1.3).

At each time step, the beam parameters $(\rho(\zeta, \tau), \mu(\zeta, \tau))$ at each grid point ζ are moved forward in time in the beam frame using a constant central momentum. Then each grid point in the beam frame (ζ, τ) is Lorentz transformed back to get the corresponding coordinate (t, z) in the laboratory frame to be accelerated. The new momentum at (t, z) can then be calculated using the field in (3.45). After the new averaged momentum is obtained, the momentum deviation μ at each grid point is scaled accordingly. The time step is scaled by the new average energy γ_0 to ensure that the corresponding time step in the laboratory frame is the same each time the bunch is accelerated to prevent too much variation in the electric field since (3.23) is only valid instantaneously when there is acceleration. The procedure is repeated for the next time step.

The more stable Lax method [25] was tested but it introduces a large numerical viscosity or diffusion for a small time step. The numerical diffusion coefficient is

$$D = \frac{(\Delta\zeta)^2}{2\Delta\tau}.$$

Compared with FTCS with the same time step and mesh size, this results in an unphysical dissipation in density which becomes non-conservative. To reduce the dissipation, a smaller mesh size had to be chosen requiring an even smaller time step to satisfy the Courant condition for stability which becomes prohibitively small. So I decided to use FTCS because it yields more physical results for the same time step and mesh size provided the time step is sufficiently small.

3.3.1 Validity of the FTCS Scheme

Since FTCS is unconditionally unstable for travelling waves [25], solutions can grow exponentially over time; the time step has to be much smaller than the Courant condition to ensure numerical stability. There is no general method for the stability analysis for a non-linear system, therefore the linearized wave equation in (3.25) is used. Following the von Neumann analysis [25], let the solution at $\zeta = n\Delta\zeta$, $\tau = j\Delta\tau$ be

$$\begin{pmatrix} \rho_{1,n}^j \\ \mu_n^j \end{pmatrix} = \xi^j e^{ikn\Delta\zeta} \begin{pmatrix} \rho_{1,0} \\ \mu_0 \end{pmatrix},$$

where ξ is the amplification factor and k is the (real) wave number. The amplification factor for FTCS is

$$\xi(k) = 1 \pm iu_0 \frac{\Delta\tau}{\Delta\zeta} \sin k\Delta\zeta,$$

and the amplitude of the amplification factor is

$$|\xi(k)| = \sqrt{1 + \left(u_0 \frac{\Delta\tau}{\Delta\zeta} \sin k\Delta\zeta\right)^2} \geq 1 \quad (3.46)$$

for all k . For the chosen time step of 1 ps, mesh size of 0.5 mm and u_0 from (3.27), (3.46) yields

$$\xi \leq \xi_{\max} = 1.0002,$$

which is only weakly unstable.

In addition, the FTCS scheme used has been tested by a non-linear, uni-directional wave equation, $w_t + ww_z = 0$, which is one of the very few non-linear PDEs that are analytically solvable. Another interesting feature about it is that if the initial condition is simple enough, the breaking time of a system can often be predicted. So it serves as a good test for a numerical method for hyperbolic systems before launching into the real problem. Five initial conditions $w(z, 0)$ have been tested: linear ($w(z, 0) = \pm z$), parabolic ($w(z, 0) = 1 - z^2$), sinusoidal ($w(z, 0) = \sin z$) and Gaussian with a standard deviation much smaller than the domain of interest. The analytic solutions and breaking times of the first three initial conditions have explicit forms and the analytic solutions agree with the numerical solutions rather well up

to the breaking times as long as an appropriate mesh size and time step are used. All except the case that $w(z, 0) = -z$ show steepening as time goes on as expected. Hence we can well trust the numerical result of the FTCS scheme for the real space charge problem.

In these calculations, the beam is initially a slug extending from $z = 0$ to -4 mm at $t = \tau = 0$. Unless otherwise stated, the bunch has an initial average momentum 390 eV/ c with zero initial energy spread everywhere and a total charge of $2.4 \times 10^9 e$. When there is acceleration, the average momentum of the bunch is accelerated to about 1 MeV/ c . All figures are plotted in the beam frame for ease of comparison.

3.3.2 Gaussian Distribution without Acceleration

Figure 3.3 shows the evolution of the normalized line density and relative momentum spread of a Gaussian beam under its own space charge force without acceleration in the beam frame. The distribution appears not only to disperse, but also both edges become steeper with time. The density distribution is symmetric and the momentum deviation is anti-symmetric at all times following (3.28) and (3.29); the momentum deviation in the head of the bunch is higher than the average momentum while the one in the tail is lower since particles at the head are pushed forward by those behind and vice versa. The momentum deviation, like the density, also steepens and increases with time. Note also the onset of the oscillation after the density becomes too steep since any discontinuity propagates along the characteristics for a hyperbolic system. Naturally one does not expect that (3.23) is still valid when the relative momentum spread increase above unity. At some point, non-linear effects which have been neglected in (3.23) start to play an important role, which may introduce diffusion. Thus the growth of the momentum spread would not continue indefinitely. But still, Figure 3.3 shows qualitatively the tendency to form a shock wave even for a Gaussian bunch given enough time.

3.3.3 Trapezoidal Distribution without Acceleration

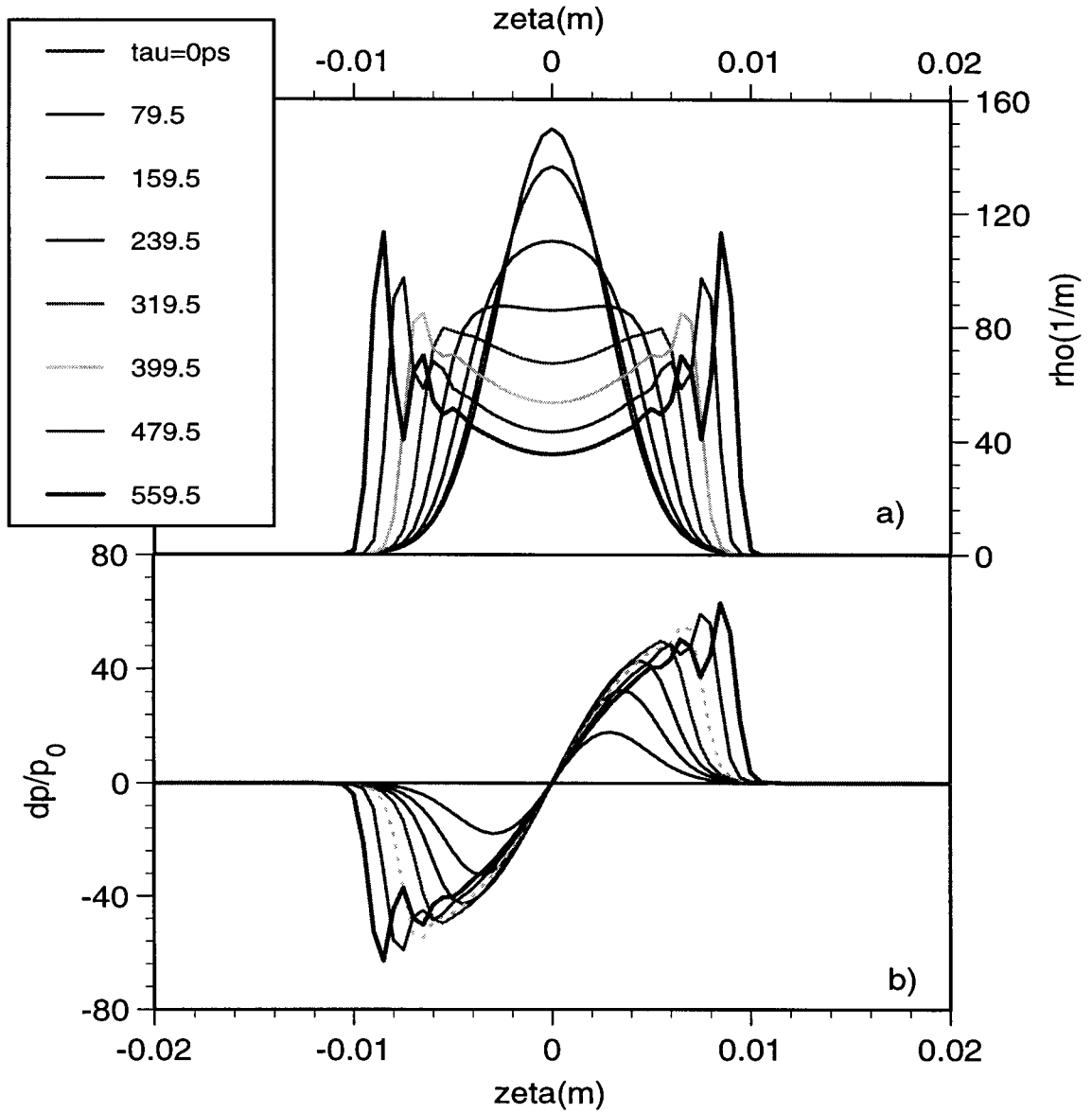


Figure 3.3: Evolution of the density a) and momentum deviation b) of a gaussian bunch in the beam frame without acceleration.

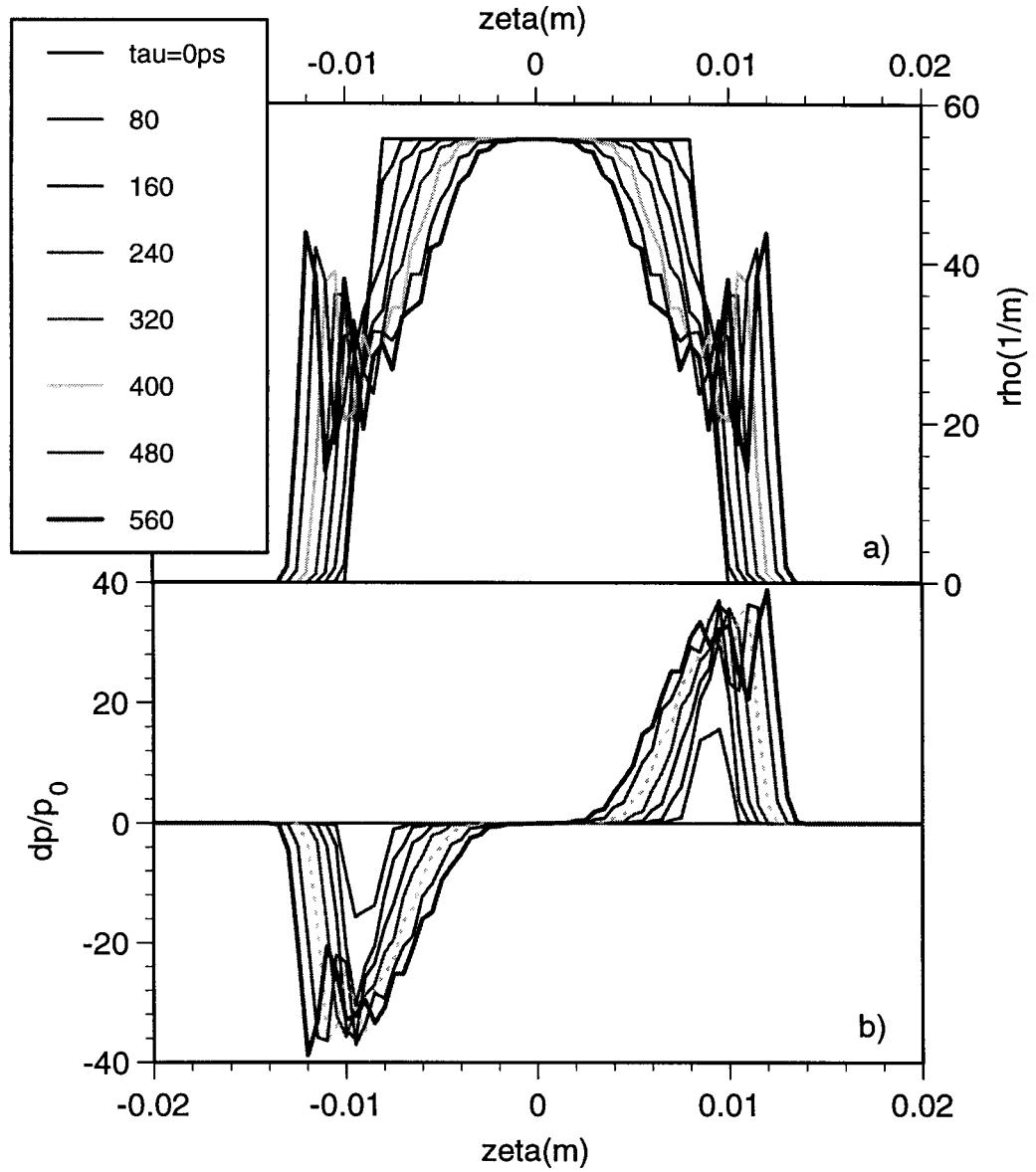


Figure 3.4: Evolution of the density a) and momentum deviation b) of a trapezoidal bunch in the beam frame without acceleration.

Figure 3.4 shows the evolution of the normalized line density and relative momentum spread in the beam frame of a trapezoidal bunch distribution under its own space charge force without acceleration. Again, we observe the same dispersion and steepening of the distribution with time. The oscillation also spreads deeper into the bunch as time goes on.

The numerical difference solution works for a shorter time for a trapezoidal distribution than a Gaussian one because the breaking time is shorter from (3.42).

3.3.4 Effect of Current Density

To see the effect of a smaller current density, Figure 3.5 shows the same case as the previous trapezoidal distribution but now with only half the electron intensity ($N_e = 1.2 \times 10^9$). The oscillation in Figure 3.5 is certainly less prominent than in Figure 3.4 since the breaking time is expected to be longer because τ_{break} depends on u which depends on the number of particles in a bunch from (3.42) and (3.38). The oscillation frequency, however, remains the same.

3.3.5 Effect of Acceleration

Figure 3.6 and 3.7 show the evolution of the density and relative momentum spread for a trapezoidal distribution in a 3D surface plot when the central momentum is accelerated to 1 MeV/ c . The relative momentum deviation initially increases but then decreases as a result of acceleration. The density spreads less rapidly compared with the one without acceleration in Figure 3.4. Though less, acceleration does not entirely prevent either the density or momentum from steepening as time goes on. This can be seen more clearly in a 2D plot in Figure 3.8 in which the last set is in a thicker line for ease of comparison. There is still a little oscillation in both the density and momentum deviation at the edges.

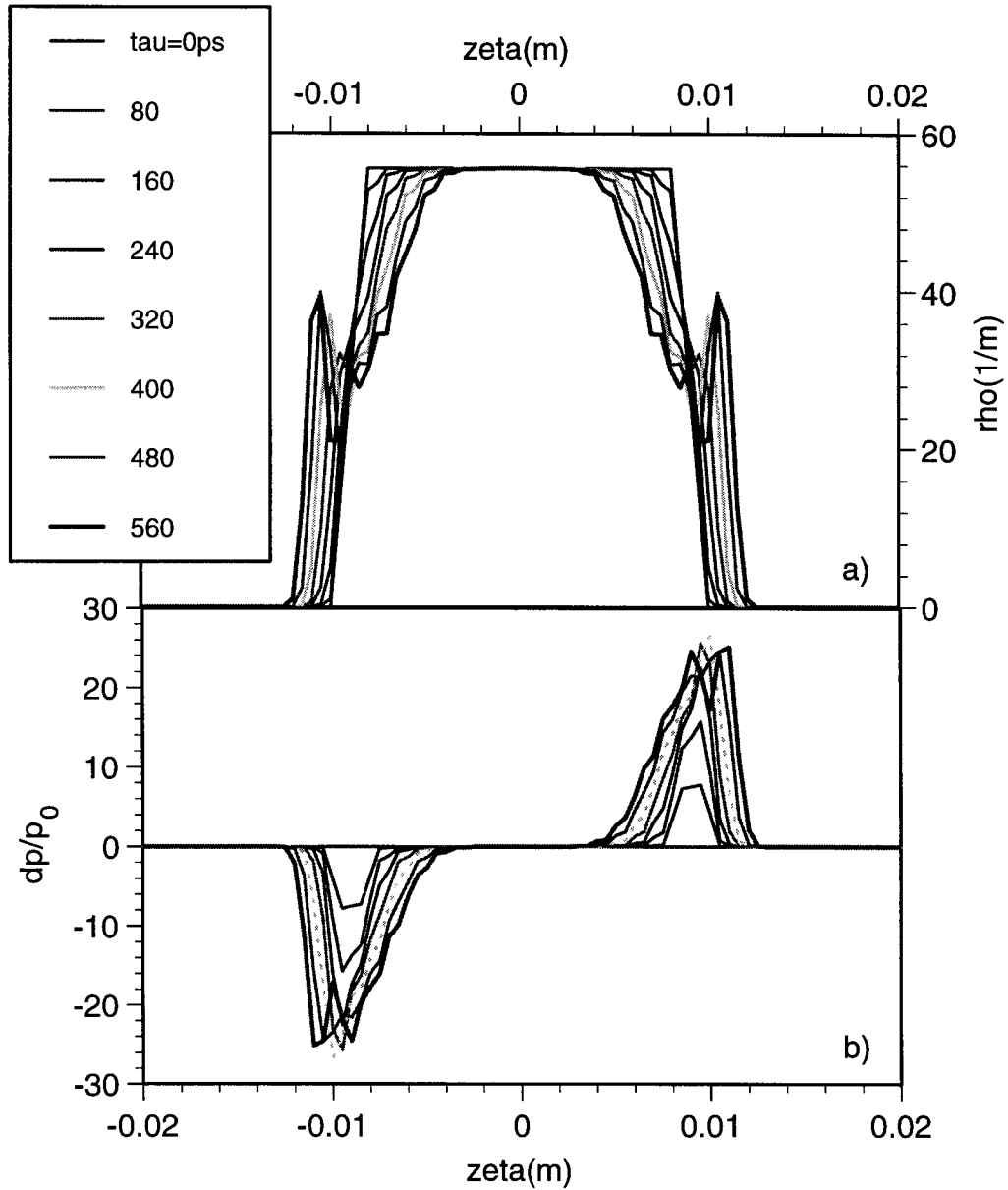


Figure 3.5: Evolution of the a) density and b) momentum deviation of a trapezoidal bunch of half of total charges in the beam frame.

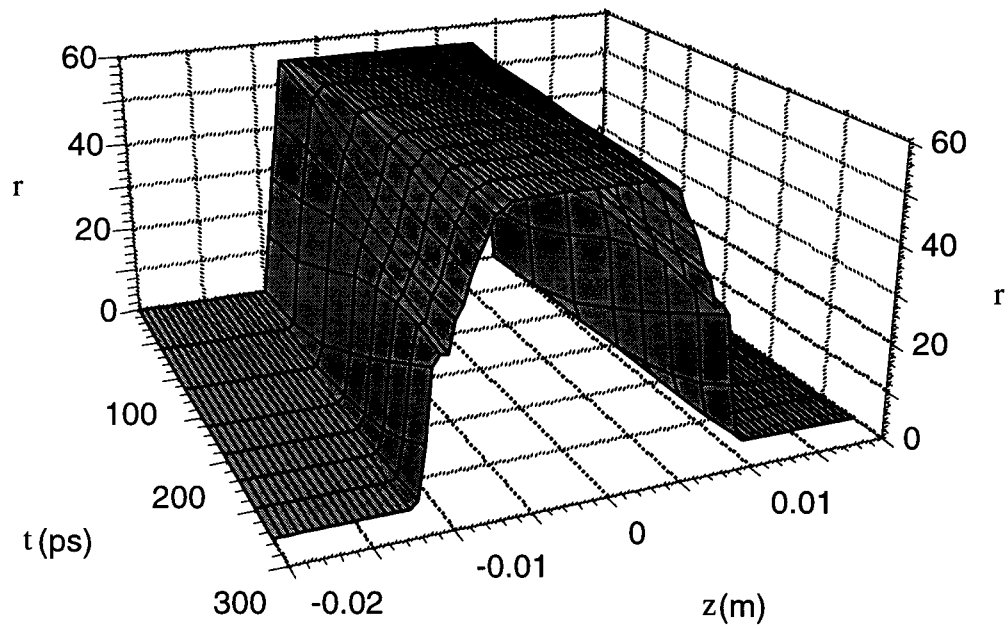


Figure 3.6: Evolution of the density of a trapezoidal bunch in the bunch frame after the center is accelerated to $1 \text{ MeV}/c$.

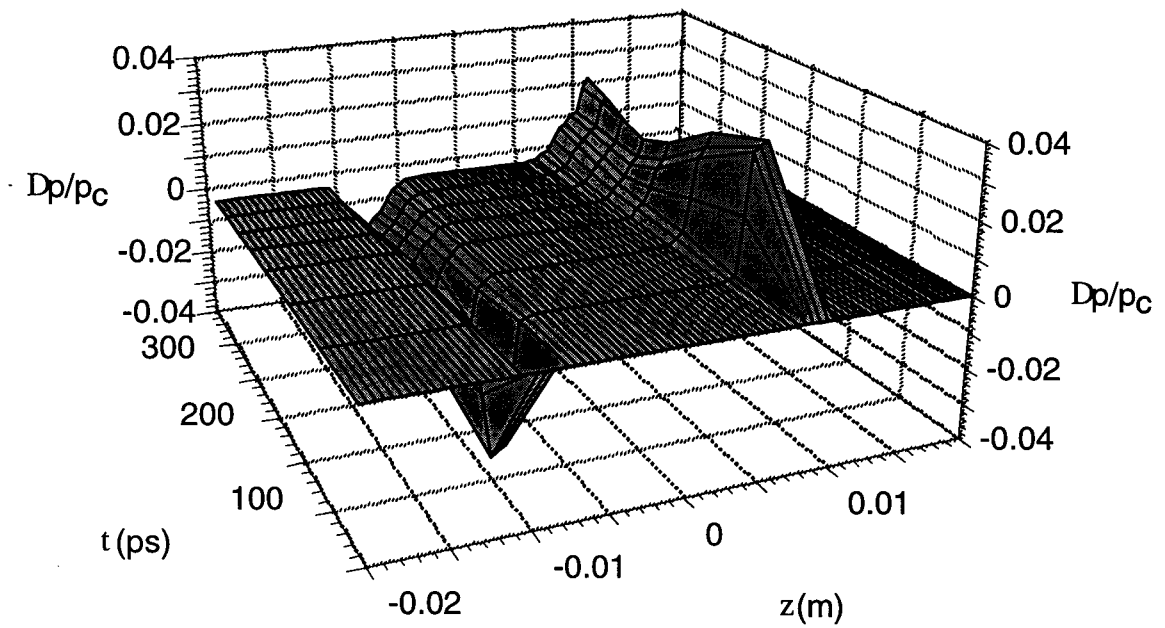


Figure 3.7: Evolution of the momentum deviation of a trapezoidal bunch in the beam frame after the center is accelerated to $1 \text{ MeV}/c$.

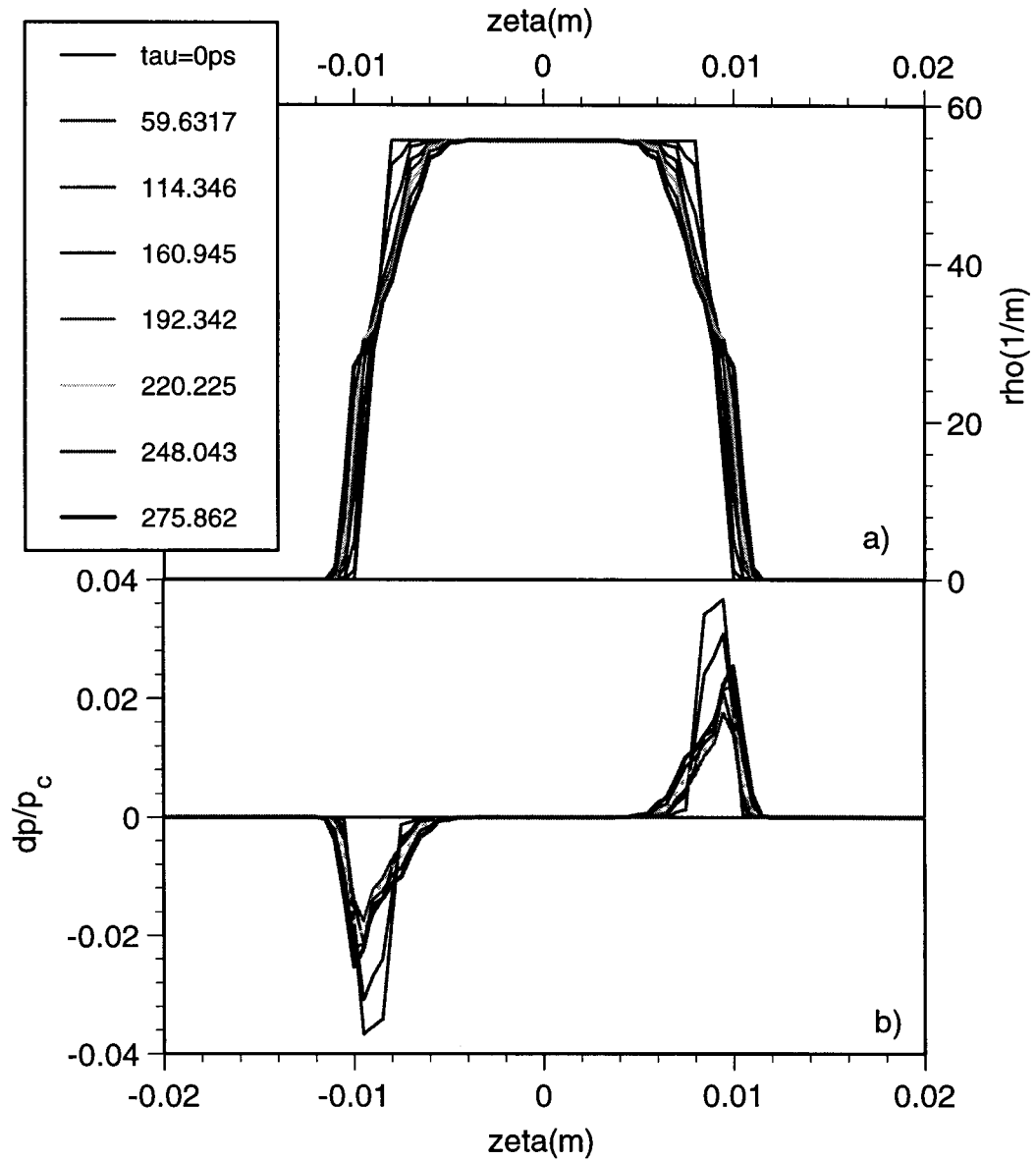


Figure 3.8: Evolution of the density a) and momentum deviation b) of a trapezoidal bunch in the beam frame after the center is accelerated to 1 MeV/c.

3.3.6 Conclusion

From the above, a low-energy beam below transition is more sensitive to the shock wave instability than a high-energy beam and acceleration is a stabilizing mechanism though it does not cause the oscillation to disappear completely. We also see oscillations in both Gaussian and trapezoidal bunches as a result of the shock wave forming and the frequency of oscillation depends largely on the variation of the density ($\partial\rho/\partial\zeta$), especially the rise time of the particle density at the beginning of a bunch. Note that the instability does not disappear even for high energy beams⁴ and for almost any bunched beam, it always has a tendency to form a shock wave given long enough time. Of course, if the density profile is smooth enough, the breaking time may be longer than the time of interest.

One should note that the first order 1D model is overly simplified for a real beam. There are approximations such as ignoring the finite temperature of a beam and the assumption that the space charge force is a line density modulation in the longitudinal direction, rather than volume modulation, of an *average* force $g\partial\rho/\partial\zeta$ for all particles. In reality, the modulation from the longitudinal space charge field may manifest in the transverse directions and the geometric factor $g = 1/2 + 2\ln(b/a)$ will depend on the beam radius a ; besides, this expression is only true for round beams and pipes. For a rectangular distribution, this approximation significantly over-estimates the longitudinal space charge force at both edges ($E_z = \pm\infty$). On the other hand, as a bunch elongates and becomes thinner, a constant g may under-estimate the space charge force since g becomes larger. But since any change of the beam radius affects the space charge field logarithmically, a constant g is not an unreasonable first approximation. Finally, the first order treatment has no diffusive terms; the inclusion of higher order terms tend to diffuse the beam and prevent the shock wave to form. With so many simplifications, the treatment is only qualitatively true. Recently, there were observations of the space charge effect such as the erosion at the edges of a low energy beam pulse [42], shock wave in a plasma tube [43] and transmission and reflection of space charge waves at bunched beam ends [44, 45].

⁴Unless, in a circular machine, the beam can be accelerated to be above transition, then it gets the negative mass instability if there is no synchrotron oscillation.

Further studies are needed to check quantitative agreement with simulations and actual beam observation.

Chapter 4

Bunch Compression and Computation

There are various effects that lengthen or *decompress* a bunch: the velocity spread, divergence effect and space charge effect. There are two methods to *compress*, that is, to shorten a bunch. The first one is by a magnetic dispersive system which utilizes the path length difference for particles of different energies. The second is acceleration by an rf field which is often called *bunching* such as rf bunching in an rf gun demonstrated in Section 2.1.1. When designing a compression system, the overall compression has to be greater than the overall lengthening. In this chapter, we will focus mainly on the velocity effect since it is the most prominent effect for a low energy beam.

When a beam travels through an ordinary component, the velocity spread introduced by the energy spread results in a difference in arrival times at the exit. The time of flight through a path length s is

$$\Delta t = \int_0^s \frac{d\sigma}{\beta(\sigma)c} \sqrt{1 + r'(\sigma)^2}. \quad (4.1)$$

where the velocity βc and transverse divergence r' can be functions of the distance. If there is no acceleration, β is a constant and can be taken out of the integral. The term involving the transverse divergence, which is of order 10^{-3} radian for a particle beam, appears in second order, and can therefore be neglected in the first order formulation.

If there is no acceleration, the difference in the arrival times between an off-momentum and the ideal, on-momentum particle is simply

$$\delta t_{\text{exit}} = \delta t_{\text{entrance}} + \frac{s(p)}{\beta c} - \frac{s(p_0)}{\beta_0 c}. \quad (4.2)$$

The subscript $_0$ represents the ideal, on-momentum particle. For a straight component such as a quadrupole or drift space, particles with higher momenta always arrive earlier, so the slope of the momentum-time in longitudinal phase space is negative, and a bunch stretches longer and longer along the beam line. For a system to serve as a bunch compressor, high-momentum particles must spend longer times in it than low-momentum ones so that all of them can arrive within a shorter time interval; that is,

$$\frac{\partial \Delta t}{\partial p} = \frac{\partial s(p)}{\partial p \beta c} > 0. \quad (4.3)$$

Such a system can reorient the negative slope in phase space into a positive one. A bending magnet has such a property but is not practical because any adjustment would deflect a beam away from the designed orbit. An alpha magnet satisfies (4.3) over a large range of energies and therefore can serve as an effective bunch compressor.

The longitudinal phase space area or longitudinal emittance is very small for the useful electrons at the gun exit under nominal running conditions (see Figure 2.11). This enables us to rotate the longitudinal phase distribution to achieve a shorter bunch length using an alpha magnet.

4.1 Overview of the Alpha Magnet

An alpha magnet is just half of a quadrupole with a magnetic field $B = -g(z, 0, x)$ [12, 46]. When a beam enters at a particular angle $\theta_\alpha = 40.71^\circ$ with respect to the y axis illustrated in Figure 4.1, the trajectories of particles enter and exit at the same point ($x = y = 0$) independent of their energies. This can be seen by solving the equation of motion inside an alpha magnet:

$$\begin{aligned} x'' &= \alpha^2 xy' \\ y'' &= \alpha^2 (zz' - xx') \end{aligned} \quad (4.4)$$

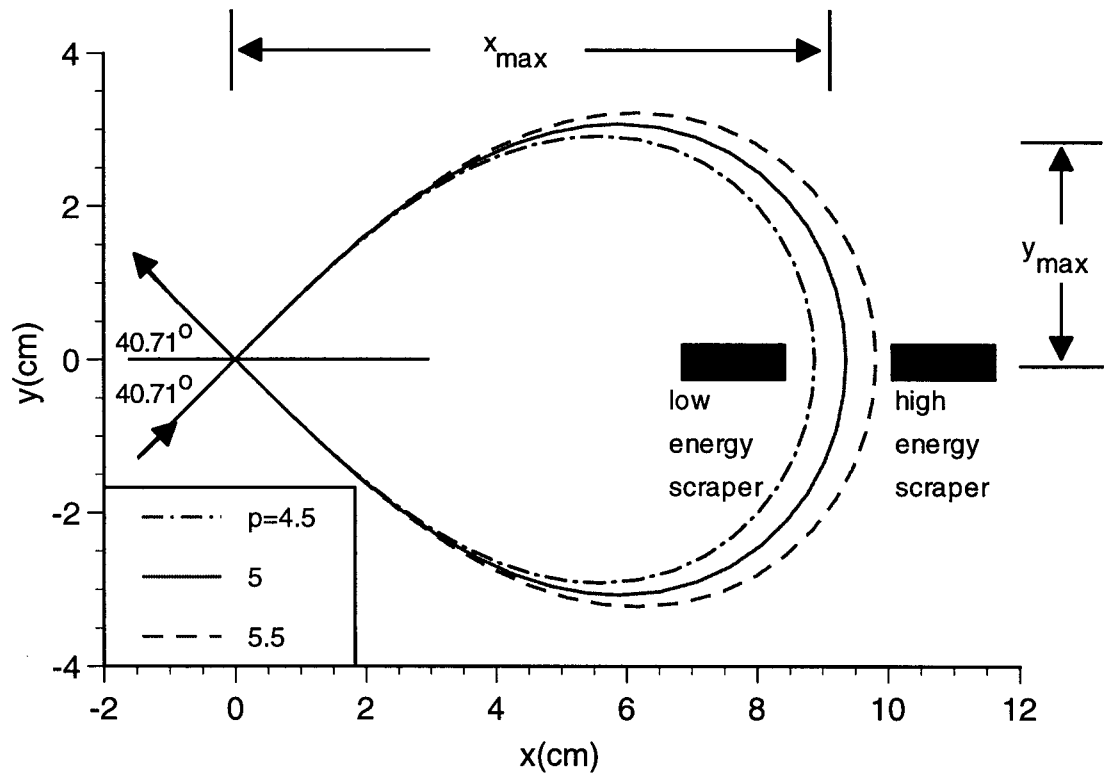


Figure 4.1: Particle trajectories in an alpha magnet for different momenta at a fixed gradient.

$$z'' = -\alpha^2 z y',$$

where $\alpha^2 \equiv gc/(\gamma\beta m_e c^2)$, $x'' \equiv d^2x/ds^2$ and $s = \beta ct$ is the path length. Note that the solution scales proportionally by the square root of the particle momentum divided by the gradient, $\sqrt{p/g}$.

The properties of an alpha magnet have been worked out so only the solution is given here [46]. The solution for an ideal trajectory ($z = 0$, $z' = 0$) follows a curve in the $x - y$ plane inside an alpha magnet

$$y(s) = \pm \frac{1}{\alpha^2} [2E(\varphi, k_0) - 2\mathbf{E}(k_0) - F(\varphi, k_0) + \mathbf{F}(k_0)], \quad (4.5)$$

where $k_0^2 \equiv (1 + \sin \theta_\alpha)/2$ and $\cos \varphi \equiv x/x_{\max}$; x_{\max} is the maximum excursion in an alpha magnet in the x direction and θ_α is the entrance angle (see Figure 4.1). The \pm sign describes the upper and lower half of the loop. $E(\varphi, k_0)$ and $F(\varphi, k_0)$ are elliptic integrals of the first and second kind and \mathbf{E} and \mathbf{F} are the corresponding complete elliptic integrals. Eq. (4.5) shows that the ideal trajectories enter and exit at the same point ($x = y = 0$) independent of the particle energies.

Other important parameters of an alpha magnet are listed below [12],

$$\theta_\alpha = 40.71^\circ \quad (4.6)$$

$$x_{\max} (\text{cm}) = 75.0513 \sqrt{\frac{\beta\gamma}{g (\text{G/cm})}} \quad (4.7)$$

$$y_{\max} (\text{cm}) = 24.62 \sqrt{\frac{\beta\gamma}{g (\text{G/cm})}}$$

$$s_{\max} (\text{cm}) = 191.655 \sqrt{\frac{\beta\gamma}{g (\text{G/cm})}},$$

where s_{\max} stands for the path length of the complete loop and y_{\max} the maximum excursion in the y direction (see Figure 4.1).

The components of the transverse transformation matrices are determined by the loop size:

$$\mathcal{R}_x = \begin{pmatrix} -1 & 1.277x_{\max} \\ 0 & -1 \end{pmatrix} \quad (4.8)$$

$$\mathcal{R}_y = \begin{pmatrix} -0.737 & 4.191x_{\max} \\ -0.109/x_{\max} & -0.737 \end{pmatrix}. \quad (4.9)$$

The negative values in the diagonal terms in \mathcal{R}_x and \mathcal{R}_y are the result of a coordinate transformation. From (4.9) and (4.8), an alpha magnet is focusing in the vertical plane and neutral in the horizontal plane. The focusing strength is inversely proportional to the loop size. It also deflects a particle with non-zero entrance angles (x', y') with respect to the ideal trajectory proportionally to the loop size.

Figure 4.1 shows ideal trajectories of electrons of different momenta in an alpha magnet. There are two energy scrapers inside our alpha magnet which can be positioned to select particles in a certain momentum bin.

4.2 First Order Matrix Formulation

It is well-known in linear beam optics that the beam coordinate at the exit of a component of length z can be expressed as the coordinate at the entrance multiplied by the transformation matrix:

$$\mathbf{u}(z) = \mathcal{R}\mathbf{u}(0) + (\text{higher order terms}),$$

or equivalently,

$$u_i(z) = \sum_j \mathcal{R}_{ij} u_j(0) + \sum_{j \geq k} \mathcal{T}_{ijk} u_j(0) u_k(0) + \sum_{j \geq k \geq l} \mathcal{U}_{ijkl} u_j(0) u_k(0) u_l(0) + \dots, \quad (4.10)$$

where

$$\mathbf{u} = \begin{pmatrix} x \\ x' \\ y \\ y' \\ \delta s \\ \mu \end{pmatrix}$$

is the six-dimensional phase coordinate of a particle and $\mu \equiv (p - p_0)/p_0$. The bunch length $\delta s = \beta_0 c \delta t$ is defined as *positive* when a particle is *behind* the ideal particle. Note that this definition of sign may not be the same in all literature. Normally, low-momentum particles ($\mu < 0$) are behind the ideal particle ($\delta s > 0$) and

high-momentum ones ($\mu > 0$) are ahead ($\delta s < 0$) so the slope of momentum-time in longitudinal phase is *negative*.

If there is no coupling between the transverse and longitudinal plane, the bunch lengthening effect from the transverse plane is of order $O(r'^2)$ which only shows up in \mathcal{T} , not \mathcal{R} . In an accelerator, $r' \sim 10^{-3}$ rad, this term is small.

For now, we are only concerned with bunch compression and only the 2 by 2 matrix for the longitudinal plane is used; that is,

$$\begin{aligned} \mathcal{R}_{\parallel} &= \begin{pmatrix} \mathcal{R}_{55} & \mathcal{R}_{56} \\ \mathcal{R}_{65} & \mathcal{R}_{66} \end{pmatrix} \\ \mathbf{u} &= \begin{pmatrix} \delta s \\ \mu \end{pmatrix} \end{aligned} \quad (4.11)$$

To compress a bunch, we require that high-momentum particles ($\mu > 0$) fall behind the ideal particle ($\delta s > 0$) and low-momentum ones ($\mu < 0$) become ahead ($\delta s < 0$). This happens only if the compressive term is *positive*:

$$\mathcal{R}_{56} > 0. \quad (4.12)$$

When designing a beam compression system, the compressive term of the overall matrix has to satisfy the above condition. And the larger \mathcal{R}_{56} , the more effective the compression is. Furthermore, for a magnetic compression system to work, the beam must have a definite correlation between the momentum spread and arrival time — δs and μ must be of *opposite* sign — $\delta s < 0$ for $\mu > 0$ or vice versa at the entrance. That is, the momentum-time dependence in phase space must have a *negative* slope — high energy particles are ahead of low energy ones. For a more monochromatic bunch obtained by a higher acceleration in our rf gun shown in Figure 2.5, the \mathcal{R}_{56} term will have no or small effect on the bunch length.

If there is no acceleration, we have the first order expansion for (4.2):

$$\begin{aligned} \delta t(z) &= \delta t(0) + \left. \frac{\partial s(p)}{\partial p} \frac{1}{\beta c} \right|_0 p_0 \mu \\ &= \delta t(0) + \frac{1}{\beta_0 c} \left[p_0 \left. \frac{\partial s}{\partial p} \right|_0 - \frac{s(p_0)}{\gamma_0^2} \right] \mu. \end{aligned} \quad (4.13)$$

So we get

$$\mathcal{R}_{56} = p_0 \left. \frac{\partial s}{\partial p} \right|_0 - \frac{s(p_0)}{\gamma_0^2}. \quad (4.14)$$

When the path length does not depend on the momentum ($\partial s/\partial p = 0$) like in a drift space or quadrupole, a bunch will lengthen due to the s/γ_0^2 term from the velocity difference. Note that this term is always present. It cannot be ignored because our beam before the linac ($\gamma \sim 5$) is not yet ultra-relativistic.

Following (4.12) and (4.14), a magnetic compression system must have the property

$$\left. \frac{\partial s}{\partial p} \right|_0 > \frac{s(p_0)}{\gamma_0^3 \beta_0} \quad (4.15)$$

so it can overcome the inherent decompression due to the velocity spread in a beam. That is, the path length difference must be large enough for different momenta to compensate the velocity effect. Transformation matrices for different components will be derived below.

4.2.1 Drift Space

For a drift of length D , we get from (4.14),

$$\mathcal{R}_D = \begin{pmatrix} 1 & -\frac{D}{\gamma_0^2} \\ 0 & 1 \end{pmatrix}. \quad (4.16)$$

Note in most literature [47], $\mathcal{R}_{56} = 0$ for a drift space because $\frac{\partial s}{\partial p} = 0$. It is no surprise that the longer a drift is, the longer a bunch becomes for a given momentum spread and the effect is vanishing when $\gamma_0 \rightarrow \infty$.

A quadrupole has the same transformation matrix as a drift space since the contribution from a finite beam divergence is of second order.

4.2.2 Dipole

Let the bend has an angle θ_0 with a bending radius ρ_0 and an arc length $l_0 = \rho_0 \theta_0$ for on-momentum particles. Since the contribution to the bunch length from the

transverse plane (\mathcal{R}_{5i}) is non-zero, the relevant matrix here is two by six. For an upright horizontal sector bend, the transformation matrix is

$$\mathcal{R}_B = \begin{pmatrix} -\sin \theta_0 & -\rho_0 (1 - \cos \theta_0) & 0 & 0 & 1 & l_0 \left(\theta_0 - \sin \theta_0 - \frac{1}{\gamma_0^2} \right) \\ 0 & 0 & 0 & 0 & 0 & 0 \end{pmatrix}. \quad (4.17)$$

A bend has a fixed, positive \mathcal{R}_{56} since θ_0 is fixed. Also \mathcal{R}_{56} is rather small for not too large deflection angles which limits the compression for a system consisting of dipole(s) only.

4.2.3 Alpha Magnet

The path length in an alpha magnet is $s_{\max} = \alpha_s \sqrt{\frac{E}{g}}$, where $\alpha_s = 191.655 \text{ (cm}\sqrt{\text{G/cm}})$ from (4.7). Using (4.14), we get the transformation matrix,

$$\mathcal{R}_\alpha = \begin{pmatrix} 1 & \frac{\alpha_s}{2} \sqrt{\frac{p_0}{g}} \left(1 - \frac{2}{\gamma_0^2} \right) \\ 0 & 1 \end{pmatrix} = \begin{pmatrix} 1 & \frac{s_{\max}(p_0, g)}{2} \left(1 - \frac{2}{\gamma_0^2} \right) \\ 0 & 1 \end{pmatrix}. \quad (4.18)$$

There are two effects in \mathcal{R}_{56} counteracting each other; the first term is the compression due to the path length difference and the second is the velocity term which is the same as in a drift space in (4.16). Note that the compressive term \mathcal{R}_{56} does not scale exactly as the square root of the momentum due to this extra term unless $\gamma_0 \rightarrow \infty$. Also counter to intuition, the weaker an alpha magnet is, the stronger the compression becomes which comes from a larger loop size for a weaker alpha magnet.

\mathcal{R}_{56} decreases with the particle energy which means that the compression is less effective for a low-energy beam due to the $1/\gamma_0^2$ term. When $\gamma_0 = \sqrt{2}$ which is 723 keV, an alpha magnet becomes “neutral” to the bunch length ($\mathcal{R}_{56} = 0$), i.e. the bunch lengthening due to the finite velocity spread cancels exactly with the compression. Below 723 keV, it ceases to compress ($\mathcal{R}_{56} < 0$) for the velocity spread is too large to be compensated by the path length difference. Therefore for an alpha magnet to be compressive, a beam must have a minimum energy of

$$\gamma_0 > \sqrt{2}. \quad (4.19)$$

Compared with a bend in (4.17), the advantages of an alpha magnet are variable compression over a wide range of momentum by changing the gradient; also unlike

a bend, the first order bunch length does not depend on the transverse phase space coordinate.

4.2.4 GTL

The transformation matrix for the beam line from the gun exit to the linac entrance, GTL, is just the product of three matrices,

$$\mathcal{R}_{\text{GTL}} = \mathcal{R}_{\text{ATL}} \mathcal{R} \mathcal{R}_{\text{GTA}}$$

where \mathcal{R}_{ATL} is the matrix for the drift space from the exit of the alpha magnet to the linac entrance and \mathcal{R}_{GTA} the one from the gun exit to the entrance of the alpha magnet since quadrupoles have the same (longitudinal) transformation matrices as drifts spaces. Using (4.16) and (4.18), we get the total matrix for GTL,

$$\mathcal{R}_{\text{GTL}} = \begin{pmatrix} 1 & \frac{s_{\text{max}}(p - g)}{2} - \frac{1}{\gamma^2} [D + \text{max} (0 \quad)] \\ 0 & 1 \end{pmatrix} \quad (4.20)$$

where D is the drift length from the gun exit to the alpha entrance plus the one from the alpha magnet exit to the end of GTL (linac entrance) and $D + \text{max}$ is the total drift length including the loop in the alpha magnet (see Figure 5.1). So, for the compression system to be effective, the alpha magnet must satisfy

$$< \frac{s_0 \left(\frac{2}{0} - 2 \right)^2}{4D^2} \approx \frac{s\beta_0 \frac{5}{0}}{4D^2} \quad (4.21)$$

according to (4.12) where we have substituted (4.7) for max . For a compression system with a given drift length and beam energy, (4.21) sets the upper limit of the alpha gradient in operation because for higher gradients, the path length differences become too little. It is important to keep this in mind when designing a compression system with an alpha magnet. For GTL, $D = 1.64 \text{ m}$, $s_0 \sim 5$ and the upper limit for the alpha magnet is 1.1 kG/cm which is more than our alpha magnet can achieve.

4.2.5 Travelling Wave Linac

If the phase slippage is ignored, the energy of a particle in a travelling wave linac increases linearly with the distance,

$$\gamma(z, \varphi) = \gamma(0) + \frac{z}{L} \Delta\gamma \cos \varphi, \quad (4.22)$$

where φ is the phase of the particle ahead the crest of the accelerating field and $\gamma(0)$ is the energy at the linac entrance; $\Delta\gamma$ is the energy gain for a particle riding on the crest and L is the length of the linac. We can get the arrival time at the linac exit by integrating $\int \frac{dz}{\beta(z)c}$,

$$t(L) = t(0) + \frac{p(L) - p(0) L}{\Delta\gamma \cos \varphi} \frac{L}{c}. \quad (4.23)$$

So the energy and arrival time for an off-momentum particle behind the ideal particle at the exit is

$$\gamma(L) = \gamma_0 (1 + \beta_0^2 \mu) + \Delta\gamma \cos(\varphi + \omega \delta t(0)) \quad (4.24)$$

$$\delta t(L) = \delta t(0) + \frac{p(L) - p_0(1 + \mu) L}{\Delta\gamma \cos(\varphi + \omega \delta t(0))} \frac{L}{c} - \frac{p_0(L) - p_0 L}{\Delta\gamma \cos \varphi} \frac{L}{c}, \quad (4.25)$$

where $\delta t(0) = \delta s(0) / (\beta_0 c)$ is the time difference between an off-momentum particle and the ideal one at the entrance. Expanding both $\delta t(L)$ and $\gamma(L)$ in the above to first order, we get

$$\mathcal{R}_{\text{TW}} = \begin{pmatrix} 1 & -\frac{p_0 L}{\Delta\gamma \cos \varphi} \left(\frac{1}{\gamma_0^2} - \frac{1}{\gamma_f^2} \right) \\ -\frac{\Delta\gamma \sin \varphi}{\gamma_0 + \Delta\gamma} k & \frac{\gamma_0}{\gamma_f} \end{pmatrix}, \quad (4.26)$$

where $k = \omega/c$ and $\gamma_f = \gamma_0 + \Delta\gamma \cos \varphi$ is the final energy for the ideal particle. Again, there are two conflicting effects in \mathcal{R}_{56} : the negative term involving $1/\gamma_0^2$ is the lengthening effect due to the initial velocity spread and the positive term involving $1/\gamma_f^2$ is the compressive effect from acceleration. The compression comes from the reduced velocity difference between low energy and high energy particles during acceleration. Normally, $\cos \varphi \approx 1$ and $\gamma_f > \gamma_0$, $\mathcal{R}_{56} < 0$ *always*, i.e. a travelling wave linac always lengthens a bunch. The compressive term from acceleration is never large enough to compensate the lengthening effect due to the initial velocity spread.

If γ_f is ultra-relativistic, the $1/\gamma_f^2$ term in \mathcal{R}_{56} can be neglected. It is kept here just for completeness. \mathcal{R}_{56} in (4.26) can be rewritten as a function of the linac acceleration $\Delta\gamma$ so we can see how the bunch length depends on the acceleration more easily:

$$\delta s(L) = \delta s(0) - \frac{2\beta_0 L (2 + \Delta\gamma \cos \varphi)}{\gamma_0 (\gamma_0 + \Delta\gamma_0 \cos \varphi)^2} \mu_0. \quad (4.27)$$

\mathcal{R}_{56} decreases with $\Delta\gamma$ and approaches zero when the acceleration is infinite. This means that the more the acceleration is, the less the decompression becomes because a particle becomes relativistic sooner and the velocity effect becomes less damaging. Compare our a linac which uses an accelerating field of 10 MeV/m with a drift of equal length, the bunch decompression, \mathcal{R}_{56} , is only 7% of a drift space.

4.3 Bunch Length Computation

Having derived the first order transformation matrices for different components, we can now use them to estimate the required strength for the alpha magnet to achieve a shortest bunch at the linac exit. At the gun exit, $p_0 \approx 5$, $\mu_0 \sim \pm 5\%$ and $\delta s_0 \sim \mp 6 \text{ ps} \doteq \mp 1.8 \text{ mm}$ from Table 2.1; the choice of sign emphasizes the negative slope between momentum-time in phase space shown in Figure 2.11. These values will be used for the first order calculation in the next section, and the ideal particle is assumed to enter the linac on the crest ($\varphi = 0$) of the rf travelling wave unless otherwise stated.

4.3.1 First Order Prediction

Since the linac always stretches a bunch ($\mathcal{R}_{56} < 0$ in (4.26)), a bunch compressed optimally to be of zero length upon entrance would attain a non-zero length upon exit. We need to compensate this by compressing a bunch to have the right length and slope in phase space such that it is shortest upon exit.

To see the lengthening effect of the linac, the bunch length at the exit as a function of the bunch length upon entrance calculated by (4.26) is plotted in Figure 4.2a). Here only the $\mu_0 = +5\%$ branch is used since the curve for $\mu_0 = -5\%$ is symmetric. We

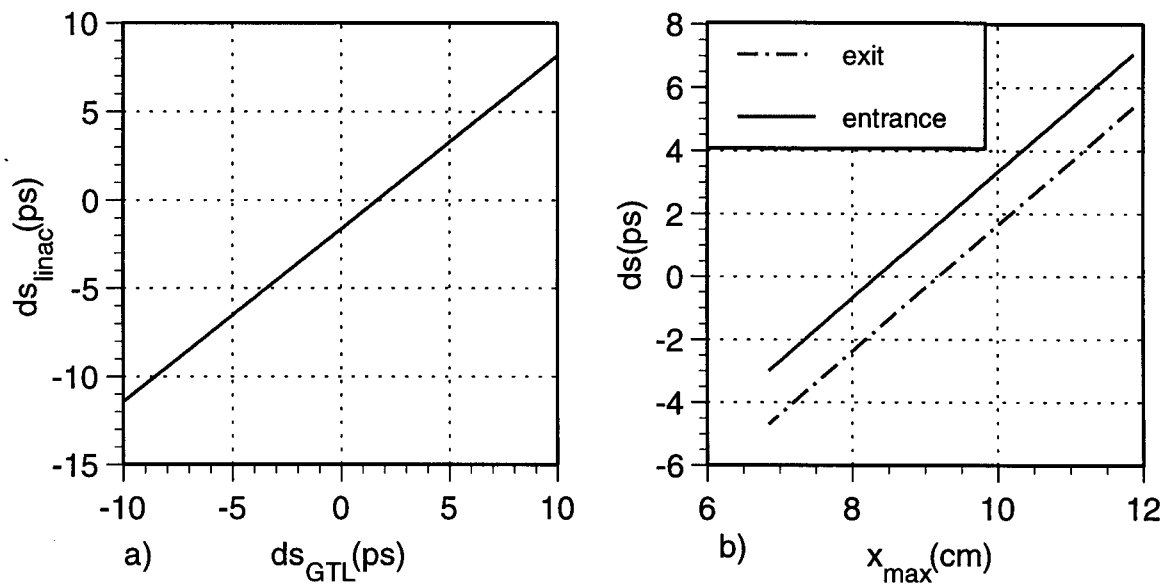


Figure 4.2: Bunch length at the linac exit as a function of the bunch length at the entrance a), and x_{max} in the alpha magnet b).

can see that if the bunch is compressed optimally to be of zero length at the entrance and all particles enter on the crest of acceleration, it spreads to be about -1.7 ps at the exit. That is, particles with $+5\%$ (-5%) momentum deviation entering the linac simultaneously on the crest with on-momentum particles become 1.7 ps ahead (behind) at the linac exit due to the velocity spread. To get a zero bunch length at the linac exit, the bunch length has to be:

$$\delta s_{\text{GTL}} \sim \pm 1.7 \text{ ps} \doteq \pm 0.5 \text{ mm.} \quad (4.28)$$

at the end of GTL for $\pm 5\%$ momentum spread from Figure 4.2a). The same sign between the bunch length and momentum spread means that particles that have a $+5\%$ (-5%) momentum deviation should be *behind* (*ahead*) the ideal particle upon entrance. That is, we need to *over-compress* a bunch to have a *positive* slope in longitudinal phase space at the linac entrance.

Now we wish to find the optimal alpha magnet setting to fulfill the condition in (4.28) at the linac entrance to have a shortest bunch at the exit. Figure 4.2b) shows the bunch length at the linac entrance (the end of GTL) and exit as a function of the maximum horizontal excursion (x_{max}) in the alpha magnet. For the same alpha loop size, the difference between the two curves in Figure 4.2b) is about 1.7 ps which is how much the bunch spreads along the linac. If we require a zero bunch length at the linac exit, x_{max} has to be about 9 cm.

We can also calculate the optimal alpha setting by using the transformation matrix of GTL in (4.20) to achieve a bunch length in (4.28) at the linac entrance for the nominal beam, we get a path length in the alpha magnet of

$$s_{\text{max}} = 23.5 \text{ cm,} \quad (4.29)$$

or equivalently, using (4.7), we have

$$\begin{aligned} x_{\text{max}} &= 9.2 \text{ cm} \\ g &= 334 \text{ G/cm} \end{aligned} \quad (4.30)$$

for the nominal beam.

Alternatively, the optimal setting of (4.30) for a zero bunch length at the linac exit can be calculated by demanding the final bunch length δs_f in the final particle

phase coordinate at the linac exit $\mathbf{u}_f = \mathcal{R}\mathbf{u}_0$, to be zero. \mathcal{R} is the overall matrix from GTL through the linac, which is the product of the transformation matrices of the linac and GTL in (4.26) and (4.20), $\mathcal{R} = \mathcal{R}_{\text{TW}}\mathcal{R}_{\text{GTL}}$. The optimal loop size inside the alpha magnet is

$$s_{\text{max}} = \frac{2}{1 - \frac{1}{\gamma_0^2}} \left[\frac{D}{\gamma_0^2} + \frac{p_0 L}{\Delta\gamma \cos\varphi} \left(\frac{1}{\gamma_0^2} - \frac{1}{\gamma_f^2} \right) - \frac{\delta s_0}{\mu_0} \right], \quad (4.31)$$

where the subscript $_0$ indicates values at the gun exit and $_f$ the final value at the linac exit. The gradient can be calculated from (4.7). With a fixed initial bunch length δs_0 , momentum spread μ_0 at the gun exit, GTL length D (excluding the alpha loop), linac entrance phase and acceleration, s_{max} in (4.31) is a function of the initial beam energy γ_0 because of the extra term involving $1/\gamma_0^2$. In other words, the loop size for the optimum compression is *not* a fixed value for all energies unless the beam is ultra-relativistic. And the gradient for the optimal loop size in (4.31) by using (4.7) does *not* scale linearly with the momentum. Note that this is unlike the geometric focusing factor, k for a regular quadrupole, which scales proportionally with the particle momentum.

To see this more clearly, the final bunch length at the linac exit versus the initial central momentum (p_0) is shown in Figure 4.3 for the optimal alpha gradient of 334 G/cm in (4.30) for a nominal bunch with a central momentum of 5, assuming μ_0 and δs_0 maintain $\pm 5\%$ and ∓ 6 ps at the gun exit. The compression only works for a very narrow range of momentum since the final bunch length varies as much as ± 4 ps for central momenta between 4.5 and 5.5; the \pm sign indicates that a bunch with a $+10\%$ (-10%) different central momentum than the nominal value have a negative (positive) slope in phase space. Or we can say that bunches with higher central momentum are *under-compressed* and lower ones are *over-compressed* at the linac exit.

The first order formulation for a linac in (4.26) does not predict any increase of momentum spread due to the non-zero bunch length at linac entrance when the entrance phase is zero. But the more exact formula in (4.22) yields an extra momentum spread of 0.1% at the linac exit for a bunch length at the entrance in (4.28) than if all particles enter the linac on the crest ($\delta s_{\text{GTL}} = 0, \varphi = 0$) at the entrance. This is

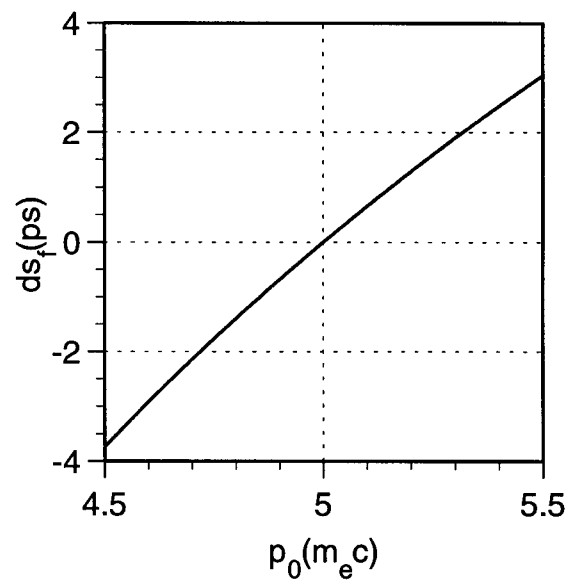


Figure 4.3: Bunch length at the linac exit versus the central momentum for an alpha gradient of 334 G/cm.

an acceptable trade-off between short bunches and momentum spread.

4.3.2 Estimation of Bunch Lengthening after the Linac

The above analysis does not consider the lengthening in the drift space after the linac. Now let us estimate how much it would be. For an accelerating field of 10 MV/m, (4.26) gives the final energy and momentum spread after the linac of

$$\begin{aligned}\gamma_f &\approx 65 \\ \mu_f &\approx \pm 0.4\% \end{aligned} \quad (4.32)$$

for $\gamma_0 \approx 5.1$ and $\mu_0 \sim \pm 5\%$ before the linac. According to (4.16), a drift space D after the linac gives a lengthening effect of

$$\mathcal{R}_{56} = 2.4 \times 10^{-4} D,$$

or ± 3 fs/m. The transition radiator is about 3.8 m downstream of the linac exit and the dipole for synchrotron radiator at the end is about 8.8 m from the linac exit (see Figure 1.5), so the lengthening would be only about 11 fs at the transition radiator and 26 fs at the dipole.

It is more efficient to compress the beam before the linac than after. One reason is GTL, which is about 1.64 m long excluding the alpha magnet, would lengthen a bunch too much due to the velocity spread if there is no compression. If there is no compression in GTL, the drift using (4.16) would give a bunch length of

$$\delta s_{\text{GTL}} \approx \delta s_0 + 63.1 \times 10^{-3} \mu_0 = \pm (1.8 + 3) \text{ mm} \doteq \pm 16 \text{ ps}, \quad (4.33)$$

at the end of GTL where δs_0 and δs_{GTL} are the bunch length at the gun exit and end of GTL (linac entrance). This is about $\pm 16^\circ$ in rf phase in the linac. In the linac, the bunch would stretch by another $\pm 0.5 \text{ mm} \doteq \pm 1.7 \text{ ps}$ using (4.26) so the final bunch length at the linac exit becomes

$$\delta s_f \approx \pm 5.4 \text{ mm} \doteq \pm 18 \text{ ps}.$$

This would require an alpha magnet of size

$$x_{\text{max}} \sim 0.55 \text{ cm}$$

after the linac for $\gamma_f = 65$, $\mu_f = \pm 0.4\%$ in (4.32) which can be hard to manufacture. For a compression system for a high-energy beam with a small energy spread, an achromat composed of bends and drifts may be more suitable than an alpha magnet.

An additional disadvantage of compressing a beam after the linac is the extra momentum spread due to the large phase difference (16°) upon the linac entrance, compared with only 1.7° in (4.28) if we compress a bunch before the linac. Even though the first order formulation for the linac in (4.26) does not predict an extra momentum spread due to a finite bunch length upon entrance if the bunch enters the linac on the crest ($\varphi = 0$), the phase difference does introduce an extra momentum spread. This undesirable momentum spread is about $\pm 4\%$ for 16° phase difference between the bunch head and tail if we use (4.22), compared with only $\pm 0.4\%$ in (4.32) when the bunch is pre-compressed in GTL.

4.3.3 Estimation of the Divergence Effect

A real beam always has a finite emittance therefore a finite transverse divergence. The slope in the particle trajectory with respect to the beam axis contributes to an extra path length.¹ For a particle with a non-zero horizontal and vertical angle of x' and y' relative to the ideal trajectory, the extra path length in a drift length D is

$$\delta s = D \left(\sqrt{1 + x'^2 + y'^2} - 1 \right) \approx \frac{D}{2} (x'^2 + y'^2). \quad (4.34)$$

which is a second order effect. Inside some components such as a quadrupole or bend, x' and y' vary with the path length, in which case (4.34) should be replaced with an integral,

$$\delta s = \int_0^l d\sigma \sqrt{1 + x'^2(\sigma) + y'^2(\sigma)} - l, \quad (4.35)$$

where l is the length of the beam line segment.

For a beam with an rms divergence $\sigma_{r'}$ and momentum spread μ , the ratio between the lengthening effect due to finite divergence to velocity spread is

$$\eta = \frac{(\gamma_0 \sigma_{r'})^2}{2\mu}, \quad (4.36)$$

¹Sometimes it is called the *emittance effect*. But it is a minomer since a bunch with a zero emittance can still have a finite divergence.

	GTL	LTD
velocity effect	$8.5 \times 10^{-5} D$	$5 \times 10^{-7} D$
η	4%	0.4

Table 4.1: Bunch lengthening due to finite divergence before and after the linac compared with the velocity effect.

from dividing (4.34) by $\mathcal{R}_{56}\mu$ using (4.16). η is smaller for a lower-energy beam than a high-energy one since the numerator $\gamma\sigma_{r'} \approx \sigma_{pr}$ remains constant and μ decreases linearly with acceleration from (4.26) due to adiabatic damping. This means that for a lower energy beam, the velocity effect is more important than the divergence effect. These two effects become comparable when the energy is large enough such that the denominator and numerator in (4.36) are comparable, i.e. when

$$\gamma_0 \approx p_0 \approx \frac{2\sigma_p}{\sigma_{pr}^2}, \quad (4.37)$$

the $1/\gamma_0^2$ in \mathcal{R}_{56} can be neglected altogether in the first order matrices in (4.16), (4.17), (4.18) and (4.26).

The extra bunch lengthening due to finite divergence before and after the linac can be estimated. Although the divergence of the beam is not a constant along the beam line, but with a proper focusing, it remains bounded in a range [12]. At the gun exit, we have $\gamma_0 \sim 5$, $\sigma_{r',0} \sim 13$ mrad, $\mu_0 \sim \pm 5\%$ from Section 2.1.2 and after the linac, $\gamma_f \sim 65$, $\mu_f \sim \pm 0.4\%$ from (4.32) and $\sigma_{r',f} \approx (\gamma_0/\gamma_f)\sigma_{r',0} \sim 1$ mrad. The relative magnitude between the divergence and velocity effect in bunch decompression is estimated in Table 4.1. The divergence effect introduces $\pm 4\%$ extra path length in GTL on top of the velocity effect. This is about $\pm 20 \mu\text{m} \doteq \pm 70$ fs if the bunch is compressed to be ± 0.5 mm $\doteq \pm 1.7$ ps long at the linac entrance as in (4.28). Not surprisingly, the divergence effect is much more damaging in GTL than in LTD when the beam energy is not yet fully relativistic.

From Table 4.1, the divergence effect on the bunch length becomes almost comparable to the velocity spread effect after the linac. Since we have shown in the previous section that after the linac, the bunch lengthening due to the velocity spread can be ignored, this just means that both effects are negligible. Most lengthening either from the velocity or divergence effect comes from GTL where the electron beam is only

quasi-relativistic and the focusing is strong.

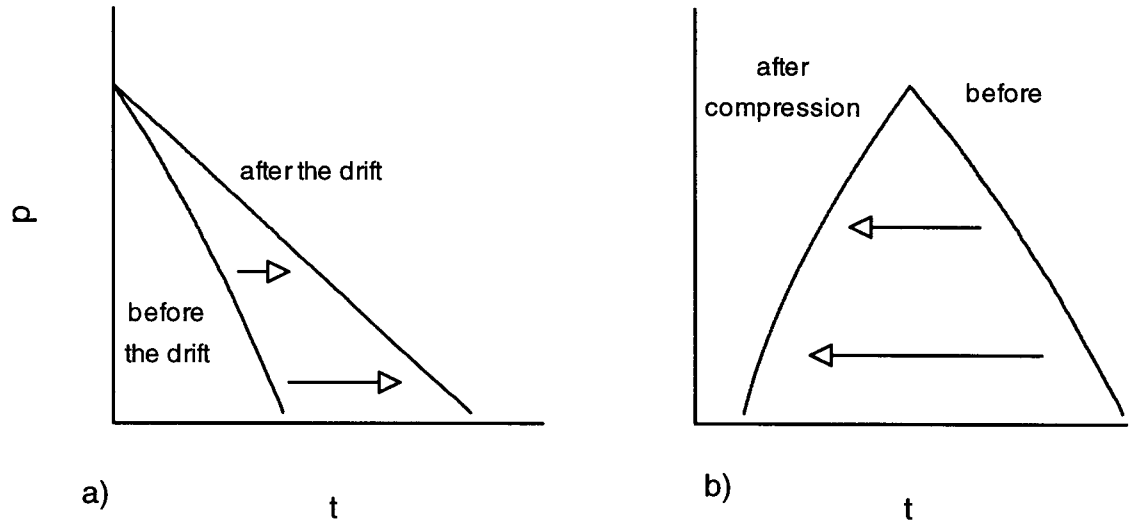


Figure 4.4: First order effect on longitudinal phase space, after a drift space due to velocity spread a), and after compression b).

There is a difference between the divergence effect which is of second order and the first order velocity effect. The latter stretches a bunch distribution in longitudinal phase space (pictured in Figure 4.4a) because of the negative \mathcal{R}_{56} . The time axis is relative to particles of highest momentum. This effect can be compensated largely by an appropriate magnetic compression system with a positive \mathcal{R}_{56} by orienting the bunch in the opposite direction shown in Figure 4.4b). Of course, if the compression system is composed of an alpha magnet, the limits for effective compression in (4.19) and (4.21) have to be met. On the other hand, the divergence effect is quadratic. It does not reorient the bunch distribution like the first order effects in Figure 4.4, instead, it stretches a bunch by “thickening” it in time. Figure 4.5 is the phase space including the divergence effect after the same drift length as in Figure 4.4a). The slope in phase space is the same except the thin line of distribution become thicker horizontally in both direction in time. Hence it cannot be corrected by a magnetic compression system. And this additional bunch lengthening due to finite divergence would remain throughout the rest of the beam line.

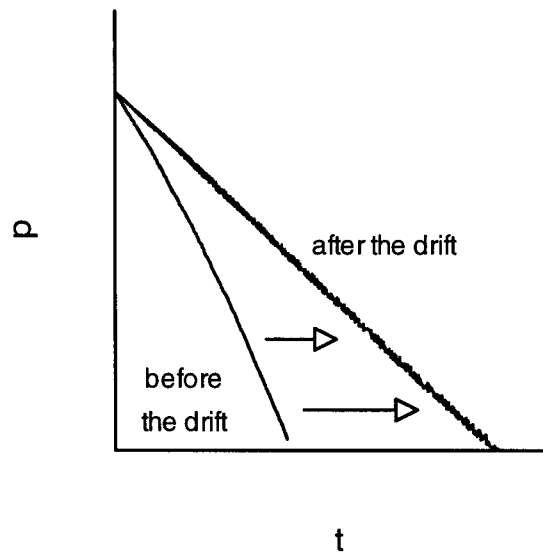


Figure 4.5: Divergence effect on longitudinal phase space after the same drift length as in Figure 4.4a).

4.3.4 Actual Calculation

The optimal setting for the alpha magnet from the first order formulation in (4.30) only serves as a starting point for iterations in actual calculation. Since the transverse divergence contributes to the bunch length as dictated by (4.1), it is necessary to know the values of the transverse as well as longitudinal phase coordinates. To know the longitudinal phase distribution of a MASK bunch at the radiation source point requires tracking the six-dimensional phase coordinates of particles throughout the beam line. In addition, this allows particle loss due to the scraping by aperture limit and the energy scrapers in the alpha magnet.

In all components except the linac, the transverse phase coordinate for each particle (x, x', y, y') is calculated by first order transverse transformation matrices (see [12, 14, 47] for transformation matrices for drift spaces and quadrupoles and (4.8) and (4.9) for an alpha magnet). The second order divergence effect on the bunch length can be included. The transverse matrix components are scaled by the momentum of each particle to take into account the higher order coupling effects between the longitudinal and transverse plane. Particles with amplitudes larger than the aperture limits anywhere throughout the beam line are discarded. The space charge effect is not included in tracking.

For a drift length D , the time of flight for the i^{th} particle is simply

$$\Delta t_i = \frac{D}{\beta_i c} \sqrt{1 + x_i'^2 + y_i'^2}. \quad (4.38)$$

For the quadrupoles, alpha magnet and linac, more elaborate calculation methods are required because the divergence is a function of the distance as in (4.1). There are two types of quadrupoles in our beam line; the longer ones can be treated as hard-edge [14] since the phase advances in them are small. But for the shorter quadrupoles, the fringe fields extend longer than the flat top in the longitudinal gradient profile shown Figure 4.6; it is more like a trapezoid. Also the focal lengths of these short quadrupoles in GTL are of the same order as the effective length, so the phase advance in each quadrupole can be as much as 60° , so the thin lens approximation [14] is not appropriate. To represent such a quadrupole more faithfully, a trapezoidal model is used [12]. Each such quadrupole is sliced into twenty pieces with linearly increasing

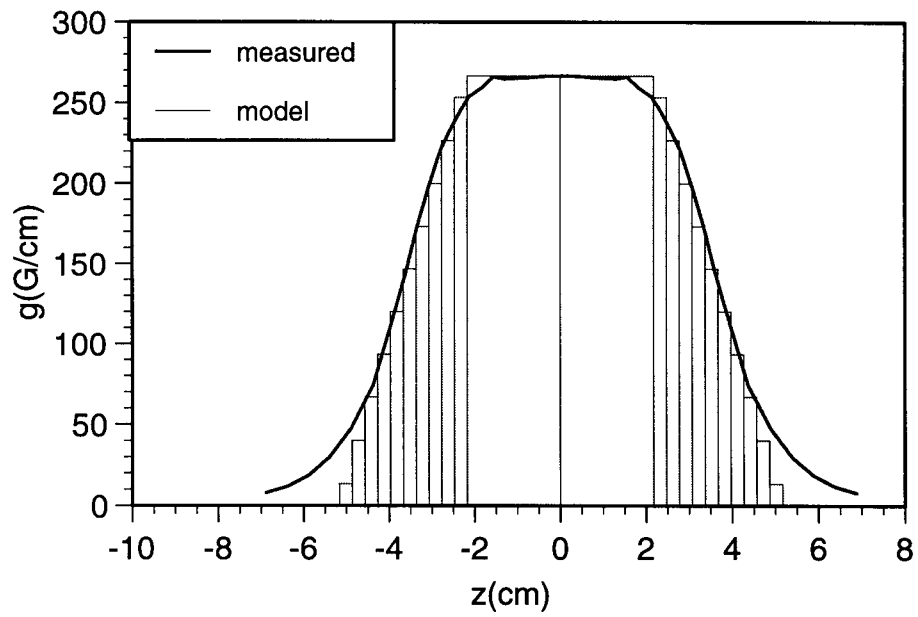


Figure 4.6: Measured longitudinal gradient profile of a short quadrupole and the slices in the trapezoidal model.

focusing in the fringe fields (see Figure 4.6). For those long quadrupoles, each is sliced into only two pieces with equal strength and length.

Each slice of a quadrupole can be treated as a thin lens — a kick sandwiched by two drifts of half the length of the slice, or fourth order symplectic expansion which is three kicks and four drift spaces [48]. It is accurate to $O(\varphi^4)$ where $\varphi = \sqrt{|k|}l_q$ is the phase advance for a quadrupole of length l_q and normalized focusing strength k . This way, the curvilinear trajectory inside a quadrupole is approximated by short segments of straight lines. In both symplectic and thin lens approximations, (4.38) is used for the drift spaces in between kicks.

In the alpha magnet, the transverse phase coordinate for each particle at the entrance is transformed by the matrices in (4.8) and (4.9). Higher order contributions to the path length from the transverse planes can be added to the first order path length in (4.7). Higher order matrices for an alpha magnet are detailed in [12].

For the linac, the coordinate of a particle has to be integrated numerically. The longitudinal phase coordinate (t, p) is integrated using the following set of coupled differential equations by a semi-implicit leap-frog method [49], assuming that $\beta_z \approx \beta$ and $p_z \approx p$,

$$\begin{aligned} \frac{dp_z}{dt} &= \frac{eE_z}{m_e c} \cos(\omega t - kz(t) - \varphi) \\ \frac{dz}{dt} &= \frac{p_z c}{\sqrt{p_z^2 + 1}} \frac{1}{\sqrt{1 + x'^2 + y'^2}}. \end{aligned} \quad (4.39)$$

There is another set of equations for the transverse planes,

$$\begin{aligned} \frac{dx}{dt} &= x' \beta c \\ x' &= \frac{p_x}{p_z}. \end{aligned} \quad (4.40)$$

The equation for the y plane is the same as for the x plane in (4.40). The accelerating field E_z in (4.39) is assumed to be constant, independent of the radial and longitudinal position. There is no radial field for the TM_{010} mode in a pill box [16], thus the transverse momenta p_x and p_y are constant throughout acceleration. The transverse coordinates are integrated implicitly. The six-dimensional phase coordinates are interpolated at the linac exit and the results from actual tracking are shown

below.

Result Without the Divergence Effect

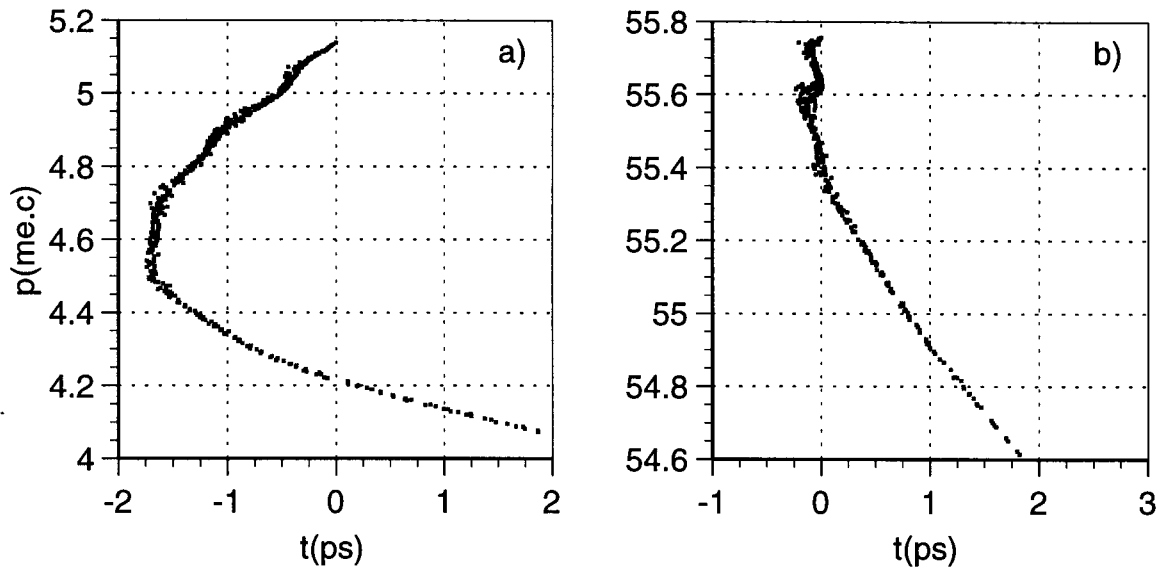


Figure 4.7: Longitudinal phase space at the linac entrance a), transition radiator b). Alpha gradient = 321.11 G/cm.

Let us ignore the divergence effect for now. Figure 4.7 shows the longitudinal phase space for a nominal beam at the linac entrance and transition radiator using an linac acceleration of 8.8 MV/m assuming that the first particles enter the linac at $\varphi = 0$.

As stated earlier, the bunch is over-compressed to have a positive slope in phase space at the linac entrance to compensate the lengthening in the linac due to the velocity spread. The final phase distribution becomes mostly upright for the useful part. The long tail from low-energy particles does not include many particles and can be discarded by closing the low energy scraper in the alpha magnet shown in Figure 4.8. The bunch still has a finite length even when the bunch distribution is upright in phase space. One factor is the oscillation in the longitudinal direction due to the shock wave instability. Also, the bunch length is intrinsically limited by the finite cathode radius because particles at larger radii undergo larger excursions in the

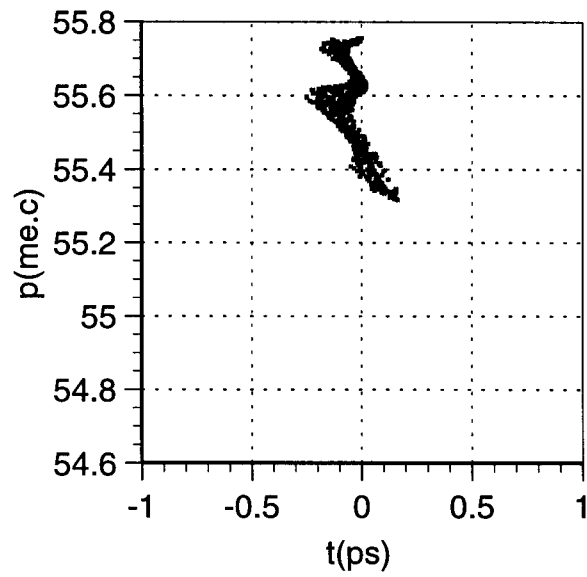


Figure 4.8: Same as Figure 4.7b) with the lower energy scraper set at $4.7 m_e c$.

gun and non-linear rf fields for off-axis particles aggravate the spread. Even without the space charge effect or non-linear fields in the gun, the bunch length is 50 – 85 fs full width because the beam radius is 3 mm at the cathode and is focused to about 1 mm at the gun exit. This ultimate limit comes from the finite size of the cathode alone.

Care must be taken in the bunch length calculation from histograms since there are only a few thousands particles in each MASK run. But to extend the form factor to high frequencies, the bin size in time has to be small which introduces statistical fluctuations at high frequency due to a finite number of simulated particles. To filter out these spurious high frequency fluctuations, Gaussian running means² of up to 9-point are performed in most calculated histograms. Also to get a better frequency resolution, large number of zeros are padded on each side of histograms. The resulting histogram and corresponding form factor which is the square of the FFT (see Section 1.2.1) at the transition radiator for the bunch distribution in Figure 4.7b) and 4.8 are shown in Figure 4.9. In the following, the temporal bin size is 0.05 ps and the frequency resolution is 0.25 THz.

From Figure 4.9, the bunch length has a *FWHM* of 0.14 ps, or an equivalent width of 0.18 ps. For a bunch length of 0.18 ps, we expect to see the spectrum at least up to 1 THz shown in Figure 4.9b). The form factor is determined mainly by the width of the main peak in time and the low-energy tail contributes only a little more at low frequency. The bunch distribution is sharper than Gaussian, so there are more higher frequency components.

Although the space charge effect is not included in these computations, we can see the effect by compressing MASK bunches with the same acceleration in the gun but different cathode current densities. For each simulated bunch, there exists a best alpha compression for the shortest bunch length. For simplicity, these bunches are not accelerated by the linac. Since to the first order, the effect of the linac on the bunch length can be compensated by a proper alpha magnet setting shown in Section 4.3.1.

The equivalent width of the shortest bunch length at the linac entrance as a

²See Appendix B for details.

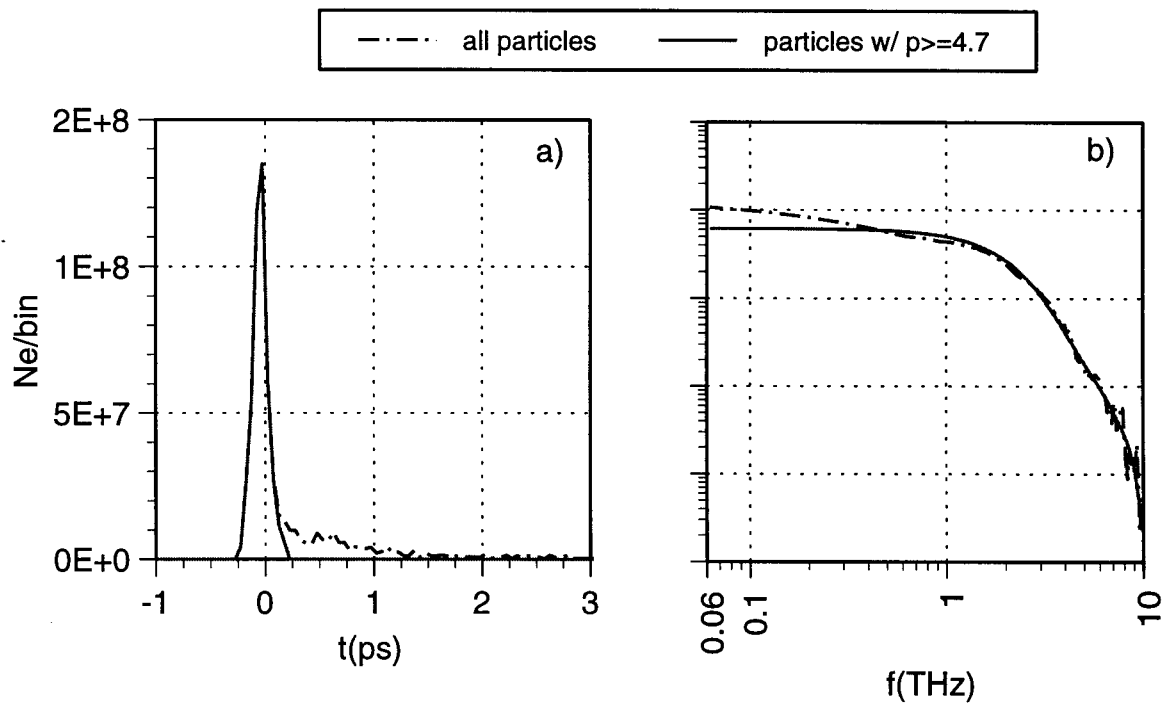


Figure 4.9: Histogram in time at the transition radiator with bin = 0.05 ps a), form factor of for all electrons and high-momentum electrons. The resolution is 0.25 THz. b) The alpha gradient = 321.11 G/cm.

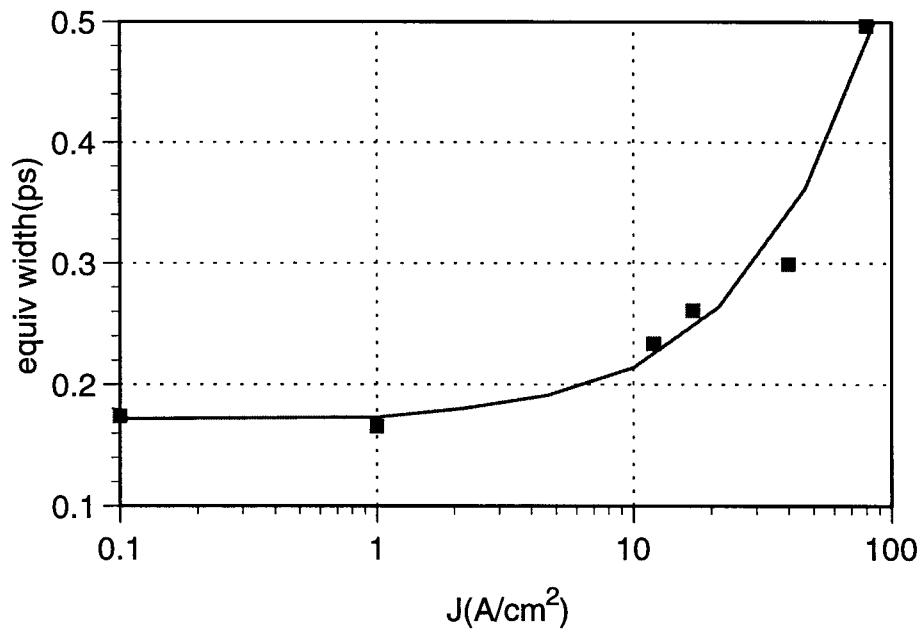


Figure 4.10: Equivalent width of the shortest bunch versus the cathode current density for a fixed acceleration in MASK.

function of the cathode current density is plotted in Figure 4.10. The curve is not constant but convex as expected. The full width of the shortest bunch as the current density approaches zero is 0.17 ps, but at a current density of 80 A/cm^2 it lengthens almost by a factor of three.

We can also calculate the peak current for the above versus the cathode current density sketched in Figure 4.11. The curve is slightly concave at high current density. The peak current for a cathode current density of 80 A/cm^2 is reduced by a factor of 3.7 compared to the peak current at a low cathode current density. Since our cathode operates slightly above 10 A/cm^2 , the space charge effect does not hurt bunch compression seriously.

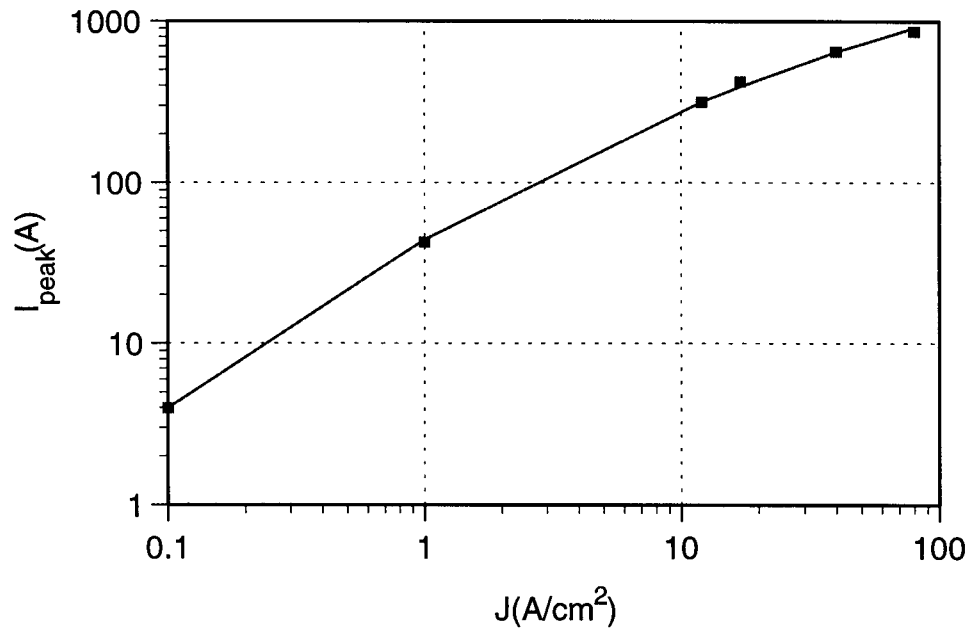


Figure 4.11: Peak electron current of the shortest bunch versus the cathode current density for a fixed acceleration in MASK.

Result including the Divergence Effect

If the divergence effect is included, proper focusing becomes very important. Figure 4.12 shows the longitudinal phase space at the transition radiator for the same

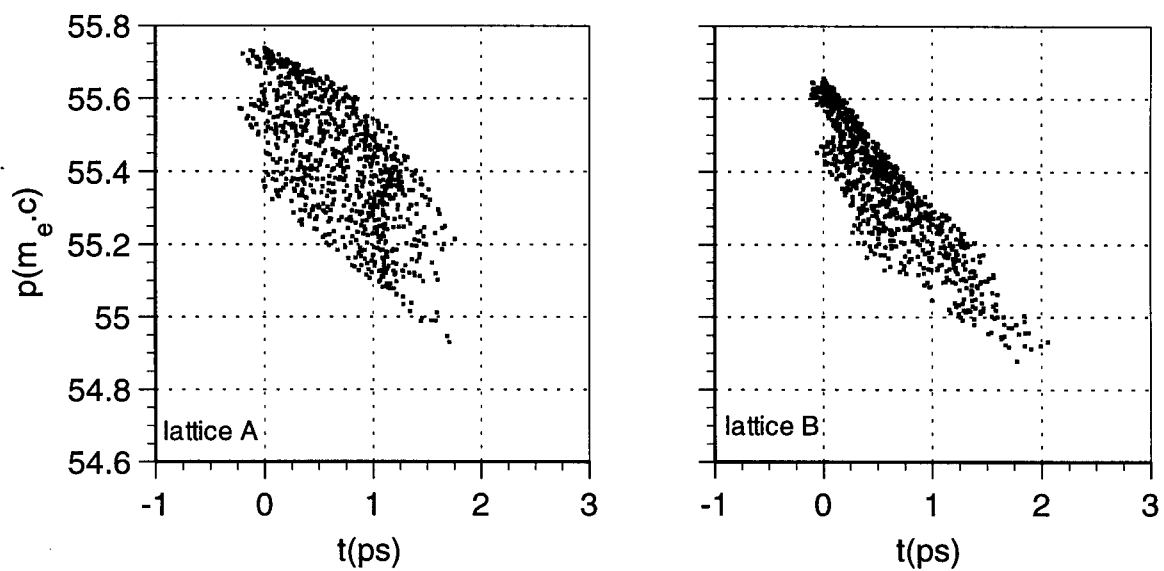


Figure 4.12: Longitudinal phase spaces at the transition radiator of the same bunch with same alpha magnet but different quadrupoles.

alpha compression and linac acceleration but different quadrupole settings. Lattice B focuses better than Lattice A in that the divergence effect hurts mainly low energy particles which spread longer than $40 \mu\text{m} \doteq 0.13 \text{ ps}$ estimated in Section 4.3.3 while the highest-energy particles stay close to centres of quadrupoles so the distribution still retains the sharp rising edge at the head of the bunch. But for Lattice A in Figure 4.12, the whole bunch stretches including the highest energy particles because they are over-focused. This is even clearer if we look at the histograms and form factors in Figure 4.13. The *FWHM*s are 1.2 and 0.94 ps for lattice A and B so the bunch length for Lattice A is 28% longer than that for Lattice B also the form factor for Lattice A is lower in high frequency. There is a little reminiscence of the space charge wave for Lattice A in Figure 4.12 which becomes more apparent when the bunch is stretched longer.

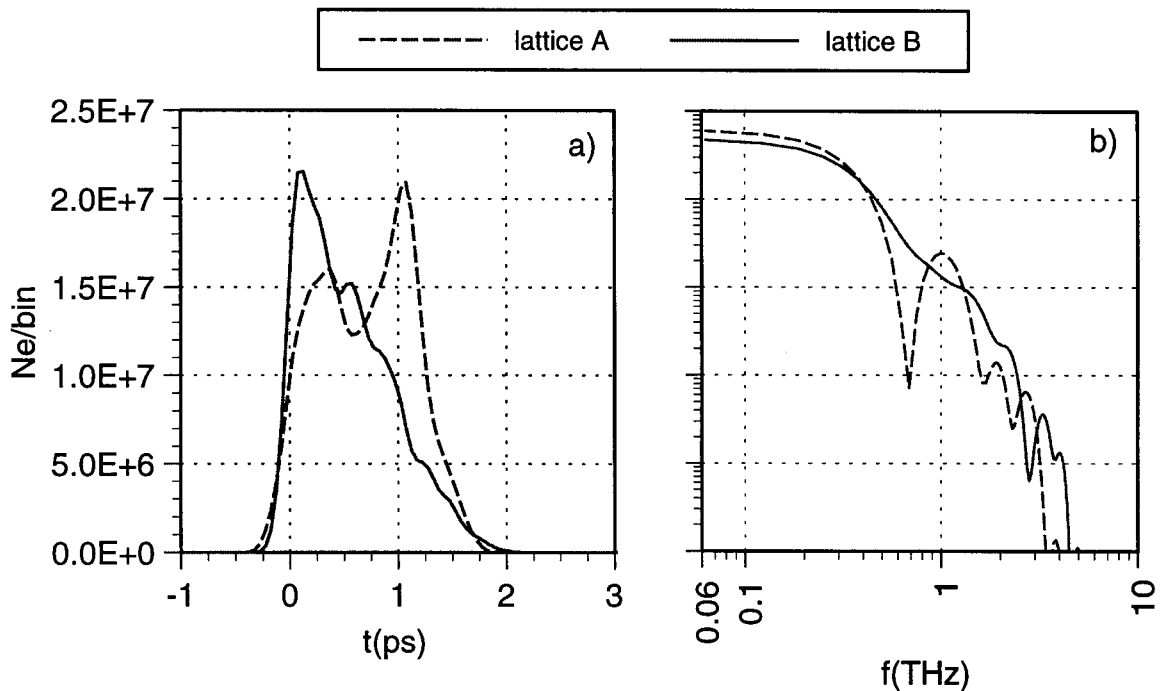


Figure 4.13: Histogram in time a) and form factor b) for Figure 4.12.

The bunch lengthening effect from the velocity effect and compression from the alpha magnet are of first order and is greater than the divergence effect in GTL.

The difference between the first and second order effect on the bunch length when there is no acceleration has been demonstrated in Section 4.3.3. While in the linac, the divergence effect is two-fold: not only does it spread low energy particles away from the bunch head, it also decreases the acceleration seen by them since the phase changes as low energy particles lag behind from (4.39).

The divergence effect is more or less independent of the bunch length or lattice because the phase advance in the betatron oscillation of the beam does not vary too much in normal operations. The GTL lattice is largely determined by the beam divergence at the gun exit, which is determined by the intrinsic emittance of the cathode in (2.2) and rf focusing in the gun. Tracking the same simulated bunch through slightly different lattices with the same alpha magnet also has verified that the bunch spreads due to the divergence effect are fairly close. Furthermore, the bunch spread from the divergence effect starts accumulating from the beginning of GTL when the beam is not fully relativistic. After the linac, there is hardly any extra spread from either velocity or divergence effect and the longitudinal bunch distribution becomes “frozen in.” If the lattice already focuses properly, there is not much one can combat the divergence effect by further tweaking quadrupoles. On the other hand, the velocity effect can be largely compensated by a compression system. This makes the divergence actually more detrimental.

Effect of the Linac Acceleration

The above calculations all use the same linac acceleration. To see the effect of the linac acceleration, the longitudinal phase space with 10% higher linac acceleration (10 MeV/m) than previous results without the divergence effect at the transition radiator is pictured in Figure 4.14.

Comparing Figure 4.14 with 4.7, a higher linac acceleration merely moves the bunch distribution up on the vertical (momentum) axis in phase space without affecting much in the horizontal (time) axis. The reason is because most electrons become fully relativistic fairly quickly in the linac; if we ignore the phase slippage and use (4.22), for an accelerating field of 10 MeV/m, an electron with an initial momentum $5 m_e c$ becomes ultra-relativistic ($\beta \geq 0.99$) after 10 cm — only $1/30$ of the

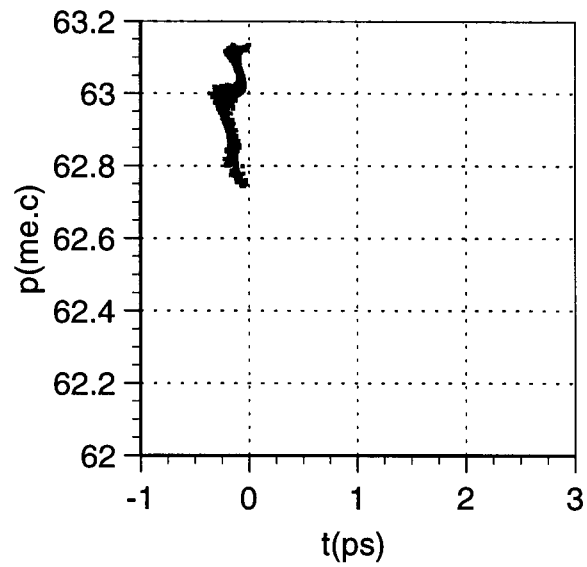


Figure 4.14: Longitudinal phase space at the transition radiator with a 10% higher linac acceleration. The low energy scraper is set at $4.7 m_e c$.

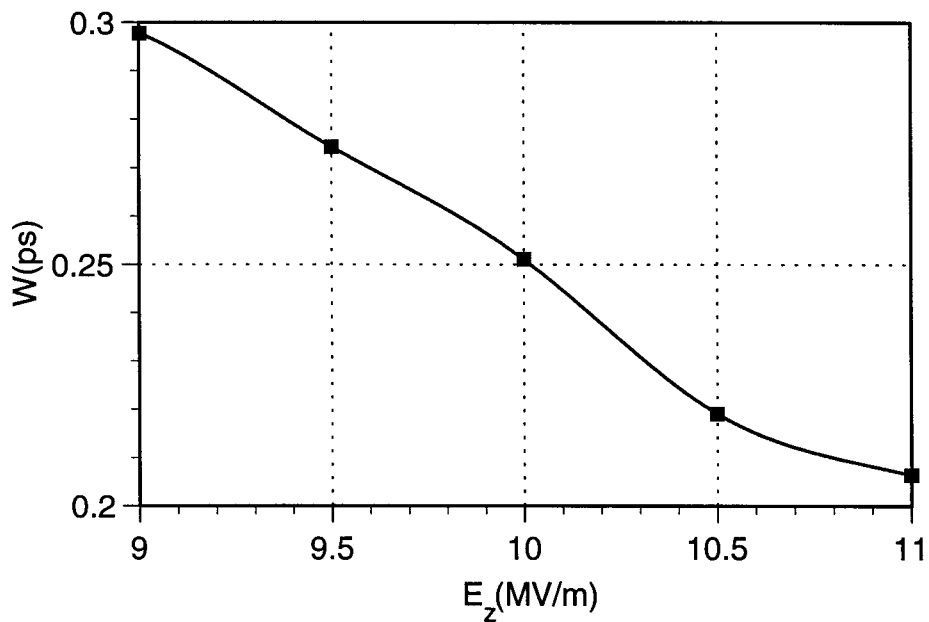


Figure 4.15: Equivalent bunch length of the nominal bunch at the linac exit versus linac acceleration.

length in the linac. Thus for most part of the linac, acceleration only increases the particle energy without changing the velocity much.

Figure 4.15 shows the equivalent bunch length of the nominal bunch at the linac exit versus the linac acceleration for an alpha gradient of 328 G/cm from actual tracking. The bunch length decreases gently toward high accelerating fields because the velocity effect stretches the bunch less and at higher accelerations. But this effect can be taken care of by a proper alpha magnet setting.

The linac acceleration is unlike the acceleration in the gun, which not only affects the momenta and exit times of particles but also the slope of the longitudinal phase distribution (see Figure 2.5). This compounded with the quasi-relativistic beam energy, the acceleration in the gun greatly affect how the compression works.

Effect of the Linac Entrance Phase

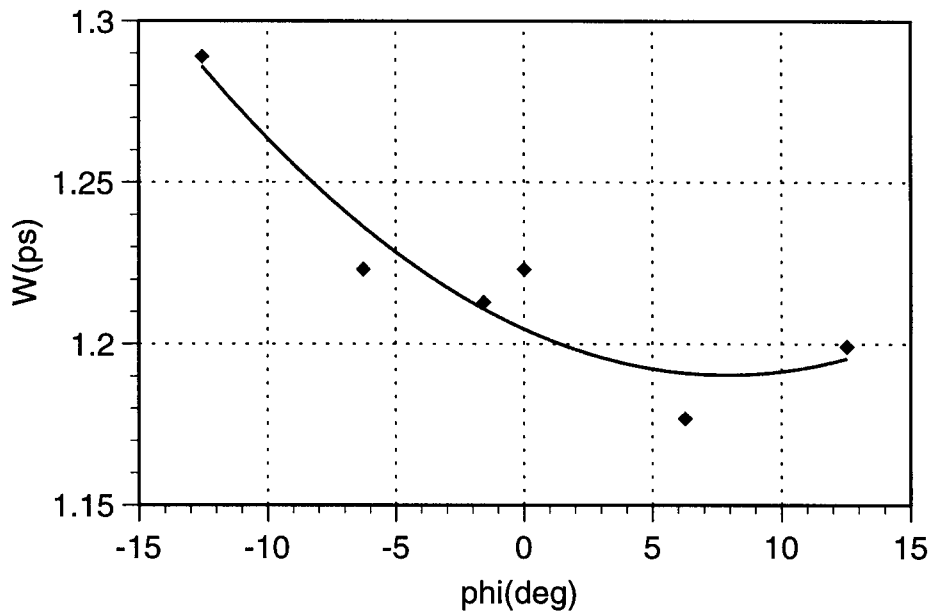


Figure 4.16: Equivalent bunch length versus linac entrance phase of the first particle for a MASK bunch.

So far, we have assumed that the first particles enter the linac at $\varphi = 0^\circ$ and now we wish to see the effect of the linac entrance phase on the bunch length which is of

second order from the transformation matrix for the linac in (4.26).

If we follow the first order matrix formulation in (4.26) and neglect the phase slippage, injecting a bunch on the crest at the linac entrance always makes it shortest at the exit. However, if the phase slippage is considered, injecting a bunch at zero phase does not always guarantee a shortest bunch at the exit. We expect that the linac phase effect is larger for a long bunch than a short one.

The calculated equivalent bunch length at the linac exit for a longer MASK bunch (~ 1 ps) after tracking throughout the beam line with a varying linac entrance phase for the first particles is sketched in Figure 4.16. The divergence effect is not included. The statistical fluctuation in bunch length calculation is much more serious than shorter bunches shown in Figure 4.7b) and 4.9 because of smaller number of particles in each bin in histograms for a fixed size bin in time.

In these calculations, the bunch is over-compressed so injecting the first particles on the crest of the linac acceleration does not give a shortest bunch. If the bunch enters slightly ahead of the crest by about 5° to allow lower energy particles to catch up, the bunch length is shorter than the one injecting on the crest by only about 5%. Therefore the effect of the linac entrance effect is much less important than the velocity spread and divergence effect.

Chapter 5

Experimental Results and Discussion

5.1 Introduction

There are two parts of the experiments: characterization of the electron beam and the radiation it produces. In order to compare measured radiation with predicted values from calculation, understanding the electron beam properties is necessary. In addition, we would like to study the impact of beam loading in the gun on the electron beam and therefore the radiation.

First, the energy distribution of the beam out of the gun and linac under various running conditions was measured. Variation of the rf power in both the gun and linac due to the finite filling time of the rf power and beam loading, especially back-bombardment, results in a large variation of the central momentum and hence the bunch length varies in a macro-pulse.

Several methods are employed to characterize the radiation generated by sub-picosecond electron bunches. Firstly, the radiation energy both from transition and synchrotron radiation were shown to be coherent. That is, the total coherent radiated energy from a macro-pulse should be proportional to the sum of squares of the intensity of micro-bunches since each bunch radiates independently and coherently.¹ Then

¹Coherence between bunches in a macro-pulse has also been achieved by a resonator, for example,

the total radiations in a macro-pulse were compared with expectations for measured electron beam currents. The average bunch length in a macro-pulse can be inferred indirectly.

Since currently the fastest streak camera is of pico-second resolution which is not sufficient for our bunches, we measure the bunch length in the frequency domain using a Michelson interferometer [52]. The principle will be described in the next section.

5.2 Setup

5.2.1 Beamline

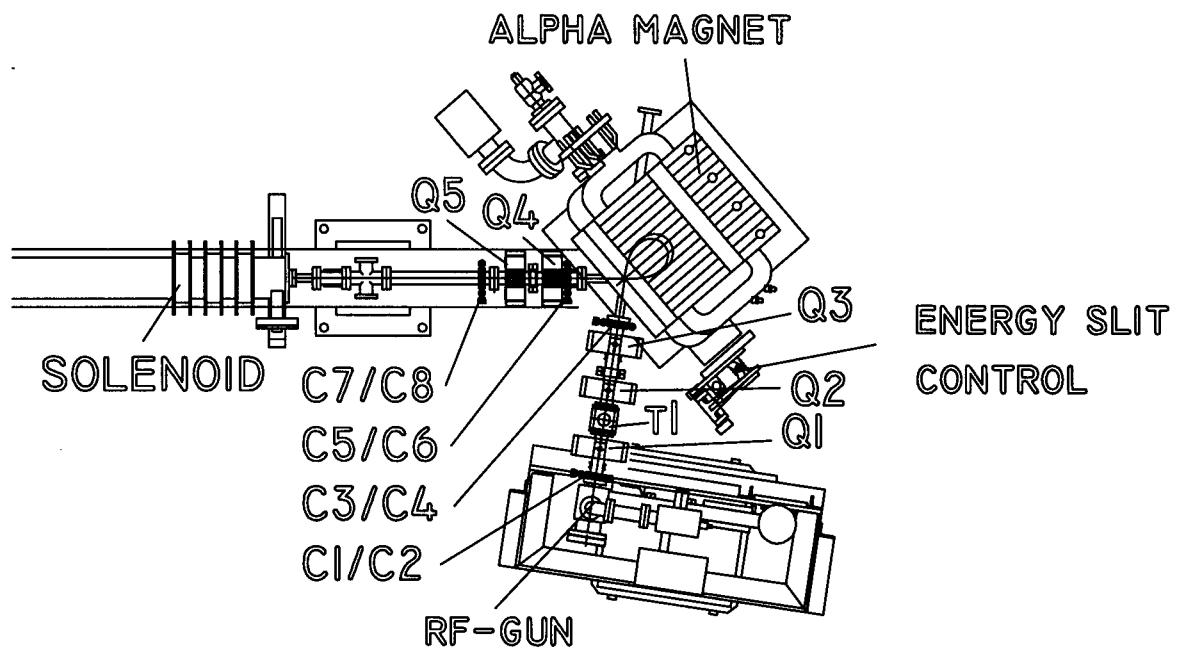


Figure 5.1: Top view of GTL.

The top views of the beamline from the gun exit to the linac entrance (GTL) and from the linac exit to the beam dump at the end (LTD) are shown in Figure 5.1 and the FEL in Pantell's groups [50] and the BRAISER cavity in SUNSHINE [51], or a Michelson scan longer than 10 cm in SUNSHINE.

5.2. There are five quadrupoles (Q1–Q5) and in GTL and four quadrupoles after the linac (Q6–Q9) for focusing. For beam steering, 13 correctors are installed along the beamline.

To monitor the electron beam, fluorescent screens plus cameras and beam current transformer toroids are used. There are two toroids in GTL: toroid 1 (T1) between Q1 and Q2, toroid 2 (T2) between Q4 and Q5 and the third (T3) and fourth one (T4) after the linac. T1 is used to monitor the total beam current out of the gun. Tracking a bunch for nominal running conditions from the gun exit to T1 shows that about 6% of particles are scraped off by the vacuum chamber before reaching T1. Therefore it is safe to assume that the T1 signal represents at least 90% of the current at the gun exit. T2 is used for momentum spectrum measurement. T3 measures the beam intensity at the transition radiator. T4 is for monitoring the beam signal after the undulator. A Faraday cup (FC) at the end of the beam line collects the total charge after the dipole that deflects the beam downward.

5.2.2 Radiation Stations

Figure 5.3 shows the side view of LTD with insets of the radiation stations. Two types of radiation were observed: transition radiation and synchrotron radiation.

Our transition radiator is a $25.4\ \mu\text{m}$ thick aluminum foil of 20 mm diameter in inset a) in Figure 5.3. The foil is supported by a copper ring oriented at a 45° angle to the beam axis. The backward radiation passes through a 1.25 mm thick high density polyethylene (HDPE) window of 19 mm diameter and 87% transmission. A copper cone channels the radiation into a room-temperature bolometer. The downstream side of the Al-foil is coated with zinc sulfide (ZnS) to monitor the electron beam size as well as its position.

At the end of the beam line, synchrotron radiation is generated when the beam is being deflected downward by a dipole shown in inset b) in Figure 5.3. A 100 mm diameter spherical mirror (M1) which is 1.3 m away from the source deflects the radiation into a copper cone through the HDPE window; another smaller copper cone again collects the radiation into the bolometer. The radiation originating from

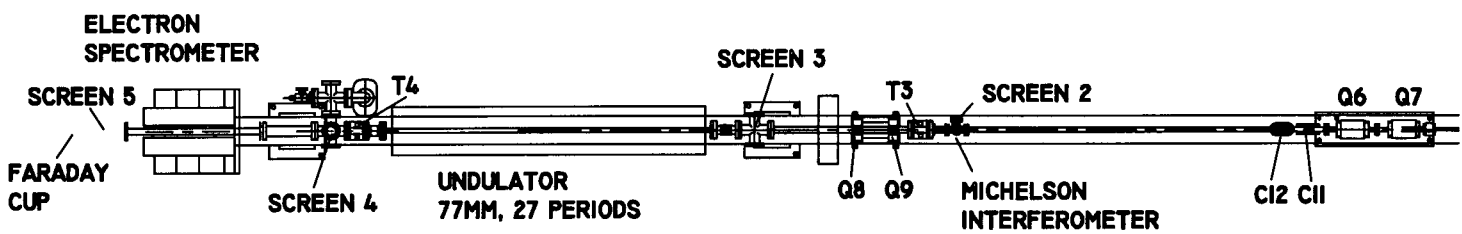


Figure 5.2: Top view of LTD.

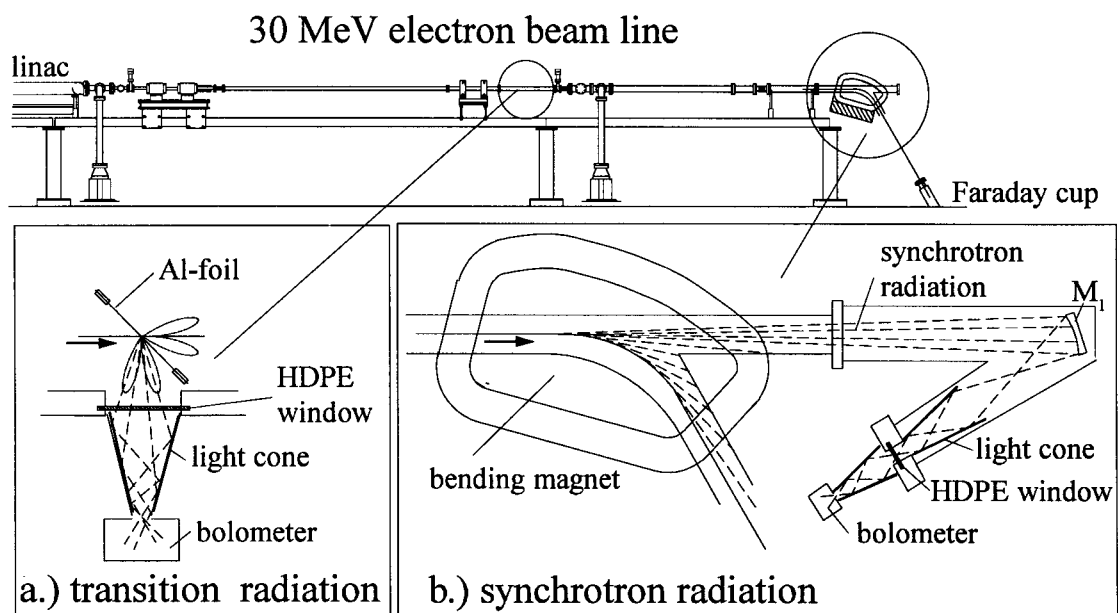


Figure 5.3: Side view of the beam line and radiation source points of a) transition radiation, b) synchrotron radiation.

both the main and fringe field of the dipole sweeps downward across M1. The net result is that the collection efficiency needs elaborate calculation.

The bolometer consists of a Molectron P1-65 LiTaO₃ pyroelectric detector of 5 mm diameter and a pre-amplifier. The sensitivity is uniform over a spectral range from visible light to millimeter waves which covers more than the full range of the expected coherent radiation. The electronic band is set at 20 Hz which is fast enough to integrate the radiated energy in a single macro-pulse without any interference with adjacent macro-pulses. The bolometer was calibrated against a Scientech thermopile power meter which was absolutely calibrated by a known electrical current. This gives an energy responsivity of 1.21×10^3 V/J for the bolometer. All following bolometer voltages quoted in this chapter are the non-amplified values.

In the total radiation measurement, the electronic noise from the fast switching device in the linac modulator were below $100 \mu\text{V}$ while the bolometer signal from a macro-pulse was of the order 0.3 V which gives a good signal to noise ratio (S/N) of 3000. In the Michelson interferometer measurements, S/N is lower, about few hundreds to 1000.

5.2.3 Michelson Interferometer

Since the frequency spectrum of transition radiation is flat and hence is identical to the form factor for a coherent source, discussed in Section 1.2.1, we can measure the bunch length by measuring the width of the pulse of transition radiation. Remember that the form factor is the square of the FFT of the bunch distribution in (1.7).

Figure 5.4 shows the schematic layout of the Michelson interferometer. It fits on a 50 by 60 cm optical table. The first mirror outside the window is a paraboloidal mirror which transforms the divergent radiation from a focal point at the radiator into a parallel beam going into the interferometer. A mylar foil is used as the beam splitter. One moveable mirror can be moved by a Newport 850-B 25 mm actuator through a Newport PMC200-P 2-axis controller which is controlled by a 486 PC through an RS-232 port. The bolometer signal is digitized and passed onto the computer by a AT-MIO-16F-5 data acquisition board by National Instruments. The autocorrelation

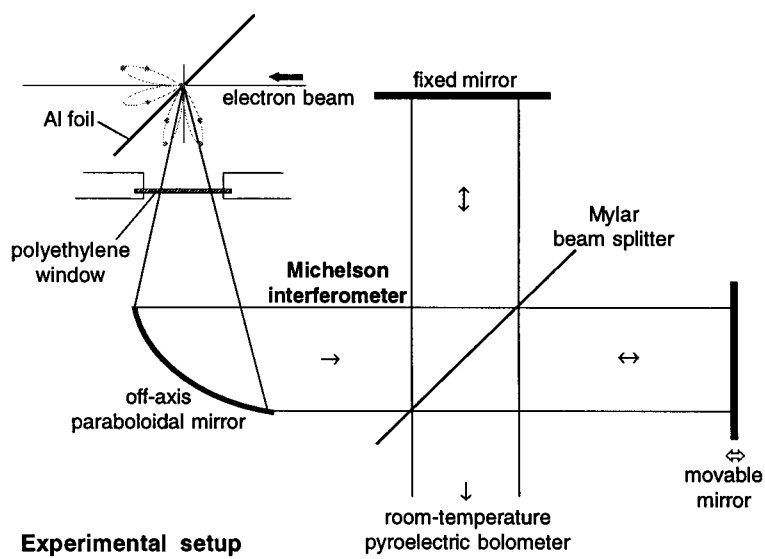


Figure 5.4: Schematic drawing of the Michelson interferometer.

measurement is done using a computer program under the LabView environment.

Assuming that the mirrors reflect perfectly, the combined signal from both arms is a function of the moveable mirror position Δ [52, 53]:

$$\begin{aligned} I(\Delta) &= \lim_{t \rightarrow \infty} \frac{1}{t} \int_{-t}^t dt |RT [E(t) + E(t + \Delta/c)]|^2 \\ &\sim 2 \left[\text{Re} \int_{-\infty}^{\infty} RTE(t) (RT)^* E^*(t + \Delta/c) dt + \int_{-\infty}^{\infty} |RTE(t)|^2 dt \right], \end{aligned} \quad (5.1)$$

where R and T are the coefficients of the reflected and transmitted field [54], and $|RT|^2$ is the beam splitter efficiency. For an ideal beam splitter $|R|^2 = |T|^2 = 1/2$. I shall drop $\lim_{t \rightarrow \infty}$ from now for simplicity.

If R and T are functions of frequency, (5.1) should be rewritten in the frequency domain,

$$I(\Delta) \sim 2 \left[\text{Re} \int_{-\infty}^{\infty} |RTE(\omega)|^2 e^{i\omega\Delta/c} \frac{d\omega}{2\pi} + \int_{-\infty}^{\infty} |RTE(\omega)|^2 \frac{d\omega}{2\pi} \right]. \quad (5.2)$$

The radiation spectrum $|RTE(\omega)|^2$ is just the Fourier transform of the *interferogram* $I(\Delta) - I_{\infty}$,

$$|RTE(\omega)|^2 \sim \int_{-\infty}^{\infty} [I(\Delta) - I_{\infty}] e^{-i\omega\Delta/c} d\Delta, \quad (5.3)$$

where $I_{\infty} \equiv I(\pm\infty) = 2 \int_{-\infty}^{\infty} \frac{d\omega}{2\pi} |RTE(\omega)|^2 = 2I(0)$. The width of the central peak of the interferogram at $\Delta = 0$ can be used to estimate the electron bunch length, for example, the central peaks in Figure 5.17a) and 5.18. For a perfect beam splitter, the *FWHM* of the interferogram for the path length difference for a rectangular bunch is simply the bunch length.

To obtain the real spectrum, the raw spectrum in (5.3) needs to be corrected by dividing the beam splitter efficiency $|RT|^2$ if it depends on frequency. For a beam splitter of index of refraction n and thickness d mounted 45° to the light pulse, if there is no absorption, R and T are [54]

$$R = -r \frac{1 - e^{i\varphi}}{1 - r^2 e^{i\varphi}} \quad (5.4)$$

$$T = (1 - r^2) \frac{e^{i\varphi/2}}{1 - r^2 e^{i\varphi}} \quad (5.5)$$

where r is the amplitude reflection coefficient of the air-mylar interface at an incident angle of 45° , $\varphi = 2kd\sqrt{n^2 - 1/2}$ and $k = 2\pi/\lambda$. Due to the finite thickness, some frequencies are suppressed completely because of destructive interference from multiple internal reflections from both sides. The result is a non-uniform transmission efficiency in frequency with periodic zeros. In the following, the index of refraction of the beam splitter, which is made with mylar, is assumed to be 1.85 [55].

5.3 Momentum Spectra of the Beam from the Gun

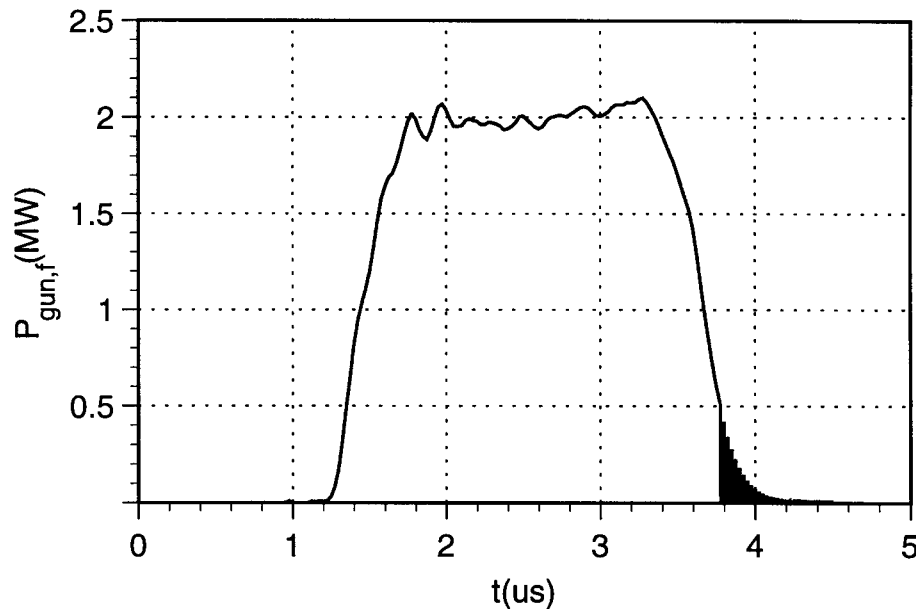


Figure 5.5: Gun power in a macros-pulse versus time.

Figure 5.5 shows how the gun power in a macro-pulse varies with time in a typical operation. The gun power rises in a time of about 800 ns then stays constant for about $1 \mu\text{s}$ and finally it decays to zero. Naturally, not all micro-bunch particle distributions are identical within a macro-pulse but vary along the macro-pulse duration.

For a given rf power, the cathode filament current must be adjusted to prevent

excessive beam loading in the gun. Also, back-bombardment can heat up the cathode additionally. This back-bombardment can be reduced by the magnetic “anti-backbombardment” coils (ABB) in the gun as will be discussed in Section 5.3.3.²

The energy scrapers in the alpha magnet can be set to allow particles in a certain momentum bin to pass through. For best momentum resolution, the loop size x_{\max} in the alpha magnet must be large since the resolution scales like

$$\frac{\delta p}{p} = 2 \frac{\delta x}{x_{\max}}. \quad (5.6)$$

For a given scraper opening δx , the momentum resolution increases with x_{\max} . Unless otherwise stated, x_{\max} was chosen to be 11 cm, limited by the width of the high energy scraper, and the resolution was set at $\pm 4\%$ which still allowed enough signal on T2. Higher resolution was tried but the signal to noise ratio became too low.

At each selected momentum value, all quadrupoles in GTL and the alpha magnet were scaled accordingly to maintain fixed geometric values — k values for the quadrupoles and x_{\max} for the alpha magnet,³ except the set with ABBs on which was taken earlier when the beamline was not yet computer controlled. The T2 signal was then averaged over 100 pulses. By scaling the quadrupoles and alpha magnet according to the momentum, the focusing was physically identical for all momenta. To avoid having to standardize the GTL magnets for each momentum bin, the data were taken in the increasing direction of momentum. The correctors were kept as low as possible because they could not be controlled remotely.

5.3.1 “Cold” Cathode Operation

Figure 5.6 shows the momentum distribution in a macro-pulse from a moderately heated cathode which is our normal operation mode and shall be referred to as a “cold” cathode. It has a smooth peak around $5 m_e c$. But this does not tell how the instantaneous momentum distribution varies with time in a macro-pulse. To see the

²ABBs were installed by Prof. Pantell’s group which shares the same gun with us.

³The beamline is currently controlled by digital-to-analog cards by Intelligent Instruments. The correctors are not controlled yet. The control program was written by the author using Turbo Vision by Borland International, Inc.

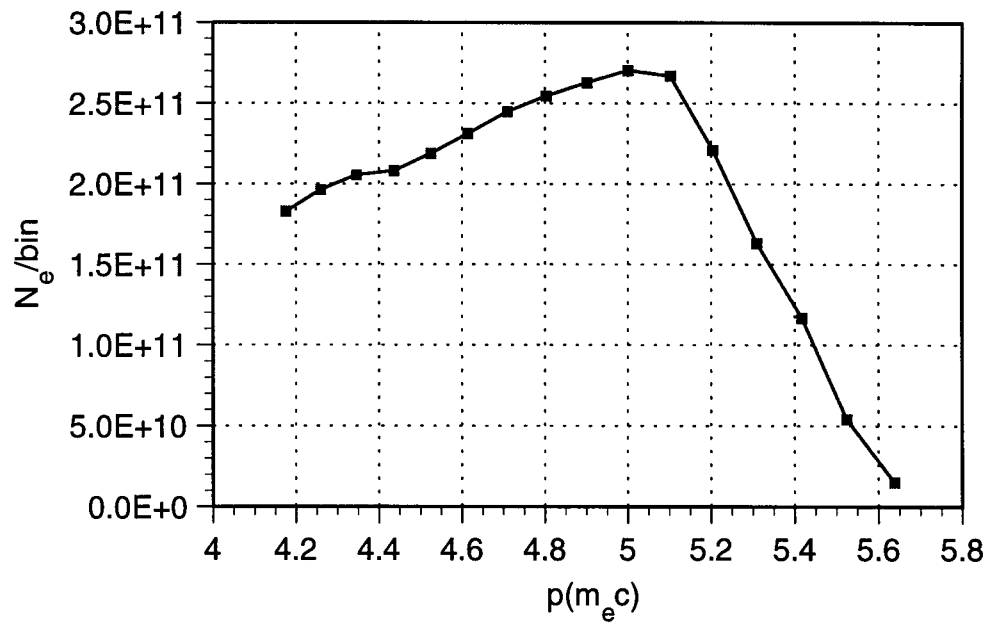


Figure 5.6: GTL electron momentum spectrum in a macro-pulse. The bin size is $\pm 4\%$.

variation of momentum and current with time due to beam loading, we need to see the energy spectrum as a function of time in Figure 5.7.

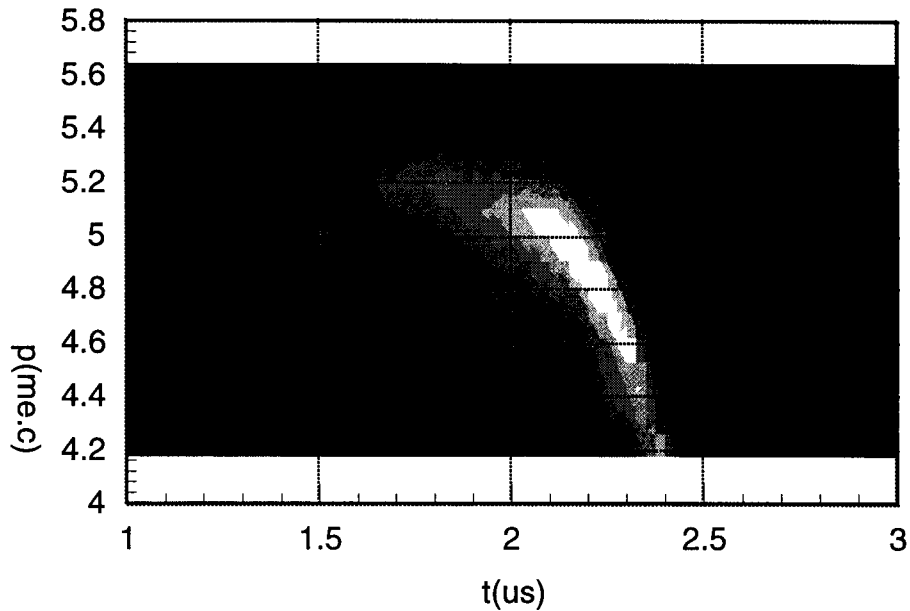


Figure 5.7: Spectral plot for a normal run (cold cathode) in a macro-pulse.

The horizontal axis in Figure 5.7 represents the time in a macro-pulse and the vertical axis the momentum. The central momentum is the most populated momentum bin. The different shades represent different current densities. As the gun power increases, so do the central momentum and beam current. The current reaches a maximum near the end of a macro-pulse for a “cold” cathode. The central momentum increases initially and reaches equilibrium for less than $0.5 \mu s$ and then decreases at the end of a macro-pulse. But the brightest spot with highest current lasts only $0.2 \mu s$ and does not concur coincidentally with the flat top of the central momentum. This can be seen more easily by plotting the central momentum and electron current versus time (Figure 5.8).

For each micro-bunch in a macro-pulse, there is an instantaneous bunch distribution with a definite central momentum and momentum spread. The vertical bars in Figure 5.8 are the *FWHM*s of the momentum distributions. They are twice to

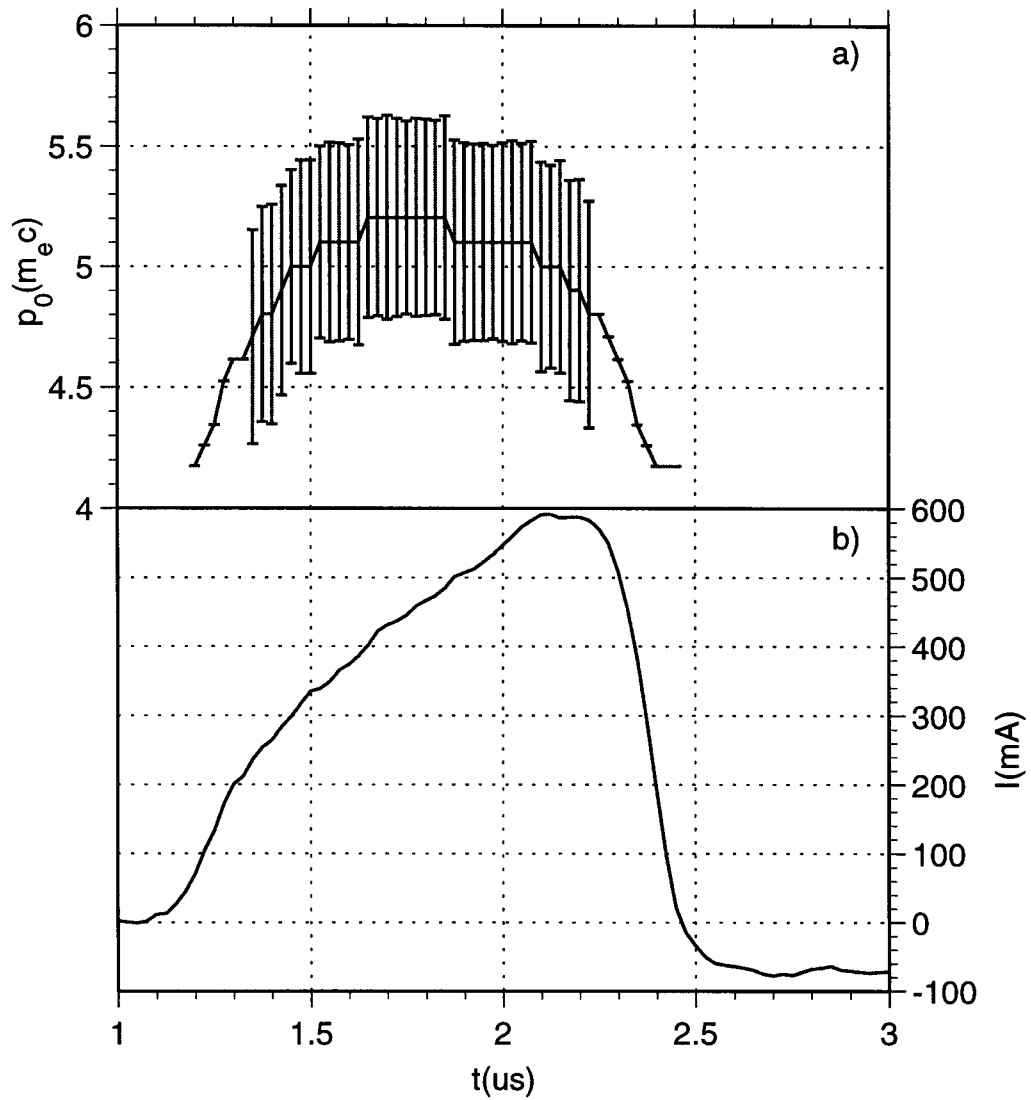


Figure 5.8: Central momentum a) and electron current b) versus time in a macro-pulse for a cold cathode.

thrice as large as prediction (see Table 2.2) partially because the speed of the electronics is much slower than the rf frequency (2856 MHz). Also signal averaging and datum filtering were done to smooth out any high frequency noise. Each point in time represents $0.025 \mu\text{s}$ which is about 71 micro-bunches.

The fact that the central momentum varies $\pm (4 - 6) \%$ around $5 m_e c$ in a macro-pulse can have a significant effect on the average bunch length and total radiation which will be demonstrated later in this Chapter.

5.3.2 “Hot” Cathode Operation

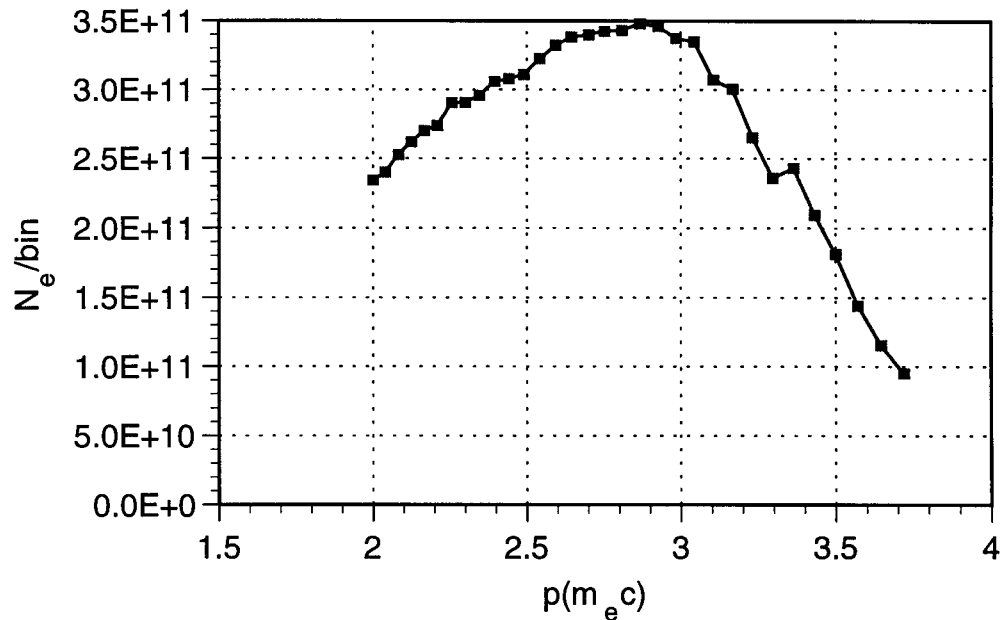


Figure 5.9: GTL electron momentum spectrum in a macro-pulse for a hot cathode. The bin size is $\pm 4\%$.

The momentum distribution in a macro-pulse for a “hot” cathode when the filament power is high is sketched in Figure 5.9. When the cathode is hotter for a fixed rf power, the beam current increases but the energies decrease compared with a “cold” cathode in Figure 5.6 due to beam loading. Figure 5.10 shows the 3D particle distribution in a spectral plot. The brightest spot with highest current coincides

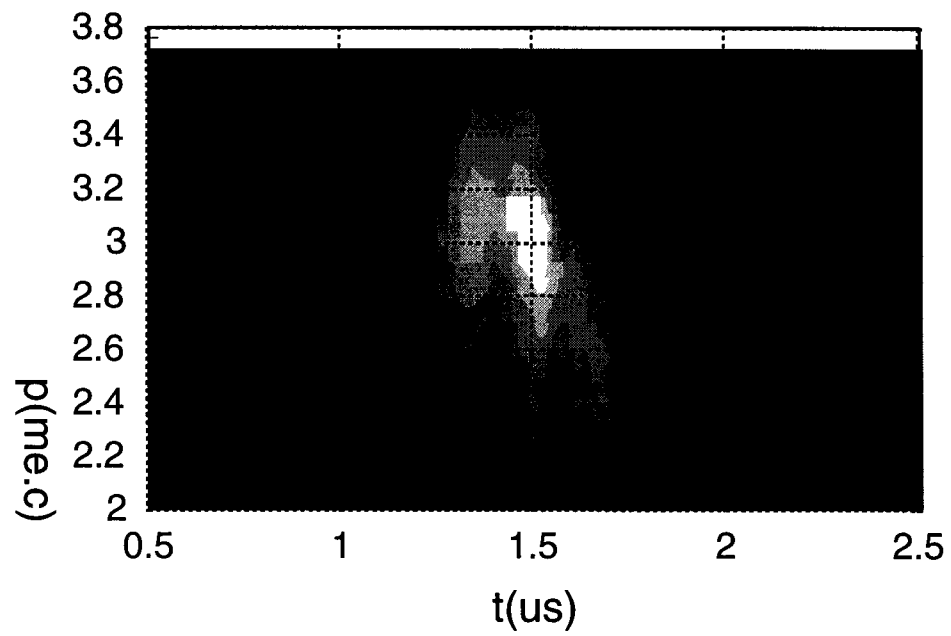


Figure 5.10: Spectral plot of a macro-pulse for a hot cathode.

with the plateau of the central momentum. The particle energies are reduced indicating that the gun power is depleted by the beam resulting in the shortening of the macro-pulse [56] as the brightest spot in Figure 5.10 lasts only slightly longer than $0.1 \mu\text{s}$. The T2 signal was much noisier than the one from a cold cathode which may be from the ineffective energy scrapers letting through particles not in the selected momentum bin. They are poorly focused and may splash the vacuum chamber and T2 contributing to noise. However, for a “hot” cathode, there may be a larger fraction of unwanted low energy particles leaking through than for a “cold” cathode. The reason for the inefficiency of the energy scrapers is not clear. Since the energy scrapers inside the alpha magnet only work perfectly for ideal particles which are on-axis and have a zero divergence on entrance, they always allow some undesirable particles not in the selected momentum window to go through and block desired ones with too large angles or displacements. Other possibilities are misalignment, since we always need a great deal of steering, depending largely on the alpha magnet setting, or alpha magnet field errors. This will be discussed later.

From the central momentum and beam signal versus time in Figure 5.11, the beam pulse clearly becomes shortened and the central momentum lower though the peak current increases. The central momentum varies about $\pm 10\%$ around $3m_e c$ in a macro-pulse, twice as much as for the “cold” cathode. Because of this undesirable pulse shortening and momentum lowering, we normally avoid operating the cathode this hot. The beam loading for a “hot” cathode is due mainly to back-bombardment which will be demonstrated in the next section.

5.3.3 ABBs On

There are two ABB coils; both have a magnetic field perpendicular to the beam direction. The first one located at the cathode redirects the back-bombarding electrons away from the cathode; the second which is near the gun exit, corrects the effect of the first coil on the forward electrons.

This set of data with the ABBs on was taken earlier before the beamline was controlled by a computer so the GTL quadrupoles and alpha magnet were not scaled

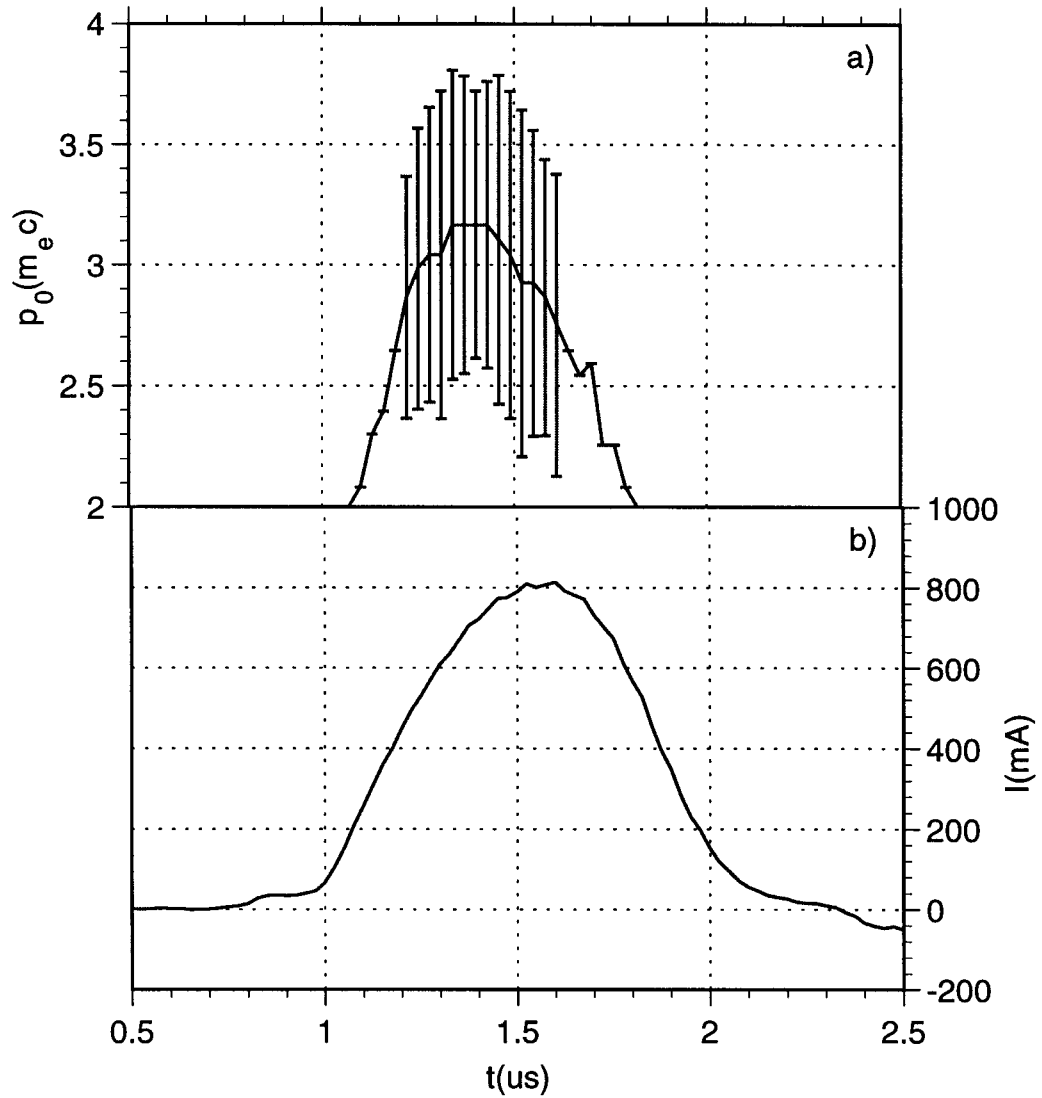


Figure 5.11: Central momentum a) and T1 signal b) versus time in a macro-pulse for a hot cathode.

according to the selected momentum bin. To select a bin, the energy scrapers in the alpha magnet were moved while the currents of all magnets were held fixed. The bin size was set at $\pm 0.05 m_e c$ and the centers of bins were chosen to avoid overlap or gapping. Since low-momentum particles were not focused properly, also the resolution at low momentum was lower according to (5.6), there were a lot fewer low energy electrons than the two previous sets in this section when the components were scaled accordingly. This may underestimate the energy spreads. Nonetheless, the result is valid qualitatively and allows an evaluation of the effectiveness of combating back-bombardment.

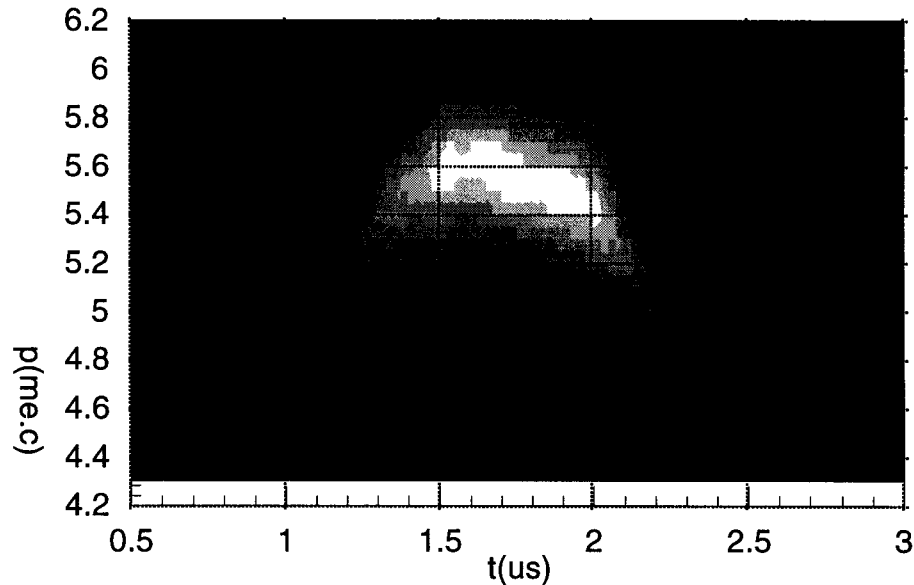


Figure 5.12: Spectral plot of a macro-pulse with the ABB's on. The bin size is $\pm 0.05 m_e c$.

From the spectral plot in Figure 5.12, we notice a lengthened pulse and the brightest spot extends longer for about $0.5 \mu s$ which is twice as long as the one for the “cold” cathode in Figure 5.7. It also coincides with the flat top of the central momentum in a macro-pulse, i.e., the cathode can maintain a constant high momentum and beam current simultaneously for a longer time.

The time variation of the central momentum and beam current are plotted in

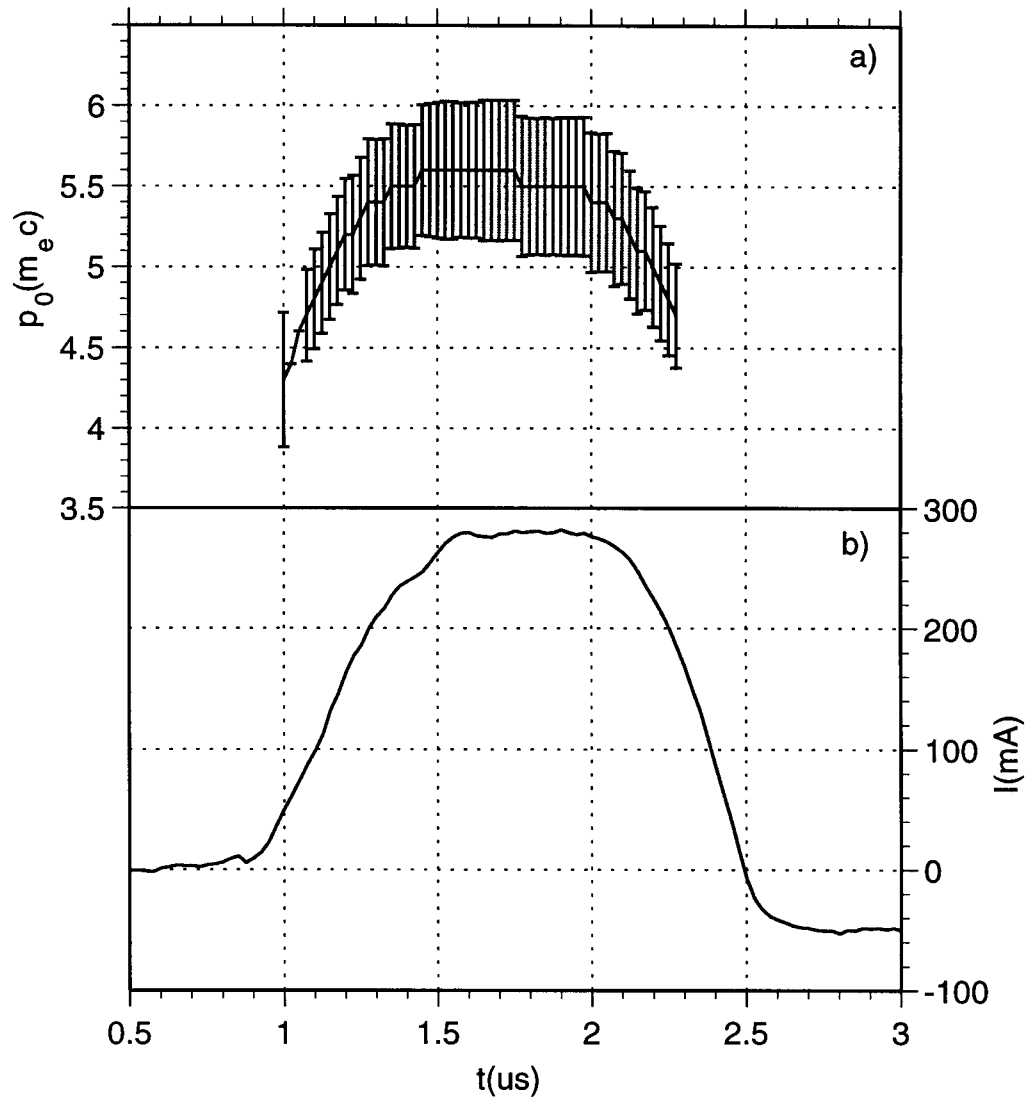


Figure 5.13: Central momentum a) and T1 signal b) versus time in a macro-pulse with the ABB's on.

Figure 5.13. The total beam current is reduced but the macro-pulse is lengthened. The central momentum throughout the macro-pulse behaves similarly to the one for a “cold” cathode, about $\pm 5\%$ around $5m_e c$. However, the gun can provide a high beam current without energy droop for a longer time. The fact that with the ABBs on, we can use a hotter cathode without pulse shortening or beam momentum lowering suggests that the beam loading mainly comes from extra heating of the cathode due to back-bombardment. Currently, the ABBs are not used most of the time for difficulty of reproducibility.

5.4 Momentum Spectrum of the Beam from the Linac

Beam loading effect is not only restricted to the gun; the beam pulse out from the linac suffers a similar pattern. Variation of the linac beam energy in a macro-pulse is worsened by the fact that the linac takes 700 ns longer than the gun to reach rf equilibrium.

In this measurement, all components in LTD — the quadrupoles and dipole, except the correctors, were scaled according to the selected momentum bin. The Faraday cup at the end has a rather large opening of 5.84 cm. This, along with the bending angle and the distance to the dipole vertex, limits the momentum resolution to $\pm 3.88\%$. The centers of all bins were chosen to avoid gapping or overlapping. The Faraday cup signal was averaged over 100 pulses. GTL was kept at a normal running condition.

Figure 5.14 shows the spectral plot. The transition of the beam current and energy in time is not very smooth due to the crude resolution. The beam momentum varies as much as $\pm 10\%$ from 26 to 32 MeV/ c in a macro-pulse, even more than the GTL beam in normal runs in Section 5.3.1. Since the linac is filled later than the gun, the plateau in the central momentum is so short, $0.2 \mu s$, that it is almost non-existent.

The effect of varying rf power in a macro-pulse in the linac on radiation is less serious than the one in the gun for the bunch length is not sensitive to the linac acceleration illustrated in Section 4.3.4. Also transition radiation scales like $\ln \gamma$ from

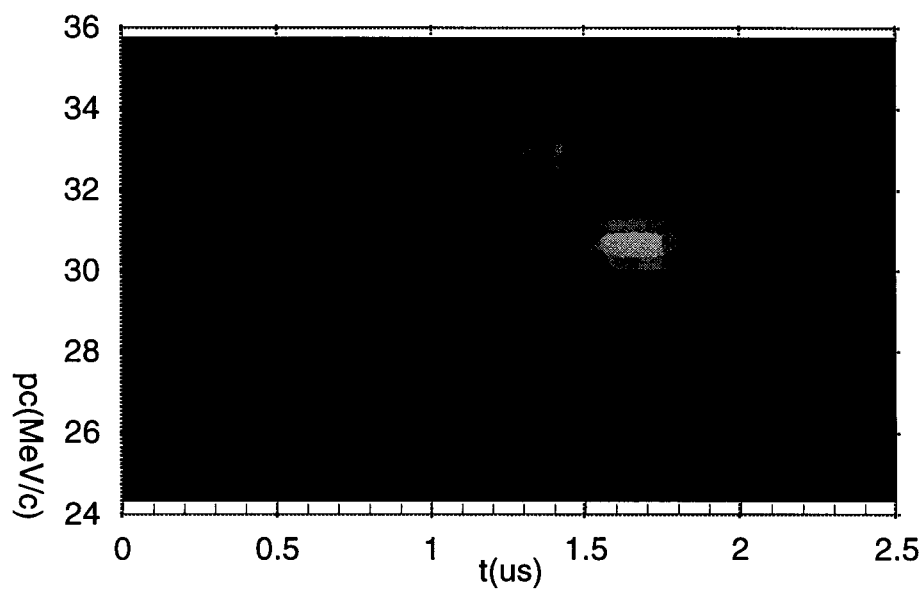


Figure 5.14: Spectral plot for a linac beam. The bin size is $\pm 3.88\%$.

(1.19) which is a slowly varying function of the beam energy. But it does pose some difficulty in focusing. As a result, we loose some 10% – 20% of the beam after GTL and slightly less than half of beam current from T1 remains at the end which is less than 300 mA.

5.5 Observation of Coherent Radiation

5.5.1 Elimination of Other Sources of Radiation

To show that the radiation from our electron bunches is coherent, we first have to eliminate the possibilities of radiation from other sources such as ionizing particle radiation hitting directly the bolometer or wake field radiation. The former might contribute to the total bolometer signal for synchrotron radiation and the latter to the transition radiation measurement.

To check for ionizing particle radiation, a vacuum gate valve was closed between the radiation source and the bolometer. The bolometer signal reduced from 0.3 V to less than 100 μ V which can be attributed to ionizing radiation reaching the bolometer. This only amounts to 10^{-4} of the signal for coherent synchrotron radiation.

Wake field radiation occurs when a charge particle interacts with the surrounding vacuum chamber structure electromagnetically. In an accelerator it is usually in the cm and mm microwave range and is most pronounced when there is a sudden change in the cross section of the vacuum chamber. The radiation can be estimated to be of order of nJ [33, 57] for the beam parameters used compared with the coherent radiation energy of several hundreds μ J. Much of wake field radiation would come from the linac structure rather than vacuum pipes. By deliberately mis-steering the electron beam after the linac away from the transition radiator, the bolometer signal reduced to below the electronic noise level although wake field would still be able to reach it. This rules out any appreciable wake field radiation.

5.5.2 Proof of Coherent Radiation

Since coherent radiation from a micro-bunch scales as the square of the number

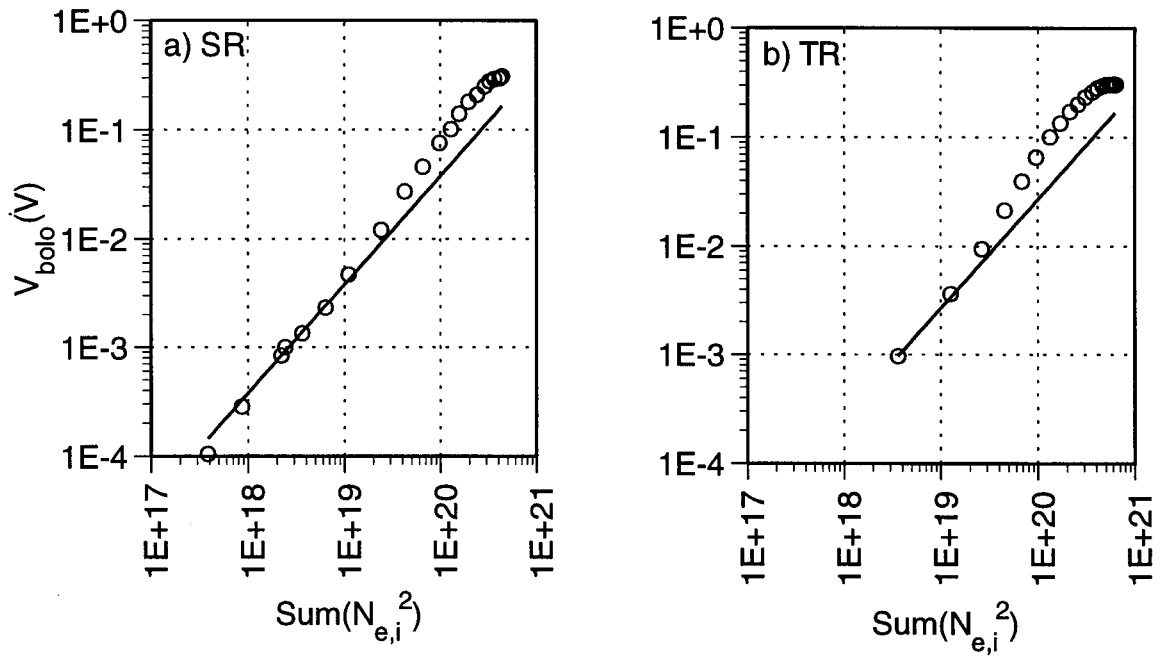


Figure 5.15: Bolometer signal versus $\Sigma_i N_{e,i}^2$ for synchrotron a) and transition radiation b).

of particles in it, the total radiation in a macro-pulse is proportional to the sum of squares of particle numbers, $\Sigma_i N_{e,i}^2$, in all micro-bunches.

The bolometer signal was measured as a function of the electron current which was varied by closing the high energy scraper in the alpha magnet with the low energy scraper fixed. Figure 5.15 shows the bolometer signal versus the sum of square of electrons in all micro-bunches for synchrotron and transition radiation. The straight lines are of slope one indicating that the signal is proportional to $\Sigma_i N_{e,i}^2$ for more than two decades which confirms that the majority of the beam indeed radiates coherently. The deviation from slope one is due to the fact that closing an energy scraper not only decreases the beam current but also can change the average bunch length within a macro-pulse (see Figure 4.7) thus the form factor (see (1.5)). This method to vary the beam current is less than ideal but the present setup does not allow control of the electron beam current without affecting either the bunch length or beam energy or both.

At the high ends of both curves in Figure 5.15, the slopes are less than one, suggesting that a small fraction of electrons does not radiate coherently. This may come from trailing particles which may be a result of the ineffective energy scrapers; or particles can migrate due to the space charge effect so the bunch distribution is not as clean as in simulation. The fact that we get a larger normalized radiation signal, which is defined as the bolometer signal in a macro-pulse divided by the sum of squares of electron numbers in a macro-pulse ($V_b/\Sigma_i N_{e,i}^2$), for a very small scraper opening, implies that the scrapers do not crop bunches as cleanly as in simulation (for example the bunch in Figure 4.8).

5.6 Radiation Power Compared with the Prediction

5.6.1 Comparison

We can calculate the expected total radiated energy for a $1 \mu\text{s}$ long macro-pulse from the measured beam current on T3 if all micro-bunches were identical, each with

	prediction	measured	
SR	1400	262	μJ
TR	4192	382	μJ

Table 5.1: Expected radiation from synchrotron (SR) and transition radiation (TR) from a $1 \mu\text{s}$ -long pulse with identical bunches of 0.18 ps long, compared with measured values.

the same equivalent bunch length of 0.18 ps as predicted by simulation (see Figure 4.7) and equal beam energy, assuming a Gaussian form factor and 100% radiation efficiency for all electrons. The predicted and measured values are listed in Table 5.1. The alpha magnet gradient was set at 321.11 G/cm which should give the shortest bunch length for the nominal beam parameters. We found that we get more radiation energy if the low energy scraper is set at $3.8 - 4.4 m_e c$ which agrees with simulation (see Figure 4.7 and 4.8). Since below these momenta, particles contribute only long tails and beam loading in the linac. The consequence is T2 only measures about half of the beam current as T1, which means only half of particles remains after the alpha magnet. This is consistent with simulation that only half of particles that exit the gun are actually useful (see Table 2.2).

For synchrotron radiation, the dipole field was 2.2 kG and we measured 4.6×10^8 rms electrons per micro-bunch on T3. A total radiation energy of $1400 \mu\text{J}$ can be expected from a macro-pulse, assuming that the angular acceptance of the optics is 40 mrad about the beam axis.

For transition radiation, we use in (1.22) and (1.23) [21] which give the angular spectral density from a dielectric plate with an arbitrary incident angle. Using the thickness of the Al-foil ($25.4 \mu\text{m}$) and Drude model [16] for the (complex) dielectric constant of Al [58], we should get $4192 \mu\text{J}$ per macro-pulse from a train of 2856 micro-bunches with an equal intensity of 3.08×10^8 electrons, assuming 100% collection efficiency. Note that the total radiation from synchrotron and transition radiation was measured on different days so the beam currents were different.

In actuality, we measured only $262 \mu\text{J}$ and $382 \mu\text{J}$ per macro-pulse for synchrotron and transition radiation, much less than what was expected. This should not be too surprising, for there are other factors that have not been considered yet such

as the optical collection efficiency, transmission efficiency through the HDPE window (87%) and most importantly, variation of the bunch length throughout a macro-pulse. Since the alpha compression only works for a narrow range of central momentum (see Figure 4.3), not all bunches in a macro-pulse are compressed optimally. Variation of the bunch length will be shown to be the largest factor that increases the average bunch length in a macro-pulse.

5.6.2 Variation of Bunch Length in a Macro-Pulse

From the momentum spectra in a macro-pulse for the beam out of the gun in Figure 5.8, the central momentum varies about $\pm 5\%$ around $5 m_e c$ in a macro-pulse. Since the alpha magnet is chosen to compress bunches with a central momentum around $5 m_e c$, the instantaneous bunch length can vary from sub-picosecond to more than a pico-second shown in Figure 4.3. This greatly affects the average bunch length over a macro-pulse. From Figure 5.7 and 5.8, the equilibrium spot with highest beam current and constant momentum band around $5 m_e c$ lasts for only about 100 ns which means less than 300 micro-bunches are optimally compressed out of almost 3000.

To compare the radiation measurements realistically, it is necessary to know the bunch length distribution as a function of time in a macro-pulse. But the actual field strength and cathode current density are immeasurable. In gun simulation, the two independent variables are the field strength and cathode current density while in experiments, we vary the total rf power which supplies both the gun and linac, and the cathode filament. There is no field probe in the gun nor current or temperature measuring device for the cathode. Also the current out of the gun is not completely independent of the rf power. From simulations, only about one fifth of electrons emitted by the cathode exit the gun for the normal range of the field strength and cathode current density (see Figure 2.17 and 2.19). From the average current on T1 in a macro-pulse in normal runs which is 600 – 700 mA, if we assume 90% transmission from the gun exit to T1, the cathode current density can be deduced to be around 12 A/cm². This also agrees with the design value for the cathode filament power [12].

To infer the field strength experimentally, one needs to know the electron energy

spectrum of each bunch in a macro-pulse and integrate it just to get the beam forward power at each instance in time. Borland tried to infer the field strength by measuring the electron beam spectrum for a very small beam current at an instance late in a macro-pulse for a given rf power, assuming that the gun had reached equilibrium then integrated the forward beam power from the spectrum [12]. But the agreement was not good without much manipulating both the impedance of the gun cavities and backward beam power. It is not clear that doing it the correct way gives a more accurate value for the field level. So I have elected to use the central momentum as a measure of the accelerating field since it is a monotonically increasing function of the peak accelerating field in simulation for a fixed cathode current density (see Figure 2.17a). That is, the peak accelerating field together with the current density define a unique bunch distribution in longitudinal phase space. From the measured central momentum as a function of time, we can infer the *effective* peak accelerating field that each micro-bunch experiences. This method is far from ideal but since we cannot measure the beam power from electrons that do not exit the gun, there is no way of telling the total power consumed by the beam. Besides, the measured rf gun power was fairly close to the total rf power in simulations (1.82 – 1.93 MW) which is an indirect validation of this method.

It is best to take all measurements on the same day to guarantee the same running condition: both electron beam spectra out of the gun and linac and all radiation measurements — total radiation in a macro-pulse, radiation energy versus beam current, Michelson scans — a long scan for the radiation spectrum and short scan for the bunch length. The reason why two Michelson scans — long and short are necessary will be explained in Section 5.7. But to do so would be impossibly long. Therefore to ensure that the same electron beam spectrum can be used in calculation for measurements on different days, it is very important to keep external running parameters such as the cathode current, rf power and water temperature, etc., the same as much as possible.

The field and bunch distribution should be semi-continuous functions of time in a macro-pulse which requires at least 2000 continuous cycles in MASK to simulate the beam loading effect in the gun which would take an unrealistically long time.

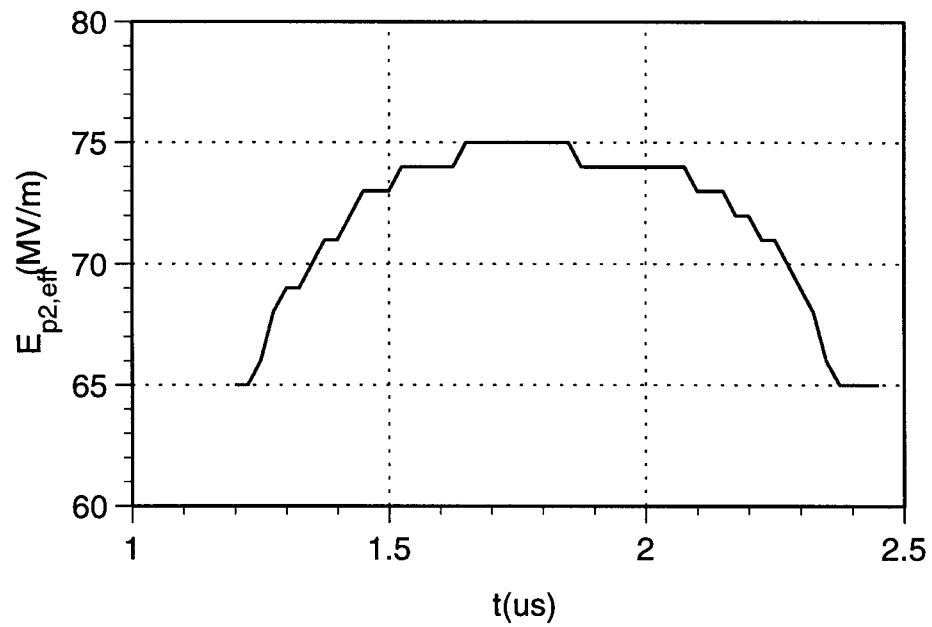


Figure 5.16: Effective peak field in the 2nd cell versus time in a macro-pulse for normal running conditions.

Besides, the effect of beam loading is equivalent to lower fields in the gun seen by later bunches [12]. From the spectral plot of the GTL beam in Figure 5.7, the inferred effective peak field in the second cell versus time in a macro-pulse for a normal run is sketched in Figure 5.16. A macro-pulse is sliced in 11 segments in time; each slice is assumed to experience a constant accelerating field discretized in 1 MV/m increment. The same linac acceleration is used in integrations since the linac acceleration affects mostly the momentum and less on the bunch length demonstrated in Section 4.3.4. The bunches are shortest for only about $0.2 \mu\text{s}$ when $E_{p2,\text{eff}} \approx 73 - 74 \text{ MV/m}$ at the beginning and end of a macro-pulse. But only the latter contributes substantially to radiation for the beam current was near maximum shown in Figure 5.7 and 5.8. Since the alpha compression works best for a narrow range of central momentum, for most part of a pulse, bunches are not compressed optimally thus the average bunch length is lengthened considerably.

5.6.3 Correction due to Collection Efficiency

The expected radiation, after taking into account variation of the bunch length, still needs to be corrected by the optical collection efficiency and the 87% transmission efficiency through the HDPE window. If the finite acceptance of the window is considered, only 36% of the total radiation is collected in transition radiation.

The collection efficiency for synchrotron radiation is complicated by a few factors [57]:

- The mirror M1 only accepts part of the radiation since it sweeps down across M1 as electrons are being deflected (see Figure 5.3b).
- The radiation from the fringe fields cannot be neglected. The fringe fields in the dipole are modelled as linear functions from zero up to the nominal value over a distance of the pole gap which is 40 mm.
- The power and opening angle of the radiation at a particular wavelength is a function of the electron beam energy and magnetic field.
- The light collecting cones have finite angular acceptances.

As a result, the collection efficiency in synchrotron radiation varies from 35% to 62% depending on the bunch length and the total collection efficiency is 52%.

5.6.4 Comparison of Expected to Measured Radiation

After including variation of the bunch length in a macro-pulse, the optical collection efficiency and HDPE window transmission, we can compare the results again from calculated bunch lengths in all slices in a macro-pulse weighted by the mean squares of the numbers of electrons measured on T3 ($N_{e,i}^2$).

For synchrotron radiation, the expected total radiated energy in a macro-pulse, after considering these factors, is tabulated below:

	P_{rad} (mJ)
simulation, ideal case	1.40
simulation including variation of the bunch length	0.48
simulation including collection efficiency (52%)	0.25
simulation including also window loss (13%)	0.22
measurement	0.26

The agreement becomes within 10%. A small part of the measured synchrotron radiation may come from vertical steering thus resulting a slightly larger value than expectation. The measured result is equivalent to the one from a 1 μs long macro-pulse with identical micro-bunches of 0.48 ps long for an intensity of 4.6×10^8 electrons.

For transition radiation, the total radiation energy in a macro-pulse is tabulated below:

	P_{rad} (mJ)
simulation, ideal case	4.19
simulation including variation of the bunch length	0.56
simulation, including window loss (13%)	0.49
measurement	0.38

Again the agreement becomes much closer. From the measured radiation and electron current, the average bunch length over a macro-pulse can be calculated to

	calculation	measured	
SR	0.22 ($\pm 10\%$)	0.26 ($\pm 3\%$)	mJ
TR	0.49 ($\pm 10\%$)	0.38 ($\pm 3\%$)	mJ
avg bunch length	0.48 ($\pm 10\%$)		ps

Table 5.2: Expected radiated energy in a macro-pulse compared with measured values for synchrotron and transition radiation after including various factors.

be about 0.48 ps. The results are summarized in Table 5.2 along with the estimated error bars in parentheses. The error in calculation comes from both the uncertainty in discretizing a macro-pulse in time and dependence of the bunch length of a simulated bunch on the temporal bin size mentioned in Section 4.3.4.

5.7 Bunch Length Measurement

The above measurements are indirect for the bunch length. To measure the bunch length more directly, a Michelson interferometer was used [52, 59]. Figure 5.17 shows a Michelson autocorrelation along with its uncorrected and corrected spectrum. The spectrum was obtained by taking a Fourier transform of the autocorrelation from (5.3). The raw spectrum needs to be corrected by dividing the beam splitter efficiency $|RT|^2$ as in (5.3). The corrected spectrum in Figure 5.17 was calculated using an index of refraction of 1.85 for mylar [55]. The spike at 3.45 THz (115.1 cm^{-1}) is an artifact from dividing the raw spectrum by the first zero of $|RT|^2$ of (5.4) and (5.5). The multiple dips in both spectra are water absorption lines [53] since the apparatus is exposed to air. The raw spectrum is a result of the combination of the bunch distributions, water absorption and thin film interference of the beam splitter. Only the envelope of the spectrum should be considered when the bunch length is of prime interest.

The thickness of the beam splitter in a Michelson interferometer should be chosen depending on the purpose of the measurement. If it is much thinner than the bunch length, the central peak in the autocorrelation appears narrower [54, 59] which introduces a larger uncertainty in inferring the bunch length. So to measure the bunch

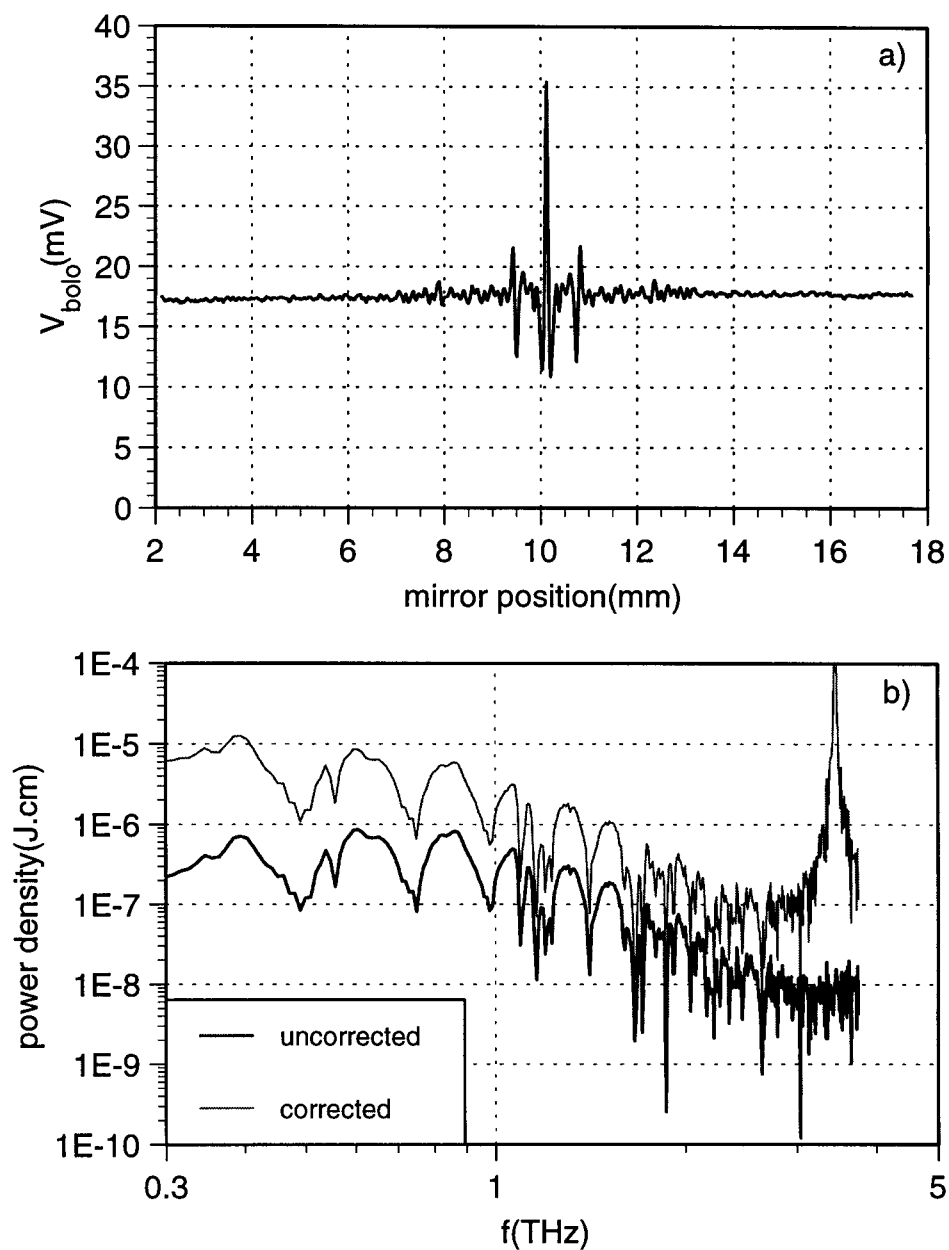


Figure 5.17: Michelson scan a) with its uncorrected and corrected spectrum b). This set was taken with a $25.4\ \mu\text{m}$ thick beam splitter and an alpha gradient of $321\ \text{G}/\text{cm}$.

length faithfully, it is better to choose a thicker splitter. But to measure the spectrum over a large range of frequency, a thinner one such as $12.5\ \mu\text{m}$ ($1/2$ mil) would be more suitable since a thicker foil suppresses high frequency response more though the theory of thin film interference does not predict this [60].

5.7.1 Comparison with the Simulation

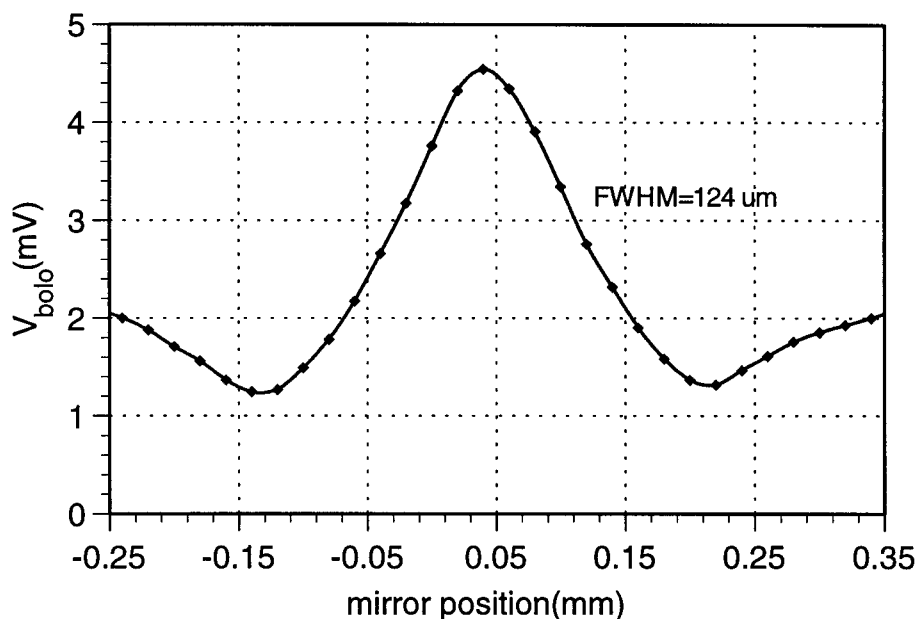


Figure 5.18: Central peak of the interferogram taken with a $127\ \mu\text{m}$ thick beam splitter. The alpha gradient was $328\ \text{G}/\text{cm}$. The $FWHM$ for the path is $248\ \mu\text{m}$.

Figure 5.18 shows a scan using a $127\ \mu\text{m}$ thick mylar beam splitter and an alpha magnet gradient of $328.2\ \text{G}/\text{cm}$; only the main peak is shown here. The $FWHM$ of the main peak is $128\ \mu\text{m}$ so the $FWHM$ for the path length difference is twice of that, $248\ \mu\text{m}$. This translates to an equivalent width between $187\ \mu\text{m}$ ($0.62\ \text{ps}$) and $245\ \mu\text{m}$ ($0.82\ \text{ps}$), for a rectangular and Gaussian distribution. The uncertainty is due to insufficient knowledge of the bunch shape; the actual bunch distribution should lie somewhere in between.

The spectrum for the same setting including the lattice and rf power, was taken using a $12.7\ \mu\text{m}$ thick beam splitter with a $20\ \mu\text{m}$ mirror step. Each point in the

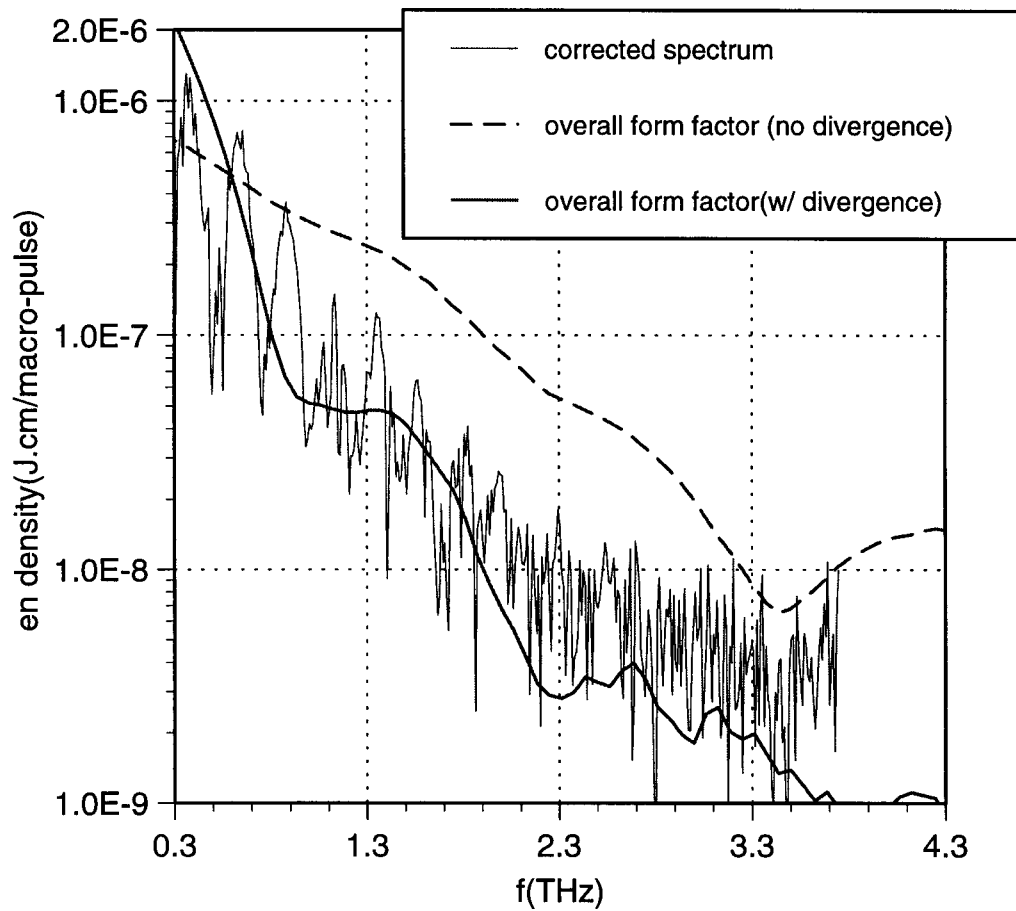


Figure 5.19: Corrected spectrum compared with the overall form factors for a scan using a $12.5\ \mu\text{m}$ thick beam splitter. The setting was the same as one used in Figure 5.18.

scan was averaged over seven pulses. The corrected spectrum and calculated overall form factors $\Sigma_i (N_{e,i} F_i)^2$ with and without the divergence effect are sketched in Figure 5.19, where F_i is the FFT of the temporal distribution of the i^{th} slice in a macro-pulse and $N_{e,i}$ is the rms number of electrons measured on T3. The overall form factors are normalized by a factor which is fitted by a least square fit between 0.3 and 3.4 THz with the envelope of the spectrum only. The low frequency noise below 0.3 THz (10 cm^{-1}) comes from the slow drift of the baseline in the scan due to the fluctuation of external parameters such as the rf power, gun or linac temperature in an almost two hour measurement.

Since transition radiation from a perfect conductor has a flat frequency spectrum, the form factors should resemble the spectrum from (1.5). Apparently, the agreement between the measured spectrum and calculation is not great before the divergence effect is included. The best fit seems to lie in between two form factors which leads us to believe that the divergence effect, although lengthens a bunch significantly, but due to misalignment and steering, the beam pipe actually scrapes off some particles that have too large displacements from the center thus reduces the damage.

To compare the measured and calculated bunch length, it is necessary to define an *average* bunch length over a macro-pulse in calculation. Since coherent transition radiation power is proportional to the square of the number of particles in a bunch and inversely proportional to the bunch length in (1.19), it is natural to define the *average bunch length* over a macro-pulse as

$$\bar{l} = \frac{1}{\langle l^{-1} \rangle} = \left(\frac{\sum_i n_i N_{e,i}^2 l_i^{-1}}{\sum_i n_i N_{e,i}^2} \right)^{-1} \quad (5.7)$$

where n_i is the number of micro-bunches in the i^{th} slice in a macro-pulse and l_i is the corresponding calculated bunch length. The comparison of the calculated average equivalent bunch length with the measured one is listed below,

measured	[0.62, 0.82]	ps
calculated (without divergence)	0.37	ps
calculated (with divergence)	1.075	ps

It confirms the observation in the spectrum in Figure 5.19 that the actual average bunch length lies between the one with and without the divergence effect. The above

values are also consistent with the bunch length of 0.48 ps indirectly deduced from earlier total radiation measurements in Table 5.2.

5.7.2 Bunch Length versus Alpha Compression

In addition to long scans for transition radiation spectra, a series of short Michelson scans using a 127 μm thick beam splitter were performed to measure the bunch length of a macro-pulse as a function of the alpha compression. During these measurements which took place on different days, the T1 signal and rf power were kept the same as much as possible to ensure that the variation of the bunch length was due mainly to the alpha compression, not other external parameters. But since the alpha magnet inevitably affects the transverse beam optics according to (4.8) and (4.9), the GTL quadrupoles need to be set accordingly to accommodate different alpha settings. In addition, misalignment in the beamline results in different corrector settings for different alpha settings, so the transmission of the electron beam through the linac varies with the alpha magnet. Although we tried to maximize both the T3 and bolometer signal simultaneously by proper steering and focusing for we want to vary the bunch length as a result of the alpha compression alone, not from extra scraping by mis-steering. Still, the T3 signal varied between 200 and 300 mA. This difference in the electron current has been taken care of by the weighted sum of the bunch length by the T3 current in (5.7) when comparing the measured and calculated bunch length.

The result — measured and calculated average bunch length with and without the divergence effect in a macro-pulse as a function of the alpha gradient is sketched in Figure 5.20. The curves deviate more at both high and low alpha gradient and the measured bunch length is shorter than predicted at both ends though the trend is similar: the compression is less effective at both high and low alpha gradient. A natural question rises: do we really measure the average bunch length in a macro-pulse dictated by (5.7)? Since the temporal bunch distribution in a macro-pulse varies from bunch to bunch, is it possible that we measure the most “prominent” bunches that contribute the most to the radiation? Let us define the most “prominent” bunches

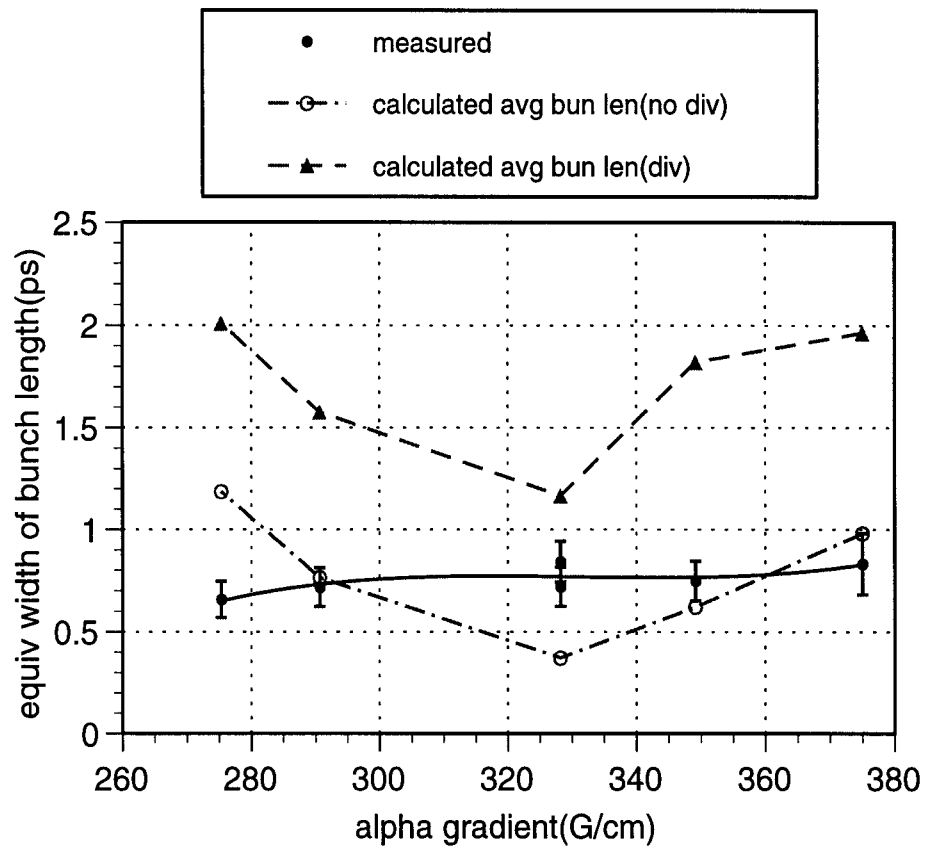


Figure 5.20: Measured and calculated average bunch length in a macro-pulse versus alpha gradient.

as having a largest $N_{e,i}^2/l_i$ value and compare again. The agreement, in Figure 5.21, improves to some extent and both curves are qualitatively similar. The reasons for discrepancy will be discussed in the next section.

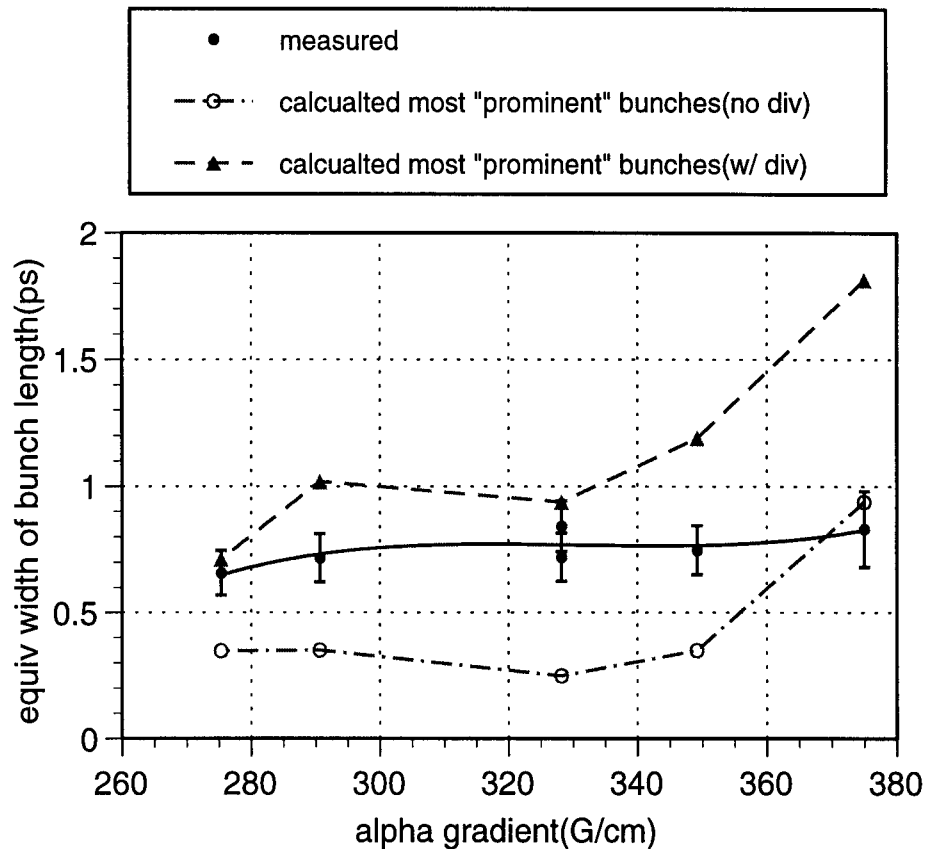


Figure 5.21: Measured bunch length and most “prominent” bunch in calculations in a macro-pulse versus the alpha gradient.

From the measured bunch length and electron current, the peak electron current can be obtained by dividing the measured maximum electron current on T3 in a macro-pulse by the measured bunch length. It is plotted as a function of the alpha gradient and bunch length in Figure 5.22 and 5.23. The error bars in both graphs represent the uncertainty between Gaussian and rectangular bunches. The maximum peak current is about 170 A. Shorter bunches tend to have higher peak current from Figure 5.23 as expected but the alpha setting that gives the highest peak electron

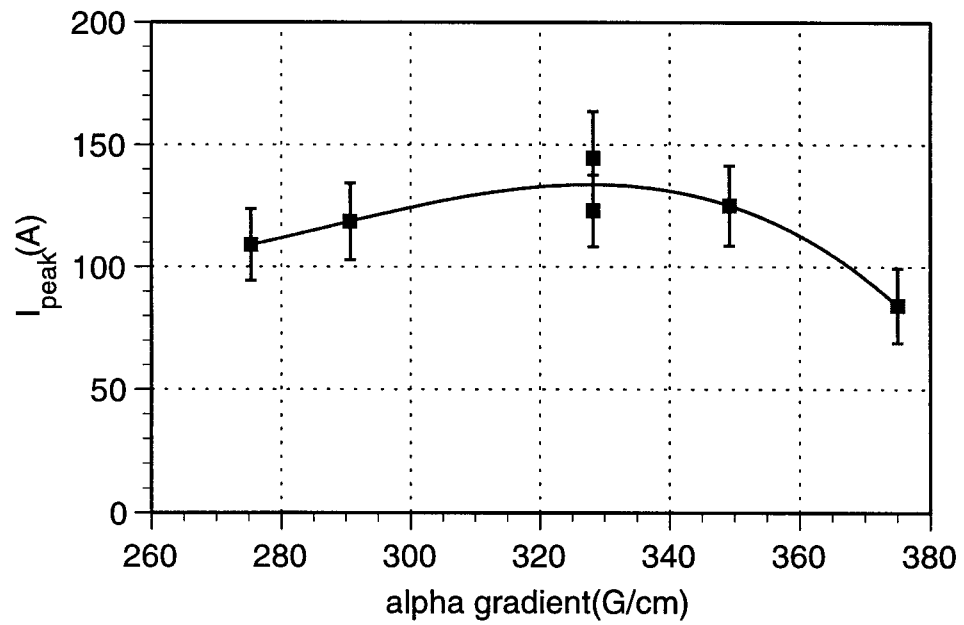


Figure 5.22: Peak electron current as a function of the alpha magnet.

current does not coincide with the shortest measured bunch length exactly. According to (4.8) and (4.9), for a particle with non-zero angle and position at the alpha entrance, the larger the loop, the larger the transverse electron beam size becomes while the smaller the loop size, the larger the vertical angle becomes upon exit (less focusing in the y plane), so the transmission through the beam line at a very low (large loop) and high (small loop) alpha setting is smaller. Thus, the peak current is a result of both the compression and beam transmission.

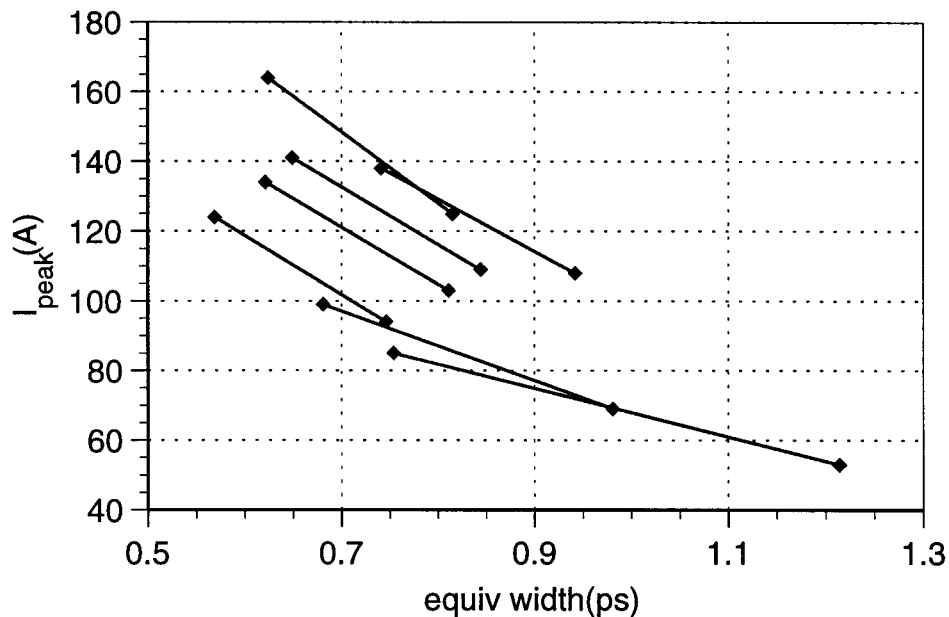


Figure 5.23: Peak electron current as a function of bunch length.

5.8 Discussion

5.8.1 Main Reasons that Limit Bunch Compression

The main limiting factors for bunch compression can be separated into two categories: the ones that affect the bunch length of a micro-bunch and the average bunch length of a macro-pulse. Most of bunch lengthening comes from GTL when electrons

are only quasi-relativistic. After the linac, the electron beam become fully relativistic and bunches become “frozen” and hardly spread at all from either the velocity spread or divergence effect. The details will be discussed below.

Micro-Bunch Factors

On the micro-bunch level, there are three major factors: the velocity spread, the divergence effect and longitudinal space charge force, in diminishing importance for our system.

Velocity Spread The time varying rf field in the gun plus the thermionic cathode produce electron bunches with large momentum spreads from quasi-relativistic down to zero (see Figure 2.5). Since bunches are not yet fully relativistic before the linac, the first order bunch lengthening in GTL due to the velocity spread is not negligible. But this effect is, to large extent, correctable by a proper setting of the alpha magnet provided that the electron beam energy and alpha magnet are within working limits in (4.19) and (4.21).

Divergence Effect The divergence effect is pretty severe for lower energy particles in GTL. Since the focusing is optimal for highest energy particles in normal operations (see Figure 4.12b), lower energy particles make larger excursions throughout the beamline. The lengthening starts accumulating from the beginning of the beam line and cannot be rid of as discussed in Section 4.3.3. Even with a proper focusing lattice and low energy particles discarded, a bunch can still have some trailing particles (for example, the bunch in Figure 4.12b). Relatively speaking, the divergence effect is more detrimental for an optimally compressed bunch which is upright in longitudinal phase space than a not-optimally compressed one.

The damage mostly comes from GTL when the beam is not fully relativistic. After the linac, electrons in a bunch hardly spread from the divergence effect due to adiabatic damping. Since the divergence of the nominal beam at the gun exit is quite large (see Figure 2.16 and Table 2.2), this in turn requires strong quadrupoles in GTL for good beam transmission through the 1.8 cm pipe radius into the linac. Especially,

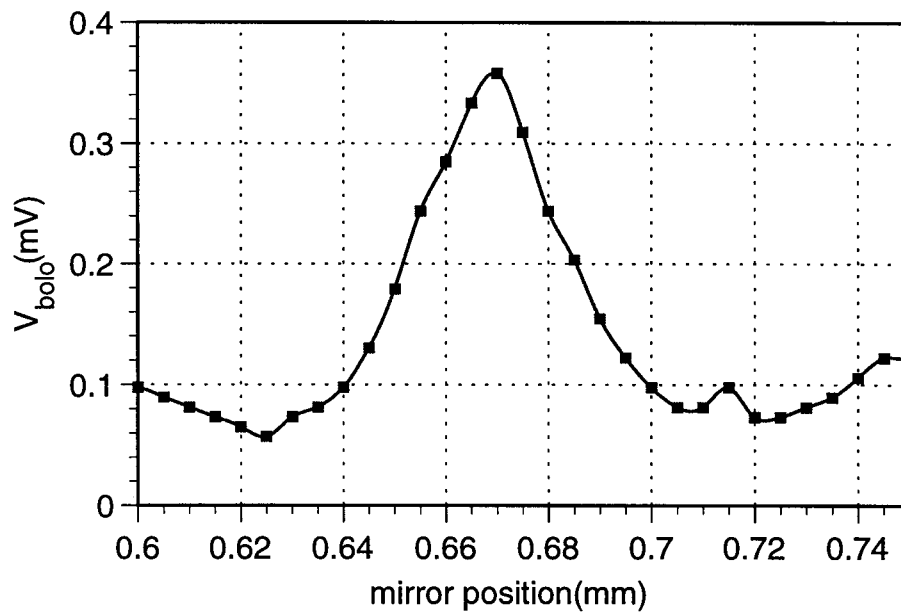


Figure 5.24: Scan for the shortest bunch, measured with a $127 \mu\text{m}$ thick beam splitter. $FWHM = 110 \mu\text{m}$ for the path length.

the first three quadrupoles — Q1, Q2 and Q3 (see Figure 5.1) have phase advances as large as 60° .

In principal, particles of large angles in transverse phase space can be discarded by scraping to allow only the core of the beam to pass through. But such a device for our system has not yet been conceived. So far the shortest bunch was measured by Hung-chi Lihn by using a small energy window in the alpha magnet and mis-steering but the price is a beam current of only 30 mA. The *FWHM* for the path difference of $110 \mu\text{m}$ shown in Figure 5.24 which gives an equivalent bunch length between 0.28 and 0.37 ps for a rectangular and Gaussian bunch. The peak current was only 28–38 A.

Longitudinal Space Charge The longitudinal space charge effect for a short bunch can become a problem, especially since it has a tendency to form a shock wave when the longitudinal density profile has a large variation. This has not been considered in tracking after the gun exit. Though it is possible that the effect is large enough that the packets in phase space (see Figure 2.24) eventually migrate after breaking of the shock front, the net result is still bunch lengthening. By comparing two simulations for a cathode current density of 12 A/cm^2 which is approximately our normal running conditions and 0.1 A/cm^2 , the bunch is lengthened by about 1.3 times shown in Figure 4.10. After the gun exit, the space charge effect would further lengthen a bunch.

Let us estimate the lengthening. If the bunch length l is much longer than its radius r , we can employ a pencil beam approximation. The longitudinal space charge force on a test electron at the edge of the bunch of total charge $N_e e$ from the whole bunch is,

$$F_{\text{sp}} = \frac{N_e e^2}{\left(\frac{l}{2}\right)^2}. \quad (5.8)$$

If the drift distance d is much smaller than l , l can be regarded as constant and the extra relative momentum deviation introduced by the longitudinal space charge is

$$\mu_{\text{sp}} \approx \frac{4N_e e^2 d}{\beta_0^2 \gamma_0 m_e c^2 l^2}, \quad (5.9)$$

where $\beta_0 c$ is the speed of the ideal particle. From (4.16), the extra bunch lengthening

is

$$\delta l_{\text{sp}} \approx \frac{4N_e e^2}{\beta_0^2 \gamma_0^3 m_e c^2} \left(\frac{d}{l} \right)^2. \quad (5.10)$$

Notice that it is a quadratic function of d/l and inversely proportional to the cube of the energy.

For a very short bunch that $l \ll r$, we can use a pancake approximation. Following the above, we get

$$\delta l_{\text{sp}} \approx \frac{2N_e e^2}{\beta_0^2 \gamma_0^3 m_e c^2} \left(\frac{d}{r} \right)^2. \quad (5.11)$$

Notice in both cases, the extra length is inversely proportional to the cube of the energy and a quadratic function of the dimension the bunch.

Now we can estimate the lengthening over a drift distance of the bunch itself ($d = l$). For GTL, $N_e \sim 10^9$, $p_0 \sim 5$, $l \sim 3.8 \text{ mm} \doteq 13 \text{ ps}$ and $r \sim 1 \text{ mm}$, we use the pencil approximation and get

$$\begin{aligned} \mu_{\text{sp}} &\sim 7 \times 10^{-4} \\ \frac{\delta l}{l} &\sim 3 \times 10^{-5}. \end{aligned}$$

For beam out of the linac, $N_e \sim 4 \times 10^8$, $p_0 \sim 59$, $l \sim 60 \mu\text{m} \doteq 0.2 \text{ ps}$ and $r \sim 1 \text{ mm}$, we use the pancake approximation,

$$\begin{aligned} \mu_{\text{sp}} &\sim 3 \times 10^{-6} \\ \frac{\delta l}{l} &\sim 7 \times 10^{-10}. \end{aligned}$$

Note that the above approximations are a pessimistic scenario since when a bunch gets lengthened, the space charge force decreases. Though the spread after the linac is much smaller than in GTL, the spread due to space charge is fairly minute for both.

The above analysis justifies the exclusion of space charge in tracking simulated bunches after the gun. The shock wave instability mostly happens early in the rf gun when the electron energy is very low shown in the reminiscence of the space charge wave structures in longitudinal phase space in Figure 2.24. This has not been a serious problem because our cathode operates at a fairly low current density, slightly

above 10 A/cm^2 . Furthermore, our peak electron current of a few hundred amperes is hardly space charge limited according to [61,62]

$$I_{\text{lim}} (\text{kA}) = \frac{8.5 \left(\gamma_0^{2\beta} - 1 \right)^{2/3}}{\ln \left(\frac{b}{a} \right)}, \quad (5.12)$$

where a and b are the radii of the beam and the beam pipe. Eq. (5.12) gives a limiting current of about 8 kA and 150 kA for our beam parameters in GTL and LTD, much larger than our peak electron current. If one wants to pursue an even higher peak current, ultimately, the maximum peak current is limited by the space charge effect.

Comparison of Factors The table below lists the fractional lengthening due to different effects of a bunch drifting for a length equal to itself in GTL and LTD, assuming a bunch length of 13 ps and 0.2 ps, momentum spread of $\pm 5\%$ and $\pm 0.4\%$, divergence of $\pm 16 \text{ mrad}$ and $\pm 1 \text{ mrad}$, respectively.

	GTL	LTD
velocity spread	1.4×10^{-3}	1×10^{-6}
divergence effect	8.5×10^{-5}	5×10^{-7}
space charge effect	3×10^{-5}	7×10^{-10}

The largest lengthening factor in either GTL or LTD is from the velocity spread which is a first order effect. But as stated earlier, this can be compensated by a proper bunch compressor, rendering the second order divergence effect the most dominant factor for a micro-bunch.

Macro-Pulse Factors

Varying RF Field in the Gun Due to the limitation of the rf power, beam loading in the gun, especially due to back-bombardment, bunches in a macro-pulse experience varying acceleration, which is discussed in Section 5.3. This results in a varying longitudinal bunch distribution with about $\pm 5\%$ variation of central momentum in GTL versus time. Since the compression of the alpha magnet works best for a narrow

range of central momenta discussed in Section 4.3.1 and 5.6.2, only about one tenth of micro-bunches in a macro-pulse contribute significantly to the radiation.

The fact that the agreement between measurements and calculations has improved significantly after including this effect shows that this is so far the largest lengthening factor for the average bunch length in a macro-pulse.

Varying RF Field in the Linac

In calculation, all simulated bunches are accelerated by the same field in the linac and enter the linac on the crest. This is not true since rf fields in the linac equilibrate later than the gun by about 700 ns. From Figure 5.14, the variation of the rf power plus beam loading in the linac yield a significant variation of the central momentum in a macro-pulse than for the gun.

The effect of the linac acceleration is more on the beam energy rather than bunch length demonstrated in Section 4.3.4. If we include this effect, the bunch length in a macro-pulse varies about $\pm(10 - 20)\%$. If we add another small factor that the radiation scale logarithmically as the beam energy, the error introduced should be around $\pm 20\%$.

5.8.2 Reasons for Discrepancy

The main reasons for bunch lengthening discussed above have been accounted for in computation except for the space charge effect and variation of rf fields in the linac. But there are other factors that have not been considered due to either practical limitations of the system or computational difficulty.

First of all, the formulation for radiation we have been using is only approximate for our system: the radiation spectrum and form factor in (1.5) are for monochromatic beams, and transition radiation discussed in Section 1.3.2 assumes an infinite wall. Also the validity of simulation such as slicing a macro-pulse into segments of constant effective accelerating field in the gun, all with a constant cathode current density, cannot be established directly. For example, the measured momentum spreads are always larger than those of simulations partially because the speed of the

electronics is too slow to resolve individual bunches. Another reason is secondary electrons generated by back-bombarding electrons can have poor parameters such as large angles and positions. Since back-bombardment is not considered by MASK, plus inadequate knowledge of the field level and cathode current density in the gun and the linac entrance phase, simulated bunch distributions in phase space only resemble actuality approximately.

These factors may explain the remaining discrepancy to why the measured bunch length can be sometimes shorter than calculation.

Momentum Spread of the Beam

As stated earlier, the radiation spectrum and form factor used are for monochromatic beams. If the energy spread is non-zero, the total radiation is the superposition from individual electrons in a bunch as in (1.2). However, the energy spread after the linac acceleration is estimated to be about $\pm 0.4\%$ in (4.32), using a mono-chromatic beam is a reasonable approximation.

Transverse Beam Distribution

By using the square of the Fourier transform of a longitudinal bunch distribution as the form factor in (1.7), we have implicitly assumed that the transverse bunch distribution is symmetric. This is not true unless the observation of radiation is on-axis ($\theta = 0$ in (1.18)) [54]. For an off-axis observation such as in our case, transverse distribution contributes to the form factor even for a azimuthally symmetric bunch. But the transverse contribution to the form factor is negligible if the beam size is small [54].

Linac Entrance Phase

Since bunches experience different acceleration in the gun before the gun equilibrates, the exit time out of the gun can be different from one bunch to the next. Bunches with higher central momenta naturally exit earlier while ones with lower central momenta exit later, shown in Figure 2.5. They are not exactly 350 ps apart.

The earlier exit time for a high-energy bunch is compensated to some extent by a larger loop inside the alpha magnet. The net effect is bunches of different central momenta entering the linac at slightly different phases. This has not been considered as the entrance phase of each micro-bunch is not measurable so each simulated bunch is assumed to enter the linac on the crest in computation.

This effect is of second order ($O(\varphi^2)$) in (4.26) if the bunch is almost riding on the crest of the acceleration ($\varphi \approx 0$). Let us make a quick estimation. Suppose the nominal bunch rides on the crest at the linac entrance, then the bunches with slightly different central momenta by $\pm 4\%$ enter the linac ahead and behind the crest by 4.4° and 3.9° for an alpha gradient of 321.1 G/cm from simulation. The small difference in the linac entrance phase would cause only 0.2% to 0.3% extra lengthening.

Index of Refraction and Absorption of the Beam Splitter

Throughout calculation, the index of refraction of the mylar beam splitter is assumed to be 1.85 over the entire range of our radiation. In fact, it can be a function of frequency.

Furthermore, literature often gives different values for the index of refraction of mylar in this frequency range [60], ranging from 1.7 to 1.9. This can result in a slightly different mylar transmission efficiency and different locations of zeros. For example, there should be a complete suppression at the first node at 3.45 THz (115.1 cm^{-1}) in the raw spectrum in Figure 5.17b) for a beam splitter of $25.4 \mu\text{m}$ thickness. Yet, there is no such a dip. It can be due to noise in the bolometer, or a wrong value for the index of refraction shifting all zeros slightly.

Also, the absorption of the beam splitter has not been considered. Actually, P. Richard showed that the absorption by the beam splitter is larger at higher frequency [53] which cannot be explained by thin film interference alone [60]. These two factors introduce some uncertainty into corrected spectra.

Misalignment of the Beamline

In computation, the beam centroid is always assumed to be perfectly centered. But

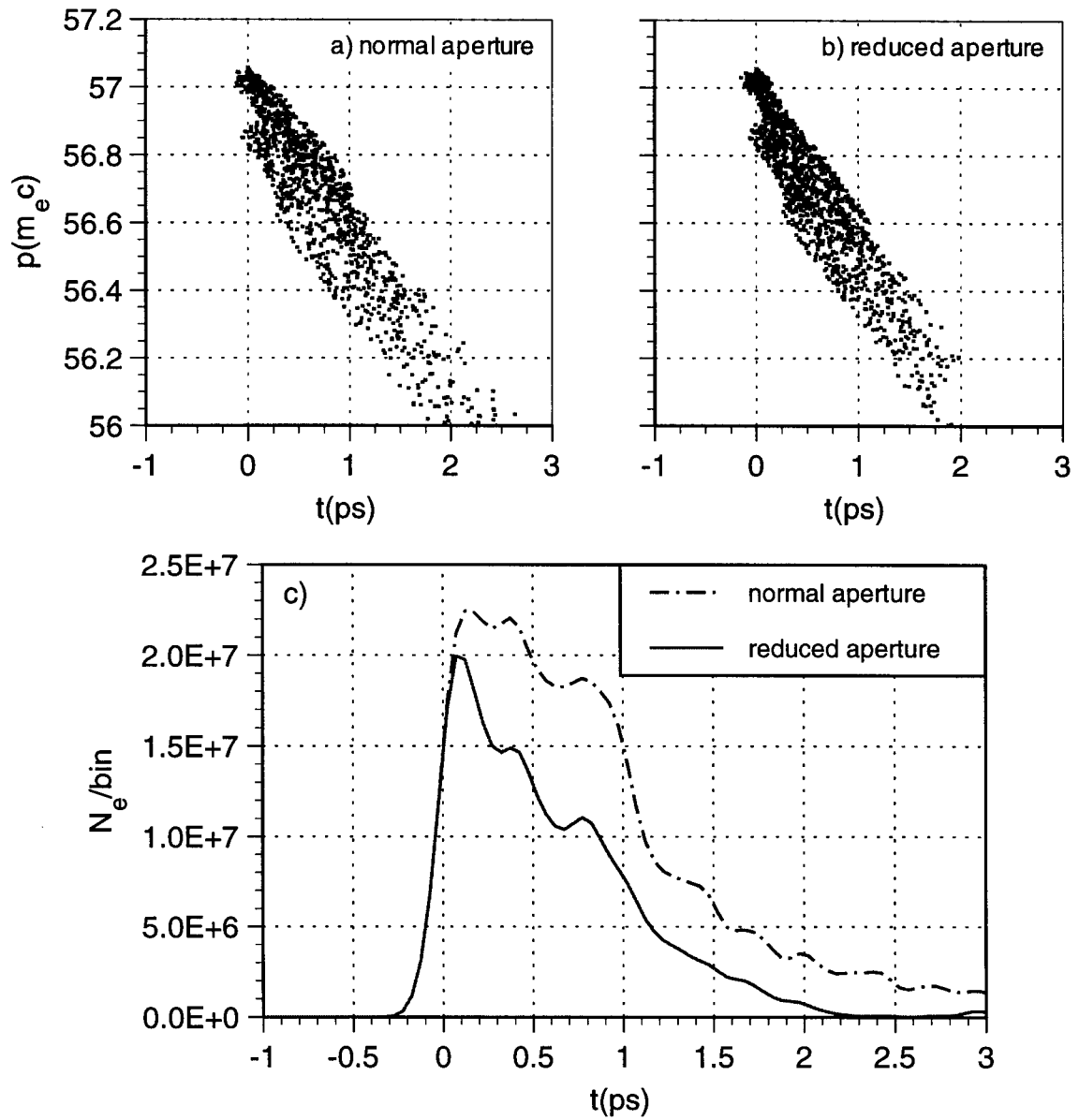


Figure 5.25: Longitudinal phase space at the transition radiator for normal a) and reduced aperture b) including the divergence effect and the corresponding histograms c).

this cannot be true since we always need a fair amount of steering due to misalignment. Also the beam pipe radius can have some additional scraping. This would reduce the bunch length only if the divergence effect is included because without it, scraping only reduces the beam intensity without affecting the bunch length. Misalignment is quite hard to take into consideration in calculation since we do not know how much and where the beam line is misaligned.

Reducing the aperture by 0.5 mm throughout the beam line in tracking may give a clue about the effect. The two longitudinal phase plots along with the histograms at the transition radiator with a normal and reduced aperture including the divergence effect are shown in Figure 5.25. The equivalent width reduces from 1.36 to 0.9 ps, 30% shorter though the intensity also reduces to 60%. The part that is scrapped off by a reduced aperture is mostly low energy particles while the highest energy particles are scarcely affected. Though the actual beam line may not be misaligned by that much everywhere, additional scraping by aperture does shorten a bunch which may explain why the measured bunch length can sometimes be shorter than calculation.

Inefficient Energy Scrapers

Since the energy scrapers in the alpha magnet only work perfectly for on-axis particles with zero angles upon entrance, they always allow some particles not in the selected momentum window to go through while blocking some particles in the selected window with too large angles or displacements. The unwanted particles may contribute to tails in bunches. Simulation shows that for the usual scraper positions — the low scraper at $3.8 - 4.5 m_e c$ and high scraper open, the effectiveness is fairly good, about 99%. That is, up to 1% of unwanted particles can leak through while about equal amount of wanted particles are blocked. The actual efficiency depends on the central momentum of a bunch and lattice.

For a smaller scraper opening, the efficiency is lower. For an opening of only $\pm 4\%$ around $5 m_e c$, it is reduced to 93% – 98%. In reality, the efficiency may be further reduced by misalignment.

In calculation, bunches are assumed to radiate coherently 100% using the measured T3 current, but in actual runnings, a small fraction of the beam may be just

trailing and not radiate coherently at all. The less than one slopes at both high ends of the curves in Figure 5.15 support this speculation. Also the energy scrapers do not work as effectively for a very narrow opening because the measured bunch length does not shorten as much as expected for a very narrow opening. The reason is still unclear. It is possible that the energy scrapers, which are made of copper block, may produce secondary electrons, or it can be due to field errors of the alpha magnet or misalignment.

Alpha Magnet Field Errors

In computation, the alpha magnet is assumed to be without any multipole errors. But due to the beam port and the vertical mirror plate at the entrance, in addition to manufacture error and misalignment, the alpha magnet is not a perfect quadrupole.

The largest field error in the alpha magnet comes from the asymmetry introduced by the beam port [12]. To know the actual effect on the bunch length, it requires integration of particle motion in the alpha magnet but we can estimate it. For the nominal beam energy and normal range of the alpha magnet gradient, the field error is no more than 20 G which translates into a gradient error up to 3 G/cm, depending on the gradient and particle position [12]. For a lower gradient (larger loop), the relative error is larger. The relative gradient field error for the operating range of our alpha magnet, between 300 and 400 G/cm, is between 0.2% to 0.6%. Since the relative loop size scales as $\delta s/s = -\delta g/g/2$, the path length error is only 0.1% to 0.3% and the worst bunch lengthening due to the field errors of the alpha magnet is no more than 0.3%.

RF Frequency

Because the temperature of the system is not controlled, the rf frequency used is rarely the designed value 2856 MHz and is often up to two or three hundreds kHz lower. The effect on the beam momentum and total charge at the gun exit has been shown to be less than 2% different even with a frequency 20 MHz lower, 2836 MHz by RFGUN [12].

For simplicity, I shall compare the RFGUN results. A third order RFGUN run at 2855.5 MHz which is lower than what we usually use confirms that it has a negligible effect on the beam parameters. For the first particles at the gun exit, there is about 0.02% difference in momentum, 0.06° difference in phase and the average output current is essentially the same. The effect should be too small to be detectable. The effect of the rf frequency will be summarized later in this section.

Cathode Position

The position of the cathode in the gun was pulled back by 0.635 mm (25 mil) during installation. Unfortunately, we did not learn this until rather later to redo all simulations. But comparing the third order RFGUN results with a pulled back cathode with ones with the designed cathode position ($z_{\text{cath}} = 0$), both with a nominal acceleration ($E_{p2} = 75$ MV/m), shows that the effect is small in longitudinal plane. At the gun exit, the maximum momentum is lowered by only 1% and the exit time for the first particles is delayed by 3.1° in phase. This is because particles now have to spend a longer time in the first cell and by the time they get to the second cell, the fields have already changed sign. Also, the output current is 3% lower.

The effect on the transverse plane is larger: the emittance of the core of the beam at the gun exit has degraded by 20%. But since the emittance of the core of the nominal beam is about 1 mm·mrad, 20% larger emittance is still small. Also the increased emittance comes mainly from a larger beam size, not the divergence which has increased by only 4%. So the larger emittance should not affect the longitudinal plane too much.

The third order RFGUN results for different rf frequencies and cathode positions compared with nominal running conditions ($f_{\text{rf}} = 2856$ MHz, $E_{p2} = 75$ MV/m, $z_{\text{cath}} = 0$) are summarized below. The emittance ϵ_x is for the core of the beam only. All values are normalized to the nominal beam parameters for ease of comparison. (Please refer to Section 2.1.2 for the parameters of the nominal beam.) In all RFGUN runs with different rf frequencies and cathode positions, there is no visible difference in the slope of momentum-time curve in longitudinal phase plane other than momentum shifting

downward slightly.

f_{rf} (MHz)	z_{cath} (mm)	$\frac{\delta p_{\text{max}}}{p_{\text{max}}}$	$\frac{\delta(I_{\text{exit}})}{I_{\text{exit}}}$	δt_{exit} (deg)	$\frac{\delta \epsilon_x}{\epsilon_x}$	$\frac{\delta \sigma_x}{\sigma_x}$	$\frac{\delta \sigma_{x'}}{\sigma_{x'}}$
2856	0	0	0	0	0	0	0
2855.5	0	0.02%	-2×10^{-7}	-0.06	-0.05%	0.3%	-0.08%
2856	-0.635	-1.04%	-3.1%	3.1	21.2%	58%	4.5%
2855.5	-0.635	-1.02%	-3.2%	3.0	21.1%	58%	4.2%

From above, the effect of the rf frequency is negligible. And since the major factors discussed in Section 5.8.2 can easily give 20% error in calculation, both effects from the rf frequency and cathode position are small in comparison.

5.9 Conclusion

5.9.1 Summary of Results

Our radiation and electron beam parameters are summarized in the table below. SUNSHINE is the first sub-picosecond electron source in operation. The coherent radiation from synchrotron and transition radiation has a broad band spectrum determined by the Fourier transform of the particle distribution. The radiation generated by sub-picosecond electron bunches fills nicely in the gap from a wavelength between $35 \mu\text{m}$ to microwave in Figure 1.1. Compared with a conventional black body radiation source at 2000 K at $100 \mu\text{m}$ wavelength, the average radiance ($\text{W}/\text{mm}^2/\text{mr}^2/100\% \text{BW}$) of our coherent transition radiation is five orders of magnitude higher [57]. It provides a feasible light source with a high average intensity in the FIR regime that is also simple to operate.

$$\begin{aligned}
 l &\geq 0.28 \text{ ps} \\
 \hat{P}_{\text{TR}} &\leq 1 \text{ MW} \\
 \hat{I} &\leq 200 \text{ A} \\
 \lambda &[35, 1000] \mu\text{m}
 \end{aligned}$$

5.9.2 How to Improve

If we want to improve the performance of the system, we need to have both shorter electron bunches and higher peak electron current at the radiation sources. There are few things that can either reduce the bunch length or improve the transmission efficiency of the electron beam through the beam line.

More RF

First and most important, our gun is limited in rf power. From the spectral plots of the GTL beam, the greatest reason that most micro-bunches in a macro-pulse are not optimally compressed is beam loading, especially due to back-bombardment. If there is more rf power, we can achieve high electron current without compromising the beam energy and maintain the equilibrium for a longer time in a macro-pulse.

Anti-backbombardment Device

Another thing that is worth investigating to shorten the average bunch length in a macro-pulse is the anti-backbombardment device in the gun since the beam loading is due mainly to back-bombarding electrons. This can be implemented in conjunction with more rf power into the gun to lengthen the equilibrium plateau in a macro-pulse that has a constant central momentum and high current. Then we can achieve simultaneously high current and momentum for a longer time hence shorter average bunch length and higher radiation energy in a macro-pulse.

Aperture Limits

The divergence effect has been shown to be the most significant effect in bunch lengthening for a micro-bunch. Most of the lengthening occurs in GTL when electrons are only quasi-relativistic. Since electron bunches out of the gun have large rms angles which require strong focusing for a good beam transmission, this results in a large extra excursion. For example, for particles with a ± 10 mrad angle, this extra path length from the transverse planes can easily be as large as tens to a hundred μm in GTL, same order as the bunch length we are striving for. What is worse is, unlike the

velocity spread effect, this is not correctable but remains and accumulates throughout the beam line.

The simulation in the previous section shows that reducing the aperture by 0.5 mm uniformly throughout the beamline can reduce the bunch length by 30% (see Figure 5.25). A simple solution is installing aperture limits in GTL to rid of particles of large displacements. Of course, this will also reduce the electron beam current.

Optimize Focusing

Another more elaborate solution to reduce the divergence effect is to redesign the focusing. To minimize this extra path length difference, gentle focusing is more desirable. For effective focusing in both x and y planes, a solenoid may be more suitable than the current setting of quadrupoles of alternating gradient because at the gun exit, the beam is cylindrically symmetric.

Focusing over the Linac

This is for ease of transmission through the linac for some electrons can get lost along and right after the linac because the aperture of the linac is only 0.9 cm at the exit and the vacuum pipe right after it has a radius of only 1.2 cm.

Beam Splitter Efficiency

To obtain the real radiation spectrum, the raw spectrum from a Michelson scan needs to be corrected by dividing the mylar beam splitter efficiency ($|RT|^2$) following (5.3). Right now, the theoretical values in (5.4) and (5.5) are used. This introduces some uncertainty in the final product — the corrected radiation spectrum. It is due partly to insufficient knowledge of the index of refraction and thickness for the beam splitter.

Furthermore, the theory of thin film interference for a constant index of refraction does not predict suppression at higher frequencies so $|RT|^2$ for different thicknesses of the beam splitter maintains same peak values with different periodicity of nodes in frequency. But in our experience, a thick beam splitter always gives less high

frequency response than a thin one, which may be due to absorption. It would be more ideal to measure the beam splitter efficiency and use it to correct the raw radiation spectrum.

Water Absorption Spectrum

In addition to the beam splitter efficiency, the other factor that obscures the real radiation spectrum is the water absorption by air, especially the lines are thicker compared to a pure water vapour [53]. We attempted to get rid of them by covering the Michelson interferometer with plastic and filled it with dry nitrogen. It did reduce the water absorption lines at higher frequency above about 1.5 THz (50 cm^{-1}) but not much below that. It would be better to subtract the water lines and recover the real spectrum if a measurement for water absorption spectrum in air is made in the near future.

Appendix A

List of Notations

A.1 Miscellaneous

ABB : anti-backbombardment coils in the gun.

$E_{pi} = \max_i E(z)$: peak acceleration field in the i^{th} cell in the rf gun.

$\epsilon_{x,y}$: emittance of the x (y) plane.

f_{rf} : the rf frequency.

FC : Faraday cup (the beam dump) at the end.

FFT: fast Fourier transform.

FIR: far-infrared.

FTCS : forward-time-centered-space difference scheme.

GTL: beam line from the gun exit to the linac entrance (see Figure 1.5).

HDPE : high density polyethylene.

\hat{I} : peak electron current.

$l_{\text{eff},i}$: effective length of the i^{th} cell in the gun.

Λ : plasma parameter.

λ_{rf} : the rf wavelength.

LTD : beam line from the linac exit to the beam dump at the end (see Figure 1.5).

p_0 : *central momentum*, the most populated momentum bin in a momentum histogram. Not necessarily equal to the average momentum unless the distribution is

symmetric.

$\mu = \Delta p/p_0$: relative momentum spread. This unusual choice of notation would become clear in Chap 3.

Q_0 : quality factor of the rf gun.

Q1-Q9 : quadrupole 1 through quadrupole 9 (see Figure 1.5).

SR : synchrotron radiation.

SUNSHINE: Stanford University Short Intense Electron Souce.

T_{cath} : normal cathode operating temperature.

T1-T4 : toroid 1 through toroid 4 (see Figure 1.5).

TR : transition radiation.

V_b : bolometer signal.

ω_p : plasma frequency.

A.2 Bunch Length

There are different ways of defining the “width” of an arbitrary distribution function $f(t)$: full width at half maximum (*FWHM*), the root of mean square (*rms*), *equivalent width* (W), etc. rms is the second moment of a distribution function

$$t_{\text{rms}} = \sqrt{\langle t^2 \rangle} \equiv \sqrt{\frac{\int_{-\infty}^{\infty} dt (t - \langle t \rangle)^2 f(t)}{\int_{-\infty}^{\infty} dt f(t)}}$$

where $\langle t \rangle$ is the *mean* which happens to be the first moment. But for a very asymmetric distribution such as our beam, the rms usually overestimates the width hence is not a good measure for the bunch length. In this thesis, when compared a bunch with calculation, the equivalent width is used,

$$W \equiv \frac{\int_{-\infty}^{\infty} dt f(t)}{f_{\text{max}}}$$

$W = \sqrt{2\pi}\sigma$ for a Gaussian distribution and full width for a rectangular bunch. Incidentally, W can be regarded as the “full width” for a Gaussian since $\int_{-W}^W f(t) dt = 99\%$.

Appendix B

Running Mean with a Gaussian Filter

When processing signals or data, it is often necessary to filter out noise which is usually made of high frequency fluctuations. For numerical simulations, the fluctuations are statistical since there are many fewer particles than in an actual beam. For example, a typical micro-bunch has $10^8 - 10^9$ electrons but there are only few thousands macro-electrons in simulations. In order to extend the form factor of a simulated bunch to high frequencies, a small bin in time is essential. But because of the finite number of particles, the finer the bin size, the more the statistical fluctuations in the high frequencies. To get a better bunch distribution statistically, it is necessary to average the data to rid of spurious high frequency components and smooth out the graininess in the data. One can employ some low pass filter in the frequency domain or a running mean, which is just the discrete convolution of a rectangular window over the raw data, in the time domain [63]. Of course, a proper sampling frequency must be used to avoid aliasing and a suitable low pass filter that passes the highest frequency of interest.

But since a rectangular window uses equal weights for all points and the Fourier transform of a rectangular function is just the sinc function, there are many nodes and high frequency lobes, also the first side lobe is only 13 dB down from the main peak shown in Figure B.1.

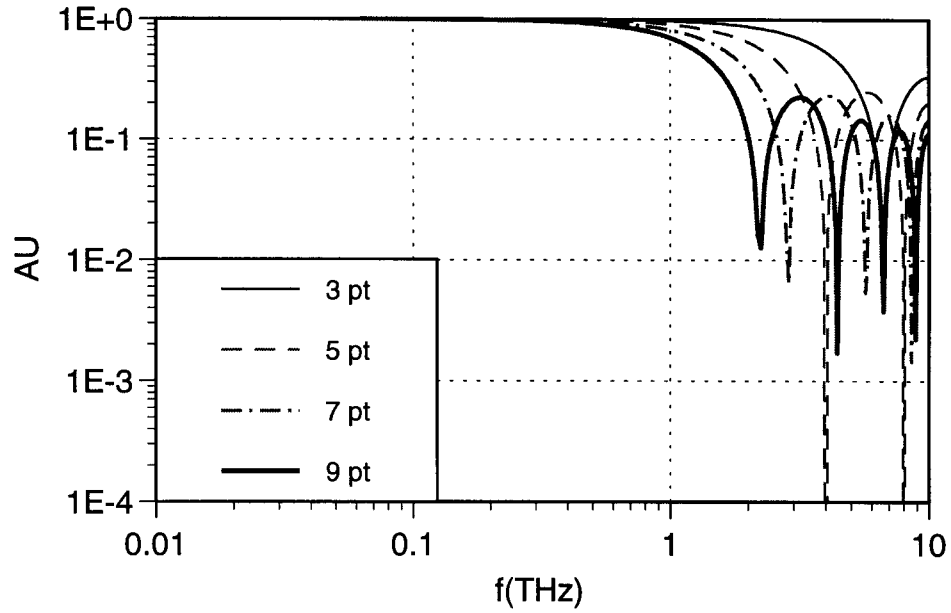


Figure B.1: FFTs of rectangular windows (equal weight) for running means of 3, 5, 7 and 9-point.

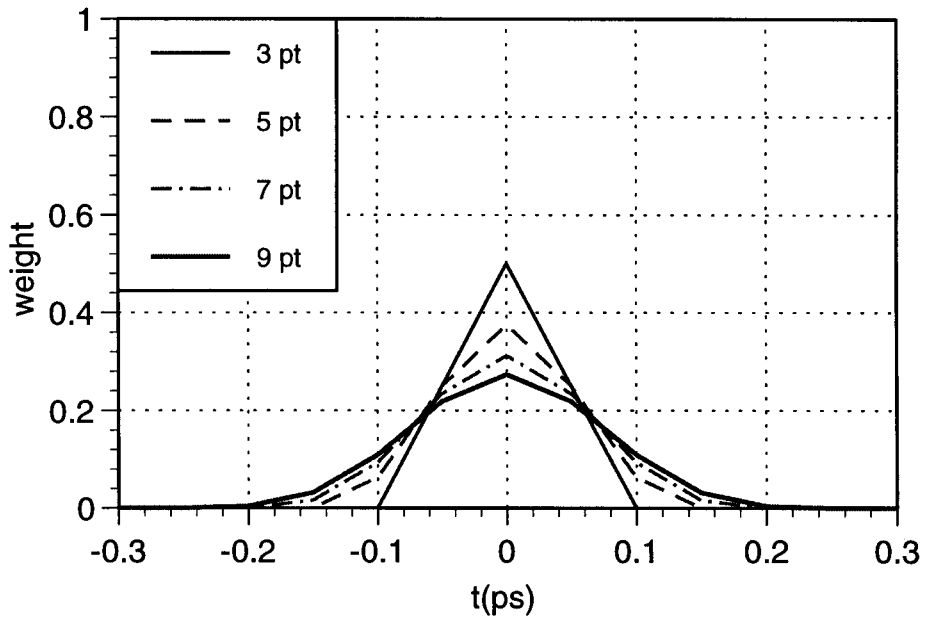


Figure B.2: Weights of binomial filters of 3, 5, 7 and 9-points in the time domain.

One easy solution is to taper the window at both ends. Hence the 3-point running mean filter has the weight ratio of 1:2:1. Performing it twice gives a 5-point filter of weight ratio 1:4:6:4:1 and three time gives a 7-point filter, and so forth [64]. In fact, the weight ratios are the coefficients of the binomial distribution, i.e. for a n -point binomial running mean, we have

$$w_i^B \sim \frac{(n-1)!}{i!(n-1-i)!}, \quad (\text{B.1})$$

apart from some normalization constant. Figure B.2 shows the binomial filter for the 3, 5, 7 and 9-point running means. This method only has a zero at the end point in the frequency space and no side lobes; Figure B.3 shows the corresponding FFTs for a bin size of 0.05 ps and span of 16 ps used in simulations. A slight inconvenience is that the node is right at the end point making it a nuisance for log scale plots.

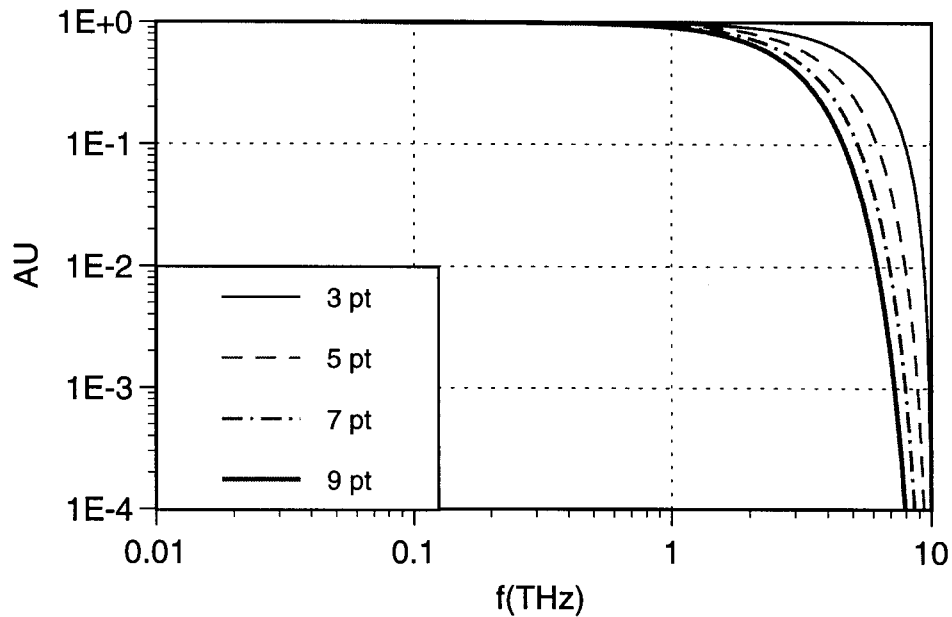


Figure B.3: FFTs of binomial windows for running means of 3, 5, 7 and 9-point.

There are other more elaborate windows for running means such as Hanning, Hamming or Blackman which are all combinations of sine and cosine functions [65]. They either reduce the side lobes at the expense of spectral resolution or vice versa.

Another natural choice is a Gaussian filter, since the Fourier transform of a Gaussian is also a Gaussian. Convolution with a Gaussian window is equivalent to treating each discrete datum point in a simulation, a delta function, as a Gaussian distribution. The weight at the i^{th} point in an n -point Gaussian running mean would be

$$w_i^G \sim \exp \left[-\frac{\left(i - \frac{n-1}{2}\right)^2 \Delta x^2}{2\sigma_n^2} \right], \quad (\text{B.2})$$

where $i = 0, \dots, n-1$ and Δx is the spacing in the time domain. Since a real Gaussian extends indefinitely, we need to choose the standard deviation for a given n so that we can truncate it beyond the end points. That is, two adjacent points right next to the end points are negligible if

$$w_{-1}^G = w_n^G = \exp \left[-\frac{(n+1)^2 \Delta x^2}{8\sigma_n^2} \right] \ll 1, \quad (\text{B.3})$$

using (B.2). Let us pick 0.01 as the threshold, then we get

$$\sigma_n = \frac{n+1}{\sqrt{8 \ln 100}} \Delta x. \quad (\text{B.4})$$

For example, for a 3-point Gaussian running mean we have

$$\begin{aligned} \sigma_3 &= 0.66\Delta x \\ w^G &= (0.194, 0.613, 0.194) \end{aligned}$$

in which w^G has been normalized.

Figure B.4 shows the Gaussian filter for running means of 3, 5, 7 and 9-point. For n larger than 3, the Gaussian filter and binomial filter are almost identical in the time domain. Figure B.5 shows the corresponding FFTs. The side lobes are the price for truncation. But compared with the FFTs of a rectangular filter in Figure B.1, the first side lobes are down to more than 48 dB of the main peak, a significant improvement. Furthermore, the simplicity in computing a Gaussian filter compared with other more elaborate windows is a clear advantage. Also since the nodes do not occur right at the discrete points in the frequency space, the Fourier transform of the convoluted result is ready for log scale.

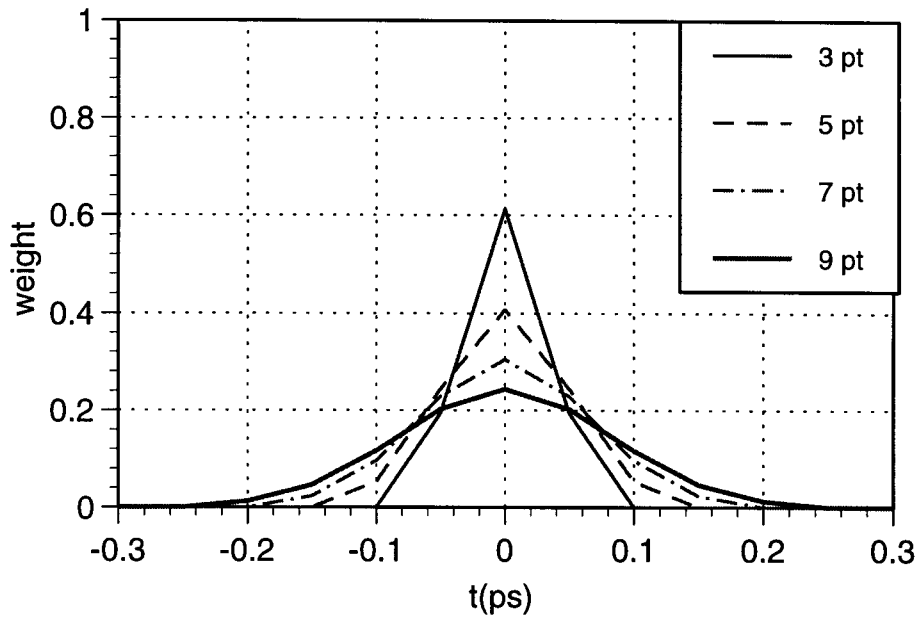


Figure B.4: Weights of Gauss filters of 3, 5, 7 and 9 points in the time domain.

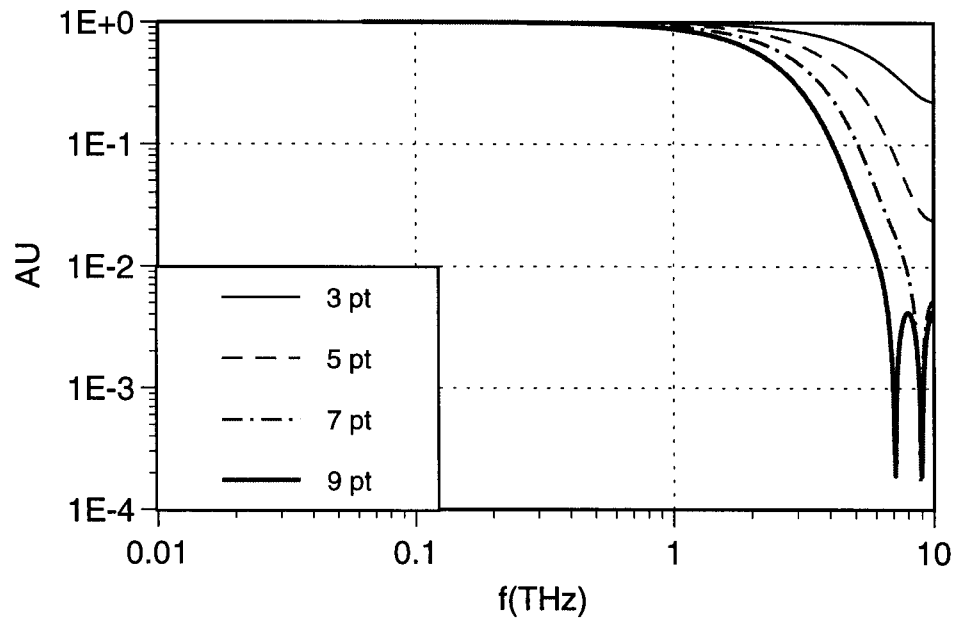


Figure B.5: FFT of Gaussian filters of 3, 5, 7 and 9-point running mean.

Bibliography

- [1] K. J. Kim. Free-electron lasers: Present status and future prospects. *Science*, 250:88–93, 1990.
- [2] H. Motz. Applications of the radiation from fast electron beam. *J. Appl. Phys.*, 22(5):527, 1951.
- [3] F. C. Michel. Intense coherent submillimeter radiation in electron storage rings. *Phys. Rev. Lett.*, 48(9):580–583, 1982.
- [4] R. Kato et al. Suppression of coherent synchrotron radiation in conducting boundaries. In S. T. Corneliussen, editor, *Proceedings of the 1993 Particle Accelerator Conference*, volume 2, pages 1617–1619, New York, USA, 1993.
- [5] T. Nakazato et al. Observation of coherent synchrotron radiation. *Phys. Rev. Lett.*, 63(12):1245–1248, 1989.
- [6] E. B. Blum, U. Happek, and A. J. Sievers. Observation of coherent synchrotron radiation at the cornell linac. *Nucl. Instr. and Meth.*, A307(2–3):568–576, 1991.
- [7] U. Happek, A. J. Sievers, and E. B. Blum. Observation of coherent transition radiation. *Phys. Rev. Lett.*, 67(21):2962–2965, 1985.
- [8] Y. Shibata et al. Observation of coherent transition radiation at millimeter and submillimeter wavelengths. *Phys. Rev. A*, 45(12):R8340–8343, 1992.
- [9] C. Pellegrini and D. Robin. Quasi-isochronous storage ring. *Nucl. Instr. Meth.*, A307, 1991.

- [10] E. Tanabe, M. Borland, M. C. Green, R. H. Miller, L. V. Nelson, J. N. Weaver, and H. Wiedemann. A 2-Mev microwave thermionic gun. In *Proc. of 14th Meeting on Linear Accelerators*, Nara, Japan, September 1989.
- [11] M. Borland, M. C. Green, R. H. Miller, L. V. Nelson, E. Tanabe, J. N. Weaver, and H. Wiedemann. Performance of the 2-Mev microwave gun for the ssrl 150 Mev linac. In *Proceedings of the 1990 Linear Accelerator Conference*, Albuquerque, New Mexico, USA, 1990.
- [12] M. Borland. *A High-brightness Thermionic Microwave Electron Gun*. PhD thesis, Stanford University, 1991.
- [13] H.-C. Lihn. Simulation of coherent synchrotron radiation from an ultra-short electron bunch. ACD-124 124, SSRL, 1982.
- [14] H. Wiedemann. *Basic Principles and Linear Beam Dynamics*, volume 1 of *Particle Accelerator Physics*. Springer-Verlag, 1993.
- [15] J. Schwinger. On the classical radiation of accelerated electrons. *Phys. Rev.*, 75(12):1912–1925, 1949.
- [16] J. D. Jackson. *Classical Electrodynamics*. John Wiley & Sons, 2nd edition, 1975.
- [17] A. Hofmann. Theory of synchrotron radiation. ACD-38 38, SSRL, 1986.
- [18] H. Wiedemann. *Nonlinear and Higher-Order Beam Dynamics*, volume 2 of *Particle Accelerator Physics*. Springer-Verlag, 1994.
- [19] L. D. Landau and E. M. Lifshitz. *The Classical Theory of Fields*, volume 2 of *Course of Theoretical Physics*. Pergamon Press, 4th edition, 1975.
- [20] L. D. Landau and E. M. Lifshitz. *Electrodynamics of Continuous Media*, volume 8 of *Course of Theoretical Physics*. Pergamon, 2nd edition, 1984.
- [21] M. L. Ter-Mikaelian. *High-Energy Electromagnetic Process in Condensed Media*. Wiley-Interscience, 1972.

- [22] A. T. Drobot. Numerical simulation of high power microwave sources. *IEEE Trans. Nucl. Sci.*, NS-32(5):2982+, 1985.
- [23] Y. C. Huang. *Design and Characterization of a Subcompact, Far-Infrared Free-Electron Laser*. PhD thesis, Stanford University, 1994.
- [24] P. A. Sturrock. *Plasma Physics: an Introduction to the theory of Astrophysical, Geophysical and Laboratory Plasmas*. Cambridge University Press, 1994.
- [25] W. H. Press, B. P. Flannery, S. A. Teukolsky, and W. T. Vetterling. *Numerical Recipes in C*. Cambridge University Press, 1988.
- [26] A. T. Drobot. Class notes for computer methods for accelerator physics, 1995 Accelerator Summer School. Thanks to H.-C. Lihn for making me aware of this condition.
- [27] K. J. Kim. Rf and space-charge effects in laser-driven rf electron guns. *Nucl. Instr. Meth.*, A275:201–218, 1989.
- [28] R. C. Davidson. *Physics of Nonneutral Plasmas*. Addison Wiley, 1990.
- [29] S. Ichimaru. *Basic Principles of Plasma Physics: a Statistical Approach*. W. A. Benjamin, 1973.
- [30] L. Lawson. *The Physics of Charged-Particle Beam*. Clarendon Press, 1977.
- [31] F. F. Chen. *Introduction to Plasma Physics and Controlled Fusion*. Plenum Press, 2nd edition, 1984.
- [32] M. Reiser. *Theory and Design of Charged Particle Beams*. John Wiley & Sons, 1994.
- [33] A. W. Chao. *Physics of Collective Beam instabilities*. John Wiley & Sons, 1993.
- [34] J. G. Wang, H. Suk, D. X. Wang, and M. Reiser. Determination of the geometry factor for longitudinal perturbations in space-charge dominated beams. *Phys. Rev. Lett.*, 72(13):2029–2032, 1994.

- [35] W. F. Ames. *Numerical Methods for Partial Differential Equations*. Academic press, 3rd edition, 1992.
- [36] E. Zauderer. *Partial Differential Equations*. John Wiley & Sons, 2nd edition, 1989.
- [37] A. L. Fetter and J. D. Walecka. *Theoretical Mechanics of Particle and Continua*. McGraw-Hill, 1980.
- [38] U. Funk, U. Krüger, K. Mika, L. Stanco, V. G. Vaccaro, and G. Wüstefeld. Mathematical and numerical methods for the nonlinear hyperbolic propagation problem, a preliminary treatment of collective space charge effects in accelerator physics. 1982.
- [39] J. M. Dawson. Nonlinear electron oscillations in a cold plasma. *Phys. Rev.*, 113(2):383–387, 1959.
- [40] T. Katsouleas and W. B. Mori. Wave-breaking amplitude of relativistic oscillations in a thermal plasma. *Phys. Rev. Lett.*, 61(1):90–93, 1988.
- [41] A. C. L. Chian. Wave-breaking condition of space-charge waves in a relativistic electron beam. *Phys. Rev. A*, 39(5):2561–2564, 1989.
- [42] A. Faltens, E. P. Lee, and S. S. Rosenblum. Beam end erosion. *J. Appl. Phys.*, 61(12):5219–5221, 1987.
- [43] A. Chuvatin and B. Etlicher. Experimental observation of a wedge-shaped density shock in a plasma opening switch. *Phys. Rev. Lett.*, 74(15):2965–2968, 1995.
- [44] J. G. Wang, D. X. Wang, and M. Reiser. Generation of space-charge waves due to localized perturbations in a space-charge dominated beam. *Phys. Rev. Lett.*, 71(12):1836–1839, 1993.
- [45] J. G. Wang, D. X. Wang, H. Suk, and M. Reiser. Reflection and transmission of space-charge waves at bunched beam ends. *Phys. Rev. Lett.*, 74(16):3153–3156, 1995.

- [46] H. Enge. Achromatic magnetic mirror for ion beams. *Rev. Sci. Instr.*, 34(4):385+, 1963.
- [47] K. L. Brown, F. Rothacker, D. C. Carey, and Ch. Iselin. Transport: a computer program for designing charged particle beam transport systems. SLAC 91, rev 2, SLAC, 1977.
- [48] A. W. Chao. Nonlinear dynamics, 1994. Class note at Applied Phys, Stanford.
- [49] J. Sebek. Private Communication.
- [50] J. F. Schmerge, J. W. Lewellen, Y. C. Huang, J. Feinstein, and R. H. Pantell. The free-electron laser as a laboratory instrument. *IEEE JQE*.
- [51] H.-C. Lihn. First observation of stimulated coherent transition radiation. PUB-95-6913 95-6913, SLAC, 1995.
- [52] H.-C. Lihn. Measurement of 50-fs (rms) electron pulses. In *AIP Conference Proceedings*, Beam Instrumentation Workshop, Vancouver, Canada, 1994.
- [53] P. L. Richard. High-resolution fourier transform spectroscopy in the far-infrared. *J. Opt. Soc. Am.*, 54:1474, 1964.
- [54] H.-C. Lihn, P. Kung, C. Settakorn, H. Wiedemann, and D. Bocek. Measurement of subpicosecond electron pulses. *Phys. Rev. E*, to be published.
- [55] R. J. Bell. *Introductory Fourier Transform Spectroscopy*. Academic Press, 1972.
- [56] Y. Huang. Beam pulse shorting phenomena in a rf electron gun. In *Proceedings of Particle Accelerator Conference*, San Francisco, USA, 1991.
- [57] P. H. Kung, H.-C. Lihn, H. Wiedemann, and D. Bocek. High-intensity coherent fir radiation from sub-picosecond electron bunches. In V. N. Similey and F. K. Tittel, editors, *Proceedings of SPIE*, volume 2118 of *Gas, Metal Vapor and Free-electron Lasers and Applications*, pages 191–201, Los Angeles, USA, 1994. SPIE.

- [58] D. Y. Smith, E. Shiles, and M. Inokuti. *The Optical Properties of Metallic Aluminum*. Academic Press Inc., 1985.
- [59] P. H. Kung, H.-C. Lihn, H. Wiedemann, and D. Bocek. Generation and measurement of 50-fs (rms) electron pulses. *Phys. Rev. Lett.*, 73(7):967+, 1994.
- [60] H.-C. Lihn. Private Communication.
- [61] R. J. Briggs. Space-charge waves on a relativistic, unneutralized electron beam and collective ion acceleration. *Phys. Fluids*, 19(8):1257+, 1976.
- [62] J. A. Nation and M. Read. Limiting currents in unneutralized relativistic electron beams. *Appl. Phys. Lett.*, 23(8), 1973.
- [63] R. N. Bracewell. *The Fourier Transform and its Applications*. McGraw-Hill, 2nd edition, 1986.
- [64] P. R. Bevington. *Data Reduction and Error Analysis for the Physical Sciences*. McGraw-Hill, 2nd edition, 1992.
- [65] L. B. Jackson. *Digital Filters and Signal Processing*. Kluwer Academic Publishers, 2nd edition, 1989.

Index

A

alpha magnet

- working limit, 89
- energy scrapers, 85, 121, 126, 157
- equation of motion, 82
- longitudinal transformation matrix, 88
- transverse transformation matrices, 84
- working limit, 88

anti-backbombardment coils, 120

B

beam loading

- in the gun, 120, 128

beam splitter

- efficiency, 119
- index of refraction, 120, 156

bunch compression

- effect of linac acceleration, 109
- effect of linac entrance phase, 111
- first order prediction, 91
- ultimate limit, 103

bunch length measurement, 140

- average bunch length, 144
- indirect, 139

the most prominent bunch, 145

versus the alpha magnet, 145

bunch lengthening, 81, 97, 153

- divergence effect, 96, 106, 150
- macro-pulse factor, 154
- space charge, 105, 151
- velocity spread, 87, 95, 149

C

coherence, 6

- diffraction limit, 12
- spatial, 12
- temporal, 8

coherent radiation, 6

- first observed, 1
- form factor, 9
- normalized signal, 134
- prediction, 1
- proof for our radiation, 132
- suppression, 10
- synchrotron, 11
- transition, 11

compression

- alpha magnet, 82
- condition, 86–87
- continuity equation, 62

Courant condition, 46

D

Debye length, 56

dispersion relation a circular wave gu

analytic, 50

discrete, 50

E

equivalent width, def, 166

F

far field limit, 8

fluid model for a charged beam, 56

form factor, 9

Gaussian distribution, 10

uniform distribution, 10

FTCS, 70

L

Lax method, 71

M

MASK, 19

mesh size upper limit, 51, 69

Michelson interferometer, 13, 118

beam splitter efficiency, 120

momentum compaction factor, 63

N

negative mass instability, 64

P

peak current

measured, 145

simulation, 33

photo-cathode, 52

plasma frequency, 43

plasma parameter, 56

R

radiation energy measurement, 135

rf gun

effect of acceleration, 37

effect of cathode current density, 40

longitudinal phase distribution, 23,
29

nominal beam paramters, 36

nominal running conditions, 25

parameters, 3

rf bunching, 25

transverse phase distribution, 36

RFGUN, 19

running mean, 167

binomial, 169

Gaussian, 104, 170

S

shock wave instability, 47

breaking time, 67

slippage factor, 63

space charge

long wave limit, 61

equation of motion, 63

geometric factor, 61

limiting current, 153

- shock wave instability, 64
- space charge wave, 64
- spectral plot for GTL beam
 - ABBs on, 128
 - cold cathode, 122
 - hot cathode, 125
 - momentum resolution, 121
- spectral plot for LTD beam, 131
- symplectic expansion of quadrupoles,
101
- synchrotron radiation, 13

T

- temperature
 - longitudinal, 57
 - transverse, 57
- transformation matrix, 86
 - alpha magnet, 88
 - dipole, 88
 - drift space, 87
 - GTL, 89
 - linac, 90
- transition energy, 63
- transition radiation, 11, 15
 - non-perfect conductor, normal incidence, 16
 - non-perfect conductor, oblique incidence, 17
 - perfect conductor, normal incidence, 15
- trapezoidal model for quadrupoles, 101

U

- useful beam, 32

V

- Vlasov equation, 62

W

- water absorption by air, 140, 164